Experimental Investigation of Effects of Surface Roughness, Wettability and Boiling-Time on Steady State and Transient CHF for Nanofluids

by

Vivek Inder Sharma

B.Tech, Chemical Engineering, Indian Institute of Technology 2007
M.S. Nuclear Science and Engineering, Massachusetts Institute of Technology 2009

SUBMITTED TO THE DEPARTMENT OF NUCLEAR SCIENCE AND ENGINEERING
IN PARTIAL FULFILLMENT OF THE REQUIREMENTS FOR THE DEGREE OF

DOCTOR OF PHILOSOPHY IN NUCLEAR SCIENCE AND ENGINEERING
AT THE
MASSACHUSETTS INSTITUTE OF TECHNOLOGY
MAY 2012

Signature of Author:

Vivek Inder Sharma
Department of Nuclear Science and Engineering
May 15, 2012

Certified by:

Jacopo Buongiorno – Thesis Supervisor
Associate Professor of Nuclear Science and Engineering

Certified by:

Thomas J. McKrell – Thesis Co-Supervisor
Research Scientist, Nuclear Science and Engineering

Certified by:

Lin-Wen Hu – Thesis Co-Supervisor
Associate Director, MIT Nuclear Reactor Laboratory

Certified by:

Kripa K. Varanasi – Thesis Reader
Associate Professor of Mechanical Engineering

Certified by:

Mujid S. Kazimi
TEPCO Professor of Nuclear Science and Engineering
Chair, Department Committee on Graduate Students

Experimental Investigation of Effects of Surface Roughness, Wettability and Boiling-Time on Steady State and Transient CHF for Nanofluids

by

Vivek Inder Sharma

Submitted to the Department of Nuclear Science and Engineering
on May 15, 2012 in Partial Fulfillment of the
Requirements for the Degree of Doctor of Philosophy in
Nuclear Science and Engineering

ABSTRACT

Critical Heat Flux (CHF) is one of the primary design constraints in a nuclear reactor. Increasing the CHF of water can enhance the safety margins of the current fleet of Light Water Reactors (LWRs) and/or increase their power output. It has been shown that a suspension of nanoparticles called nanofluids in DI water enhances the CHF of water significantly. During boiling, nanoparticles in the nanofluid develop a coating on the heater surface, which is porous and hydrophylic, leading to a higher CHF compared to water.

One of the primary objectives of this thesis is to conduct an experimental investigation of the effects of three parameters (i.e. initial roughness, initial wettability and boiling time) on the steady-state CHF of nanofluids. Experiments with DI water served as the base case for CHF values, and experiments with nanofluid were done analyze their effects on CHF. Metallic heaters made of SS304 oriented vertically in a pool of test-fluid are used for experiments. The nanofluid used in the experiments has 0.01 v% ZnO nanoparticles in DI water. Multiple experiments were done to measure CHF of DI water (base-case) and test nanofluid for varied initial surface roughness (R_a), surface wettability and different pre-boiling times. Results indicate that compared to water, nanofluids enhanced CHF by an average of 77% (ranging from 25% to 150% for different surface and experimental conditions). It was also observed that the effect of nanofluids in increasing CHF was less pronounced if the initial heaters contained a superhydrophilic surface coating before use with nanofluids as opposed to the initial heaters being bare and uncoated. Additionally, the thickness of the nanocoating appeared to plateau after approximately 30 – 40 minutes of boiling time, and additional pre-boiling times of up to 8 hours did not have any effect on nanocoating development or CHF.

The other objective of this work is to assess the applicability of nanofluids to accident scenarios in nuclear reactors, which are accompanied by rapid power transients. Such situations are simulated by rapidly increasing heat flux through the heater elements from 0 to CHF in short time frames of 1, 10 and 100 s. It was observed that for nanofluid tests, nanocoatings started to generate on the heater surface in as short time frames as 10 and 100 s, and the nanocoatings enhanced CHF, compared to DI water, by approximately 20%. However, for 1 s tests, nanofluids did not enhance the CHF, and nanocoatings were not detected at the heater surface. Additionally, pre-boiling the heater surfaces in the nanofluid caused a CHF enhancement for all three rates of power increase.

Thesis Supervisor:	Jacopo Buongiorno, PhD
Title:	Associate Professor of Nuclear Science and Engineering Carl R. Soderberg Professor of Power Engineering
Thesis Co-Supervisor:	Thomas J. McKrell, PhD
Title:	Research Scientist, Nuclear Science and Engineering
Thesis Co-Supervisor:	Lin-wen Hu, PhD
Title:	Associate Director, MIT Nuclear Reactor Laboratory
Thesis Reader:	Kripa K. Varanasi, PhD
Title:	Associate Professor, Mechanical Engineering

Acknowledgements

This work would not have been possible without the constant support and encouragement from several people from faculty, staff, students, friends and my family.

I would like to extend my deepest gratitude to Prof. Jacopo Buongiorno for providing me the opportunity to work on this project. It was a rewarding and a great learning experience to overcome various challenges in my research through his guidance and encouragement.

Thanks to Dr. Tom McKrell for the endless hours spent on discussing various aspects of my experiments and the experimental set-up. I learnt a great deal about engineering in general, and materials and electronics in particular by working with you.

Thanks also to Dr. Lin-wen Hu for your support and encouragement during my thesis work.

I would also like to thank Dr. Kripa Varanasi for serving as a part of my committee and my thesis reader, as well as several interesting insights and thoughts provided pertaining to the results of my experiments in this work.

A big thanks is due to Areva for sponsoring this research endeavor.

Thanks to the NSE administration including Peter Brenton, Dorian Cohen, Heather Barry, Clare Egan, Linda Arduino and Rachel Morton for helping me with different tasks ranging from logistical support to computer and IT issues.

Dr. Gordon Kohse, thank you for allowing me to use the spot welder in your lab throughout my thesis work.

Thanks to the entire nanofluids team for their support and ideas throughout the progress of my work. Thanks to Eric Forrest for training me on multiple equipments, to Bren Philips for his time and support in helping me use the IR camera and the Confocal Microscope, to Dr. Bao Truong for sharing his experiences working with nanofluids, and to Harry O'Hanley for helping me with the layer-by-layer coating technique.

Thanks to Dr. Yong Zhang in the Center for Materials Science and Engineering for all his help and technical expertise with the SEM.

Thanks to Chris Love for showing me how to use the Contact Angle Goniometer in a short time frame, and accommodating my needs in his schedule.

This work would have been incomplete without the support and encouragement from my friends and colleagues at MIT. From NSE, Dr. Bo Feng and Dr. Yu-Chih Ko, thank you for helping me transition into the life at MIT. Having you as friends made it really easy for me. Emmy Lin, I had a great time with you and Yu-Chih in Japan, and at MIT. Thanks to classmates who I had the pleasure of developing friendships with: Dustin

Langewisch, Paul Romano, Dr. Joe Fricano, Koroush Shirvan and anyone else who I might have inadvertently missed.

Outside of NSE, I was supported by my friends, who were always there for me to support me, and whose friendship I will always cherish for my entire life. Dr. Sukant Mittal, Dr. Srikanth Patala, Dr. Dipanjan Sen, Vivek Raghunathan, Sumeet Kumar, Harish Sundaresh and Vignesh Sundaresh – you guys made life at MIT fun and easy. Thanks for being my family at MIT and helping me in times of need. Thanks for all the good times and experiences that we shared outside of the academic life at MIT.

Thanks to Ankur Mani, Haitham Hassanieh and Eugen Zgraggen who were my roommates for the bulk of my time at MIT. Thanks to Dr. Venkataramanan Saoundararajan and Barghavi Govindarajan who guided my in my first year at MIT.

Lastly, I would like to thank my family for believing in me throughout my student life. Thanks to my sister, Deepika Sharma, for her encouragement and love. Special thanks to my girlfriend, Shilpa Batra. You greatly inspired and motivated me. Thank you for being my support system for the last 2 years. Most of all, I thank my parents, Mr. Nirmal Inder Sharma and Mrs. Madhu Sharma for raising me the way did, for always encouraging me and believing in me all these years. You made innumerable sacrifices to get me where I am, and I am fortunate to have you as my parents. I dedicate this thesis to you.

Vivek Inder Sharma

Table of Contents

1. INTRODUCTION 23
1.1. BACKGROUND: BOILING AND CRITICAL HEAT FLUX 26
1.1.1. Review: Nucleation *28*
1.1.2. Literature Review: Critical Heat Flux *29*
1.2. LITERATURE REVIEW: NANOFLUIDS 38
1.3. THESIS MOTIVATION AND OBJECTIVES 45
1.4. THESIS ORGANIZATION 48

2. NANOFLUIDS 50
2.1. NANOFLUID CHARACTERIZATION 50
2.1.1. Concentrated Nyacol DP5370 nanofluids *51*
2.1.1.1. Concentration 51
2.1.1.2. pH 52
2.1.1.3. Density 53
2.1.1.4. Particle Size 55
2.1.1.5. Composition 59
2.1.2. Diluted test nanofluids *61*
2.1.2.1. pH 61
2.1.2.2. Density 61
2.1.2.3. Surface Tension 62
2.1.2.4. Thermal Conductivity 63
2.1.2.5. Viscosity 64
2.2. SUMMARY OF NANOFLUID CHARACTERIZATION 65

3. POOL BOILING FACILITY 66
3.1. APPROACH 66
3.1.1. Experiments *66*
3.1.2. Post-test Analysis *67*
3.1.2.1. HR-SEM 67
3.1.2.2. Confocal Microscopy 67
3.1.2.3. Contact Angle 68
3.2. EXPERIMENTAL SET UP: INDIVIDUAL COMPONENTS 69
3.2.1. Test heater *70*
3.2.2. Power Supply and Electrodes *74*
3.2.3. Cu Blocks *79*
3.2.4. Test vessel *82*
3.2.5. Shunt *84*
3.2.6. Voltage Drop *86*
3.2.7. Thermocouples *87*
3.2.8. Hot Plate *88*
3.2.9. Condenser and Chiller *89*
3.3. COMPLETE POOL BOILING FACILITY 90
3.4. DAQ 91

4. STEADY-STATE TESTS 93
4.1. NANOFLUID DILUTION 93
4.2. TEST PROCEDURE 94
4.2.1. PBF Clean Up *94*
4.2.2. PBF Assembly *94*

4.2.3. Test Fluid Transfer 95
4.2.4. Degassing 96
4.2.5. Measurement of Initial Heater Resistance 96
4.2.6. Heat Up to CHF and Recording Data 96
4.2.7. PBF Disassembly 97
4.2.8. Data Reduction: Obtaining Boiling Curve 97
4.3. UNCERTAINTY ANALYSIS 98
4.4. TEST MATRIX 100
4.4.1. Surface Roughness 101
4.4.1.1. Roughness Control 101
4.4.1.2. Pre-Test Surface Analysis 104
4.4.1.3. Results 109
4.4.1.4. Post-Test Surface Analysis 111
4.4.2. Wettability 120
4.4.2.1. Wettability Control 120
4.4.2.2. Pre-Test Surface Analysis 125
4.4.2.3. Results 130
4.4.2.4. Post-Test Surface Analysis 131
4.4.3. Pre-Boiling Time 136
4.4.3.1. Pre-Boiling Time Control 137
4.4.3.2. Pre-Test Surface Analysis 137
4.4.3.3. Results 137
4.4.3.4. Post-Test Surface Analysis 142
4.5. SUMMARY/DISCUSSION OF STEADY-STATE TEST RESULTS 159

5. TRANSIENT TESTS 163
5.1. LITERATURE 163
5.2. MOTIVATION 170
5.3. TEST PROCEDURE 171
5.3.1. Heat up to CHF 171
5.3.2. Data Recording and Analysis 173
5.3.2.1. Definition of CHF 176
5.4. TEST MATRIX 177
5.5. RESULTS 177
5.6. POST-TEST SURFACE ANALYSIS 179
5.7. SUMMARY/DISCUSSION OF TRANSIENT TEST RESULTS 185

6. CONCLUSIONS, MAJOR CONTRIBUTIONS AND FUTURE WORK 188
6.1. CONCLUSIONS 188
6.2. MAJOR CONTRIBUTIONS 190
6.3. RECOMMENDATIONS FOR FUTURE WORK 191

7. APPENDIX A 193
7.1. TEMPERATURE COEFFICIENT OF RESISTIVITY (TCR) FOR SS304 193
7.2. RELATIONSHIP BETWEEN T_{BULK} AND T_W 196
7.3. AXIAL VARIATION OF T_{BULK} AND T_W 198
7.4. AGREEMENT BETWEEN FG AND POWER SUPPLY OUTPUT 205
7.5. CURRENT GAIN BY CSM 208

8. APPENDIX B: COMPLETE EXPERIMENTAL DATA 210
8.1. STEADY-STATE TEST DATA FOR DIFFERENT SURFACES (SECTION 4.4.1) 210

8.2. STEADY-STATE TEST DATA FOR DIFFERENT WETTABILITIES (SECTION 4.4.2) 213
8.3. STEADY-STATE TEST DATA FOR DIFFERENT PRE-BOILING TIMES (SECTION 4.4.3) 215
8.4. TRANSIENT TEST DATA (SECTION 5.5) 222
8.5. TRANSIENT EXPERIMENT BOILING CURVES (SECTION 5.5) 224
9. APPENDIX C: CHF MODEL COMPARISON 229
9.1. HEATER ORIENTATION 229
9.2. SURFACE WETTABILITY 232
9.3. POROSITY 233
9.4. COATING THICKNESS 237
10. REFERENCES 239

List of Figures

Figure 1-1: Typical pool boiling curve 28

Figure 1-2: Bubble formation over cavities in a heated surface 29

Figure 1-3: Vapor structure near heated surface at high heat fluxes, as depicted in [15]. 31

Figure 1-4: Representation of droplet of fluid on a flat surface showing its contact angle (θ) 32

Figure 2-1: Variation of sample weight in TGA for one of the experimental runs. The weight of the sample stabilizes after some time indicating complete evaporation of water, leaving behind only the nanoparticles 52

Figure 2-2: Particle size distribution obtained by DLS 57

Figure 2-3: TEM images of two sections on the TEM grid: a) A region with multiple nanoparticles settled near each other, b) isolated nanoparticles 58

Figure 3-1: Technique for measuring advancing (left) and receding (right) contact angle (from ref. [79]) 69

Figure 3-2: Required current and voltage drops for different thicknesses of SS304 to attain a heat flux of 2000 kW/m^2 71

Figure 3-3: Schematic of the heating element (dimensions in cm) 72

Figure 3-4: 3-D view of the heating element 73

Figure 3-5: Picture of the 24" x 12" x 0.036" SS304 sheet used to cut the heating element from 73

Figure 3-6: Picture of the SS304 heater element 74

Figure 3-7: Picture of the power supply used in the experiments 75

Figure 3-8: Front and side view of the copper electrodes. The heater is mounted between two such electrodes (dimensions in cm) 76

Figure 3-9: Top and side view of the lid used to seal the test section (dimensions in cm) 77

Figure 3-10: 3-D view of the lid used to seal the test section 77

Figure 3-11: The side view of the lid with the Cu-electrodes, showing the positions of the electrodes when the heater is mounted between them (dimensions in cm) 78

Figure 3-12: Photograph of the PBF lid with Cu-electrodes 79

Figure 3-13: Layout of Cu-blocks used to mount heaters in PBF 80

Figure 3-14: Photograph of one surface of the Cu-blocks 81

Figure 3-15: Photograph of other surface of the Cu-blocks 81

Figure 3-16: Photograph of the test heater mounted in the PBF using Cu-blocks 82

Figure 3-17: Top and Front view of the cylindrical beaker used as the test bath (dimensions in cm) 83

Figure 3-18: Photograph of the test vessel, with the gasket on top 84

Figure 3-19: Photograph of the shunt used to measure current 84

Figure 3-20: Photograph of the shunt in the actual circuit 85

Figure 3-21: Spot-welds across the heated length. The spot-welded wires go to DAS 86

Figure 3-22: Photograph showing the two thermocouples (TCs) used to measure bath temperature 87

Figure 3-23: Photograph of the hot plate used to maintain the contents of the test-bath at 100 ^{0}C 88

Figure 3-24: Photograph of the condenser used 89

Figure 3-25: Photograph of the chiller used to supply chilled water to the condenser 90

Figure 3-26: The complete assembled PBF 91

Figure 3-27: Photograph of the Agilent 34980A unit 92

Figure 3-28: Photograph of the 34921T card used in the 34980A unit 92

Figure 4-1: Oven used to pre-heat the test fluid 95

Figure 4-2: Pictorial representation of the sandblasting procedure 102

Figure 4-3: Photograph of the sandblasting cabinet 103

Figure 4-4: Photographs of sandblasted (left) and smooth/polished (right) heaters showing the difference in their surface texture/reflectance, visible to the naked eye 104

Figure 4-5: Confocal scan of an unused sandblasted heater (R_a = 1.27 μm) 105

Figure 4-6: Confocal scan of an unused smooth heater (R_a = 0.06 μm) 105

Figure 4-7: SEM image of an unused sandblasted heater showing a rough texture 106

Figure 4-8: SEM image of an unused smooth heater 107

Figure 4-9: Static contact angle of a droplet of DI water on unused sandblasted (left) and smooth (right) heater surfaces 108

Figure 4-10: Static contact angle of a droplet of DI water on representative boiled sandblasted (left) and smooth (right) heater surfaces 109

Figure 4-11: Post-test SEM image of heater used for SB_DIW 112

Figure 4-12: Post-test SEM image of heater used for SB_NF, at different magnifications. ZnO nanoparticles, coated on the surface, are clearly visible 114

Figure 4-13: Post-test SEM image of heater used for Sm_DIW 114

Figure 4-14: Post-test SEM image of heater used for Sm_NF, at different magnifications. ZnO nanoparticles, coated on the surface, are clearly visible 116

Figure 4-15: EDX scan from one of the heaters tested with nanofluid. Clear Zn signal confirms that the deposits are from the ZnO particles in the nanofluid 116

Figure 4-16: Confocal scan of heater used for SB_DIW (R_a = 1.35 μm) 117

Figure 4-17: Confocal scan of heater used for SB_NF (R_a = 1.33 μm) 118

Figure 4-18: Confocal scan of heater used for Sm_DIW (R_a = 0.08 μm) 118

Figure 4-19: Confocal scan of heater used for Sm_NF (R_a = 1.68 μm) 119

Figure 4-20: Static contact angle of a droplet of DI water on sandblasted (left) and smooth (right) heaters tested till CHF in nanofluid 120

Figure 4-21: Schematic of LbL method. Particles of alternating charge adhere to the surface of the substrate, the process is repeated until desired number of bilayers are achieved 122

Figure 4-22: Photograph of the Zeiss HMS Programmable Strainer used for coating heater elements with LbL coatings, to change initial surface wettability 123

Figure 4-23: Schematic of the LbL process. *Illustration courtesy of Erik Williamson*.. 124

Figure 4-24: Photograph of the furnace used for calcination 124

Figure 4-25: SEM image of an unused LbL sandblasted heater at different magnifications, clearly showing SiO_2 nanoparticles 126

Figure 4-26: SEM image of an unused LbL smooth heater at different magnifications, clearly showing SiO_2 nanoparticles 127

Figure 4-27: EDX data from an unused LbL sandblasted heater, confirming Si signal 128

Figure 4-28: Confocal scan of an unused LbL sandblasted heater (R_a = 1.24 μm) 128

Figure 4-29: Confocal scan of an unused LbL smooth heater (R_a = 0.14 μm) 129

Figure 4-30: Static contact angle of a droplet of DI water on unused LbL sandblasted (left) and unused LbL smooth (right) heater surfaces 130

Figure 4-31: Post-test SEM image of heater tested for LbLSB_DIW, showing that SiO_2 nanoparticles deposited by LbL method stay intact during the experiment 132

Figure 4-32: Post-test SEM image of heater tested for LbLSB_NF, showing an additional layer of ZnO nanoparticles 132

Figure 4-33: Post-test SEM image of heater tested for LbLSm_DIW, showing that SiO_2 nanoparticles deposited by LbL method stay intact during the experiment 133

Figure 4-34: Post-test SEM image of heater tested for LbLSm_NF, showing an additional layer of ZnO nanoparticles 133

Figure 4-35: Confocal scan of an LbLSB_DIW heater (R_a = 1.05 μm) 134

Figure 4-36: Confocal scan of an LbLSB_NF heater (R_a = 2.48 μm) 135

Figure 4-37: Confocal scan of an LbLSm_DIW heater (R_a = 0.13 μm) 135

Figure 4-38: Confocal scan of LbLSm_NF heater (R_a = 2.22 μm) 136

Figure 4-39: CHF for different heater surface/fluid combinations for varying pre-boiling times. Error bars show the standard deviation in CHF data 141

Figure 4-40: Post-test SEM image of heater tested for Sm_DIW_0hr 142

Figure 4-41: Post-test SEM image of heater tested for Sm_DIW_1hr 143

Figure 4-42: Post-test SEM image of heater tested for Sm_DIW_4hr 143

Figure 4-43: Post-test SEM image of heater tested for Sm_DIW_8hr 144

Figure 4-44: Confocal scan of the heater tested with Sm_DIW_0hr (R_a = 0.08 μm) 144

Figure 4-45: Confocal scan of the heater tested with Sm_DIW_1hr (R_a = 0.16 μm) 145

Figure 4-46: Confocal scan of the heater tested with Sm_DIW_4hr (R_a = 0.16 μm) 145

Figure 4-47: Confocal scan of the heater tested with Sm_DIW_1hr (R_a = 0.09 μm) 146

Figure 4-48: Post-test SEM image of heater tested for SB_NF_0hr 147

Figure 4-49: Post-test SEM image of heater tested for SB_NF_1hr 147

Figure 4-50: Post-test SEM image of heater tested for SB_NF_4hr 148

Figure 4-51: Post-test SEM image of heater tested for SB_NF_8hr 148

Figure 4-52: Confocal scan of the heater tested with SB_NF_0hr (R_a = 2.18 μm) 149

Figure 4-53: Confocal scan of the heater tested with SB_NF_1hr (R_a = 1.48 μm)..... 149

Figure 4-54: Confocal scan of the heater tested with SB_NF_4hr (R_a = 1.75 μm)..... 150

Figure 4-55: Confocal scan of the heater tested with SB_NF_8hr (R_a = 2.12 μm)..... 150

Figure 4-56: Post-test SEM image of heater tested for Sm_NF_0hr..... 151

Figure 4-57: Post-test SEM image of heater tested for Sm_NF_1hr..... 152

Figure 4-58: Post-test SEM image of heater tested for Sm_NF_4hr..... 152

Figure 4-59: Post-test SEM image of heater tested for Sm_NF_8hr..... 153

Figure 4-60: Confocal scan of the heater tested with Sm_NF_0hr (R_a = 1.68 μm)..... 153

Figure 4-61: Confocal scan of the heater tested with Sm_NF_1hr (R_a = 3.63 μm)..... 154

Figure 4-62: Confocal scan of the heater tested with Sm_NF_4hr (R_a = 2.54 μm)..... 154

Figure 4-63: Confocal scan of the heater tested with Sm_NF_4hr (R_a = 3.74 μm)..... 155

Figure 4-64: Confocal scan showing both the wiped (cleaned) and nanocoated areas on a heater tested with nanofluid. Average Z-heights of both areas is calculated. Their difference gives the average nanocoating thickness developed..... 157

Figure 5-1: Typical heat transfer processes for saturated DI water (from ref. [90])..... 165

Figure 5-2: Transient CHF trend for saturated water (case 1) showing the initial increase, then decrease, followed by an increase in CHF with decrease in exponential period (from ref. [90])..... 167

Figure 5-3: Photograph of the function generator to program the power supply for providing desired current outputs..... 172

Figure 5-4: Photograph of the U2542A unit used for data acquisition during transient tests..... 173

Figure 5-5: Pin configurations for the INA210 CSM..... 174

Figure 5-6: Progress of a transient experiment with t_o = 1 s. The vertical solid line is defined as the point where CHF happens..... 177

Figure 5-7: Post-test SEM image of heater used for Tr_NF100..... 180

Figure 5-8: Post-test SEM image of heater used for Tr_NF10..... 181

Figure 5-9: Post-test SEM image of heater representative of 1 s transient test..... 181

Figure 5-10: EDX data from the heater representative of 1 s transient test. The absence of Zn signal confirms that there are no nanocoating deposits formed in such short time 182

Figure 5-11: Confocal scan for heater used for Tr_NF100 (R_a = 2.67 μm) 183

Figure 5-12: Confocal scan for heater used for Tr_NF10 (R_a = 0.97 μm) 183

Figure 5-13: Confocal scan for heater representative of 1 s transient test (R_a = 1.42 μm) 184

Figure 5-14: Static contact angle of droplet of water on heaters used for Tr_NF100 (left), Tr_NF10 (center) and heater representative of 1 s transient test (right) 185

Figure 7-1: Photograph of the heater used for the TCR measurement 194

Figure 7-2: Plots of TCR measurement data (both sets) 195

Figure 7-3: Pictorial representation of the heater-fluid combination 196

Figure 7-4: Schematic of heaters with insulated back, showing the locations of three TCs used. The insulation shown here is glued to the surface of heater 199

Figure 7-5: Photograph of the heater with insulated back, with attached TCs. In this picture, TC3 was disconnected during assembly. The location of TC3 is shown with broken arrow 200

Figure 7-6: Measured temperatures at the insulated wall by the three thermocouples... 201

Figure 7-7: Schematic for calculating relation between T_{ins} and T_{bulk} 202

Figure 7-8: Comparison for T_{bulk} measurement from two different methods 205

Figure 7-9: Function Generator voltage and the output power supply current. Current increases from 0 to 83A in ~ 1s 206

Figure 7-10: Function Generator voltage and the output power supply current. Current increases from 0 to 180A in ~ 10 s 207

Figure 7-11: Function Generator voltage and the output power supply current. Current increases from 0 to 183A in ~ 100 s 207

Figure 7-12: CSM gain verification exercise, showing the voltage input to the CSM (secondary axis) and the CSM output (primary axis) 209

Figure 8-1: Boiling curves for DI water tests for sandblasted and smooth heaters 211

Figure 8-2: Boiling curves for sandblasted heaters, with DI water and nanofluid 211

Figure 8-3: Boiling curves for smooth heaters, with DI water and nanofluid 212

Figure 8-4: Boiling curves for sandblasted heaters, both uncoated and LbL coated 214

Figure 8-5: Boiling curves for smooth heaters, both uncoated and LbL coated 214

Figure 8-6: Boiling curves for sandblasted heaters, with DI water, for various pre-boiling times 216

Figure 8-7: Boiling curves for smooth heaters, with DI water, for various pre-boiling times 216

Figure 8-8: Boiling curves for sandblasted heaters, with nanofluid, for various pre-boiling times 218

Figure 8-9: Boiling curves for smooth heaters, with nanofluid, for various pre-boiling times 218

Figure 8-10: Boiling curves for sandblasted heaters, with nanofluid, for various pre-boiling heat fluxes and times (at constant total pre-boiling heat) 219

Figure 8-11: Boiling curves for LbL coated sandblasted heaters, with nanofluid, for various pre-boiling times 220

Figure 8-12: CHF for different heater surface/fluid combinations for varying pre-boiling times 221

Figure 8-13: Boiling curves for 100s transient experiments (both DI water and nanofluid) 226

Figure 8-14: Boiling curves for 10s transient experiments (both DI water and nanofluid) 226

Figure 8-15: Boiling curves for 1s transient experiments (both DI water and nanofluid) 227

Figure 8-16: Boiling curves for 100s transient experiments for nanocoated heaters (both DI water and nanofluid) 227

Figure 8-17: Boiling curves for 10s transient experiments for nanocoated heaters (both DI water and nanofluid) 228

Figure 8-18: Boiling curves for 1s transient experiments for nanocoated heaters (both DI water and nanofluid) 228

Figure 9-1: Forces acting on a bubble on heater surface (from ref. [26]) 230

Figure 9-2: Comparison of experimental data with models/correlations including effect of heater orientation 232

Figure 9-3: Comparison of experimental data with Kandlikar correlation including effect of surface wettability 233

Figure 9-4: Comparison of experimental data with various correlations for the effect of coating porosity 237

List of Tables

Table 1-1: Review of researches on HTC 43

Table 1-2: Review of researches on CHF 44

Table 1-3: The experimental test matrix for the steady-state CHF tests 47

Table 1-4: The experimental test matrix for the transient CHF tests 48

Table 2-1: ZnO wt % in Nyacol DP5370 nanofluid, obtained with TGA for 3 different samples 51

Table 2-2: Verification of VWR pH of standards at room temperature 53

Table 2-3: pH measurements of Nyacol DP5370 nanofluid at room temperature 53

Table 2-4: Density measurements for Nyacol DP5370 nanofluid 55

Table 2-5: Nanoparticle size measured by DLS 56

Table 2-6: NAA analysis data for DP5370 nanofluids 59

Table 2-7: pH measurements of test nanofluids at room temperature 61

Table 2-8: Surface Tension measurement for DI Water 62

Table 2-9: Surface Tension measurement for test nanofluid 63

Table 2-10: Thermal conductivity measurement for DI Water 63

Table 2-11: Thermal conductivity measurement for test nanofluid 64

Table 2-12: Viscosity measurement for DI Water 64

Table 2-13: Viscosity measurement for test nanofluid 65

Table 3-1: Specifications of shunt used for current measurements 85

Table 3-2: Specifications of thermocouples used to measure bath temperature 88

Table 4-1: Accuracy of experimental measurements 99

Table 4-2: Sample uncertainty values for q'' = 1000 kW/m^2 100

Table 4-3: Summary of contact angle measurements on unused heaters 108

Table 4-4: Summary of CHF tests done for investigating effects of roughness 110

Table 4-5: Summary of CHF tests done for investigating effects of wettability 131

Table 4-6: Summary of CHF tests done for investigating effects of boiling time of DI water on sandblasted heaters 138

Table 4-7: Summary of CHF tests done for investigating effects of boiling time of DI water on smooth heaters 138

Table 4-8: Summary of CHF tests done for investigating effects of boiling time of nanofluid on sandblasted heaters 139

Table 4-9: Summary of CHF tests done for investigating effects of boiling time of nanofluid on smooth heaters 139

Table 4-10: Summary of CHF tests done, varying the pre-boiling heat flux and time, but at the same total integrated heat 140

Table 4-11: Summary of CHF tests done, investigating the effects of boiling time of nanofluid on LbL coated sandblasted heaters 141

Table 4-12: Summary of confocal microscopy data for different heaters, tested with nanofluid for various pre-boiling times 158

Table 5-1: Results for transient tests on uncoated heaters for various values of t_o 178

Table 5-2: Results for transient tests on nanocoated heaters for various values of t_o 179

Table 5-3: Summary of confocal microscopy data for uncoated sandblasted heaters tested with nanofluid for various transient tests 184

Table 7-1: Data for TCR measurement #1 194

Table 7-2: Data for TCR measurement #2 194

Table 8-1: Summary of CHF tests done for investigating effects of roughness 210

Table 8-2: Summary of CHF tests done for investigating effects of wettability 213

Table 8-3: Summary of CHF tests done for investigating effects of pre-boiling time of DI water on sandblasted heaters 215

Table 8-4: Summary of CHF tests done for investigating effects of pre-boiling time of DI water on smooth heaters 215

Table 8-5: Summary of CHF tests done for investigating effects of pre-boiling time of nanofluid on sandblasted heaters 217

Table 8-6: Summary of CHF tests done for investigating effects of pre-boiling time of nanofluid on smooth heaters 217

Table 8-7: Summary of CHF tests done, varying the pre-boiling heat flux and time, but at the same total pre-boiling heat 219

Table 8-8: Summary of CHF tests done, investigating the effects of pre-boiling time of nanofluid on LbL coated sandblasted heaters 220

Table 8-9: Summary of transient tests for uncoated heaters for various values of t_o 222

Table 8-10: Summary of transient tests for nanocoated heaters for various values of t_o 223

Nomenclature

Symbols

α	-	Temperature co-efficient of resistivity	[Ω/Ω-^{0}C]
A_{ht}	-	Area of heat transfer	[m^2]
c_p	-	Specific heat capacity	[J/kg-^{0}C]
d_H	-	Hydrodynamic diameter	[m]
g	-	Acceleration due to gravity	[m/s^2]
h	-	Heat transfer coefficient	[W/m^2-^{0}C]
h_{fg}	-	Enthalpy of vaporization	[J/kg-^{0}C]
$h_{nat.\ convec.}$	-	Natural convection heat transfer coefficient	[W/m^2-^{0}C]
$h_{nucleate}$	-	Nucleate boiling heat transfer coefficient	[W/m^2-^{0}C]
I	-	Current	[A]
k	-	Thermal conductivity	[W/m-^{0}C]
λ_c	-	Critical wavelength	[m]
μ	-	Fluid dynamic viscosity	[Pa-s]
ϕ	-	Angle of heated surface with horizontal	[degrees]
q''	-	Heat flux	[W/m^2]
q''_{CHF}	-	Critical heat flux	[W/m^2]
$q''_{operating}$	-	Nuclear reactor operating heat flux	[W/m^2]
ρ	-	Density	[kg/m^3]
ρ_g	-	Density of saturated vapor	[kg/m^3]
ρ_l	-	Density of saturated liquid	[kg/m^3]
R	-	Resistance	[Ω]
R_{100}	-	Resistance at 100 ^{0}C	[Ω]
R_a	-	Surface Roughness	[μm]
σ	-	Surface tension	[N-m]
t_0	-	Ramp time for transient tests	[s]
T_{bulk}	-	Bulk temperature	[^{0}C]
T_w	-	Wall temperature	[^{0}C]
T_{sat}	-	Saturation temperature	[^{0}C]
τ_d	-	Hovering time of a bubble	[s]

θ	-	Contact angle of fluid on surface	[degrees]
ΔV	-	Potential drop across heater	[V]
ΔV_{shunt}	-	Potential drop across shunt	[V]

Subscripts

f	-	saturated liquid
g	-	saturated vapor
nf	-	nanofluid
np	-	nanoparticle
sat	-	saturation
w	-	wall

Superscripts

o	-	degrees
"	-	inches

Acronyms

BWR	-	Boiling Water Reactor
CHF	-	Critical Heat Flux
DAS	-	Data Acquisition System
DI	-	De-Ionized
DLS	-	Dynamic Light Scattering
DNBR	-	Departure from Nucleate Boiling Ratio
ECCS	-	Emergency Core Coolant System
HR-SEM	-	High Resolution Scanning Electron Microscope
HTC	-	Heat Transfer Coefficient
IVR	-	In-Vessel Retention
LbL	-	Layer-by-Layer
LOCA	-	Loss of Coolant Accident
LWR	-	Light Water Reactor

MDNBR	-	Minimum Departure from Nucleate Boiling Ratio
NAA	-	Nuclear Activation Analysis
NRC	-	Nuclear Regulatory Commission
PBF	-	Pool Boiling Facility
PAH	-	Poly(allyl) Hydrochloride
PWR	-	Pressurized Water Reactor
SDS	-	Sodium Dodecyl Sulphate
TCR	-	Temperature Coefficient of Resistivity
TGA	-	Thermogravimetric Analysis

1. Introduction

The global energy needs have been growing rapidly in the recent decades owing to rapid industrialization and development across the world. With the growing energy demands, there has been an increased interest in exploring additional forms of energy. Nuclear energy, in particular, has garnered significant attention due to its high energy density, as well as the lack of carbon emissions associated with it. As such, continuing efforts to enhance safety of nuclear reactors have generated an unprecedented interest in devising more efficient heat removal systems with better cooling properties. Most of the current fleet of nuclear reactors in the world depend on boiling of water coolant as the mechanism of removing heat generated in the reactor during nuclear reactions, and subsequently converting this removed heat into electricity. Light Water Reactors (LWRs) employ water as their coolant, due to its high heat capacity and attractive nuclear properties as well as abundance in nature. As the flowing coolant comes in contact with the nuclear fuel rods being heated up due to the nuclear fission reaction, it starts to boil, absorbing energy from the fuel rods. In Pressurized Water Reactors (PWRs), because of the high operating pressure, the coolant water on average does not undergo a phase change. However, locally in the core, in proximity of the hottest fuel rods subcooled nucleate boiling takes place under normal operating conditions. The resulting steam is rapidly condensed by the surrounding subcooled water. On the other hand, in Boiling Water Reactors (BWRs), saturated water coming in contact with the hot rods turns into steam, which is sent directly to the turbine. At high heat flux levels, the heat transfer mechanism can change from nucleate boiling to film boiling. During film boiling the heat source (fuel rods, in this case) are engulfed with a vapor film, which poorly transfers heat away from the heat source. This limit of the heat flux where the boiling mechanism changes from (highly efficient form of heat removal) nucleate boiling to (extremely poor) film boiling, is called Critical Heat Flux (CHF). The deterioration in the process of heat removal from the fuel rods, in turn, leads to rapid escalations in the cladding and fuel temperatures and can cause the cladding material to

fail, thus releasing dangerous fission products. Hence, nuclear reactors are required to operate at power levels, which are below that corresponding to CHF. Defining Departure from Nuclear Boiling Ratio (DNBR) as

$$\boldsymbol{DNBR} = \frac{q''_{CHF}}{q''_{operating}} \qquad \text{Eq. 1.1}$$

where q''_{CHF} is the heat flux corresponding to CHF and $q''_{operating}$ is the reactor operating heat flux, for safety reasons, the nuclear reactors in the US are required by the Nuclear Regulatory Commission (NRC) to operate at power levels such that the minimum value of DNBR in a reactor, also known as MDNBR ≥ 1.3 [9]. Therefore, CHF of coolant (water) is one of the main thermal limits to the power level at which nuclear reactors can be operated at under normal conditions. Hence, there is considerable value in increasing the CHF of water as it has two potential benefits:

a. A higher CHF of the primary coolant (water) may enable nuclear reactors to operate at a higher power, thus allowing for power uprates in the current fleet of LWRs.

b. A higher CHF of water will increase the CHF safety margins of nuclear reactors, operating at current power levels, thus enhancing their tolerance for abnormal occurences.

Several techniques to enhance the CHF of coolants have been investigated by researchers. They are often classified into *active* (requiring external changes to heater) or *passive* (requiring no external changes to heater) methods, according to Rohsenow et al [2]. Typical active approaches to increase CHF include vibration of the heated surface or the cooling fluid (to increase the bubble departure frequency), coating the surface with porous coatings (to increase the number of active nucleation sites) and applying an

external electric field (to facilitate the bubble departure from the surface) [3]. But one recent passive way of increasing CHF for water, that has garnered increased attention amongst many researchers worldwide, is to create a colloidal suspension of solid nanoparticles in water, called nanofluids [4, 5]. There are various materials of choice for the dispersed nanoparticles – chemically stable metals (such as Cu, Au and Ag), metal oxides (such as Al_2O_3, SiO_2 and ZrO_2) and different forms of carbon (such as diamond, graphite, fullerene etc.). Boiling tests on these engineered nanofluid coolants have demonstrated them to have a significantly higher CHF (generally, an enhancement ranging from 20% to more than 100%) compared to water. Such experimental findings have furthered the interest in using nanofluids as more efficient coolants in various cooling systems, including nuclear reactors. However, the applications of nanofluids as primary coolant for LWRs, particularly PWRs, are limited by the design constraints imposed by carefully controlled chemistry of the coolant and the extreme radiation environment inside the reactors: it is still unclear how the nanofluids react to the high radioactivity in the reactor, and affect the nuclear properties of water. Nanofluids can be potentially used as coolants in reactor safety systems during abnormal events and accident conditions, when safe shutdown, without core melting and radioactivity release is the priority, and coolant chemistry is not the primary concern. For example, during a loss of coolant accident (LOCA) in a nuclear reactor, the system starts losing the high-pressure primary coolant as steam. Under such a scenario, the core is cooled by vapor instead of liquid, causing highly ineffective heat removal from the core. Although automatic shutdown of the nuclear reactors is activated following accident conditions, there is still an appreciable amount of decay heat in the core. To prevent core melting due to the decay heat, cold water from the emergency core coolant system (ECCS) is injected into the system to cool the core down. Due to their enhanced cooling behavior, nanofluids can conceivably be used as the ECCS coolant. Buongiorno et al evaluated the potential use of nanofluids for use as the ECCS coolant, and have shown that nanofluids as ECCS coolant can lead to higher peak-cladding-temperature margins during a large-break loss of cooling accident (LOCA) [6]. In the same study, the authors also concluded that employing nanofluids for In-Vessel Retention (IVR) applications in case of severe accidents could enable a 40% enhancement in heat removal. Dewitt, in his PhD thesis,

also investigated applications of nanofluids during IVR, by performing flow boiling experiments on downward facing heaters, and concluded that nanofluids can afford 70% enhancement in CHF with just 30 minutes of boiling time [7]. These studies show that nanofluids could lead to more efficient heat removal mechanisms in different scenarios in nuclear reactors.

One section of this chapter will be devoted to discussing the existing literature and results reported in the literature on boiling of nanofluids. However, since boiling and CHF are the primary subjects of this thesis, the basics of boiling and CHF are first summarized here.

1.1. Background: Boiling and Critical Heat Flux

Let us imagine a hot body in contact with a coolant. Assume that the wall temperature (interface between body and coolant) is at temperature T_w and bulk coolant is at temperature T_{sat}, with $T_w > T_{sat}$. Nukiyama was the first researcher to attempt to investigate the relationship between the wall temperature/wall superheats (wall superheat is defined as $T_w - T_{sat}$) and heat flux between the wall and the coolant [8]. The relationship between the heat flux and wall temperature can be written, according the Newton's law of cooling, as

$$q''_{CHF} = h(T_w - T_{sat}) \qquad \text{Eq. 1.2}$$

where h is known as the heat transfer coefficient (HTC). Nukiyama found that, on increasing the power generated in the hot body, the heat flux rose sharply but the temperature of the body increased only slightly. At a particular value of heat flux, the body temperature rose abruptly. This relationship between the wall superheat and the heat

flux can be plotted on curves called boiling curves. Figure 1-1 below shows a typical pool-boiling curve. At low wall superheats, the heat transfer mechanism is natural convection. In this regime, the cold coolant next to the hot body gets heated up. Thus its density is decreased and it rises up due to buoyancy, leading to the relatively colder coolant to come in contact with the hot plate again. This process continues steadily and allows for the plate to be cooled. The line AB in Figure 1-1 shows the natural convection regime. On increasing heat flux, as the wall temperature (and hence the wall superheat), is increased further, the onset of nucleation boiling takes place; this is represented by the point B in Figure 1-1. During nucleation, vapor entrapped in a nucleation site grows into vapor bubbles. As the level of heat flux increases, these bubbles keep growing, and eventually depart the surface, allowing for fresh liquid to contact the hot surface. Since vapor formation during nucleation is associated with a phase change in the coolant, the coolant can absorb very high amounts of heat for relatively small increase in wall temperature. With increasing wall superheat, the number of active nucleation sites goes on increasing until nucleation reaches a fully developed state. This regime is called the fully developed nucleate boiling and is the most efficient form of heat transfer. In Figure 1-1, the line BC denotes the nucleate boiling regime. Since the amount of heat exchanged between the surface and the coolant is very high for a small increase in the wall superheat, the slope of the line BC ($h_{nucleate}$) is much larger than line AB ($h_{nat.\ convec.}$). Eventually, at very high heat fluxes (such as at point C), the surface becomes engulfed with vapor and a stable vapor film develops, which prevents fresh liquid from reaching the surface, thus causing the HTC to drop dramatically. Since at this point, the hot surface is covered with a film of vapor, this regime of boiling is called film boiling. In a flux controlled environment, at this flux level, the curve transitions to point D. Since vapor is a much worse conductor of heat compared to liquid, the local temperature of the plate surges rapidly on reaching point C, which can also lead to burnout of the material [2, 9].

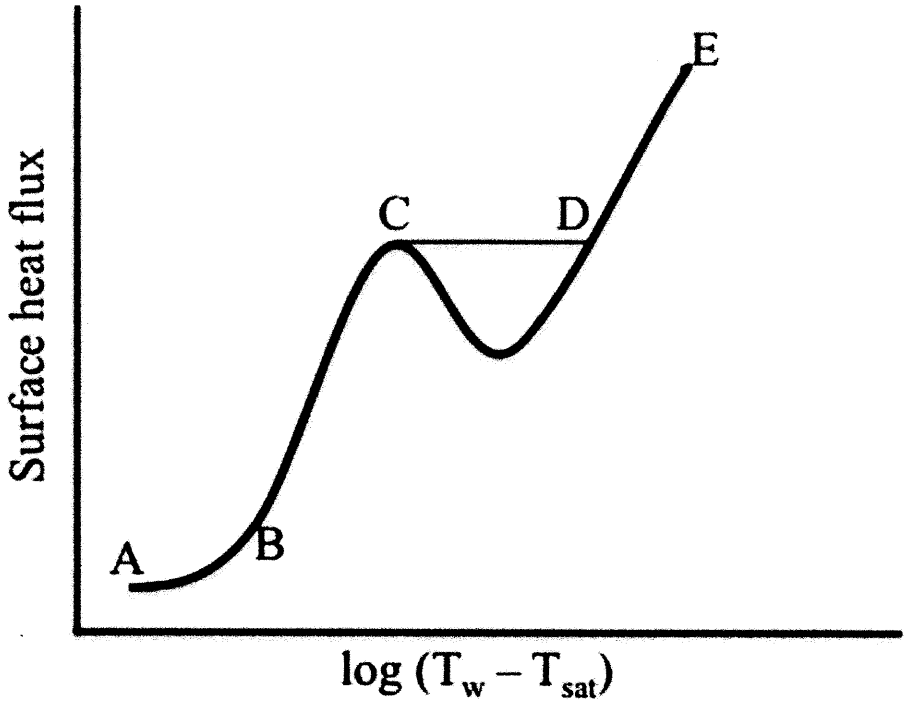

Figure 1-1: Typical pool boiling curve

1.1.1. Review: Nucleation

Detailed investigation of a hot surface being cooled by a liquid coolant in the nucleate boiling regime has shown that individual bubble streams emerge from single spots on the interfacial surface. Observing these spots under a microscope reveals the presence of cavities or scratches at the locations of the bubble formations. It is postulated that these cavities contain trapped air or vapor in them, which leads to the formation of bubbles. As the temperature of the surface is increased, the trapped air or vapor starts to expand and forms a bubble. Eventually at a particular radius of the bubble, it departs from the surface, allowing for the liquid to close in on the same cavity, trapping vapor beneath it. This trapped vapor acts as the source of the next bubble. This process of bubble formation and departure continues, and is responsible for cooling the surface. Figure 1-2 depicts this

situation pictorially, with stage 1 being the trapped air/vapor and stages 2-5 showing the growth of the vapor into a bubble before eventually departing from the surface. If the number of nucleation sites increases, more heat is transferred from the surface to the coolant, hence, higher is the heat transfer coefficient [10].

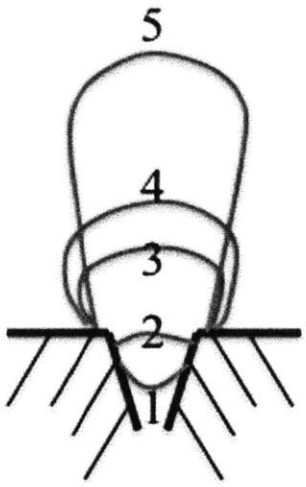

Figure 1-2: Bubble formation over cavities in a heated surface

1.1.2. Literature Review: Critical Heat Flux

As discussed previously, during boiling, CHF is said to occur when the heated surface is covered with a film of vapor, and cannot be cooled directly by the liquid coolant. Although there have been several efforts by multiple researchers to study the details of this complex phenomenon, it is not yet completely understood.

Kutateladze proposed that near critical heat flux, it becomes a hydrodynamic phenomenon rather than bubble generation and departure, with the destabilization of two-phase countercurrent flow existing close to the heating surface [11]. He proposed the following correlation for CHF

$$q''_{CHF} = Kh_{fg}\rho_g^{0.5}[\sigma g(\rho_l - \rho_g)]^{1/4} \qquad \text{Eq. 1.3}$$

where h_{fg} denotes the enthalpy of vaporization, ρ is the density, g is the acceleration due to gravity, and subscripts l and g refer to the liquid and vapor state. Experimentally, K was found to be 0.16 for 'large', upward-facing flat plates.

Rohsenow and Griffith postulated that the increased number of bubbles at higher heat fluxes inhibit liquid from rewetting the surface [12]. They proposed the following correlation

$$\frac{q''_{CHF}}{h_{fg}\rho_g} = C\left(\frac{g}{g_s}\right)^{\frac{1}{4}}\left[\frac{\rho_l - \rho_g}{\rho_g}\right]^{0.6} \qquad \text{Eq. 1.4}$$

The value of C is 0.012 m/s, g is the local acceleration due to gravity and g_s is the standard acceleration due to gravity.

Zuber extended Kutateladze's hypothesis and considered the formation of vapor jets above nucleating bubbles and flow of fluid towards the heated surface, between vapor jets [13]. On increasing heat flux, the velocity of the vapor in the jets increases. Due to the high vapor velocities, an imbalance between the flow induced pressure forces inside the vapor and the surface tension force in the jet walls is created, leading to instability of the vapor jets. He proposed that Taylor and Helmholtz instabilities are responsible for CHF condition. He obtained the same correlation as suggested by Kutateladze, but proposed a value of K = 0.131. The Zuber correlation though was valid only for infinite plates. Lienhard and Dhir modified Zuber's correlation to include the effect of size and geometry [14].

Haramura and Katto extended the Hydrodynamic Instability Theory of Kutateladze-Zuber above with additional modifications to the model [15]. They superimposed Helmoholtz Instability on a vapor-liquid interface of columnar vapor stems in a liquid layer wetting a heated surface. They observed a thin stable liquid film underneath the collapsing bubbles. This liquid macrolayer also contained several vapor stems, feeding the vapor mushroom above. This mushroom is considered to be made up of several individual bubbles that have coalesced. The thickness of this macrolayer was observed to be related to the critical wavelength of Helmholtz instability. The model is depicted by Figure **1-3** below. In the figure, v_l is the velocity of the falling liquid and v_v is the velocity of the rising vapors.

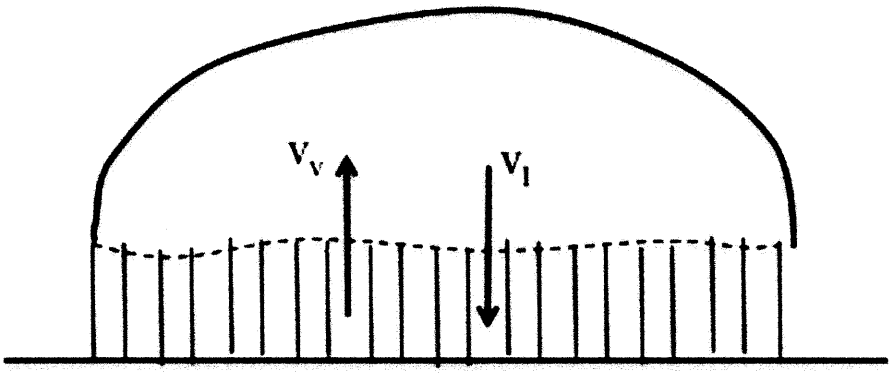

Figure 1-3: Vapor structure near heated surface at high heat fluxes, as depicted in [15]

According to the model, the vapor bubble hovers on top of the macrolayer for time τ_d before departing from the surface. During this time, the bubble grows due to the vaporization of the liquid in the macrolayer beneath. If the liquid macrolayer is not replenished with additional liquid before the departure of the bubble, CHF happens.

However most of these models and correlations are based solely on the thermal and hydrodynamics of the processes involved during CHF. But CHF also depends on the

physic-chemical characteristics of the heated surface, such as the surface energy, porosity, surface roughness, wettability, porosity etc., which these models fail to take into consideration. The wettability of the surface, for example, determines the extent of contact between the fluid and the heated surface. A measure of the wettability is the contact angle of a droplet of the fluid on the surface (θ). Contact angle is the angle a drop of fluid makes with the surface. Greater the contact angle, lower is the surface wettability. Conversely, a lower contact angle signifies a much higher wettability. Higher wettability simply means that a droplet of fluid spreads over a larger area of the surface, and generally means a higher critical heat flux because during boiling it becomes more difficult for the surface to get completely dry. The following section summarizes the key finding on the effects of these additional parameters on the CHF, available in literature.

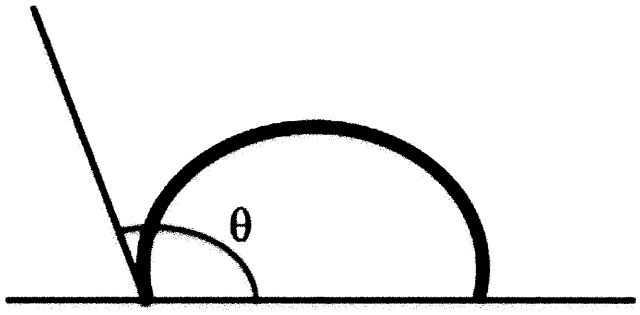

Figure 1-4: Representation of droplet of fluid on a flat surface showing its contact angle ($\boldsymbol{\theta}$)

Effect of contact angle was investigated by few researchers. Kirishenko and Chernikov developed the following correlation to include contact angle as a parameter [16]

$$q''_{CHF} = 0.171 h_{fg}\sqrt{\rho_g}\left[\sigma g(\rho_l - \rho_g)\right]^{\frac{1}{4}} \frac{(1+0.324*10^{-3}\theta^2)^{\frac{1}{4}}}{\sqrt{0.018\theta}} \qquad \text{Eq. 1.5}$$

Although this correlation captured the correct trends in the values of CHF with varying wettability, it failed to accurately predict the critical heat flux values for water.

Wang and Dhir also developed a model for dependence of boiling heat transfer on wettability [17]. They observed that the number of active nucleation sites, at a fixed heat flux, started to decrease with an increase in surface wettability. Phan et al investigated the effects of wettability on boiling further [18]. They concluded that the bubble departure diameter increased with an increase in wettability, whereas the bubble departure frequency decreased as the wettability increased. They postulated that contact angle that effects boiling phenomenon is not just of one kind, but differentiated it into separate effects of the micro- and macro-contact angles. The macro-contact angle is the contact angle of a liquid droplet on a surface, on a larger scale (this is the contact angle referred to in the normal use of the term). However, during nucleate boiling, the liquid micro-layer underneath a bubble evaporates rapidly due to the high heat flux condition. Therefore, at a smaller scale, the curvature of the liquid-vapor interface changes further from the macro-contact angle, leading to the emergence of what is called the micro-contact angle.

Wen and Wang altered the surface wettability by adding surfactants to the base fluids [19]. They observed that increasing wettability led to an increase in heat transfer coefficient. However, this method of changing wettability has the drawback of also changing the other thermo physical properties of the fluid, such as surface tension, which can also have a separate effect on the boiling phenomenon. B. A. Phillips, in his Masters Thesis, controlled the surface wettability by depositing layers of hydrophilic nanoparticle coatings on the surface, using a layer-by-layer technique [20]. Increasing the wettability by these hydrophilic coatings, he observed a 100% enhancement in the CHF of water.

Other than the wettability, orientation of the heater also has a marked effect on pool boiling CHF. Several researchers explored the effects of orientation on CHF. The general trend observed by several independent studies was that CHF decreases as orientation changes from upward-facing horizontal to vertical to downward facing horizontal. Vishnev [21], El-Genk and Guo [22], Chang and You [23], and Brusstar and Merte [24], all developed correlations incorporating the effects of heater orientations on CHF, for fluids ranging from water to cryogenic and non-cryogenic fluids. Their respective correlations are:

$$\frac{q''_{CHF}}{q''_{CHF,0^0}} = \frac{(190-\phi)^{0.5}}{190^{0.5}} \qquad \text{Eq. 1.6}$$

$$\begin{cases} q''_{CHF} = C_{CHF,f}(\phi)\rho_g h_{fg}\left[\frac{\sigma(\rho_l-\rho_g)g}{\rho_g^2}\right]^{\frac{1}{4}} \\ C_{CHF,water}(\phi) = 0.034 + 0.0037(180-\phi)^{0.656} \end{cases} \qquad \text{Eq. 1.7}$$

$$\frac{q''_{CHF}}{q''_{CHF,0^0}} = 1.0 - 0.000120\phi\tan(0.414\phi) - 0.122\sin(0.318\phi) \qquad \text{Eq. 1.8}$$

$$\frac{q''_{CHF}}{q''_{CHF,0^0}} = \begin{cases} 1.0 & 0^0 < \phi \le 90^0 \\ (sin\phi)^{12} & 90^0 \le \phi < 180^0 \end{cases} \qquad \text{Eq. 1.9}$$

where ϕ is the angle of heated surface to horizontal.

Howard and Mudawar conducted photographic studies of pool boiling in various geometries to understand the CHF mechanism for different orientation regimes [25].

They concluded that based on the mechanism for CHF, the heater orientations can be divided into three broad regimes: upward facing ($0 < \phi \leq 60^0$), near vertical ($60^0 < \phi \leq 165^0$) and downward facing ($165^0 < \phi \leq 180^0$). Their experiments showed that in the upward facing orientation, the vapors formed during boiling rise vertically upwards, owing to buoyancy. They observed large vapor jets, consistent with models by Zuber [13] and Lienhard [14], as well as boiling within a thin surface liquid layer, as postulated by Haramura and Katto [15], in the upward facing orientation. However, the vapor behavior was observed to change drastically for the near-vertical orientations. Here, the vapors travelled along the surface of the heater, and the liquid-vapor interface was seen to be wavy. This interface travelled along the surface, and boiling was sustained by liquid entrainment near the lower edge of heater, as well as in wetting fronts, where the liquid-vapor interface makes contact with the surface. Between the wetting fronts, the heater experiences dry-out. In downward facing orientations, stratification of vapor along the heated surface was observed. This happens due to the inability of vapors to leave the surface because of buoyancy. They developed the following correlation for near vertical heater orientation CHF:

$$q''_{CHF} = \frac{1}{8}\left(\frac{\pi}{3}\right)^{1/4} \rho_g h_{fg} \left[\frac{\sigma(\rho_f - \rho_g)g}{\rho_g^2}\right]^{(1/4)} \qquad \text{Eq. 1.10}$$

Noting that the effect of contact angle on CHF suggests that the interface conditions at the bubble base play a pivotal role in CHF, Kandlikar developed a model to predict CHF, including the effects of contact angle and heater orientation [26]. His model was based on a balance of all forces acting on a bubble – surface tension forces, force due to change in momentum, and gravitation force. He postulated that CHF occurs when the force due to the momentum change pulling the bubble interface into the liquid along the heated surface exceeds the sum of the forces holding the bubble (surface tension and gravity). The bubble then expands along the heater surface and blankets it. Due to the gravitational

forces incorporated in the model, Kandlikar was able to account for the variations in CHF due to heater orientation. This model gave the following correlation for CHF:

$$q''_{CHF} = h_{fg}\rho_g^{1/2}\left(\frac{1+cos\theta}{16}\right)\left[\frac{2}{\pi}+\frac{\pi}{4}(1+cos\theta)cos\phi\right]^{1/2}[\sigma g(\rho_l-\rho_g)]^{1/4} \quad \text{Eq. 1.11}$$

Pioro et al provided a detailed review of the parameters effecting boiling [27]. They discuss the effects of surface roughness, heater material thermo physical properties, heater thickness, wettability and orientation on nucleate boiling. With different conditioning of the surface, the density of the nucleation sites can vary, and hence the nucleate boiling can vary too. One of the commonly accepted surface characteristics is the average surface roughness, which is a measure of the texture of a surface. Different values of surface roughnesse can imply differences in the number density and/or size of the cavities on the surface, and hence the HTC and CHF can vary with varying surface roughness. Previous experimental data for boiling of water on stainless steel tubes, shows that compared to polished tubes, rougher tubes have a higher HTC at different flux levels [28, 29]. Ferjancic and Golobic altered the surface of heaters made out of stainless steel 302 and 1010 by different sandpapers and etching in H_2SO_4, and investigated effects of different surfaces on pool boiling CHF of water as well as FC-72 [30]. They observed an increase in CHF of water for rougher heaters compared to the smooth heaters, although the enhancement was small. In the range $0.02 < R_a < 1.5\ \mu m$, fitting their experimental data, they obtained the relation for steel 302 with R_a

$$q''_{CHF} = 18.684\ln(R_a) + 475.29 \quad \text{Eq. 1.12}$$

and for steel 1010, they obtained

$$q''_{CHF} = 28.562\ln(R_a) + 420.46 \qquad \text{Eq. 1.13}$$

with R_a in μm and q''_{CHF} in kW/m^2.However, they also found the roughened surface, if further treated by acid etching, gave higher CHF enhancement. While the surface roughness of the modified surfaces is higher than that of the plain one, surface roughness was not enough to explain the enhancement in CHF observed.

Golobic et al investigated the effects of heater thermal properties and size on critical heat flux [31]. Conducting experiments on horizontally suspended, vertically oriented ribbon heaters, they concluded that the conductance/capacitance effects of heater materials could also effect CHF. Additionally, CHF was seen to increase with increasing thickness of the heater before reaching an asymptotic value. Beyond a certain asymptotic thickness, the effect of thickness on CHF was negligible. The influence of heater thickness and material was expressed as a function of the thickness (2δ), density (ρ), specific heat (c) and thermal conductivity (k) of the heater

$$\frac{q''_{CHF}}{q''_{CHF,asy}} = 1 - e^{-\left[\frac{\delta(\rho ck)^{0.5}}{2.44}\right]^{0.8498} - \left[\frac{\delta(\rho ck)^{0.5}}{2.44}\right]^{0.0581}} \qquad \text{Eq. 1.14}$$

Tachibana et al studied the effect of heater thermal properties and concluded that CHF increases as (i) the thermal conductivity of heater increased and (ii) the heat capacity per unit surface area increased [32]. Wen and Wang [19] also investigated the effects of surface roughness on boiling. They altered the wettability of water by adding different surfactants – sodium dodecyl sulfate (SDS), Triton X-100 and octadecylamine. They noticed that roughness enhanced the HTC for Triton X-100 but decreased it for SDS solution.

From the literature summarized above, it is evident that CHF is a highly complex phenomenon, which cannot just be explained on the basis of hydrodynamic models, as was done in the beginning of CHF investigations. This intricate process can vary significantly depending on several factors such as heater surface conditioning, wettability, heater thermophysical quantities, size as well as geometry and orientation. The models proposed so far do analyze the effects of most of the above-mentioned parameters. However, the major shortcoming of the correlations is that the experiments designed to develop the correlations did not allow for control of one surface parameter at a time; for example, changing the roughness automatically changes the surface wettability, and can also create capillary (wicking effects).. There is need for further investigations, and development of models and correlations, which can isolate clearly the separate effects of these parameters on the value of CHF. One such study is under way at MIT [**Error! Reference source not found.**].

1.2. Literature Review: Nanofluids

Ever since addition of nanoparticles to water displayed enhanced CHF, different nanofluid researchers have carried out experimental studies on multiple nanofluids, and efforts to explain the mechanism of the CHF enhancement have been ongoing since the last decade. Researchers have also investigated potential enhancements in thermal conductivity of nanofluids, as well as in their heat transfer coefficient. A variety of nanoparticles have been investigated – ranging from oxides (Al_2O_3, SiO_2, ZnO, CuO etc.) to metals (Au, Ag, Pt) to carbon nanoparticles. Researchers have also experimented with different base fluids – water, cryogenics etc.

Kakac et al showed that nanofluids have a higher thermal conductivity and heat transfer coefficient compared to water [34]. Meibodi et al also noticed similar enhancements and attributed the conductivity enhancement to the Brownian motion of nanoparticles suspended in solution, as well as the development of an interfacial layer between the

nanoparticles and the base fluid [35]. It was widely considered that the dispersion of a high concentration of nanoparticles in the base fluid lead to an anomalous enhancement in its thermal conductivity, higher than that suggested by the effective medium theory. However, a recent international benchmark of nanofluids thermal conductivity by Buongiorno et al. indicated that there is no anomalous enhancement of thermal conductivity of nanofluids beyond the prediction of the effective medium theory [36]. Also, the study found that nanofluid thermal conductivity increases with higher nanoparticle concentration and lower base fluid thermal conductivity in accordance with the effective medium theory.

While the potentially higher thermal conductivity of the nanofluids is what attracted most researchers, initially, to investigate nanofluids, it is the enhancement in CHF provided by nanofluids, in both flow and pool boiling applications, that has attracted more attention recently. You et al were the first researchers to observe a considerable CHF enhancement in alumina nanofluids [37]. Since then, nanofluid pool boiling has generated a lot of curiosity and efforts to understand the underlying mechanism for the observed differences in the pool boiling behavior of nanofluids and water. You et al [37] tested alumina nanofluids (water-based) with copper metal providing the heated surface. The tested concentration of nanoparticles ranged from 0 g/l to 0.05 g/l. They noticed as high as 200% enhancement in CHF of nanofluids, compared to the base case (water). It was observed that at very low nanoparticle concentrations, the enhancement in CHF increased with increasing nanoparticle concentration. However, the continuing increase in CHF was not observed beyond 0.01g/l. Also, at a fixed heat flux, the bubble departure diameter increased and the bubble departure frequency decreased, with the addition of nanofluids. Thus, there was evidence of change in boiling parameters, with the addition of nanoparticles to the solution.

Kim et al [38] conducted experiments of titania and alumina nanofluids, in water, on electrically heated metal wires. They observed an increase in CHF with the nanofluids, with the enhancement increasing with nanoparticle concentration up to 0.1% vol.

concentration. SEM analysis of the heaters, post-testing, showed the presence of coatings of the nanoparticles on the heater. They also did experiments with similar nanocoated heaters, with plain water, and obtained the same order of enhancements in CHF as those of bare heaters with nanofluid. This led to the conclusion that the nanocoating developed during the experiment was responsible for enhancing the CHF. Vassallo et al did CHF measurements for 0.5 v% silica nanofluids on cylindrical NiCr wires submerged in a pool [39]. They also obtained an enhancement in CHF for nanofluids, compared to water. Additionally, they too noticed a coating of nanoparticles developed on the heater surface and attributed CHF enhancement to this coating. However, from the boiling curves for both water and nanofluid, they concluded that the heat transfer coefficient of water was not effected by the addition of the nanoparticles. Bang and Chang reported a nanocoating layer formed on the surface of the heater [40]. This coating was not only seen in pool boiling, but also in flow boiling experiments as well. Kim et al [41] measured subcooled flow boiling CHF of alumina, diamond and zinc oxide nanofluids and also found nanoparticles deposited on the surface of the heater. As a result of the nanoparticle coatings, the surface wettability of the heaters increases, which would explain the enhancement in the CHF [41, 42]. Kim et al reviewed the prevalent theories for CHF and demonstrated that the higher wettability can produce CHF enhancement consistent with the experimental observations [41, 42].

Having observed similar nanocoatings, Kwark et al proved that the nanoparticle deposition, forming the nanocoating on the surface of the heater, was a direct result of the nucleate boiling [43]. They conducted several experiments and ruled out that the nanocoating could be formed by other factors such as gravitational effects, electric fields, natural convection etc. They used the microlayer evaporation concept of Zhao [44] to theorize that, when the microlayer begins to absorb heat from the surface during a nucleation event, the base fluid evaporates, helping the bubble to grow. However, the nanoparticles in the microlayer, associated with the fluid, "fall down" on the surface and stick to it, forming the nanocoating.

To ascertain that the change in wettability due to nanocoating development is the primary reason for an enhanced CHF with nanofluids, several researchers modified the surface wettability by controlled methods such as oxidation [45], hydrophilic coatings [20, 46] and hydrophobic coatings [20, 46]. The surfaces with increased wettability (obtained by these controlled methods) showed similar enhancement in CHF with pure water as surfaces unmodified surfaces with nanofluids. The surfaces with a lowered wettability had a deterioration in CHF with pure water. This further backs the conclusion that the increased wettability due to the nanocoating developed during nanofluid boiling is the primary mechanism for CHF enhancement. However, as shown by O'Hanley, the intrinsic wettability alone does not affect the CHF, but CHF enhancements occurs as a consequence of an increased porosity which causes an enhanced wettability [33].

Yang and Liu [47] made a water-based functionalized nanofluid by surface functionalizing the ordinary silica nanoparticles, which made the nanoparticles water-soluble. The functionalizing was done by grafting silanes to the surface of silica nanoparticles. The authors observed marked differences between pool boiling heat transfer characteristics of functionalized and traditional nanofluids. While the nanoparticles in the traditional nanofluid formed a porous coating on the surface of the heater, no such coating was observed for functionalized nanofluids because of the nanoparticles having dissolved in water in the latter case. The functionalized nanofluid did not show any change in CHF compared to water. This further proved that the nanocoating developed during boiling is the root cause of CHF enhancement. However, the functionalized nanofluid did enhance the HTC slightly.

It must be noted that the process of the development of the nanocoatings is non-uniform. Since the nanoparticle deposition is driven by the boiling process, it develops in an uncontrolled manner. These nanocoatings can act to either increase or decrease the surface roughness. If the base heater material is highly smooth, the nanoparticles actually increase the surface roughness. However, if the heater surface is rough, and the size of

cavities on the surface is much larger than the size of the nanoparticles, then the nanoparticles can start to deposit inside the cavities. In such a case, they can act to smoothen out the surface, leading to a reduction in its roughness. Such an effect was noticed by Das et al [48].

Several other similar studies on nanofluid boiling behavior, and its impact on the CHF and HTC have been reported. The findings of all the studies bear one similarity: that the nanoparticles in solution are observed to coat on the heater surface, and change the surface morphology. They are seen to change the surface roughness (either increase or decrease it) and make the surface more hydrophilic. However, different studies report different trends as far as the CHF enhancement is concerned. Some studies show an enhanced CHF, while there are also studies that report deterioration in CHF of nanofluids compared to water. Similarly, there are conflicting reports on the behavior of HTC of nanofluids compared to water, in different experiments and studies. Key researches on HTC of nanofluids is summarized in Table 1-1, and on CHF of nanofluids is summarized in Table 1-2.

Since the nanofluids in most of the investigations are highly diluted, their thermo physical properties (viscosity, surface tension, thermal conductivity, density, specific heat capacity, latent heat of vaporization) are similar to DI water [49, 50]. Hence, the changes in boiling behavior of nanofluids is attributed solely to the modifications of the surface morphology, caused by the developed nanocoatings, which further changes the dynamics of boiling, and changes HTC and CHF.

Table 1-1: Review of researches on HTC

Author	Nanofluid	Heating Surface	Effect
You et al. [37]	Al_2O_3 – water	Rectangular Cu surface	No effect
Das et al. [51, 52]	Al_2O_3 – water	Cu tube	Deterioration
Witharana et al. [53]	Au – water SiO_2 – water SiO_2 – glycol	Circular Plate	Enhancement Deterioration Deterioration
Tu et al. [54]	Al_2O_3 – water	Ti-film plate	Enhancement
Kim et al. [55]	Al_2O_3 – water	Rectangular Cu surface	No effect
Vassalo et al. [39]	SiO_2 – water	NiCr wire	No effect
Jr. et al. [56]	Al_2O_3 – water ZnO – water	Rectangular Cu surface	No effect
Wen et al. [57]	Al_2O_3 – water	Circular stainless steel surface	Enhancement
Bang et al. [40]	Al_2O_3 – water	Rectangular surface	Deterioration
Kim et al. [42]	Al_2O_3 – water SiO_2 – water TiO_2 – water	Stainless steel wire Rectangular stainless steel surface	Deterioration
Truong [58]	Al_2O_3 – water SiO_2 – water	Stainless steel wire	Enhancement
Liu et al. [59]	CNT – water	Rectangular Cu surface	Enhancement
Kathiravan et al. [60]	Cu – water	Rectangular stainless steel surface	Deterioration
Kwark et al. [43]	Al_2O_3 – water	Rectangular Cu surface	No effect or deterioration
Soltani et al. [61]	Al_2O_3 – water	Stainless steel cylinder	Enhancement
Suriyawong et al. [62]	TiO_2 – water	Circular Cu surface Circular Al surface	Enhancement or deterioration Enhancement

Table 1-2: Review of researches on CHF

Author	Nanofluid	Heating Surface	Effect
You et al. [37]	Al_2O_3 – water	Rectangular Cu surface	Enhancement
Tu et al. [54]	Al_2O_3 – water	Ti-film plate	Enhancement
Kim et al. [55]	Al_2O_3 – water	Rectangular Cu surface	Enhancement
Vassalo et al. [39]	SiO_2 – water	Ti-film plate	Enhancement
Jr. et al. [56]	Al_2O_3 – water ZnO – water	Rectangular Cu surface	Enhancement
Milanova et al. [63]	SiO_2 – water	NiCr wire	Enhancement
Kim et al. [64]	TiO_2 - water	NiCr wire	Enhancement
Kim et al. [42]	Al_2O_3 – water SiO_2 – water TiO_2 – water	Stainless steel wire Rectangular stainless steel surface	Enhancement
Truong [58]	Al_2O_3 – water SiO_2 – water	Stainless steel wire	Enhancement
Coursey et al. [45]	Al_2O_3 – water Al_2O_3 – ethanol	Circular Cu surface Oxidized Circular Cu surface	Enhancement
Jeong et al. [65]	Al_2O_3 – water	Stainless steel wire	Enhancement
Liu et al. [59]	CNT – water	Rectangular Cu surface	Enhancement
Kathiravan et al. [60]	Cu – water	Rectangular stainless steel surface	Enhancement
Kwark et al. [43]	Al_2O_3 – water	Rectangular Cu surface	Enhancement
Kim et al. [66]	Al_2O_3 – water TiO_2 – water	Rectangular Cu surface	Enhancement

1.3. Thesis Motivation and Objectives

CHF is a highly complex phenomenon. There are multiple parameters, which can effect CHF, and need to be taken into account, simultaneously, to accurately predict CHF. Raising the CHF can have significant benefits for the nuclear industry as it can allow for generating higher power with the current fleet of reactors and/or increase safety margins. Nanofluids have shown promise in their use as advanced coolants. Based on their enhanced CHF, it is expected that nanofluids can help achieve more efficient cooling systems for high power density systems such as current electronic devices and nuclear reactors [67, 68]. Buongiorno et al also proposed the use of nanofluids for in-vessel retention (IVR) purposes [69]. However, as summarized in the previous sections, different researchers have reported conflicting results and there is still no universal consensus behind the exact mechanism for the CHF enhancement and alteration in HTC with nanofluids. The scatter in the CHF and HTC database could be due to differences in the nanoparticle materials, size, shape and loading, differences in experimental procedures (e.g., boiling time prior to CHF) and, importantly, differences in the surface conditions (i.e., roughness, wettability) of the heaters used in the experiments. The mechanisms of nanofluid CHF enhancement and change in HTC are not yet clearly understood. It is required to gain a better understanding of the effects of suspended nanoparticles on boiling heat transfer and critical heat flux in order to be able to apply nanofluids to nuclear reactor applications.

Even though several research groups have reported contradicting findings for the behavior of CHF and/or the heat transfer coefficient, it is widely accepted that the changes in the boiling behavior of nanofluids compared to water occur due to the nanoparticles depositing as a coating over the heater surface during boiling. This nanocoating increases the wettability of the heater and may increase the surface roughness and porosity, thus enhancing the CHF of the nanofluid.

The first objective of this work is to conduct a detailed investigation of the effects of different parameters on the steady-state CHF of nanofluids. In this part (called 'Steady-state Tests' from this point onwards), the initial surface roughness, surface wettability and the pre-boiling time for developing nanocoating thickness are changed one by one, and their effects on CHF are investigated. ZnO nanofluids at a dilution of 0.01 v% of ZnO are employed. In order to loosely approximate the fuel rod geometry, the heaters will be oriented vertically. During the tests, initial surface roughness, initial wettability and pre-boiling time (i.e. the time for which the heater is pre-boiled in the nanofluid before the heat flux is increased to CHF) are varied, and their effects on the nanoparticle deposition are examined, in steady state. Different pre-boiling times would imply different extents of time available for the nanoparticles to deposit on the heater surface, thus potentially giving different thicknesses of the nanocoatings developed. This will allow the inspection of the trend that CHF follows with the increasing thickness of the nanocoating – whether the CHF increases monotonically with the increasing thickness, or does it saturate or even start dropping off after a certain maximum nanocoating thickness. The boiling time will be varied between 0 and 8 hours. The upper limit of 8 hours is dictated by the limitation of finishing each experiment within one day, since the experiments cannot be run overnight for safety reasons. Moreover, the nanocoatings can alter the roughness of the heater surface. Hence, the effects of the nanocoatings on a smooth heater will be compared to that on a rough heater surface, in terms of the changes in the CHF. Heaters with different surface finish will be employed for this comparison: smooth surface finish ($R_a \sim 0.1$ μm) and rough finish ($R_a \sim 1$ μm). Furthermore, the coatings increase the surface wettability, i.e. the static contact angle of water on the nanocoated surface is smaller than that on an uncoated surface. So, it will be investigated if the CHF is enhanced by the nanofluids if the heater surface is initially highly wettable. This comparison will be done by observing the nanofluid CHF for surfaces having initial contact angles of $\sim 80^0$ and $< 20^0$ for water. Table **1-3** below summarizes the test matrix that we will investigate for the steady-state CHF tests.

Table 1-3: The experimental test matrix for the steady-state CHF tests

Parameter	Mode of control	Values Explored
Initial Surface Roughness	Sandblasting with glass beads/ Order heaters with different surface finish	Ra = 0.1μm and 1 μm
Initial Wettability	Hydrophilic surface coatings	$< 20^0$ (with pre-coating) and ~ 80^0 (uncoated)
Boiling Time	Vary time to boil before bringing the heater to CHF	0 < t < 8 h

Secondly, during abnormal conditions, such as different accident scenarios, thermal power in nuclear reactors is not constant, but varies with time. However, all the pool boiling studies on nanofluids so far have been conducted at steady state. To be able to use nanofluids for nuclear applications, an understanding of what effect the nanofluids have on boiling and CHF during such power transients is also required. Hence, the second objective of this thesis is to study the nanoparticle-deposition effects on CHF during rapid heat-flux excursions. Previous studies on reactivity-initiated accidents, such as rod ejection events, show that the power transients in nuclear reactors, during abnormal events last for approximately 0.25 – 0.50 s [70, 71]. The sample heaters will be loaded in our pool boiling facility containing the boiling fluid, and the set-up will be brought to the saturation conditions. The heat flux through the test heaters will, then, undergo excursions from zero to its maximum value (or till CHF is achieved), in time t_0 s (called ramp-time), by varying the current passed through the test heaters linearly with time. The current (in amperes) through the heater will be the following function of time:

$$I = I_o \frac{t}{t_0} \qquad \text{Eq. 1.15}$$

where I_o is the maximum current that can be passed through the heater and its value is 450 A. These tests will be called 'Transient Tests' from here on in this thesis. The accident scenarios of interest to us are the ones where the power transients in nuclear reactors last over a few seconds or a few tens of seconds (such as a steam line break or a loss of flow accident). So, in our experiments, we will investigate three values of t_o (1 s, 10 s and 100 s). Additionally, we will experiment with 4 different heater-test fluid combinations – uncoated heaters in water, uncoated heaters in nanofluid, heaters with nanoparticles coated on surface in water, and heaters with nanoparticles coated on surface in nanofluid. The test matrix for the transient CHF tests is summarized in Table 1-4.

Table 1-4: The experimental test matrix for the transient CHF tests

Variable	Type
Heater Surface	Uncoated or pre-boiled in nanofluid
Test Fluid	Water or 0.01v% ZnO
Time for CHF up rate (t_o)	1, 10, 100 s

1.4. Thesis Organization

The rest of this thesis consists of 5 additional chapters. Chapter 2 discusses the nanofluids used in the experiments, and describes the complete characterization efforts carried out both for the concentrated (as-received) as well as diluted (test) nanofluids.

In Chapter 3, the experimental set-up and facility used to perform the tests is described. It also discusses the approach used in carrying out the experiments, and the subsequent post-test analyses required to draw conclusions from the testing.

Chapter 4, then discusses the results obtained for the steady-state CHF tests. In this chapter, the modes of controlling the 3 parameters (roughness, wettability and pre-boiling time) are described, followed by their respective results, as well as results of post-test analyses.

Chapter 5 begins with a review of the transient CHF mechanisms for DI water, reported in literature so far. In this chapter, the differences between the CHF values for transient and steady state tests are discussed. This is followed by the description of the transient CHF tests, and the set-up modifications required for those tests. Subsequently, the results for the transient tests are discussed, followed by the post-test analyses results for heater surfaces.

Chapter 6 concludes the thesis by providing a summary of the relevant findings obtained in this work, and providing recommendations for the future work.

2. Nanofluids

Nanofluids are colloidal suspensions of nano-scaled particles in the base fluid. Commonly used base fluids are water, refrigerants, oils etc. Zn addition during the reactor operation (in the form of $Zn(CH_3CO_2)_2$ in PWRs and ZnO in BWRs) is used in Areva's nuclear reactors [72] to inhibit corrosion [73-76]. It is desirable to not introduce many foreign elements into the nuclear reactor chemistry. As the bigger goal of the thesis is to assess if nanofluids can make a positive difference to nuclear reactor operations, ZnO nanofluids were chosen for this work. The base fluid for the nanofluids throughout this thesis is de-ionized water (DI water). There have been previous experiments done in the MIT research group with varying nanoparticle concentrations (0.001 v%, 0.01 v% and 0.1 v%) [7, 42, 50]. However, it was seen that the volume concentration of nanofluids does not have a strong influence on the CHF enhancement. Hence, the middle concentration of 0.01 v% was used for this thesis. The dilute nanofluids with 0.01 v% ZnO are obtained by adding additional DI water to a concentrated nanofluid solution with known concentration. The concentrated nanofluid solution, manufactured by Nyacol Nano Technologies, was sent to us by the project sponsor Areva. According to the vendor specifications, the as-received nanofluids (called Nyacol DP5370 nanofluid from this point onwards), are 30% ZnO by weight, with a pH of 9.5 and average particle diameters between 50 and 90 nm.

2.1. Nanofluid Characterization

Before beginning the actual experiments, we completed a detailed characterization of both the as-received Nyacol DP5370 nanofluids, as well as the diluted test nanofluids (0.01 v% ZnO). This part of the thesis will detail the results of the characterization exercise.

2.1.1. Concentrated Nyacol DP5370 nanofluids

2.1.1.1. Concentration

Since the dilution of the Nyacol DP5370 nanofluids to the test concentration depends on its initial concentration, it is important to accurately measure the concentration of the as-received nanofluid solution. The nanofluid concentration measurement was done using the Thermogravimetric Analysis (TGA) at Harvard University. TGA was performed with the TA Instruments Q5000 SA Thermogravimetric Analyzer – 957000.902. Concentration calculation using TGA involves the measurement of the weight of a nanofluid sample over a period of time. The sample (nanofluid) is placed in a pan and it is weighed using a high-precision balance. Then, the temperature of the system is raised causing the water from the nanofluid to evaporate; evaporation of water is confirmed by a continual loss in the weight of the sample in the pan. The process is continued till the entire water evaporates, leaving behind only the nanoparticles. The end of the process is indicated by the stability of the measured weight of the contents in the pan. Finally, the ratio of the final to the initial weight gives the weight percentage of the nanoparticles in the nanofluid. Table **2-1** shows the measurements done on 3 different samples. Figure **2-1** shows the variation in the sample weight, against time, for one sample. The average weight percentage of the ZnO nanoparticles in the Nyacol DP5370 nanofluids was obtained as 29.523%, which is within 2% of the nominal value of 30% reported by Nyacol.

Table 2-1: ZnO wt % in Nyacol DP5370 nanofluid, obtained with TGA for 3 different samples

Sample	ZnO wt %
1	31.04
2	28.56
3	28.97
Average	**29.523**

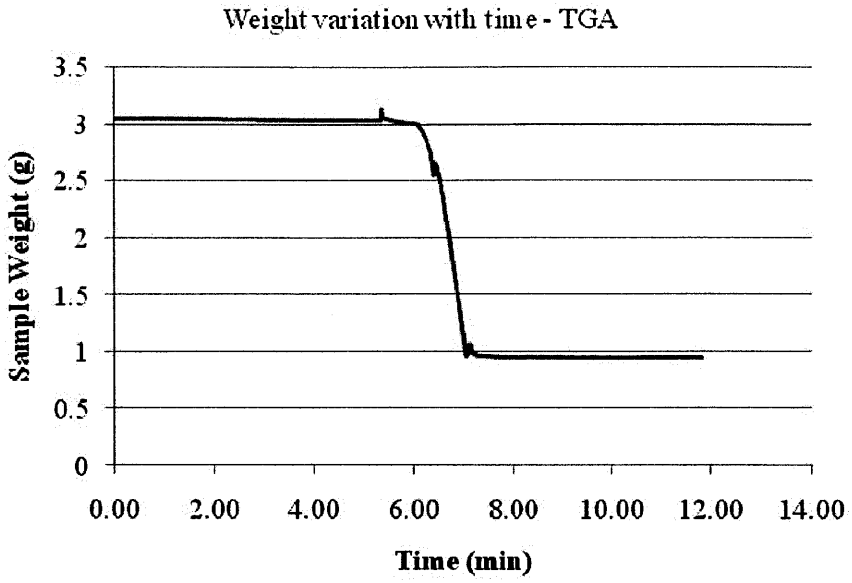

Figure 2-1: Variation of sample weight in TGA for one of the experimental runs. The weight of the sample stabilizes after some time indicating complete evaporation of water, leaving behind only the nanoparticles

2.1.1.2. pH

The stability of the nanofluids is a critical factor while carrying out the experimental analysis. If the nanofluids do not stay stable and agglomerate, it can lead to settling of the nanofluids, which is undesirable. The Nyacol DP5370 nanofluids stay stable if the pH is maintained between 8 and 10, at room temperature [77]. According to the vendor, the pH of the as-received ZnO nanofluids is maintained at 9.5. An undisclosed surfactant is also added in the nanofluid solution by Nyacol, to prevent against agglomeration of nanoparticles. We carried out the verification of the pH of the Nyacol DP5370 nanofluids by measuring it in the lab. The calibration of the pH meter used was first completed by measuring the pH of 3 standards (results shown in Table **2-2**) obtained from VWR International. After the pH meter was calibrated, the pH of the Nyacol DP5370 nanofluids was measured. Table **2-3** shows the results of pH measurements on 3 different Nyacol DP5370 nanofluid samples. The average pH obtained was 8.92.

Table 2-2: Verification of VWR pH of standards at room temperature

Sample	Standard pH	Measured pH
pH standard 4	4.0	3.97
pH standard 7	7.0	7.02
pH standard 10	10.0	9.92

Table 2-3: pH measurements of Nyacol DP5370 nanofluid at room temperature

Sample	Measured pH
1	8.92
2	8.90
3	8.93
Average	**8.92**

2.1.1.3. Density

The density of the nanofluid is measured by directly measuring the weight of a known volume of the nanofluid. An average nanofluid density of 1.273 g/cc was measured by this procedure. Once the nanofluid density was calculated, it was used to calculate the density of the ZnO nanoparticles using the following procedure. A known volume V of the nanofluid is weighed. The weight is denoted as X. From Section 2.1.1.1, the concentration of the Nyacol DP5370 nanofluid is 29.523%. Thus weight of ZnO nanoparticles is given by

$$W_{ZnO} = 0.29523\,X \qquad \text{Eq. 2.1}$$

and weight of water is given by

$$W_{H_2O} = (1 - 0.29523)X = 0.70477\,X \qquad \text{Eq. 2.2}$$

If the density of water is denoted as ρ_l, the volume of water is obtained as

$$V_{H_2O} = 0.70477\,\frac{X}{\rho_l} \qquad \text{Eq. 2.3}$$

The volume of ZnO nanoparticles then can be obtained as

$$V_{ZnO} = \mathrm{V} - V_{H_2O} \qquad \text{Eq. 2.4}$$

which can then be used to calculate the ZnO particle density as

$$\rho_{ZnO} = \frac{W_{ZnO}}{V_{ZnO}} \qquad \text{Eq. 2.5}$$

For these measurements, a micropipette was used to take out the volume V of the nanofluid. The value of V used was 2 ml. Using ρ_l = 0.998 g/cc (at STP) the measurements were done on 5 different Nyacol DP5370 samples. Table **2-4** summarizes the measurements made in the lab. An average value of ρ_{DP370} = 1.2679 g/cc and ρ_{ZnO} = 3.58 g/cc was calculated. However, the nominal density of ZnO is 5.675 g/cc [78]. This discrepancy in the calculated value of the particle density is due to the hydration of ZnO to $Zn(OH)_2$, which causes the decrease in the density.

Table 2-4: Density measurements for Nyacol DP5370 nanofluid

Sample	X (g)	ρ_{DP5370} = X/V (g/cc)	W_{ZnO} (g)	V_{H2O} (cc)	V_{ZnO} (cc)	ρ_{ZnO} (g/cc)
1	2.5423	1.2712	0.7506	1.7953	0.2047	3.667
2	2.5316	1.2658	0.7474	1.7878	0.2122	3.522
3	2.5436	1.2718	0.7509	1.7962	0.2038	3.684
4	2.5218	1.2609	0.7445	1.7808	0.2192	3.396
5	2.5398	1.2699	0.7498	1.7936	0.2064	3.633
Average		**1.2679**				**3.580**

2.1.1.4. Particle Size

The size of the nanoparticles in the nanofluid was also measured. Dynamic Light Scattering (DLS) as well as imaging by Transmission Electron Microscopy (TEM) were employed to obtain the size distribution of the particles.

DLS is based on the principle of scattering of light from the particles in a suspension. It measures the Brownian motion of the particles and relates it to the particle size. DLS measures the translational diffusion coefficient of the particles suspended in a fluid, from which the particle size can be computed by using the Stokes-Einstein equation:

$$d_H = \frac{kT}{3\pi\mu D} \qquad \text{Eq. 2.6}$$

where d_H is the hydrodynamic diameter, D is the translational diffusion coefficient of the suspended particles, k is the Boltzmann's constant, T is the absolute temperature, and μ is the fluid viscosity. It is noteworthy that the diameter measured by DLS refers to how the

particle moves through the fluid. It is the equivalent diameter of a sphere that has the same translational diffusion coefficient as the particle, which in turn depends not only on the particle core but also on any surface structures that might be present on the particle.

We carried out DLS using a Brookhaven Instruments Co. (Holtsville, NY) system consisting of a model BI-200SM goniometer, a model EMI-9865 photomultiplier, a model BI-9000AT digital correlator, and a Coherent Innova 90C Series ion laser (Santa Clara, CA) operated at 514 nm, at the Institute of Soldier Nanotechnologies at MIT. All measurements were made at room temperature and the nanofluids were filtered using a 0.45 μm Acrodisc syringe filter. We carried out measurements on 5 samples diluted to ~37 ppm ZnO from the Nyacol DP 5370 ZnO nanofluid, by adding water. Table **2-5** summarizes the DLS measurements made for these samples. Figure **2-2** shows the DLS data obtained from one of the measurements. The average particle diameter, over the 5 tested samples, was seen to vary between 38 – 68 nm, which is consistent with the vendor specified size of 50 – 90 nm.

Table 2-5: Nanoparticle size measured by DLS

Sample	Nanoparticle size (nm)
1	38.8
2	50.3
3	59.4
4	61.2
5	68.3

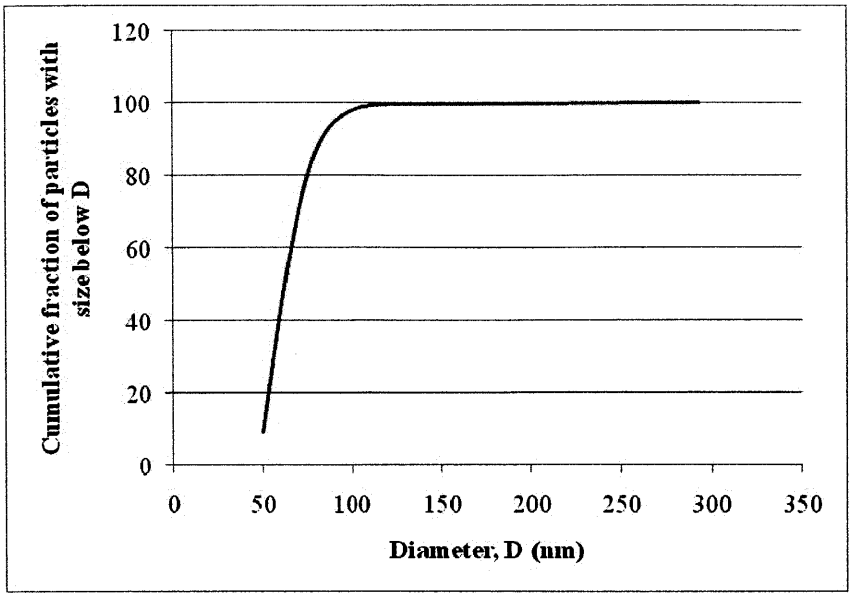

Figure 2-2: Particle size distribution obtained by DLS

Nanoparticle size estimation was also done using imaging by TEM. TEM was carried out using a JEOL 2010F, in the Center of Materials Science and Engineering (CMSE) at MIT. The TEM samples were prepared by pouring a small volume of dilute nanofluids (~37 ppm ZnO prepared from Nyacol DP5370 ZnO nanofluid) on a standard 3 mm diameter copper TEM grid. The grid with the nanofluid on it was kept in a hot oven until water evaporated completely from it, leaving behind the nanoparticles in the grid. This grid was eventually subjected to TEM. Figure **2-3** shows two representative TEM images, displaying regions where multiple nanoparticles had settled on the grid in (a) and regions with isolated nanoparticles in (b).

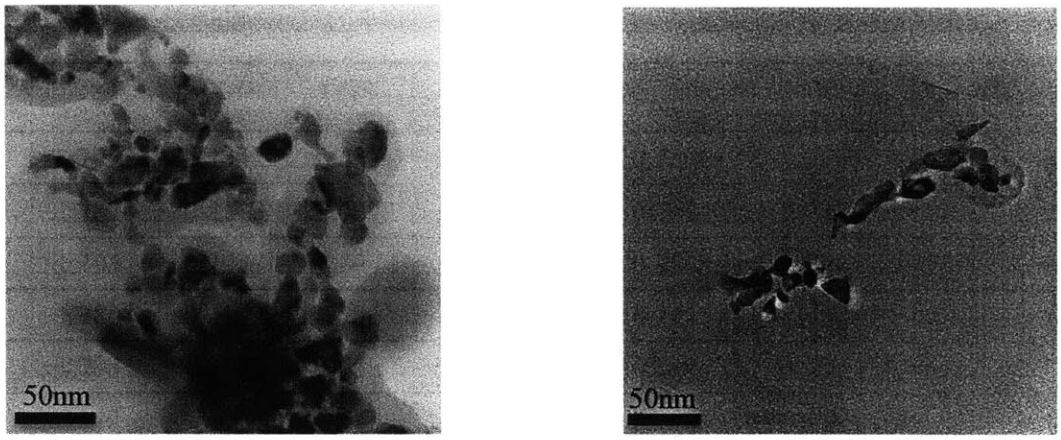

(a) (b)

Figure 2-3: TEM images of two sections on the TEM grid: a) A region with multiple nanoparticles settled near each other, b) isolated nanoparticles

It should be noted that in comparison with the nanoparticle size calculated by DLS, the TEM images show that most of the nanoparticles are individually smaller than 30 nm and lie in the 15 – 25 nm size range. As is evident from Figure **2-3** (b), for some nanoparticles, the aspect ratio is significantly different from 1 (for perfect sphere). There are 3 possible reasons for the discrepancy between the DLS and TEM measured diameters. First, DLS provides a measure of the hydrodynamic diameter of the particles, which might also involve the effect of the dispersant molecules (an undisclosed polyacrylate dispersant is used in the Nyacol DP5370 ZnO nanofluids) which could get attached to the surface of the nanoparticles, leading to a significantly higher particle size calculated by DLS than by TEM. Second, DLS measures the diameter of an equivalent sphere, and the fact that the nanofluids do not have an aspect ratio of 1 can also give rise to different particle size measured by DLS. Third, the nanoparticles in the nanofluid agglomerate with each other, causing the DLS to measure the diameter of the agglomerates rather than the individual particles, hence leading to a higher particle size.

2.1.1.5. Composition

To complete the characterization of the Nyacol DP5370 nanofluid, we also completed a Nuclear Activation Analysis (NAA), to obtain the precise chemical composition of the as-received nanofluids. NAA was performed, on the Nyacol DP5370 nanofluid, by the technical team at the Nuclear Reactor Laboratory at MIT. Table **2-6** below shows the constituents found in the nanofluid along with their concentrations and the irradiation time for the nanofluid.

Table 2-6: NAA analysis data for DP5370 nanofluids

Elements ID	Concentration (PPM)	Uncertainty (%)	Irr. Time in (min)
Al	59.17	13.73	1
Cl	50.05	15.59	1
La	0.29	13.86	15
Mg	275.26	8.37	1
Mn	28.84	4.70	1
Na	2100.56	3.20	15
Sb	10.87	2.40	15
Zn	229768.62	0.80	15

As shown in Section 2.1.1.1, the concentration of the DP5370 nanofluids was measured to be 29.523 wt% ZnO. Also, density of the DP5370 nanofluid was measured to be 1.2679 g/cc (as shown in Table **2-4**).

Thus, 1 l of nanofluid = 1.2679 kg nanofluid

= 0.29523*1.2679 kg ZnO

= 0.29523*1.2679 *65/81 kg Zn

$= 0.300382$ kg Zn

Therefore, expected concentration of Zn is 300382 ppm. However, according to Table **2-6**, the concentration of Zn obtained by NAA is 229768 ppm, i.e. the concentration of Zn measured by NAA is lower than the expected concentration. One of the possible explanations for this observation is that the DP5370 nanoparticles start to settle over time, even though the pH measurements confirm that the nanofluids should stay stable. Moreover, there is not much evidence of settling to the naked eye. It must be noted that the nanofluids are always vigorously shaken before making any measurements.

Secondly, trace amounts of other elements (such as Al, Cl, Mg, La, Mn, Na and Sb) are found in the nanofluid as shown in Table **2-6**. However, the relatively high measured concentration of Na of 2100 ppm suggests that a Na-containing compound might have been intentionally added by Nyacol. We hypothesized that compound to be NaOH to maintain the pH of the solution. However, since the pH of nanofluid is 9, this implies (under this assumption)

$$[OH^-] = [Na^+] = 10^{-5}\,M$$

Thus, weight of Na in 1 l of nanofluid $= 23 * 10^{-5}$ g $= 0.23$ mg

Thus, expected concentration of Na (if it were present as NaOH) $= 0.23$ ppm.

However, the concentration of Na measured by NAA is much higher. This suggests that Na is likely present in the solution in some other form. Unfortunately, the exact amount and chemical form of the dispersant could not be ascertained because Nyacol refused to disclose this information.

2.1.2. Diluted test nanofluids

The diluted test nanofluids with 0.01 v% ZnO are prepared by diluting the DP5370 nanofluids with DI Water, as will be described in Section 4.1. The diluted 0.01 v% ZnO nanofluids will be referred to as "test nanofluids" from this point onwards in the thesis. After dilution, they were characterized for their thermo physical properties as summarized in the following sections.

2.1.2.1. pH

As mentioned in Section 2.1.1.2, to ensure stability of nanofluids, their pH should range between 8 and 10. To verify stability of diluted nanofluids, their pH was also measured post-dilution. Table 2-7 summarizes the measurements made on 3 samples at room temperature. The average pH of the diluted nanofluids was measured to be 8.66. Hence, it is concluded that the diluted test-nanofluids remain colloidally stable.

Table 2-7: pH measurements of test nanofluids at room temperature

Sample	Nanoparticle size (nm)
1	8.73
2	8.85
3	8.41
Average	**8.66**

2.1.2.2. Density

The density of the test nanofluids can be estimated as

$$\rho_{nf} = \phi\rho_{np} + (1 - \phi)\rho_l \qquad \text{Eq. 2.7}$$

where ϕ is the volumetric concentration of the nanoparticles in solution, ρ_{np} is the density of the suspended nanoparticles, and ρ_l is the density of the base fluid. For 0.01 v% ZnO nanofluids, the density is estimated to be 0.9985 g/cc, which is only slightly different from the value of pure water of 0.998 g/cc.

2.1.2.3. Surface Tension

The surface tension of the diluted nanofluids was measured, at room temperature, using the KSV Sigma 703 Digital Tensiometer. The tensiometer uses the Wilhelmy Plate Method. As the base case, the surface tension of DI Water was also measured. Table **2-8** summarizes the measurements made for 3 samples of DI water, and Table **2-9** summarizes the measurements made for 3 samples of the test-nanofluid. The average surface tension of DI Water was measured to be 70.9 mN/m, and the average surface tension of test-nanofluid was 71.3 mN/m. This represents only a 0.56 % increase in surface tension of test-nanofluid, compared to DI Water.

Table 2-8: Surface Tension measurement for DI Water

Sample	**σ (mN/m)**
1	70.7
2	70.8
3	71.1
Average	**70.9**

Table 2-9: Surface Tension measurement for test nanofluid

Sample	σ (mN/m)
1	71.4
2	71.3
3	71.3
Average	**71.3**

2.1.2.4. Thermal Conductivity

The thermal conductivity of the diluted nanofluids was measured, at room temperature, using the KD2-pro thermal properties analyzer. The thermal conductivity of DI Water was also measured as the base case. Table **2-10** summarizes the conductivity measurements for 5 different samples of DI Water, and Table **2-11** summarizes the measurements for 5 different sample of the test-nanofluid. The average thermal conductivity values for DI Water and test-nanofluid were measured to be 0.642 W/mK and 0.617 w/mK, respectively. This represents a 3.89 % decrease in thermal conductivity of test-nanofluid, compared to DI Water. Such small difference is well within the experimental uncertainty of the KD2-pro instrument [36].

Table 2-10: Thermal conductivity measurement for DI Water

Sample	k (W/mK)
1	0.629
2	0.679
3	0.695
4	0.616
5	0.592
Average	**0.642**

Table 2-11: Thermal conductivity measurement for test nanofluid

Sample	k (W/mK)
1	0.578
2	0.583
3	0.636
4	0.646
5	0.643
Average	**0.617**

2.1.2.5. Viscosity

Dynamic viscosity measurements of the diluted nanofluids were carried out using a Cannon-Fenske Opaque (Reverse Flow) Viscometer, at room temperature. The viscosity of DI Water was also measured as the base case. Table **2-12** and Table **2-13** summarize the viscosity measurements for 3 different samples each of DI Water and the test-nanofluid, respectively. The average viscosity for DI Water and test-nanofluid were measured to be 0.877 Pa-s and 0.880 Pa-s, respectively. Again, the viscosities of DI water and test-nanofluid are observed to be the same, within experimental uncertainties.

Table 2-12: Viscosity measurement for DI Water

Sample	μ (Pa-s)
1	0.872
2	0.889
3	0.871
Average	**0.877**

Table 2-13: Viscosity measurement for test nanofluid

Sample	μ (Pa-s)
1	0.868
2	0.888
3	0.884
Average	**0.880**

2.2. Summary of nanofluid characterization

Complete characterization of both the as-received, concentrated, DP5370 ZnO nanofluid and the diluted test-nanofluid was carried out prior to the experiments. The concentration of the DP5370 nanofluids was measured to be 29.523 wt% ZnO, which is in good agreement with the vendor specified value of 30 %. pH measurements on both the concentrated and the dilute nanofluids confirm that the nanofluids stay stable. With the Nuclear Activation Analysis done on samples prepared from DP5370 nanofluids, trace impurities of certain elements were detected. However, appreciable amounts of sodium were observed to be present in the nanofluid. Sodium could be present in the form of the undisclosed surfactant added by the Nyacol to the DP5370 nanofluids to prevent agglomeration. Measurement of nanoparticle size, in solution, yielded higher size ranges of the nanoparticles, than specified by Nyacol. This is possible, either due to a higher particle size in-solution because of the surfactant adding to the particle size, or due to the high aspect ratio (as seen by the TEM measurements on dried nanoparticles), which could give, rise to a higher hydrodynamic diameter than the diameter of the nanoparticles. It was also seen that the thermo physical properties of the highly diluted test-nanofluids do not deviate significantly from those of DI water. Therefore, any changes observed in boiling behavior of nanofluids, compared to DI water, must be attributed to surface phenomena, not change in boiling fluid.

3. Pool Boiling Facility

This chapter, first, describes the approach used to conduct the experiments, and complete the post-test analyses for the heaters to investigate the effect of nanofluids compared to DI water, on CHF. After detailing the approach, it describes the pool boiling facility (PBF) used for the experiments. The capabilities of the experimental set-up are discussed. Here, all the individual components of the PBF are detailed, with their functionality and requirements.

3.1. Approach

3.1.1. Experiments

To achieve the objectives mentioned in Section 1.3, we use a unique PBF constructed in the laboratory. For all the experiments, the heater element is loaded in the PBF described below, and the experiment is completed. In this thesis, a metallic heater element is used. The heater is resistively heated by passing DC current through it. During the progress of the experiments, the voltage drop across the heater (ΔV) and current passing through the heater (I) are measured, and the heat flux transferred to the test-fluid is calculated as

$$q'' = \frac{I(\Delta V)}{A_{ht}} \quad \text{Eq. 3.1}$$

where A_{ht} is the surface area of heat transfer. The heat flux is increased during the experiment until CHF happens, at which point the heater breaks and the experiment ends. All the measurements made are recorded using an Agilent Data Acquisition System

(DAS). For all conditions and parameters, tests are run with both DI water (for the base-case) as well as the test-nanofluid.

3.1.2. Post-test Analysis

After the completion of the tests, surface analyses are done on the tested heaters, to investigate the effects of nanofluids on CHF. The analyses include imaging using a High Resolution Scanning Electron Microscope (HR-SEM) to compare the surfaces of the clean and tested heaters qualitatively, Confocal Microscopy to quantify the surface roughness, and Contact Angle measurements to examine the surface wettability.

3.1.2.1. HR-SEM

The SEM imaging is done by using a Jeol 6320 HR-SEM in the Center for Materials Science and Engineering (CMSE) at MIT. For imaging, electrons accelerated through a voltage of 10 kV are used. The surfaces, after testing, are imaged at various magnifications: 850X, 10,000X, 27,000X and 60,000X in order to analyze the surface in more qualitative detail. With SEM imaging, Energy Dispersive X-Ray Spectroscopy (EDX) analysis is also done on samples, to confirm the elements present on the surface.

3.1.2.2. Confocal Microscopy

While SEM imaging is able to provide a qualitative picture of the surfaces, and the changes that occur at the surface as a result of various experiments, it is desirable to quantify the surface topology too. This quantification is done in term of the changes in surface roughness that happen over the course of an experiment. The measure for surface roughness is the arithmetic average of surface peak to valley amplitude (R_a). Confocal

microscopy is done using an Olympus LEXT OLS3000 system at the Schlumberger Doll Research Center in Cambridge, MA. The confocal microscope is able to topographically scan the surface of heaters in 3D. This is done by fixing a focal plane (z), and scanning a 256 μm x 256μm rectangular (x-y) plane for that focal plane, and recording the data. Then, the focal plane is changed in z-direction and another scan is completed. The focal plane is altered, in steps, until the entire topography of the surface is scanned. The data collected, by means of the scans, is then processed by the software to generate 3D images of the scanned rectangular area.

3.1.2.3. Contact Angle

Finally, contact angle measurements (for DI water) are completed to examine the effects of nanofluids on the wettability of the heater surfaces. Contact angle is measured at room temperature, using the rame-hart Model 500 Advanced Goniometer/Tensiometer. Two types of contact angle measurements were done: static and dynamic. Static contact angle is the contact angle of a still liquid droplet on a surface. However, dynamic contact angle is that of a droplet with a moving surface-liquid interface. To measure the advancing contact angle, liquid is added gradually to a static drop of liquid. On addition of liquid, the shape of the droplet begins to change, until it reaches a point where the liquid-surface interface begins to move. The contact angle at the point in time when this movement of the interface occurs is called advancing contact angle. Similarly, receding contact angle is measured by gradually removing the liquid from a static droplet on the surface. The contact angle when the liquid-surface interface begins to move is called receding contact angle. These scenarios are pictorially represented in Figure **3-1**.

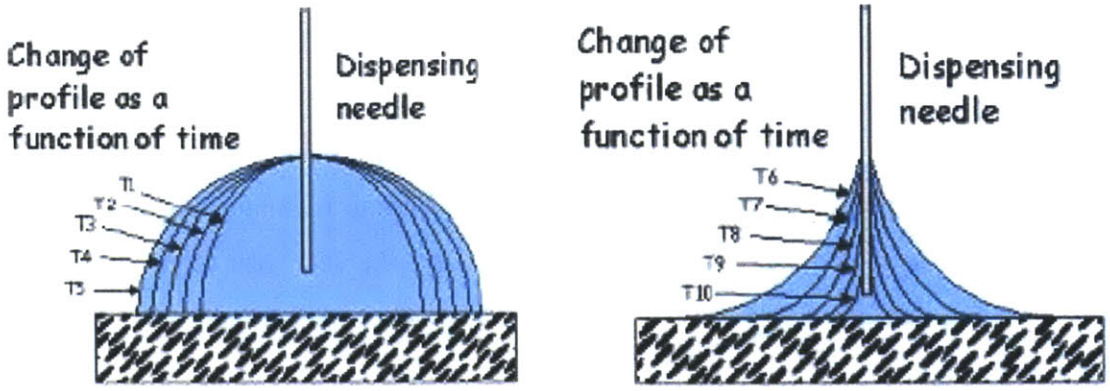

Figure 3-1: Technique for measuring advancing (left) and receding (right) contact angle (from ref. [79])

3.2. Experimental Set Up: Individual Components

This section will detail the heater and the facility that has been developed for the experiments. Before discussing the details of the design, first the experimental conditions, that the facility needs to be able to operate at, are noted.

In this thesis, two test fluids will be used throughout – DI water (as the benchmark case) and water-based 0.01v % ZnO nanofluid (test-nanofluid). The experiments will be conducted at fluid conditions of 1 atm and 100 ^{0}C, i.e. saturated conditions for water. The test-nanofluids have the same thermo physical properties as DI water. They also have the same saturation temperature at atmospheric pressure as verified by Kim in his thesis [80]. The pH of the nanofluids during the experiments is expected to vary between 6 and 10, depending upon the temperature of the nanofluids, with the nanofluids having a higher pH at room temperature and the lower value at the boiling conditions. The heaters are cut out of a sheet of SS304 (the heater design is described below) using water jet cutting. In order to approximate the fuel rod geometry, the heaters will be oriented vertically in the

PBF. The PBF was designed so as to allow for easy disassembly, for making the rinsing/cleaning of the test bath in between two tests easier. The PBF bath is made out of transparent material (quartz) for easy visualizations of the boiling process during the experiments. Furthermore, since the test fluid will be boiled in the PBF for up to 8 hours, the fluid level needs to be maintained in the PBF. In order to maintain the fluid level in the facility during the course of the entire experiment, the PBF has to be completely sealed, while maintaining the internal pressure at 1 atm, which is accomplished by a reflux condenser.

3.2.1. Test heater

In this thesis, to obtain the required power and flux levels, Joule's effect was utilized to heat a metallic heater by passing DC current through it. A metal was chosen as the material of choice, to replicate the metallic fuel cladding material used in nuclear reactors. However, due to the high cost, high electrical resistivity and difficulty in obtaining large supplies of zircalloy (the actual material used for nuclear fuel clad), stainless steel was chosen as the heating element material instead. Out of the available alloys, alloy 304 was selected as per the request made by Areva. The heater material will be called SS304 from here on.

Howard and Mudawar have discussed a hydrodynamic model for CHF in the near-vertical heater orientation [25]. They discuss the formation of periodic wetting fronts due to a disturbance in the liquid-vapor interface becoming unstable. It is noted in their work that the formation of the wetting fronts is fully developed if the heater length is greater than $3\lambda_c$ where λ_c is the critical wavelength for the fluid, given by

$$\lambda_c = 2\pi\sqrt{\frac{3\sigma}{(\rho_v - \rho_l)g}} \qquad \text{Eq. 3.2}$$

For DI water properties at 1 atm and 100^0 C, λ_c is calculated to be ~ 1 cm. This was used as a guideline while designing the test heater element, and a minimum length of required heater was set at 3 cm. The width of the heater was set at 5 mm to limit the maximum current required to achieve the target heat flux range. Since the resistivity of SS304 is relatively low, higher cross section for current flow would mean a very high current requirement for obtaining required flux levels. In the experiments here, for vertical configuration, a conservative estimate of the absolute maximum expected CHF was set at 2000 kW/m^2. To gain an estimate, using the resistivity of SS304 to be 0.000072 ohm-cm [81], a calculation of the current and voltage required to obtain a heat flux of 2000 kW/m^2, for a 3 cm x 5 mm heater for varying thicknesses between 0 and 1 mm, was done. **Figure 3-2** shows the required I & ΔV calculated. In order to have a mechanically robust design, a thickness of 0.036" (0.09144 mm) was chosen.

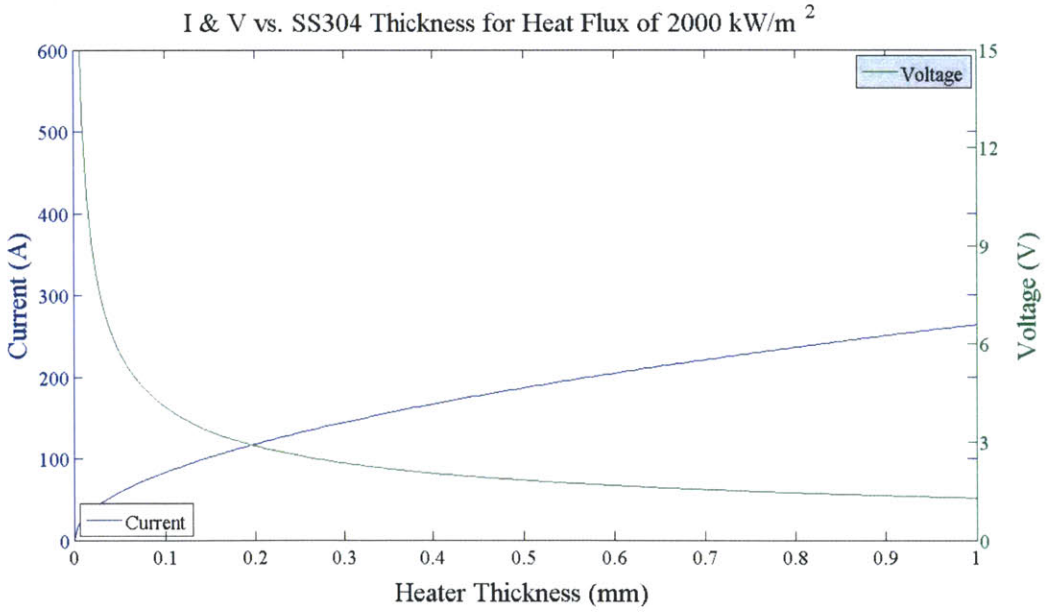

Figure 3-2: Required current and voltage drops for different thicknesses of SS304 to attain a heat flux of 2000 kW/m^2

The length of the entire element is 9.4 cm, with the heated length of 3.4 cm (the rest of the heater area is not used in the heat exchange between heater and fluid, but is utilized in mounting the heater in the PBF, shown in **Figure 3-16** in Section 3.2.3). **Figure 3-3** shows the schematic of the heating element used in this work, with **Figure 3-4** showing the 3-D view of the same.

The heating element is cut out of a standard 24" x 12" x 0.036" sheet of SS304 material ordered from McMaster Carr (Part# 9785K32). This sheet is subjected to water jet cutting at the MIT Hobby Shop, and the layout shown in **Figure 3-3** is cut out of it. **Figure 3-5** shows one of the SS304 sheets used, after cutting several heaters out of it. Figure 3-6 shows an actual heater cut out of SS304 sheet.

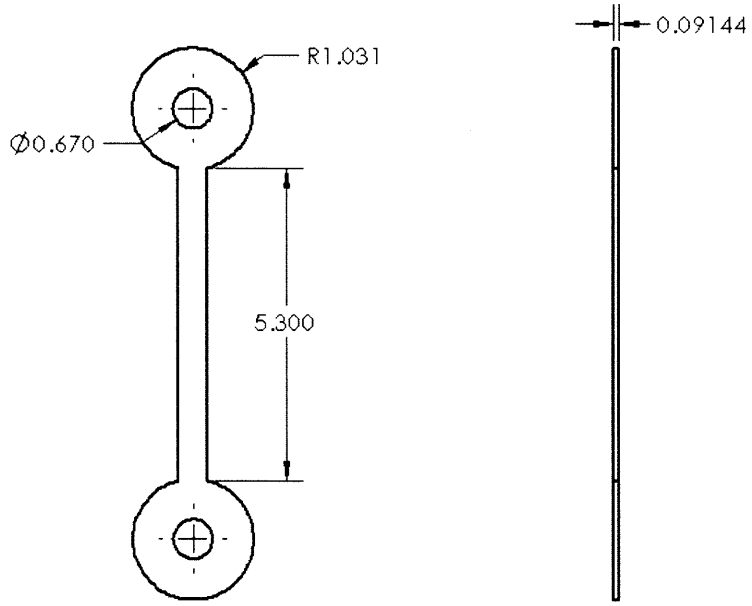

Figure 3-3: Schematic of the heating element (dimensions in cm)

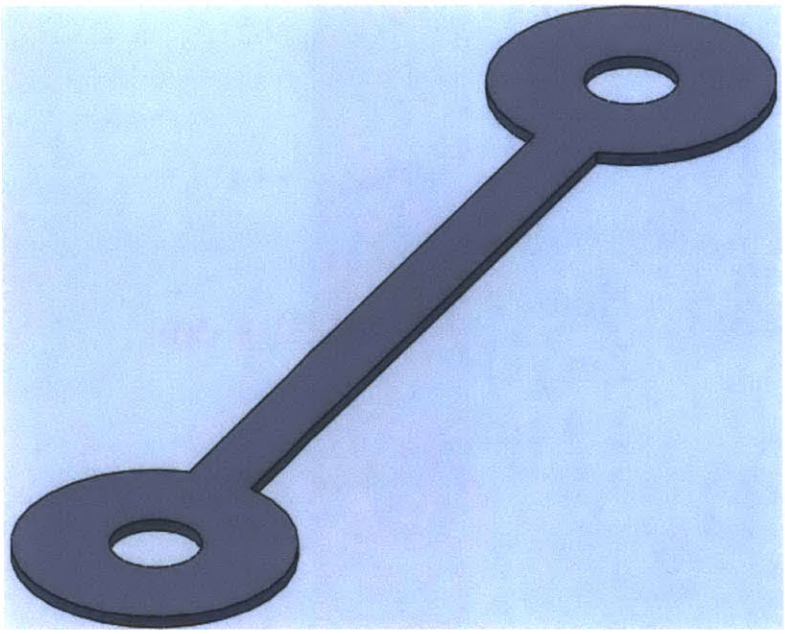

Figure 3-4: 3-D view of the heating element

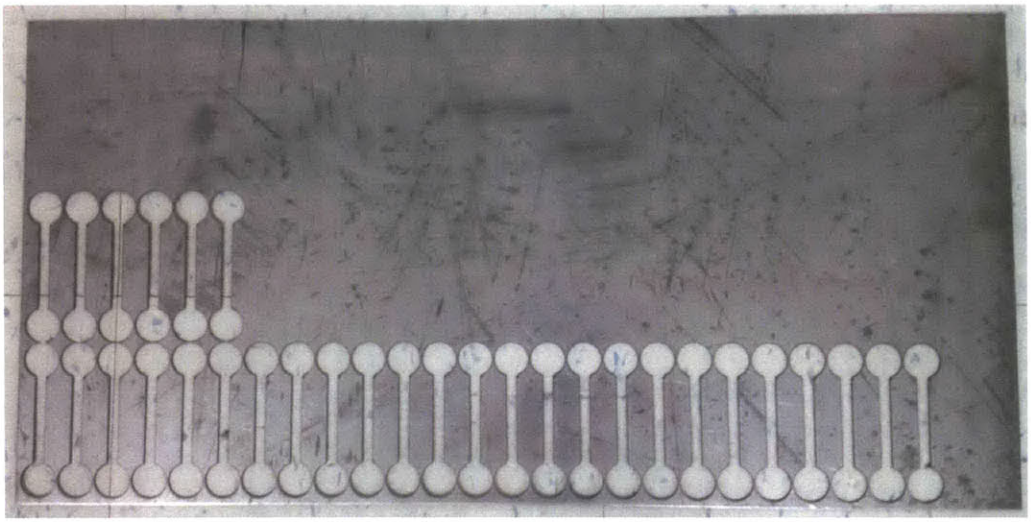

Figure 3-5: Picture of the 24" x 12" x 0.036" SS304 sheet used to cut the heating element from

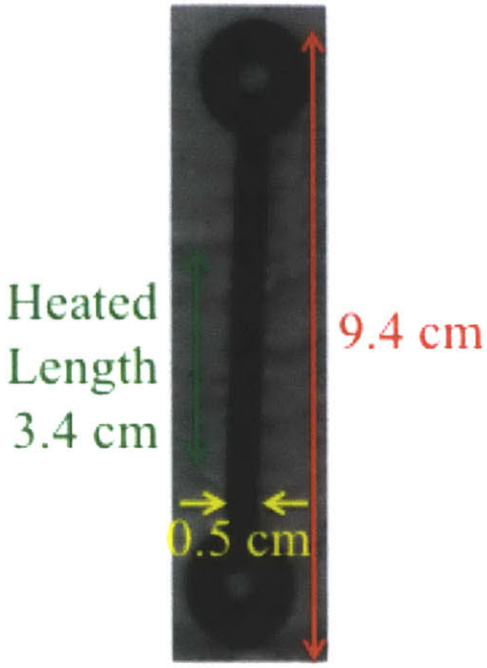

Figure 3-6: Picture of the SS304 heater element

The test-heater is completely submerged in the pool of the test fluid, during the experiments. Thus, boiling occurs on both surfaces of the heater.

3.2.2. Power Supply and Electrodes

The heating element is powered by a Genesys 10 kW power supply. It has a maximum output current of 500 A, and a maximum output voltage of 20 V. The power supply is shown in Figure 3-7.

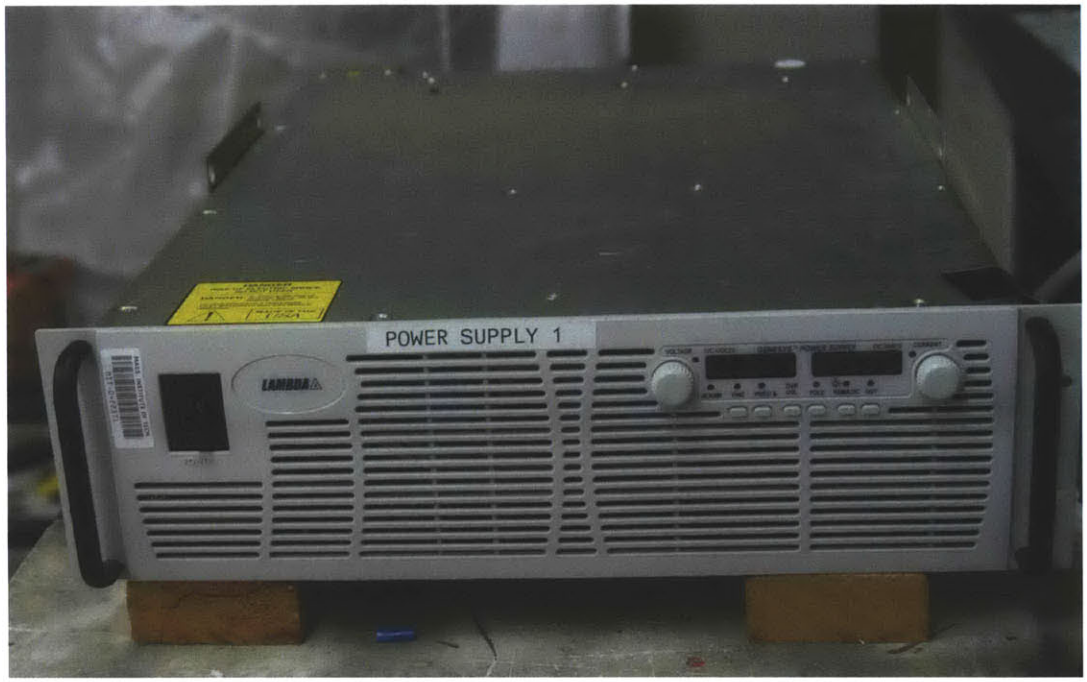

Figure 3-7: Picture of the power supply used in the experiments

The heater is connected to the power supply by means of two electrodes. The electrodes are made out of Cu, and are cylindrical rods with a diameter of 1 cm and a length of 30 cm. These Cu-rods are connected to a polycarbonate plate measuring 36 cm x 23 cm, which acts as the top lid for the experimental set-up. The top lid has 4 circular penetrations. Two penetrations have a diameter of 1 cm each, allowing for the Cu-rods to pass through them. The test heater is mounted between the lower ends of the copper rods, and the top ends of the rods are connected to the power supply cables. The copper electrodes are maneuverable in the vertical direction, such that the length of both rods beneath the lid can be varied, allowing for different lengths of the test heaters to be used. The 3rd and 4th penetrations in the lid have a diameter of 1.3 cm each. One of these is used for a reflux condenser and the other to insert thermocouples and voltage taps into the test bath for temperature measurements during the course of the experiment.

Figure 3-8 shows the drawing of the Cu-electrodes. **Figure 3-9** is a drawing of the top- and side-views of the top lid of the PBF, with the penetrations for different fixtures. **Figure 3-10** is a 3-D view of the top lid, and **Figure 3-11** shows a drawing of the lid with the Cu-electrodes inserted through it. **Figure 3-12** is a photograph of part of the PBF showing the lid and the Cu-electrodes.

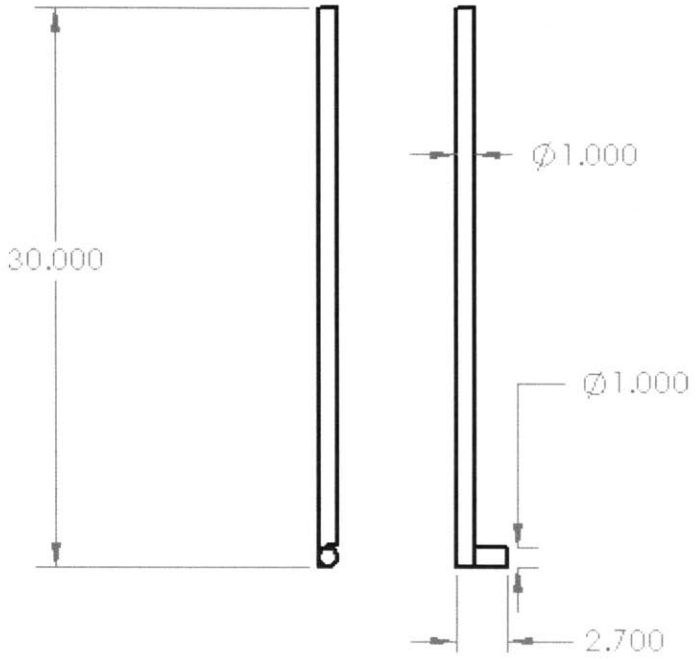

Figure 3-8: Front and side view of the copper electrodes. The heater is mounted between two such electrodes (dimensions in cm)

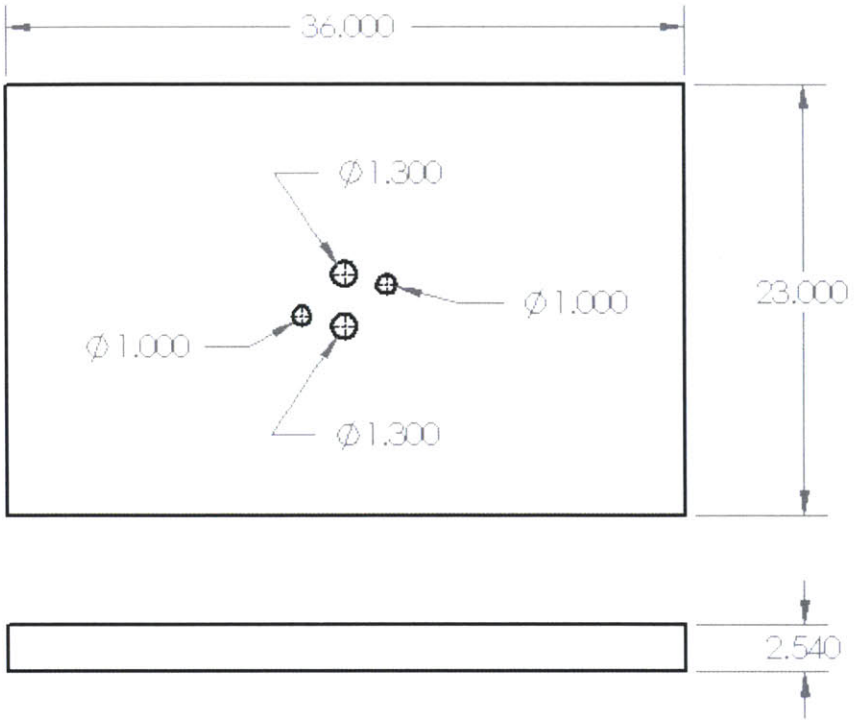

Figure 3-9: Top and side view of the lid used to seal the test section (dimensions in cm)

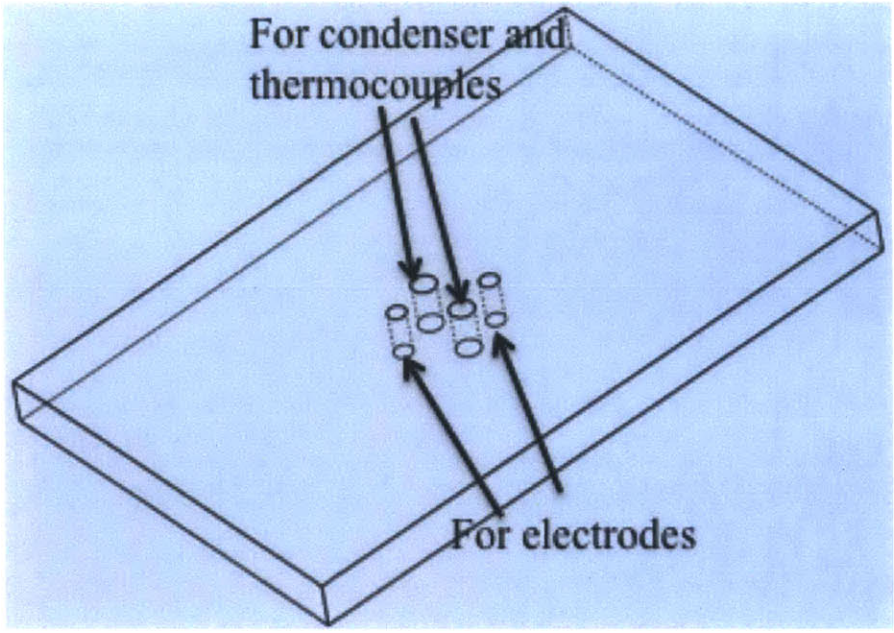

Figure 3-10: 3-D view of the lid used to seal the test section

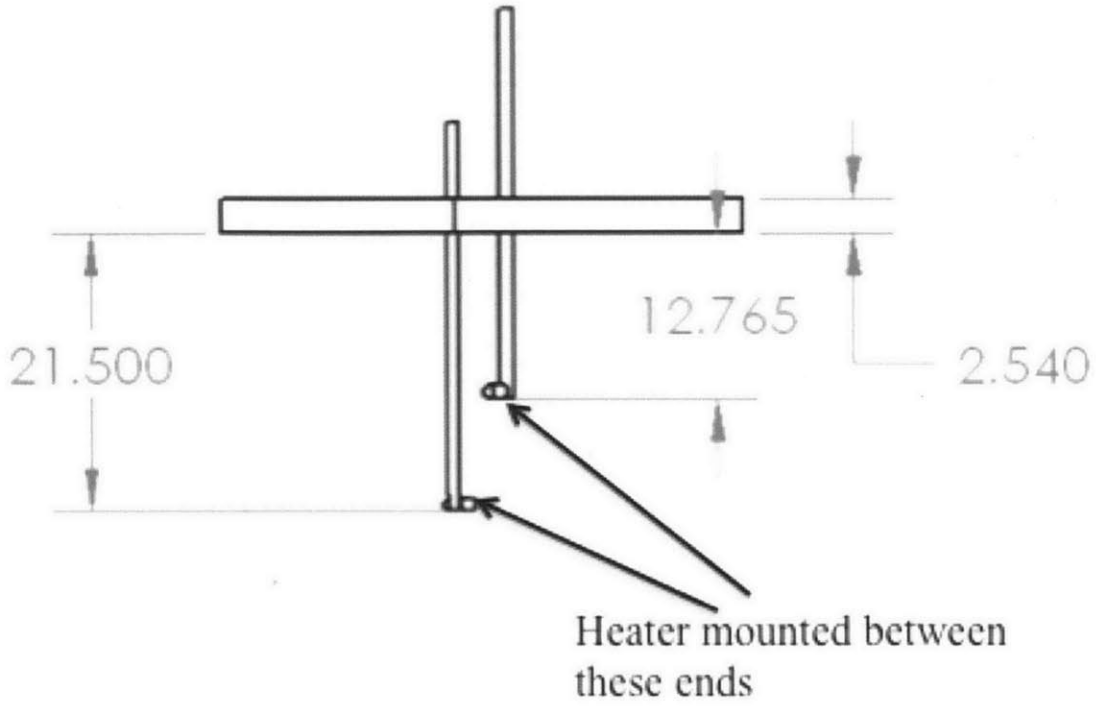

Figure 3-11: The side view of the lid with the Cu-electrodes, showing the positions of the electrodes when the heater is mounted between them (dimensions in cm)

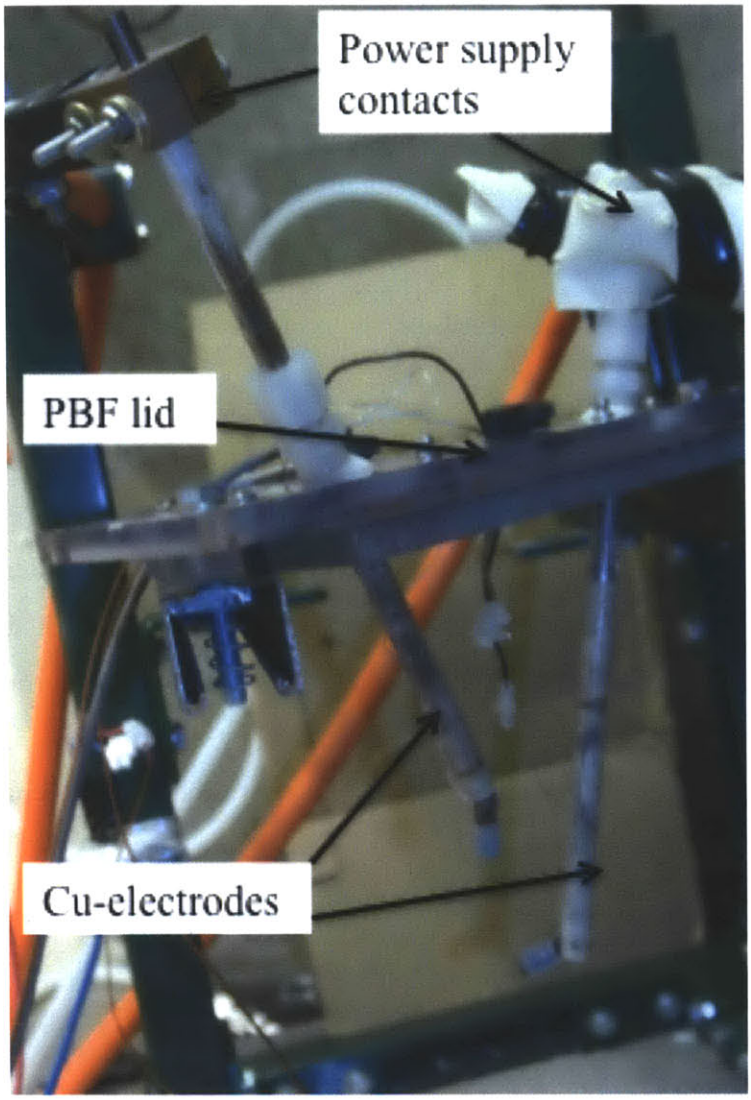

Figure 3-12: Photograph of the PBF lid with Cu-electrodes

3.2.3. Cu Blocks

The heater element is mounted between the Cu-electrodes by screwing them to the electrodes, using Cu-blocks. These Cu-blocks are cut out using an electric saw in the MIT Hobby shop, from a 0.25" thick Cu plate. The layout of the Cu-blocks is shown in **Figure 3-13**. During boiling, the bubbles formed rise vertically upwards due to buoyancy, travelling along the heater surface. Since the Cu-blocks used have a substantial thickness,

perfectly cubical blocks could potentially hinder the rising bubbles, and could lead to accumulation of bubbles under the Cu-blocks near the heater top. This can lead to the localized area being covered by large amounts of bubbles, giving rise to an artificial CHF. In order to prevent this from happening, a slight taper was introduced in the Cu-blocks, as shown in **Figure 3-13**, to allow smooth passing of bubbles. The bubbles, after rising to the top of the heater surface, are able to smoothly slide along the tapered area of the blocks, without accumulating under them (verified by using High Speed Video camera). Due to this tapering in Cu-blocks, they cover partial length of the heater. Heat exchange in these areas, is between Cu-blocks and test-fluid. However, since the blocks are extremely thick compared to the SS304 heater, the heat flux exchanged between the blocks and the test-fluid is negligible. Additionally, voltage taps on the sample allow for an accurate measurement of the heat generated in the test section. Hence, for CHF calculations, only the part of heater exposed to the test-fluid is important. **Figure 3-14** and **Figure 3-15** show both surfaces of the clean Cu-blocks used. **Figure 3-16** is a photograph showing the actual Cu-blocks used to screw the heater element to the Cu-electrodes, to mount it vertically.

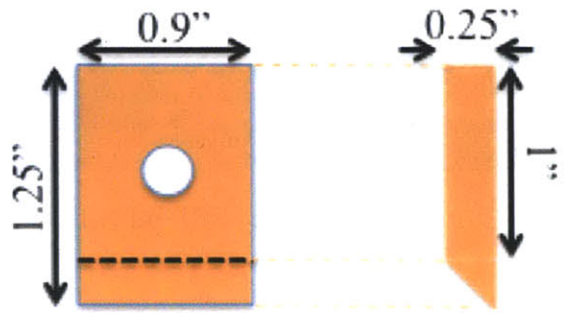

Figure 3-13: Layout of Cu-blocks used to mount heaters in PBF

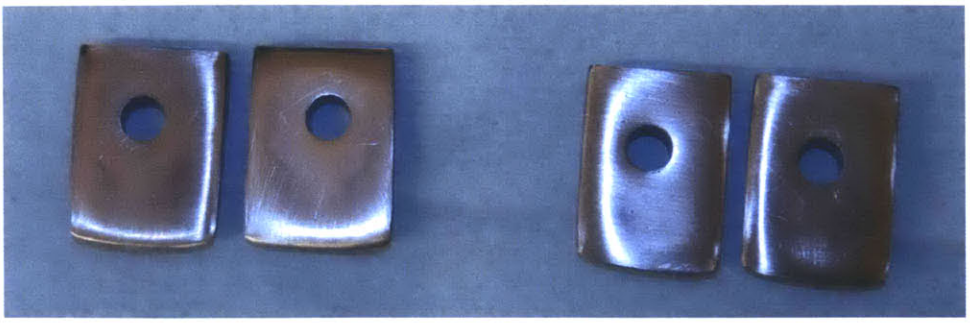

Figure 3-14: Photograph of one surface of the Cu-blocks

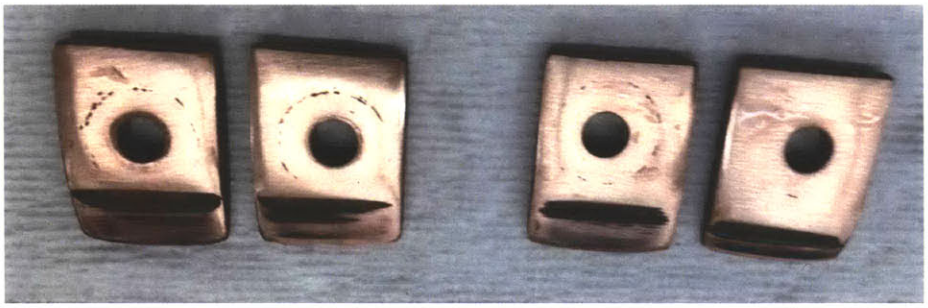

Figure 3-15: Photograph of other surface of the Cu-blocks

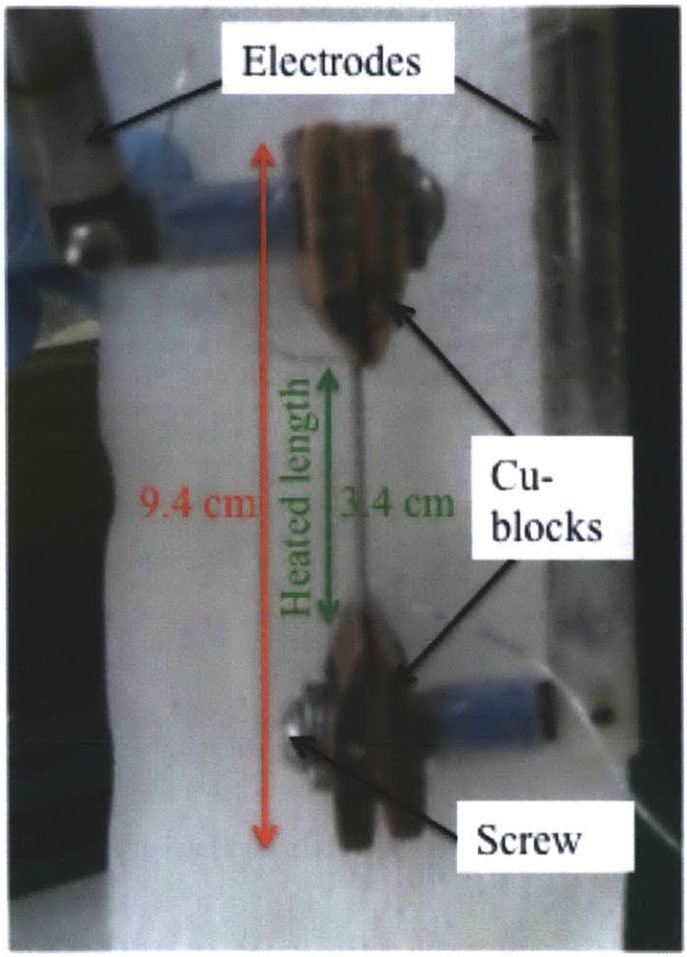

Figure 3-16: Photograph of the test heater mounted in the PBF using Cu-blocks

3.2.4. Test vessel

The heater, mounted as shown in **Figure 3-16**, is submerged in a pool of the test-fluid, allowing for boiling to happen from both surfaces of the heater. This test-fluid is housed in a test vessel that surrounds the mounted heater. The test vessel is a cylindrical beaker made out of quartz, and acts as the primary test bath containing the test fluid. Quartz is transparent, allowing for visualizations of the boiling process, and can withstand the experimental conditions. This beaker has an inner diameter of 18.5 cm, a wall thickness of 0.5 cm and a height of 25 cm. The test bath, surrounding the test-heater, is placed on a hot plate, which is eventually placed on a lab-jack. The lab-jack level is raised to press

the test bath top against the PBF lid tightly. To ensure proper sealing of the test bath, a rubber gasket (made of silicone foam, McMaster Part# 85925K403) is placed between the beaker and the lid. **Figure 3-17** shows the schematic of the top and front views of the test vessel, with **Figure 3-18** being a photograph of the test vessel.

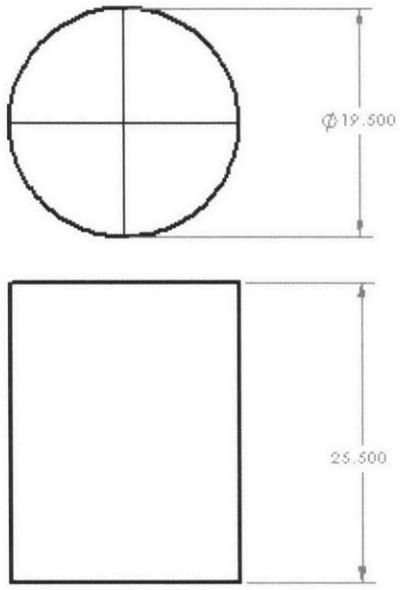

Figure 3-17: Top and Front view of the cylindrical beaker used as the test bath (dimensions in cm)

Figure 3-18: Photograph of the test vessel, with the gasket on top

3.2.5. Shunt

In order to accurately measure the current passing through the heater, a 125 $\mu\Omega$ (800A, 100 mV) shunt was used in the circuit. Current measurement is done by measuring the potential drop across the shunt and dividing that potential drop by the shunt resistance. **Figure 3-19** shows a photograph of the shunt used, and **Figure 3-20** shows the shunt in the power supply cables, as employed in the test set-up. **Table 3-1** details the specifications of this shunt.

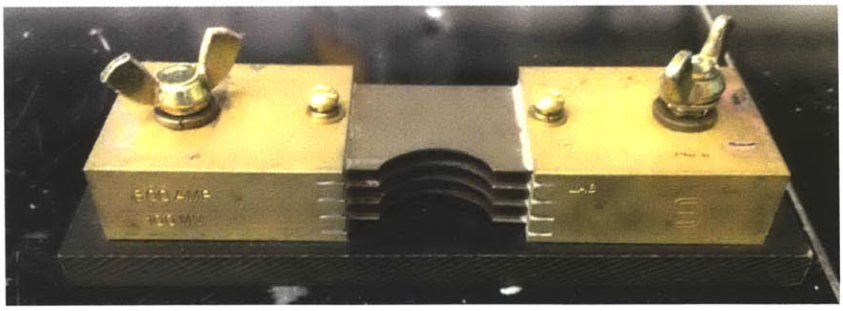

Figure 3-19: Photograph of the shunt used to measure current

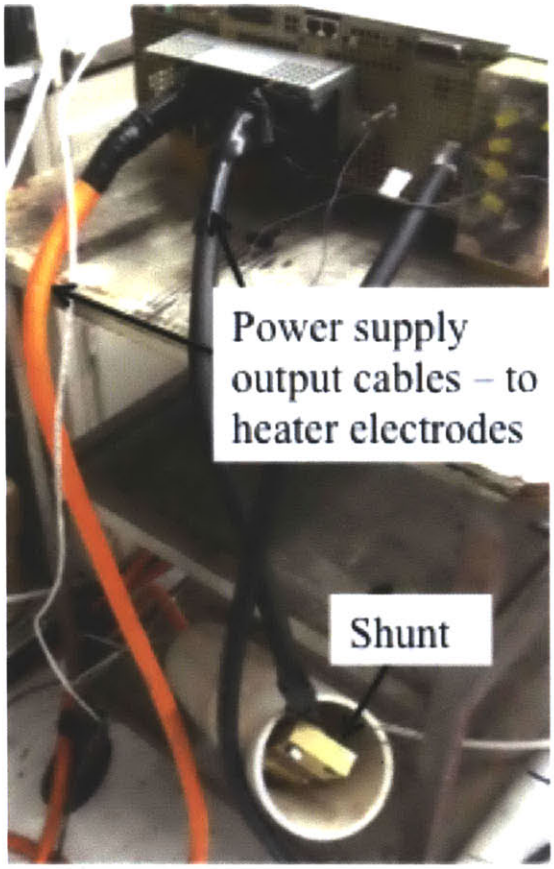

Figure 3-20: Photograph of the shunt in the actual circuit

Table 3-1: Specifications of shunt used for current measurements

Manufacturer	Simpson
Current Limit	800 A
Voltage Limit	100 mV
Stated Accuracy	1% of value

3.2.6. Voltage Drop

In order to accurately calculate the power generated (and hence the heat flux) in the heater at any instant, accurate voltage drop (ΔV) measurement across the heated area is required. Since the total heater length is longer than the heated length, SS316 wire is spot-welded to both ends of the heated length on the flat surface of the heaters. These wires are then connected to the Data Acquisition System (DAS), to accurately measure the potential drop across the heated length of the heater. **Figure 3-21** shows the wires spot-welded across the heated length, and the electrical connections that eventually go to the DAS.

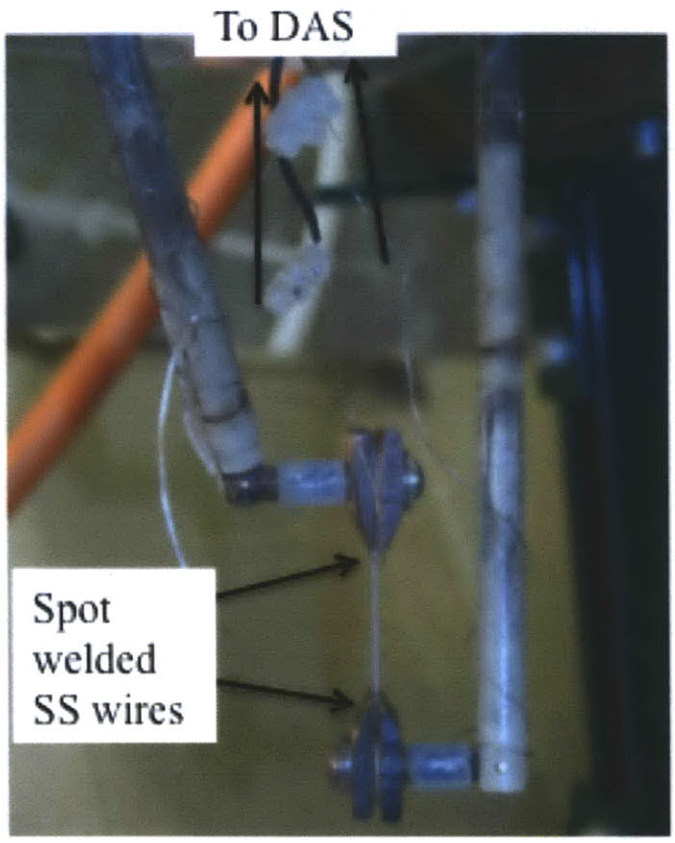

Figure 3-21: Spot-welds across the heated length. The spot-welded wires go to DAS

3.2.7. Thermocouples

All the experiments in this work are carried out at atmospheric pressure, and 100 ^{0}C. In order to confirm the temperature of the test fluid pool, the temperature of the pool is measured throughout the duration of an experiment. The fluid temperature measurements are made by using Type-T thermocouples (with specifications detailed in **Table 3-2**). The thermocouples are inserted in the test vessel through one of the 1.3 cm penetrations in the PBF lid (described in Section 3.2.2). In order to ensure uniformity of bath temperature in the entire test-fluid volume, two thermocouples are used, separated by an approximate vertical distance of 10 cm (one each near each pair of Cu-blocks used to mount heaters in PBF). **Figure 3-22** shows a photograph of the two thermocouples (TCs) as used in the PBF. The temperatures measured by the two TCs were within $\pm 1^0$C of each other, which is within the range of their measurement accuracy.

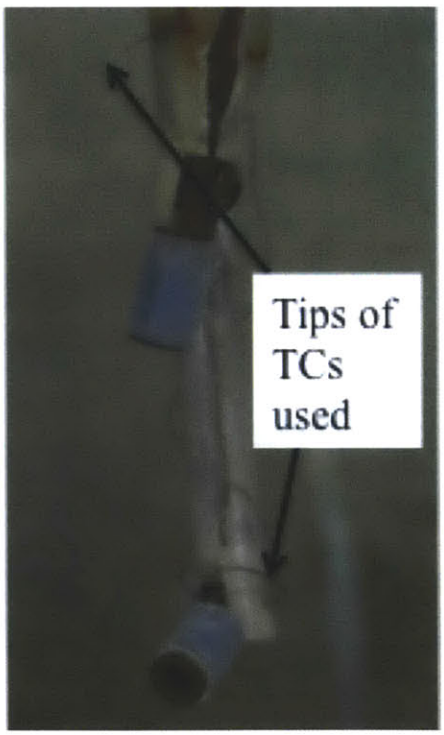

Figure 3-22: Photograph showing the two thermocouples (TCs) used to measure bath temperature

Table 3-2: Specifications of thermocouples used to measure bath temperature

Manufacturer	Omega
Type	T-type
Model	TT-T-20
Maximum Temperature	260 ^{0}C
Length	12"
Stated Accuracy	$\pm$1 ^{0}C

3.2.8. Hot Plate

In order to heat the test-fluid in the vessel to 100 ^{0}C, and maintain its temperature, the test vessel, with the fluid in it, is placed on a 698 W hot plate, manufactured by Corning. Figure 3-23 shows a photograph of the hot plate used in the set-up.

Figure 3-23: Photograph of the hot plate used to maintain the contents of the test-bath at 100 ^{0}C

3.2.9. Condenser and Chiller

In order to be able to allow boiling for as long as 8 hours, the PBF is completely sealed. Additionally, any steam formed during boiling is condensed back to water, and the condensate drips back into the PBF. This is done by using a reflux condenser. The condenser is mounted in the last remaining opening in the PBF lid, with a diameter of 1.3 cm. The condenser is connected to a 1350W Lauda Chiller that supplies the chilled water required for condensation of steam to water. Figure 3-24 and Figure 3-25 show the condenser and the chiller respectively.

Figure 3-24: Photograph of the condenser used

Figure 3-25: Photograph of the chiller used to supply chilled water to the condenser

3.3. Complete Pool Boiling Facility

The components described in Section 3.2 are assembled together to form the completed PBF. The assembled PBF is shown in Figure 3-26.

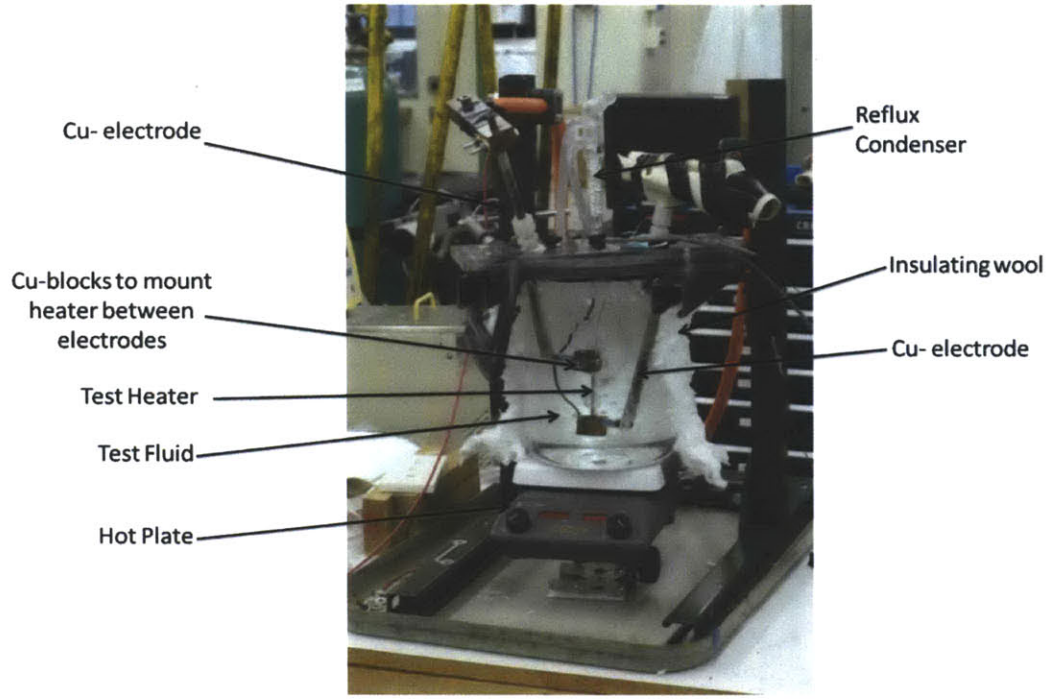

Figure 3-26: The complete assembled PBF

3.4. DAQ

The data, during the steady-state experiments is recorded by an Agilent 34980A data acquisition system. The data card used within the unit is the 34921T card. The 34921T card has 44 numbered channels. For the steady-state tests, the voltage across the sample, voltage across shunt and temperatures at both the thermocouples are measured through channels 1, 2, 4 and 5 respectively. Through the data card, the system receives analog differential voltage signals from the various respective instrumentations, and the signals are converted into digital and recorded by the 34980A unit. The recorded values are then converted into meaningful data such as voltage, current, power, flux etc. by simple mathematical calculations done through the Benchlink software for the 34980A unit. **Figure 3-27** and **Figure 3-28** show the 34980A unit and the 34921T data card, respectively.

Figure 3-27: Photograph of the Agilent 34980A unit

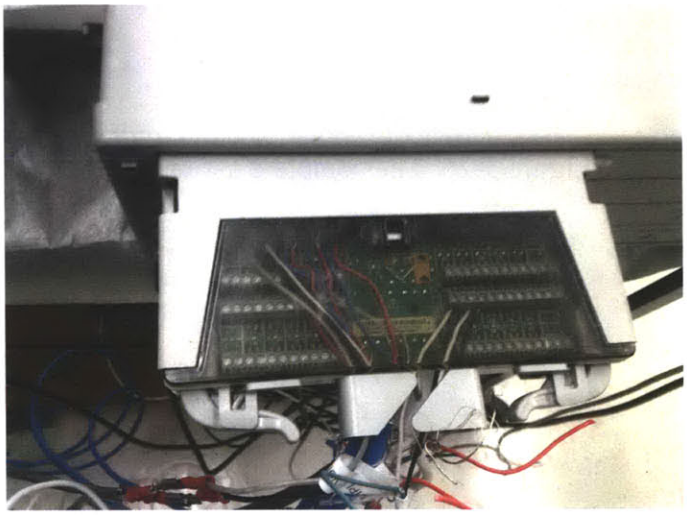

Figure 3-28: Photograph of the 34921T card used in the 34980A unit

4. Steady-State Tests

To investigate the effects of nanofluids on CHF, several experiments are run in steady state after mounting the test heaters in the PBF described in Chapter 3. For each of the three parameters of interest, namely initial surface roughness, surface wettability and pre-boiling time, everything else in the PBF was kept the same with the only change being in the test fluid. Experiments with DI water served as the base case for CHF values, and the experiments with nanofluids were done to analyze their effects on CHF. Each experiment (i.e. combination of particular surface conditioning and test-fluid) is repeated at least twice to ensure repeatability. However, if for any experiment, the CHF obtained in the two test runs varies from the mean CHF by more than 20%, the experiment is repeated more times in order to gather enough data to be confident in the CHF values. After gathering data for multiple experiments for the same experimental conditions, Pierce's criterion [82] is used to eliminate data outliers. The following sections will detail the test procedures as well as the results obtained for the steady-state tests.

4.1. Nanofluid Dilution

The Nyacol DP5370 nanofluids are diluted down to the test concentration of 0.01 v% ZnO. The dilution exercise prepares 4500 ml of diluted nanofluids, which is the volume of test-fluid used for each test. The dilution is carried out by mixing 4500 ml of DI water with *V ml* of Nyacol DP5370 nanofluid. Using the results obtained for the density of DP5370 nanofluid, as discussed in Section 2.1.1.3, the following analysis is used to calculate the required volume of concentrated nanofluid (*V ml*).

Weight of V ml of DP5370 nanofluid = V*1.2679 g

Weight of ZnO in V ml of DP5370 nanofluid = V*1.2679*0.29523 g

Volume of ZnO in V ml of DP5370 nanofluid = V*1.2679/3.58 ml

Volume of ZnO required = 0.01% of 4500 ml = 0.45 ml

Thus,

$$\frac{1.2679*0.29523*V}{3.57} = 0.45 \qquad \text{Eq. 4.1}$$

Solving this, we get V = 4.30 ml.

4.2. Test Procedure

The test procedure consists of the following steps:

4.2.1. PBF Clean Up

The PBF is cleaned thoroughly. This includes rinsing the PBF lid twice with DI water. During this step, the Cu-electrodes are also rinsed by acetone, followed by DI water, twice. The Cu-blocks are cleaned thoroughly by using a sandpaper to remove any oxide formed on it from the previous test, and then rinsed with acetone and DI water, twice. The test vessel is also cleaned with acetone and DI water.

4.2.2. PBF Assembly

Two SS316 wires are spot welded across the heated length of the test heater, as explained in the Chapter 3. The heater is then mounted vertically between the Cu-electrodes of the PBF using the Cu-blocks. The Cu-electrodes remain in connection with the power supply

in between the tests. The spot-welded wires are connected to the DAS to allow for measurements of voltage drop across the heater during experiments. The test vessel is then brought in, under the mounted heater, and placed on the hot plate. The hot plate is further kept on a lab-jack, and the lab-jack is raised to push the test vessel against the PBF lid, to ensure proper sealing. The two thermocouples are inserted from the PBF lid. This completes the assembly of the PBF.

4.2.3. Test Fluid Transfer

After PBF assembly, the 4500 ml of the test-fluid (DI water or nanofluid) is pre-heated in a 1200 W (shown in Figure **4-1**) microwave oven for 40 min. This pre-heating brings the test fluid temperature to roughly 85 ^{0}C. After pre-heating, the test fluid is transferred to the test vessel by using a funnel. After the fluid transfer is complete, the condenser connected to the chiller is mounted in the PBF.

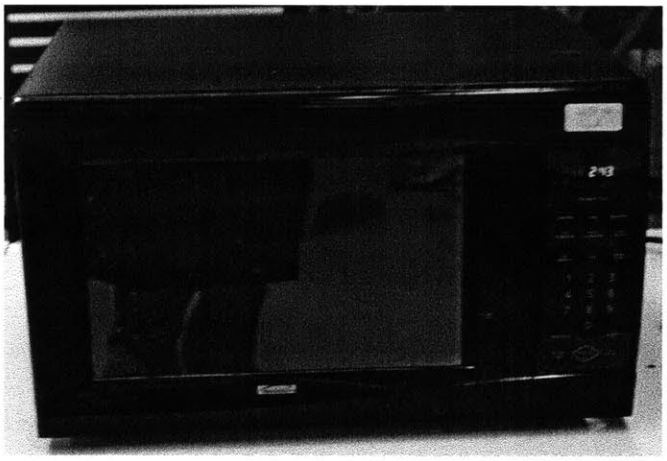

Figure 4-1: Oven used to pre-heat the test fluid

4.2.4. Degassing

After transferring the test-fluid to the PBF, the hot plate is turned on. This is done to serve two purposes: to heat the pre-heated fluid to 100 ^{0}C, and to remove any non-condensable gases from the test fluid. This process takes roughly 30 min.

4.2.5. Measurement of Initial Heater Resistance

Once the contents of the test vessel are confirmed to be at 100 ^{0}C by the measurements on the two thermocouples used, they are left as such for 5 minutes, to allow the submerged heater to reach the same bulk temperature as the surrounding fluid. After this, the resistance of the heater is measured, and is called R_{100}. The resistance measurement is done by passing 3.5 A and 6.9 A of current through the heater for 30 sec each, and measuring the corresponding voltage drop across the heater. Dividing the voltage drop by the current passing through the heater, R_{100} is obtained and recorded. Power produced in the heater at these current levels is 0.08W and 0.30W, respectively, which is low enough that it does not effect the bulk heater temperature, and hence its initial resistance R_{100}.

4.2.6. Heat Up to CHF and Recording Data

After recording R_{100}, the experiment is begun by supplying DC current from the power supply to the heater element. During the entire experiment, data is recorded by using the Agilent 34980A with the 34921T card. Data is recorded at an interval of 2 seconds. The recorded values are: current passing through the heater (I), voltage drop across the heater (ΔV), and the temperatures of the two thermocouples in the bath. Using the instantaneous values of I and ΔV, and the surface area of the heater, the instantaneous heat flux transferred to the fluid, as well as the instantaneous resistance of the heater, are calculated at each step. Current (hence the heat flux) is increased slowly, in discrete steps, with the

current (and heat flux) kept constant at each incremental step for 2.5 – 3 min. This is done to allow for the heat transfer process to reach steady state. After the 2-5 – 3 min wait, flux is increased again by increasing current supplied by power supply. This process is continued until the resistance of the heater rises abruptly, owing to an increase in the heater temperature because of change in heat transfer mechanism to film boiling. This point can be visually seen by the orange glow of the heater. At this juncture, in most cases, the heater ruptures at the location of CHF, and is broken into 2 pieces. This observation terminates the experiment, and the flux at which this happens is defined as CHF. The recorded data is saved as a Microsoft Excel file.

4.2.7. PBF Disassembly

After CHF is reached, the experiment is terminated. At this point, the PBF is disassembled. This involves dismounting the tested heater, cleaning the Cu-blocks using sand paper, and rinsing the Cu-electrodes and all the other PBF components with DI water. The dismounted heater is stored in a 50 ml centrifuge tube, and kept in a desiccator for post-test surface analysis.

4.2.8. Data Reduction: Obtaining Boiling Curve

After the end of the experiment, the collected data in the excel file is post-processed as described here, to obtain the boiling curve for the experiment. As mentioned above, the set-up is kept at each current (flux) level for 2.5 – 3 min, and the data is collected by DAS at an interval of 2 s. For each incremental step, an arithmetic mean of all the desired values (current, voltage across heater, heater resistance) collected over the 2.5 – 3 min duration is calculated (let us denote those means as $\overline{I_i}, \overline{\Delta V_i}$ *and* $\overline{R_i}$, respectively for an incremental step *i*). It must be noted that for data collected ($I_i, \Delta V_i$ *and* R_i) at each incremental step, the standard deviation is smaller less than 0.5%. There is negligible

variability in the data collected at each incremental step Using the temperature coefficient of resistivity (TCR)[1] of SS304, denoted by α, $\overline{T}_{bulk,i}$ is calculated as

$$\overline{T}_{bulk,i} = \frac{1}{\alpha}\frac{\overline{R_i} - R_{100}}{R_{100}} + 100 \qquad \text{Eq. 4.2}$$

Once $\overline{T}_{bulk,i}$ is obtained, it is used to calculate the wall temperature $\overline{T}_{w,i}$[2]. Finally, for each incremental step, the average flux is calculated as

$$\overline{q''}_i = \frac{\overline{I_i} * \overline{\Delta V_i}}{A_{ht}} \qquad \text{Eq. 4.3}$$

where A_{ht} is the area of heat transfer between the heater and fluid. Eventually, for each incremental step, heat flux is plotted against the wall superheat to generate the boiling curves. The boiling curves terminate at CHF. Note here that, it is assumed that the wall and bulk temperatures of the heater do not vary in the axial direction. Hence T_w and T_{bulk} are assumed to be constant for the entire heater length, in our calculations[3].

4.3. Uncertainty Analysis

[1] The calculation of TCR is discussed in detail in Appendix A

[2] The detailed mathematical analysis for the relationship between $\overline{T}_{bulk,i}$ and $\overline{T}_{w,i}$ is shown in Appendix A

[3] Experimental verifications of the fact that $\overline{T}_{bulk,i}$ and $\overline{T}_{w,i}$ are constant throughout the axial positions are shown in Appendix A

The experimental uncertainty in the measured instantaneous heat flux can be approximated by using the reported accuracies of the equipment used for the recording the data. The accuracies of the various measurements required to calculate heat flux are summarized in Table **4-1** (here L and W are the heated area length and width, respectively).

Table 4-1: Accuracy of experimental measurements

Quantity	Accuracy
ΔV (V)	0.004 + 0.0007% of ΔV
ΔV_{shunt} (mV)	0.005 + 0.004% of ΔV_{shunt}
ΔR_{shunt} (mΩ)	0.0000083
ΔL (mm)	0.1
ΔW (mm)	0.1

Using Bevington and Robinson's method of uncertainty propagation [83], for a function, which is a product of two measurement variables (x = uv), the error (standard deviation) in the measurement of the function can be calculated as

$$\frac{\Delta x}{x} = \sqrt{\left(\frac{\Delta u}{u}\right)^2 + \left(\frac{\Delta v}{v}\right)^2}$$

Since current passing through the heater (I), is measured by measuring ΔV_{shunt}, we can write

$$\frac{\Delta I}{I} = \sqrt{\left(\frac{\Delta V_{shunt}}{V_{shunt}}\right)^2 + \left(\frac{\Delta R_{shunt}}{R_{shunt}}\right)^2}$$

The uncertainty in measurement of area of heat transfer can be written as

$$\frac{\Delta A}{A} = \sqrt{\left(\frac{\Delta L}{L}\right)^2 + \left(\frac{\Delta W}{W}\right)^2}$$

and, the uncertainty in measurement of heat flux can be written as

$$\frac{\Delta q''}{q''} = \sqrt{\left(\frac{\Delta I}{I}\right)^2 + \left(\frac{\Delta V}{V}\right)^2 + \left(\frac{\Delta A}{A}\right)^2}$$

For a heat flux of 1000 kW/m^2, the uncertainty values are shown in Table **4-2**.

Table 4-2: Sample uncertainty values for q'' = 1000 kW/m^2

q'' (kW/m^2)	I(A)	V_{shunt} (mV)	ΔV (V)	$\Delta I/I$	$\Delta A/A$	$\Delta q''/q''$
1000	250	15.064	1.59	0.00003	0.02	0.0202

4.4. Test Matrix

As discussed in the objectives in Section 1.3, the first objective of this thesis is to correlate the effects of individual parameters – surface roughness, wettability and pre-boiling time – on nanofluid CHF. In the following sections, now, the results of experiments exploring effects of these parameters, individually, are discussed.

4.4.1. Surface Roughness

In Section 1.1.2 and Section 1.2, the surface effects on CHF, and the effects of nanofluids on surfaces during boiling were discussed. It was summarized that during boiling, nanoparticles present in the nanofluid develop a nanocoating on the surface, which can increase/decrease its roughness and porosity, hence altering the density of nucleation sites and the nucleation process, effecting CHF. So, we conduct experiments with DI water, as well as nanofluids, to examine the effects of two surfaces, which differ in their initial roughness, on CHF. Two values of initial surface roughness (R_a) were explored: ~0.1 μm and ~1 μm.

4.4.1.1. Roughness Control

The heater element described in 3.2.1 and shown in Figure 3-6 is subjected to different surface conditioning to obtain the two values of the surface roughness. In order to obtain the heaters with the lower value of R_a, the heater elements are sent to an external vendor (Ramco Machine, LLC) for polishing to mirror finish. These heaters will be referred to as "smooth heaters" from this point onwards.

To achieve the higher surface roughness on the heater element, the cut-out element is first cleaned with a sandpaper, to remove any dust/residue on the surface, followed by two cleaning cycles (in order) of DI water, acetone and ethanol. Eventually, the cleaned heaters are rinsed again with DI water before subjecting to a "sandblasting" process to roughen the surface. Sandblasting is carried out using an Econoline Siphon Abrasive Blasting Mini Cabinet (model 0308 mini). Sandblasting is achieved by passing compressed air through a specifically designed delivery blast gun consisting of a boron carbide nozzle and air jet. It is a blast gun that combines compressed air with abrasive media via a siphon. In this procedure, glass beads with diameters in the range 105 – 210

μm, and air compressed to a pressure of 80 psi (5.44 atm) is used. The blast gun is held perpendicular to the heater surface at a distance of 8 – 10 cm from the surface of the heater to be sandblasted. Glass beads are then blasted on to the surface and the gun is moved slowly along the length of the heater and back. Blasting on one surface is carried out for a total of 20 sec. Then the heater is turned over and the same steps are followed on the other side to obtain sandblasted heater surface. Figure **4-2** is a pictorial representation of the sandblasting procedure followed, and Figure **4-3** shows a photograph of the Econoline Sandblasting Cabinet used. These rougher heaters are called "sandblasted" heaters at all instances from here on, in this thesis. After sandblasting the heaters, they are again subjected to cleaning, by rinsing with DI water, acetone, ethanol and DI water (in this order).

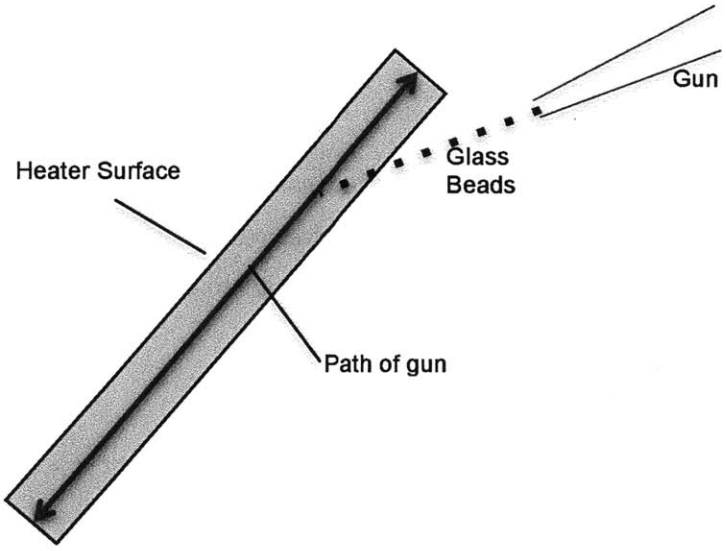

Figure 4-2: Pictorial representation of the sandblasting procedure

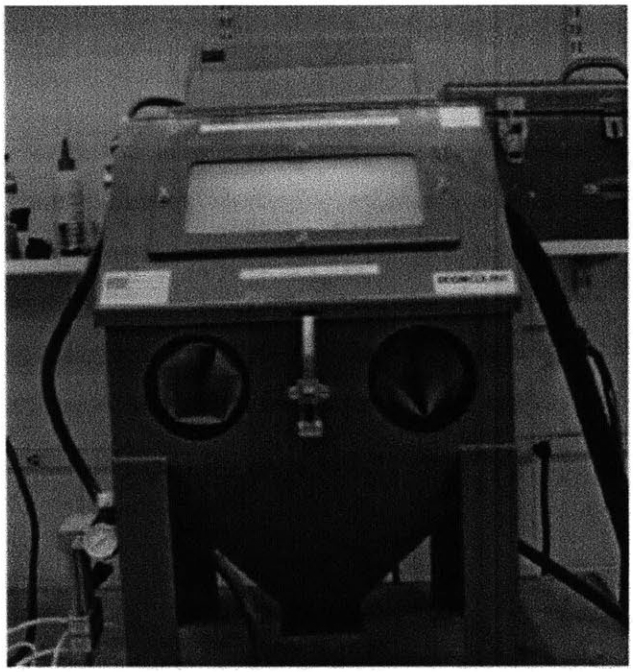

Figure 4-3: Photograph of the sandblasting cabinet

Samples of both heaters prepared by following the discussed procedures are shown in Figure **4-4**.

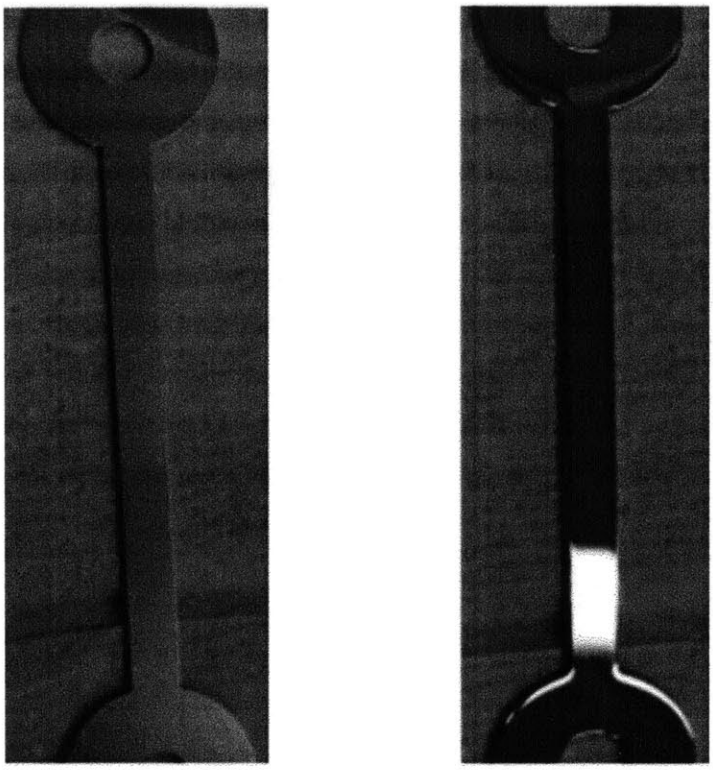

Figure 4-4: Photographs of sandblasted (left) and smooth/polished (right) heaters showing the difference in their surface texture/reflectance, visible to the naked eye

4.4.1.2. Pre-Test Surface Analysis

Surface roughness measurements on the unused smooth as well as sandblasted heaters were done using confocal microscopy. Figure **4-5** and Figure **4-6** show the confocal scans from the unused sandblasted and smooth heaters, respectively. From these figures, the difference in the surface texture or morphology of sandblasted and smooth heaters is evident. Analysis of the data obtained by multiple measurements using the confocal microscope showed that R_a for unused sandblasted heaters varied between 1.05 and 1.30 μm. On the other hand, R_a for unused smooth heaters varied between 0.05 and 0.09 μm. Thus, the target R_a values for two comparative surfaces were achieved by sandblasting and polishing of the heater elements.

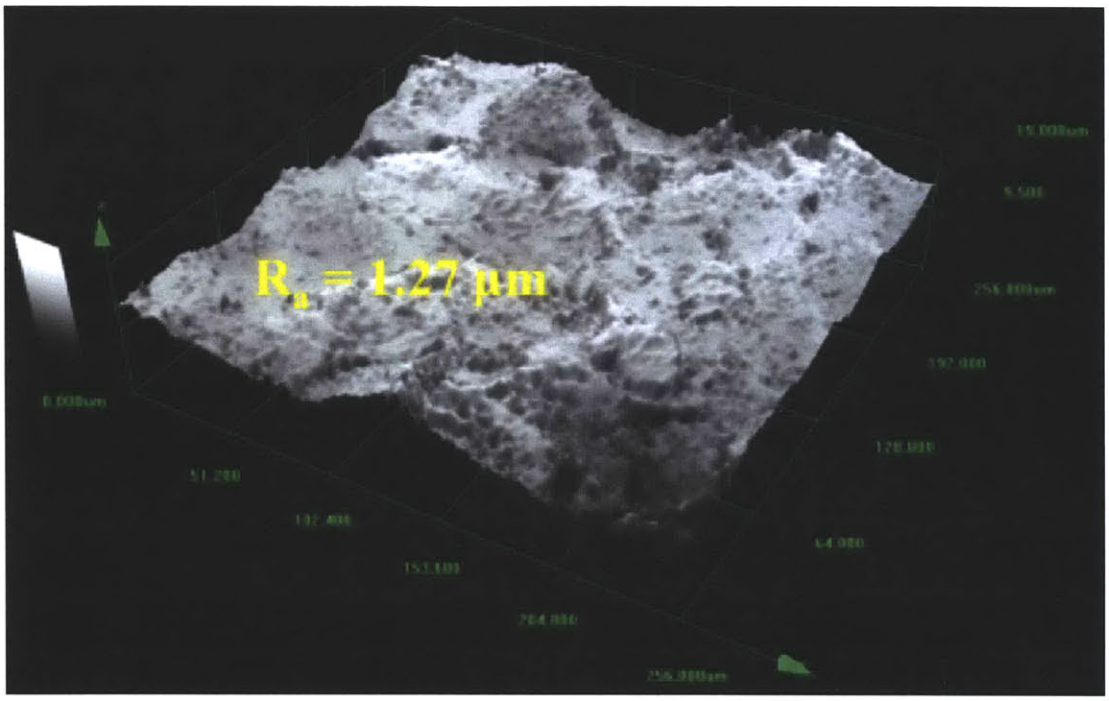

Figure 4-5: Confocal scan of an unused sandblasted heater (R_a = 1.27 µm)

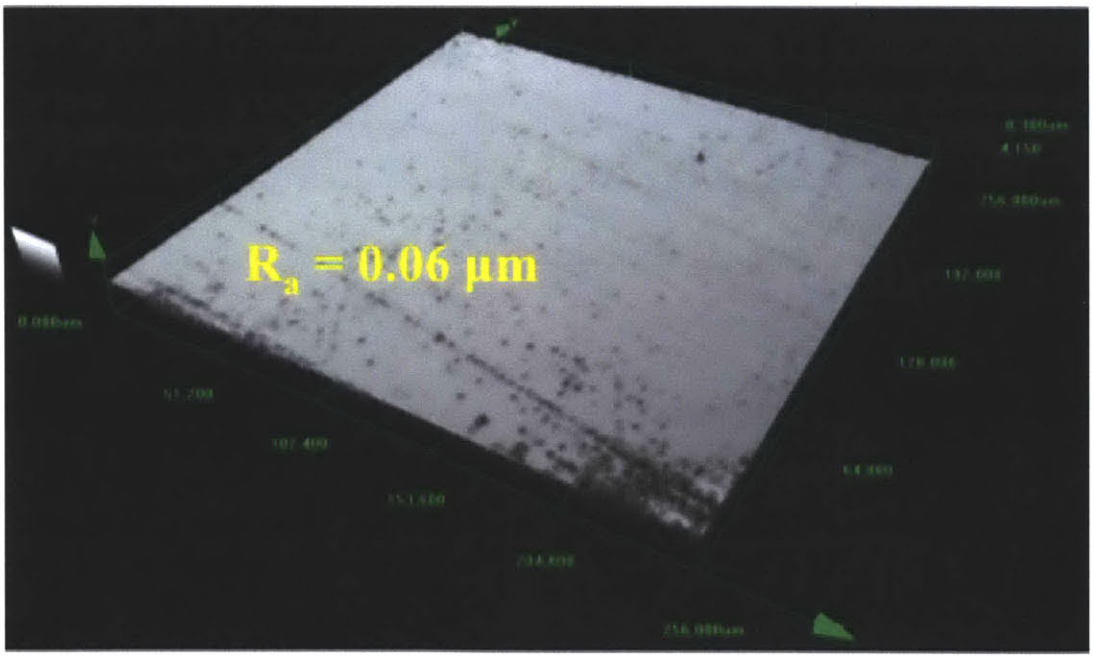

Figure 4-6: Confocal scan of an unused smooth heater (R_a = 0.06 µm)

The surface of the unused sandblasted and smooth heaters was also examined under a SEM to qualitatively compare both surfaces, to complement the quantitative comparison obtained by confocal microscopy. **Figure 4-7** and **Figure 4-8** show these images for both surfaces. Comparing these figures, the difference in the surface is seen clearly. Like confocal scans, SEM images also show the rough surface texture of the sandblasted heaters, while the polished heaters are extremely smooth.

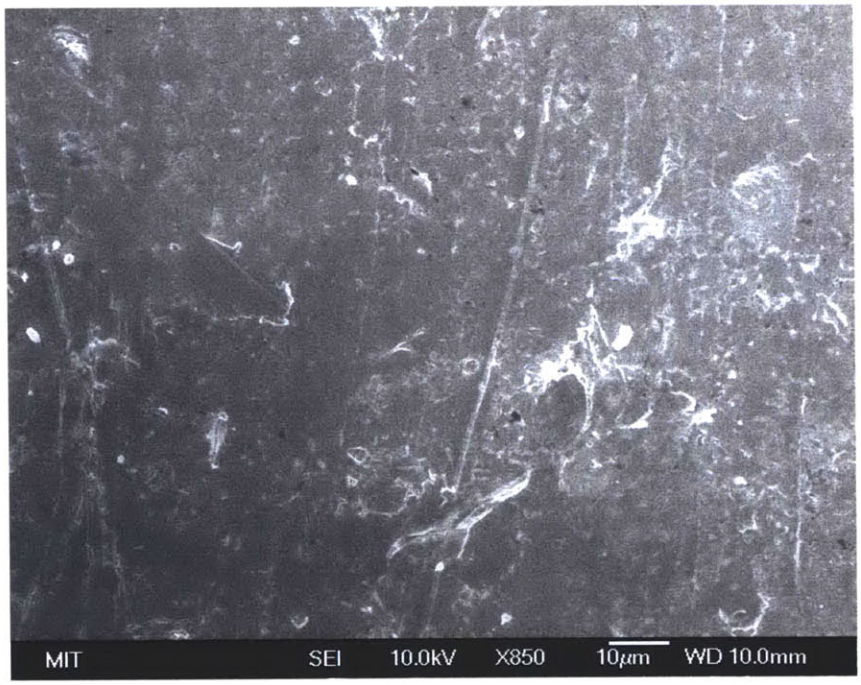

Figure 4-7: SEM image of an unused sandblasted heater showing a rough texture

Figure 4-8: SEM image of an unused smooth heater

The surface analysis of the unused heaters was completed by measuring the contact angle (static, advancing and receding) of a droplet of DI water on their surface, to quantify their wettability. **Figure 4-9** below shows the static contact angle measurement on unused sandblasted and smooth heaters. **Table 4-3** summarizes the contact angle measurements made on unused sandblasted and smooth surfaces. The static contact angle of DI water on sandblasted heater was seen to be ~70^0 whereas the static contact angle on smooth heater was ~100^0, thereby indicating a marked difference in their initial wettabilities. As seen in **Table 4-3**, the advancing contact angle for sandblasted and smooth heaters are ~80^0 and 120^0 respectively. For the smooth heaters, the advancing and receding contact angles are ~18^0 and ~70^0 respectively.

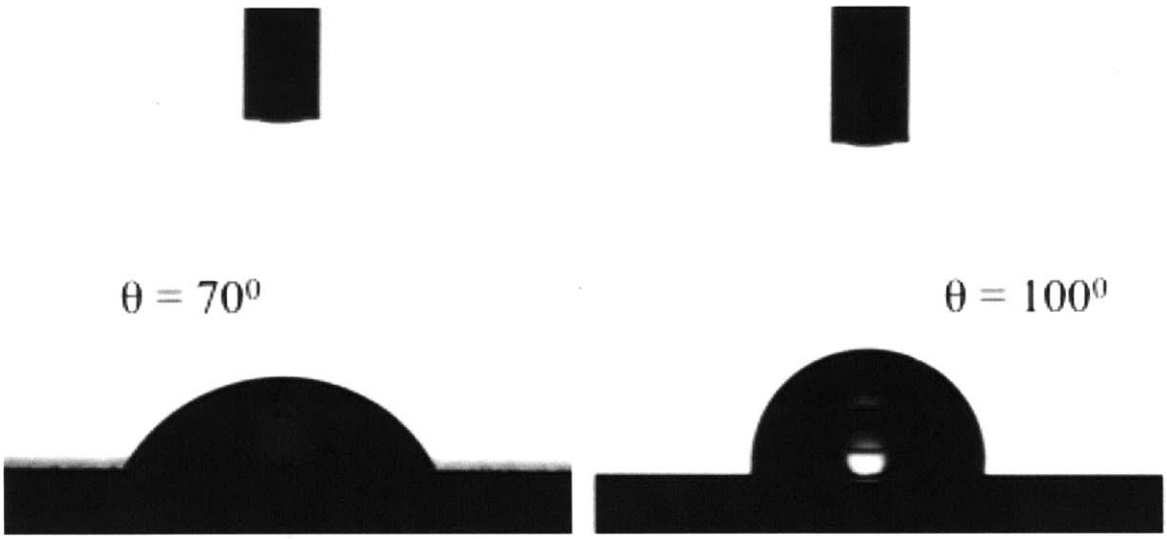

Figure 4-9: Static contact angle of a droplet of DI water on unused sandblasted (left) and smooth (right) heater surfaces

Table 4-3: Summary of contact angle measurements on unused heaters

Heater	Measurement	Contact Angle (degrees)		
		Static	Advancing	Receding
Sandblasted	1	70	83	18
Sandblasted	2	71	82	17
Smooth	1	105	115	70
Smooth	2	109	120	80

The contact angles seen in **Figure 4-9** are higher than expected for metallic surfaces. This could be due to the adsorption of hydrocarbons, at room temperature from the atmosphere, on the surface of the heaters for minimization of surface energy. However, these hydrocarbons could evaporate or burn off during boiling when the heater is at temperatures higher than 100 ^{0}C. Hence, it is possible that the contact angle measurements shown above (taken on heaters that are not subjected to boiling) do not represent the true heater surface that undergoes boiling. In order to verify/reject this hypothesis of alteration of contact angle due to hydrocarbon deposition on surface, one

sandblasted and one smooth heater each were boiled in DI water for a period of 1 hour at a flux of 250 kW/m^2. Post-boiling, the heater was allowed to cool to room temperature, while still immersed in DI water in order to prevent any absorption/adsorption from atmosphere. The cooled heater was then subjected to contact angle measurements immediately (again, in order to minimize the time for any potential hydrocarbon adsorption on the surface). **Figure 4-10** shows static contact angle (measured at room temperature) for the representative boiling sandblasted and smooth heaters. The static contact angles for both surfaces are seen to be 27^0 and 45^0, respectively. These values are lower than those for unused sandblasted and smooth heaters (shown above), and are a closer representation of the surface wettability during boiling. For the same heaters, the advancing/receding contact angles were seen to be $33^0/10^0$ for sandblasted and $60^0/10^0$ for smooth heaters. Thus, both sandblasted and smooth heater surfaces that are a closer representation of the surface during boiling have the same receding contact angle.

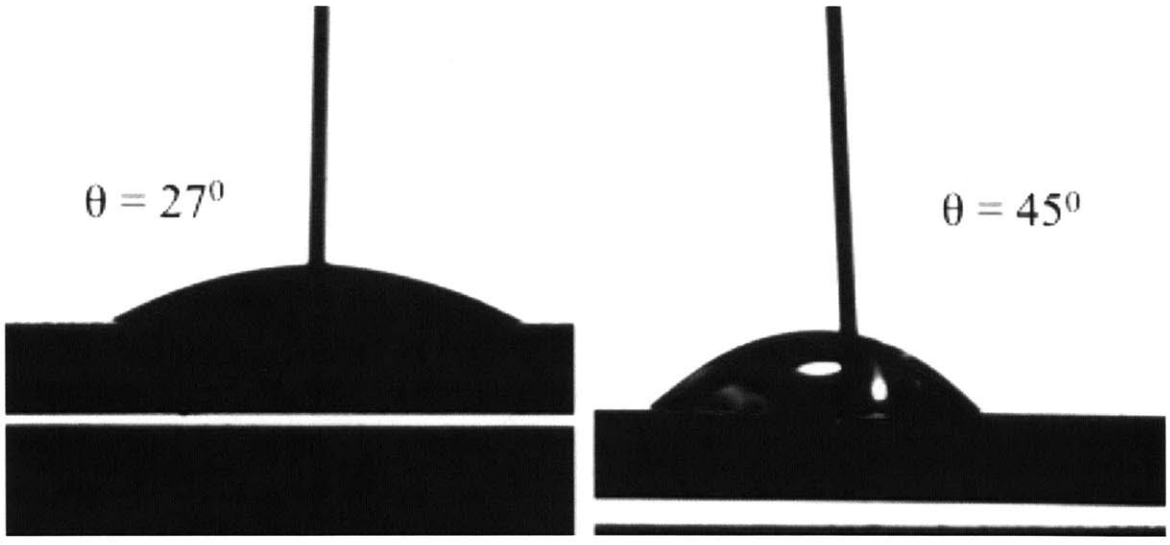

Figure 4-10: Static contact angle of a droplet of DI water on representative boiled sandblasted (left) and smooth (right) heater surfaces

4.4.1.3. Results

Two tests, each with sandblasted and smooth heaters, were run in DI water to determine the base case CHF. Then, to investigate the effect of nanofluids on CHF for both these surfaces, multiple tests with both heater surfaces were run with nanofluids as well. **Table 4-4** summarizes the results from the CHF tests done[4]. For nanofluid tests with smooth heaters, the variation in observed CHF values was high, so this test was repeated 5 times, instead of the normal 2 repetitions.

Table 4-4: Summary of CHF tests done for investigating effects of roughness

Experiment No.	**Heater**	**Test-Fluid**	**Average CHF (kW/m^2)**	**Standard Deviation in CHF (kW/m^2)**
SB_DIW	Sandblasted	DI water	511.5	17.67
Sm_DIW	Smooth	DI water	465.5	14.85
SB_NF	Sandblasted	0.01 v% ZnO nanofluid	1296.5	2.12
Sm_NF	Smooth	0.01 v% ZnO nanofluid	708.5	106.94

It is observed that even though there is a marked difference in the initial surface roughness of sandblasted and smooth heaters, as well as the wettability (measured through contact angle measurements), both surfaces exhibit similar CHF with DI water: 511.5 kW/m^2 for sandblasted heaters, and 465.5 kW/m^2 for smooth heaters. While this observation appears surprising, it has been confirmed by a separate independent investigation [33], which has shown that the intrinsic surface roughness or wettability does not affect CHF, unless combined with a variation in porosity. The CHF, predicted by most commonly accepted correlations by Zuber [13], is 980 kW/m^2. However, Zuber correlation is for horizontal configuration of heaters, while the heaters in this work are

[4] **Table 4-4** shows the averaged CHF values of multiple (two or more) repetitions for each experiment. This routine will be followed throughout this thesis. Complete data from each experiment is provided in Appendix B: Complete Experimental Data

oriented vertically. The correlations by El-Genk and Guo [22] and Vishnev [21], for CHF variation with angle to the horizontal, suggests the CHF for vertically oriented heaters to be ~800 and 750 kW/m^2, respectively. Using the receding contact angle for the heaters boiled to remove the hydrocarbons (~10^0), the expected value of CHF propsed by the Kandlikar correlation is 840 kW/m^2. Even though the CHF observed in experiments here was even lower than that suggested by these correlations, it must be noted that the correlations do not account for the shape or the surface conditioning of the heaters. Additionally, there is a high degree of repeatability in CHF for the DI water experiments with both sandblasted and smooth heaters. This repeatability serves to conclude that the facility is benchmarked, and that the observed CHF values are the accurate values for the heater configuration used in this work.

With nanofluids, sandblasted heaters show a significant enhancement in CHF: 1296.5 kW/m^2 from 511.5 kW/m^2 for DI water. Thus, CHF enhancement for nanofluids is confirmed. Additionally, CHF for smooth heaters also increases with nanofluid. However, two things stand out for nanofluid tests for smooth heaters, compared to sandblasted heaters. Firstly, the magnitude of enhancement for smooth heaters, though significant (from 466 kW/m^2 with DI water to 785 kW/m^2 with nanofluid), is lower than that observed for sandblasted heaters. Secondly, smooth heaters exhibit a much larger variance in CHF values, compared to sandblasted heaters.

4.4.1.4. Post-Test Surface Analysis

Figure 4-11 and **Figure 4-12** show post-test SEM images of sandblasted heaters tested with DI water and nanofluid, respectively. From the images it is evident that, for tests with nanofluids, nanoparticles begin to coat on the heaters. However, as expected, no coatings or surface modifications are observed for tests with DI water. The same observation holds true for smooth heaters tested with DI water and nanofluid, as seen from **Figure 4-13** and **Figure 4-14**. EDX is carried out on the heater surfaces that show

evidence of nanocoatings, to confirm the chemical signature of these coatings. **Figure 4-15** plots one such EDX graph, clearly showing the Zn-peaks, confirming the nanoparticles coated on the surface to be ZnO from the nanofluid.

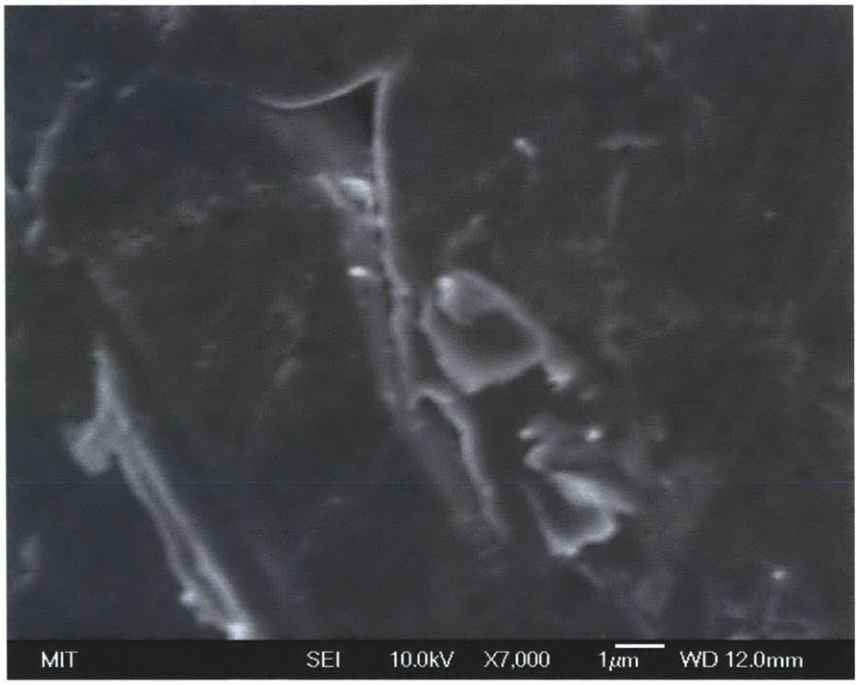

Figure 4-11: Post-test SEM image of heater used for SB_DIW

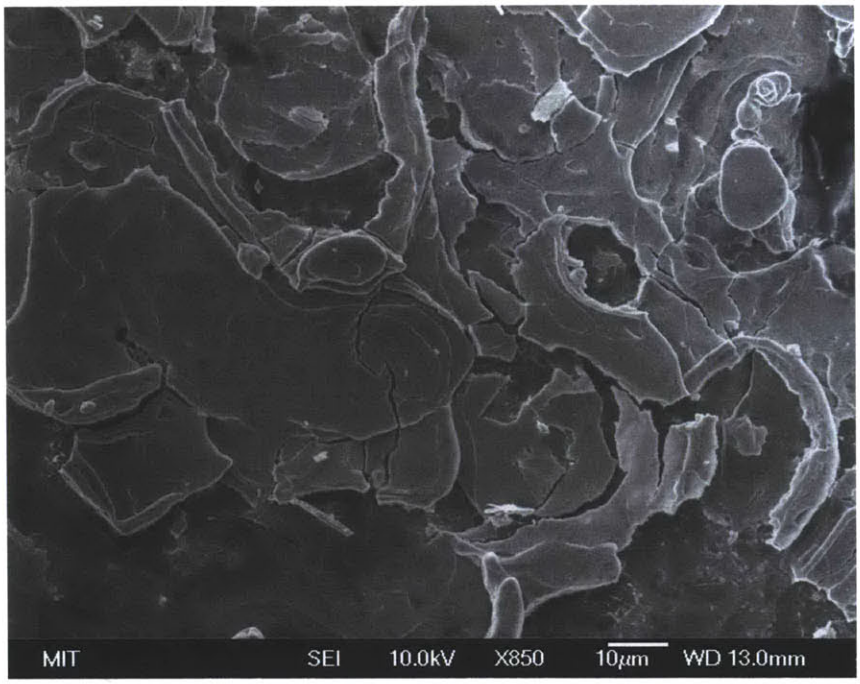

(a) 850X

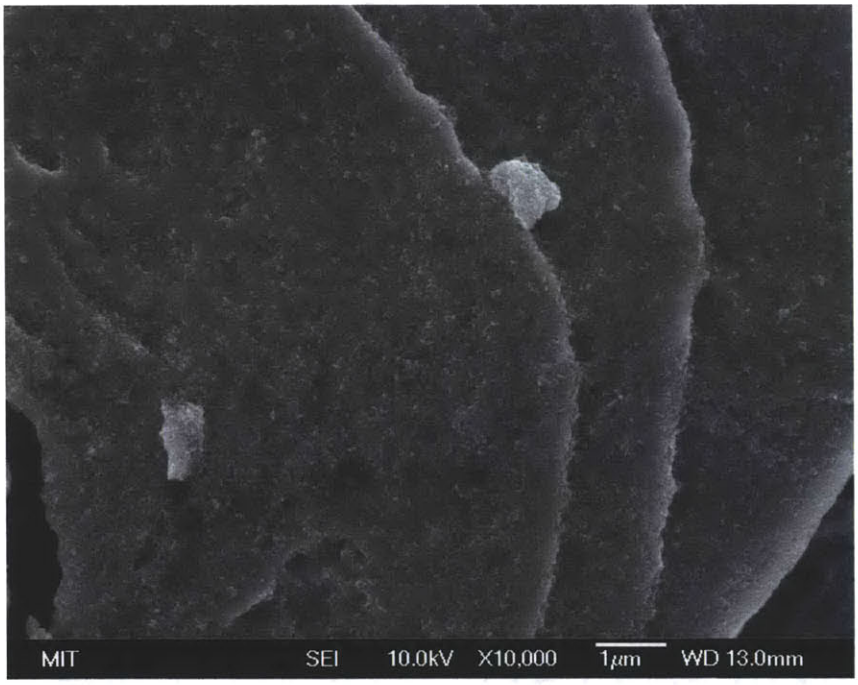

(b) 10,000X

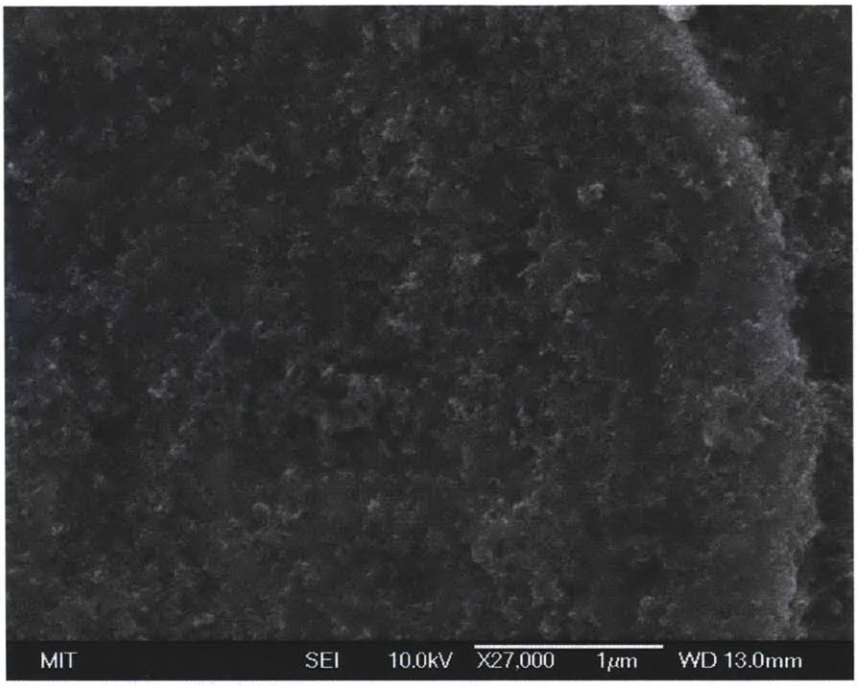

(c) 27,000X

Figure 4-12: Post-test SEM image of heater used for SB_NF, at different magnifications. ZnO nanoparticles, coated on the surface, are clearly visible

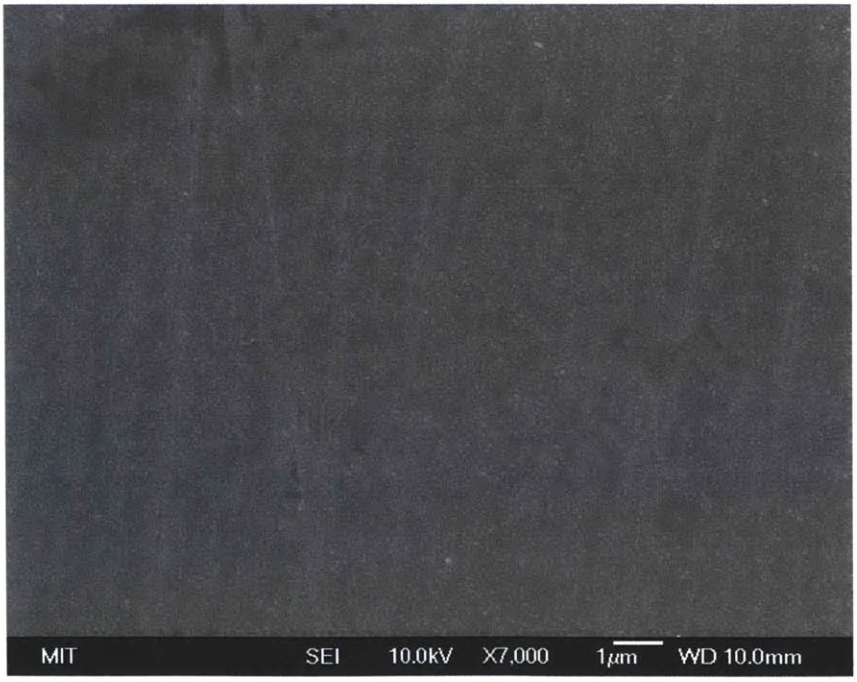

Figure 4-13: Post-test SEM image of heater used for Sm_DIW

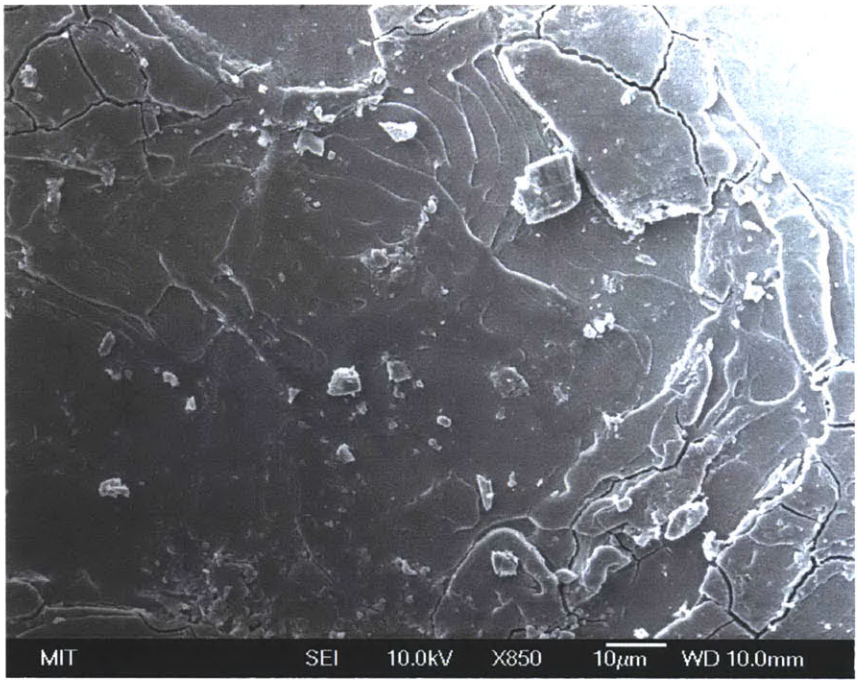

(a) 850X

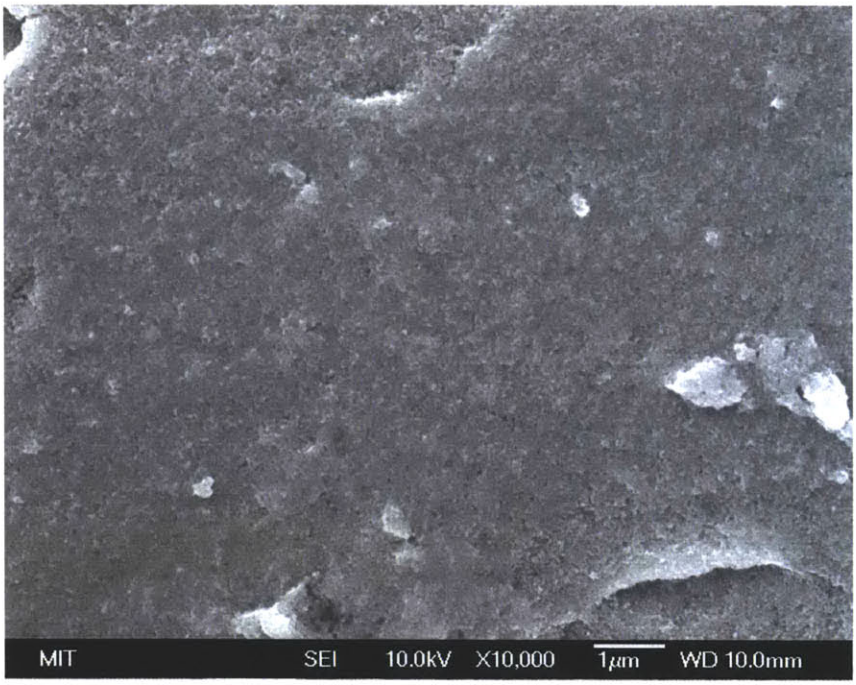

(b) 10,000X

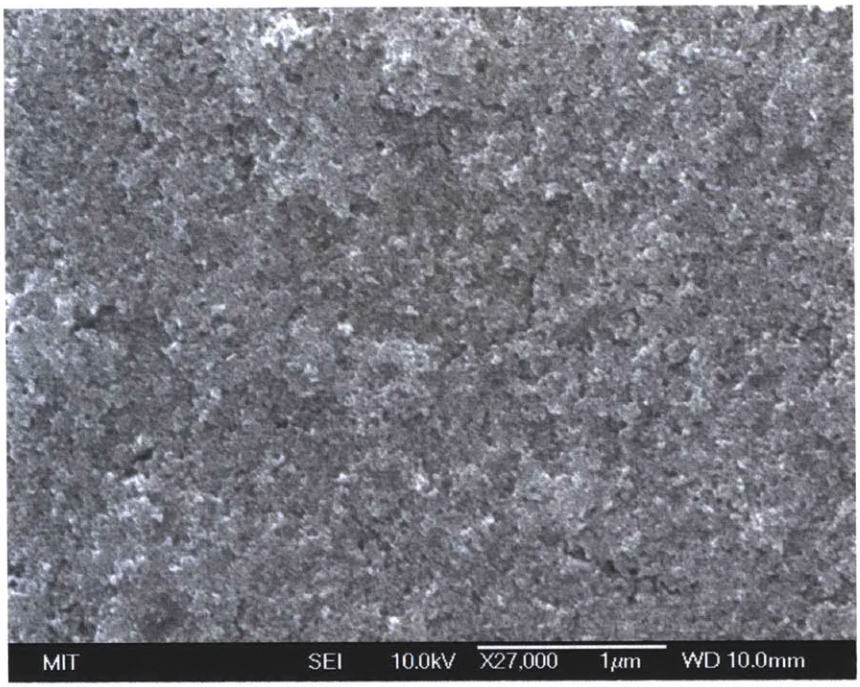

(c) 27,000X

Figure 4-14: Post-test SEM image of heater used for Sm_NF, at different magnifications. ZnO nanoparticles, coated on the surface, are clearly visible

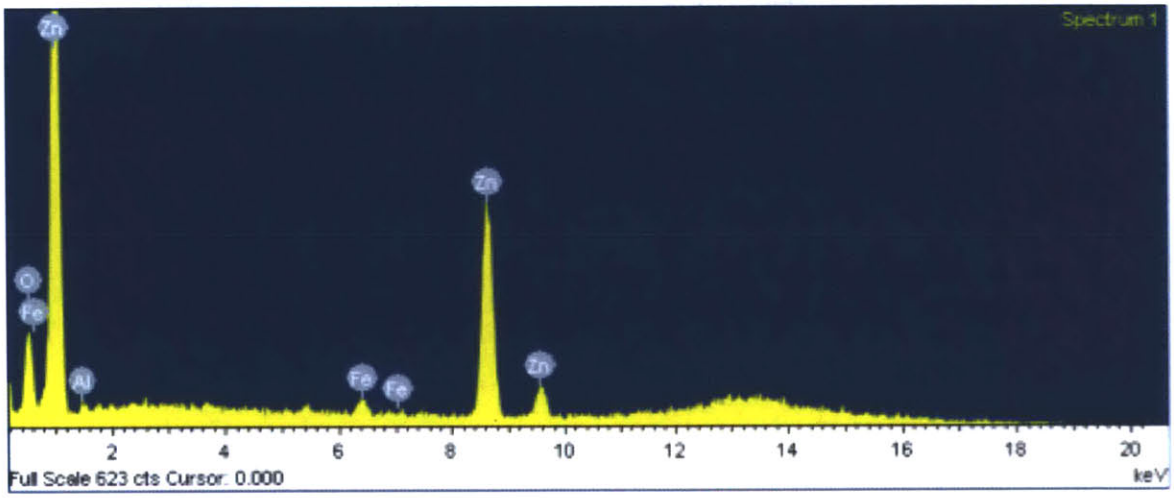

Figure 4-15: EDX scan from one of the heaters tested with nanofluid. Clear Zn signal confirms that the deposits are from the ZnO particles in the nanofluid

Post-test confocal microscopy was also done to examine the effects of testing on surface roughness, and representative images for sandblasted and smooth heaters tested with DI water and nanofluid are shown below. From **Figure 4-16** and **Figure 4-18** it is observed that the texture of the heaters does not change significantly after testing with DI water. This observation is expected, since DI water does not contain any element in it that would modify the surface. **Figure 4-17** and **Figure 4-19**, on the other hand, clearly show different texture compared to unused sandblasted and smooth heaters, indicating the development of nanocoatings consistent with the qualitative images obtained by SEM. It is also noted that for sandblasted heaters, R_a does not change significantly, after testing with nanofluids, compared to an unused surface (1.33 μm after testing, compared to 1.25 μm before testing). However, for smooth heaters, the change in R_a is much more drastic (1.68 μm after testing, compared to 0.06 μm before testing).

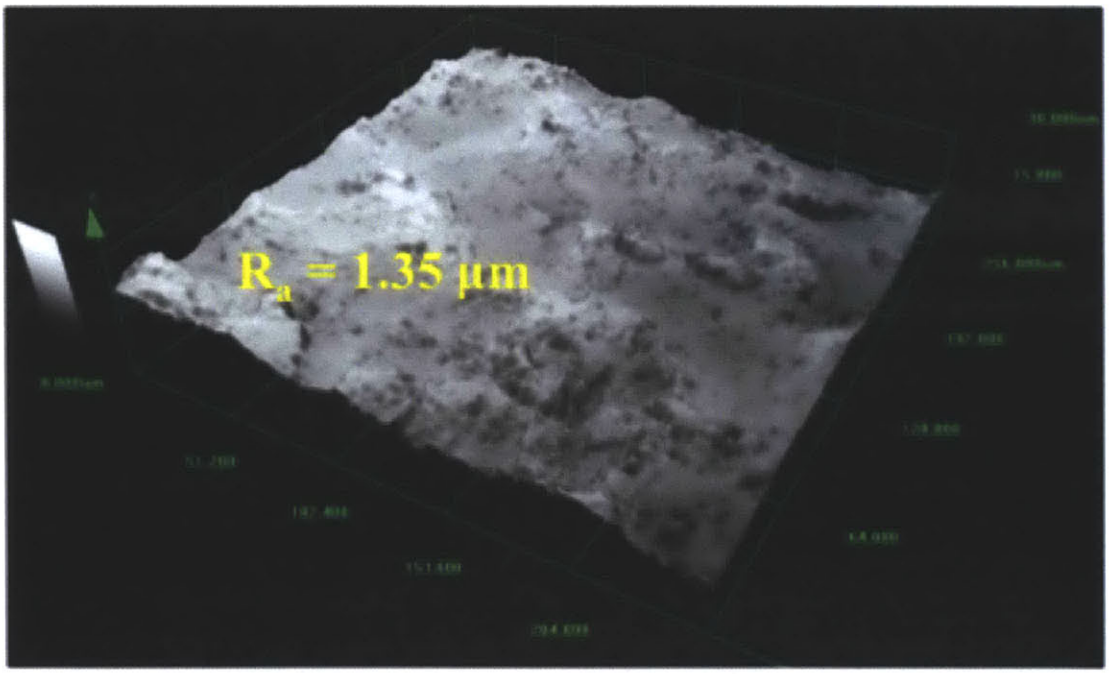

Figure 4-16: Confocal scan of heater used for SB_DIW (R_a = 1.35 μm)

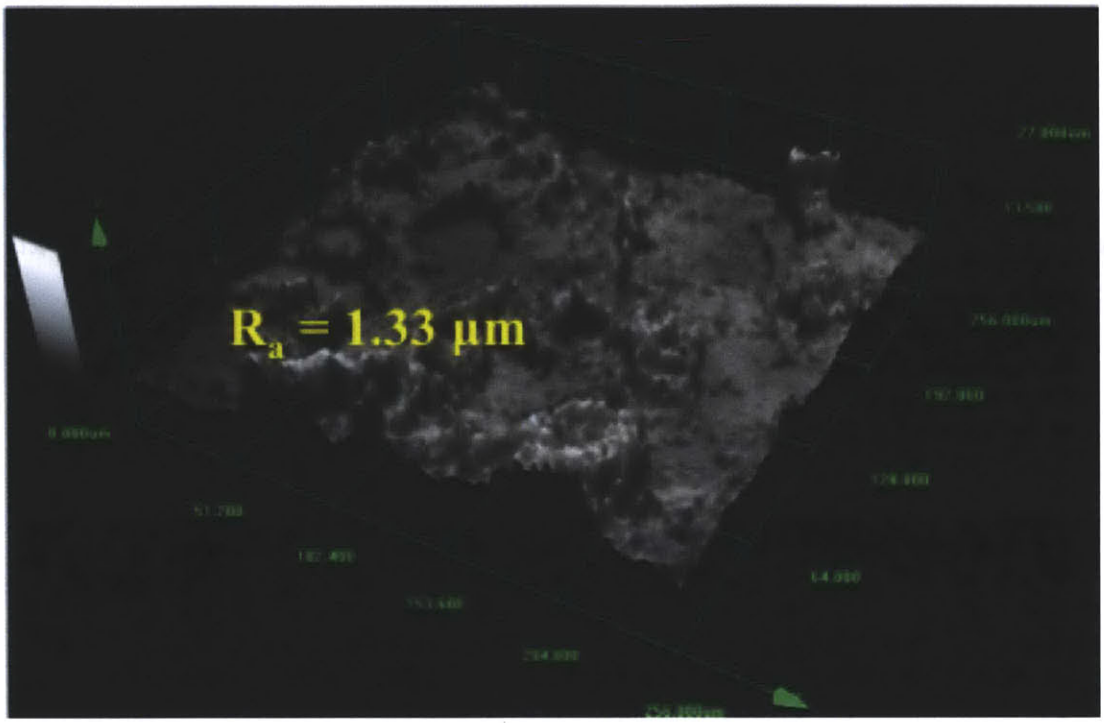

Figure 4-17: Confocal scan of heater used for SB_NF (R_a = 1.33 μm)

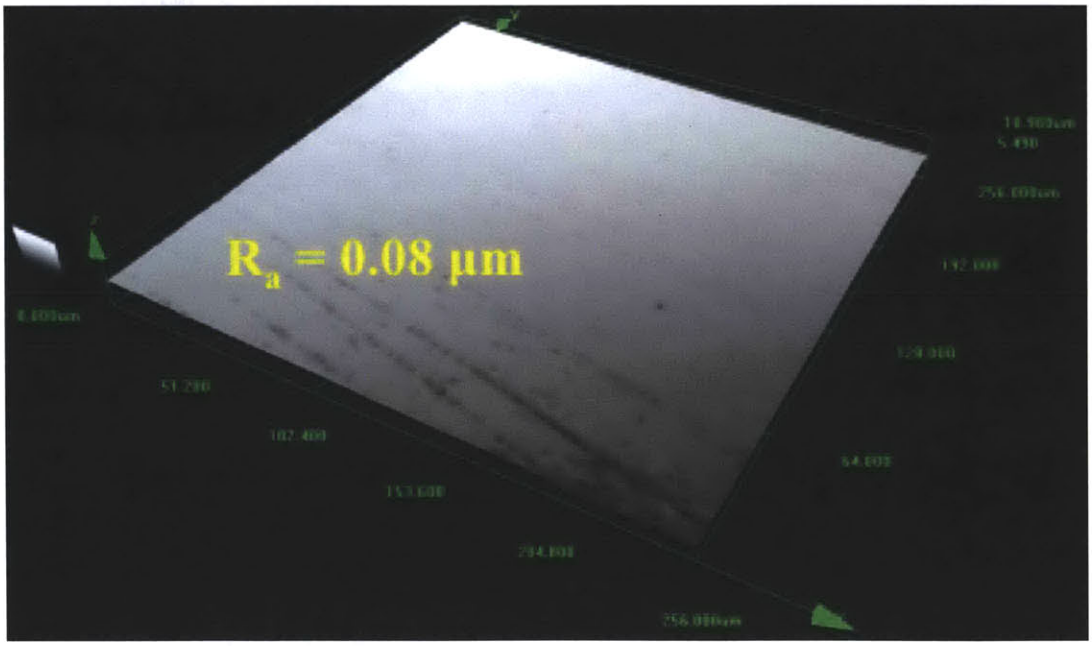

Figure 4-18: Confocal scan of heater used for Sm_DIW (R_a = 0.08 μm)

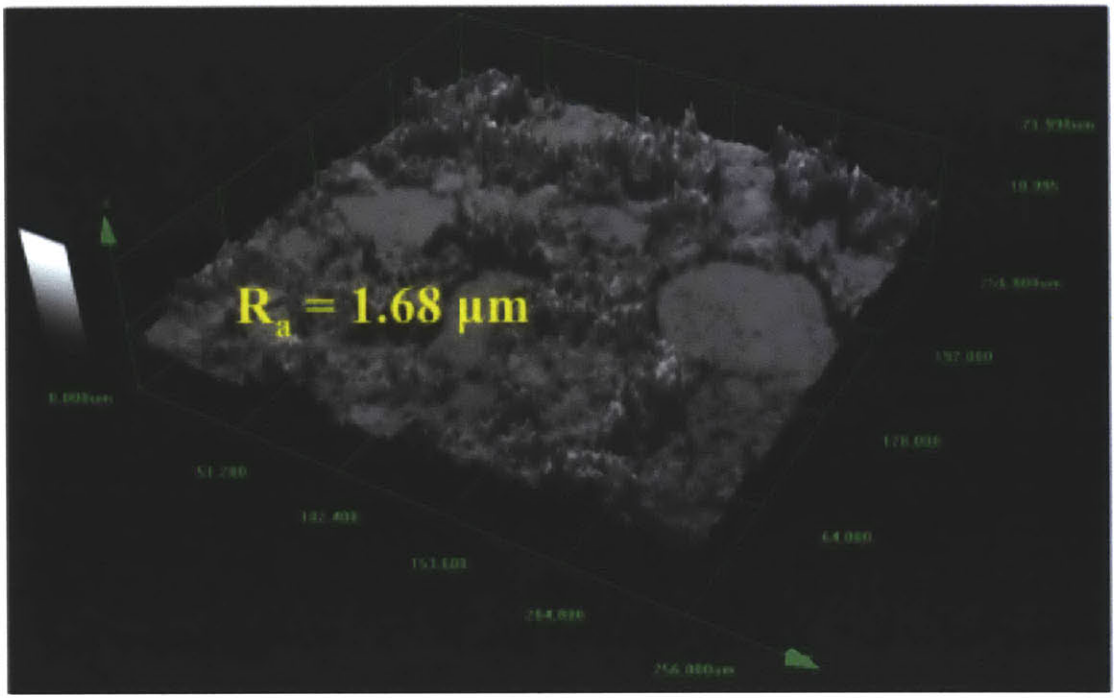

Figure 4-19: Confocal scan of heater used for Sm_NF (R_a = 1.68 μm)

Contact angle measurements for heaters tested in nanofluid were completed to quantify the changes in their wettability. **Figure 4-20** shows the static contact angle measurements for both (sandblasted as well as smooth) surfaces. It is seen that, owing to the nanocoating formed during boiling, the wettability of both surfaces increases significantly. Since the static contact angles on heaters tested with nanofluid are extremely low, and the water droplet completely spreads on the surface, dynamic contact angle measurements on these surfaces were not possible.

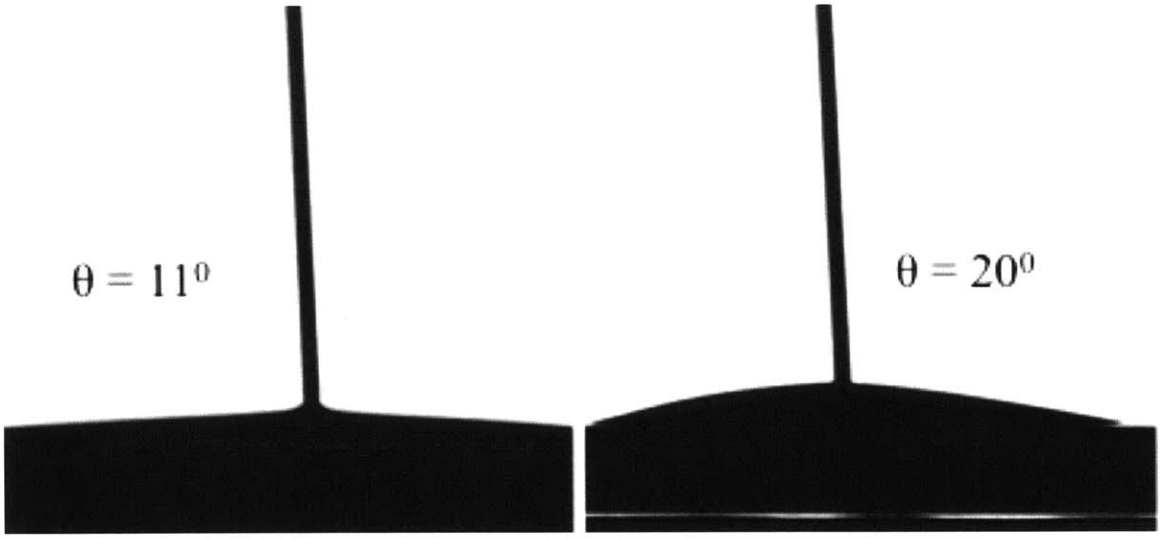

Figure 4-20: Static contact angle of a droplet of DI water on sandblasted (left) and smooth (right) heaters tested till CHF in nanofluid

4.4.2. Wettability

The nanofluid coatings developed on the surface of heaters have been seen to enhance the wettability of the surface; and this enhanced wettability is considered to be one of the mechanisms responsible for an enhanced CHF with nanofluids [38, 41, 42, 45, 46]. Thus, in order to investigate the effects of wettability, the wettability of the sandblasted and smooth heaters was modified by means of layer-by-layer (LbL) coatings of SiO_2 nanoparticles, in controlled conditions, before using the heaters for CHF tests with DI water and nanofluids. This was done to explore if nanofluids and nanocoatings developed during boiling have appreciable effects on CHF if the heater surface is initially highly hydrophilic.

4.4.2.1. Wettability Control

A LbL method is used to control the wettability of both the sandblasted as well as the smooth heater surface. The LbL technique is an aqueous chemical technique that involves adhesion of multiple layers to the surface of a substrate by depositing layers of particles, with alternating charge. **Figure 4-21** shows a schematic of this technique. The LbL method allows for careful control of the bilayers attached to the surface, thus enabling a controlled modification of the surface wettability. In this thesis, the thin-film coatings, applied to SS304 heater element, comprised of SiO_2/polymer bilayers.

As represented in **Figure 4-21**, the LbL process consists of attaching layers of alternately charged particles to the surface of the substrate (heater element in this case). For LbL coatings used in this work, the positively charged species was a solution of poly(allylamine) hydrochloride (PAH, nominal M_n = 70,000 g/mol), while a solution of SiO_2 nanoparticles in DI water provides the negatively charged species. The PAH solution with a concentration of 10mM was prepared by adding 1.4055 g of granular PAH chips to 1500 ml of DI water. The PAH particles were dissolved in DI water by using a magnetic stirrer. The resulting solution was titrated to a pH of 7.5 by titrating it with a 1M NaOH solution. For the preparation of the SiO_2 solution, 4.65 g of H_3BO_3, 5.55 g of KCl, 1.29 g of NaOH, 8.7675 g of NaCl and 7.73 g of a standard SiO_2 solution[5] containing 5 wt.% SiO_2 nanoparticles (50 nm in size) were mixed with 1500 ml of DI water, and the contents thoroughly stirred.

[5] The solution is ordered from polysciences.com, part# 24040-10

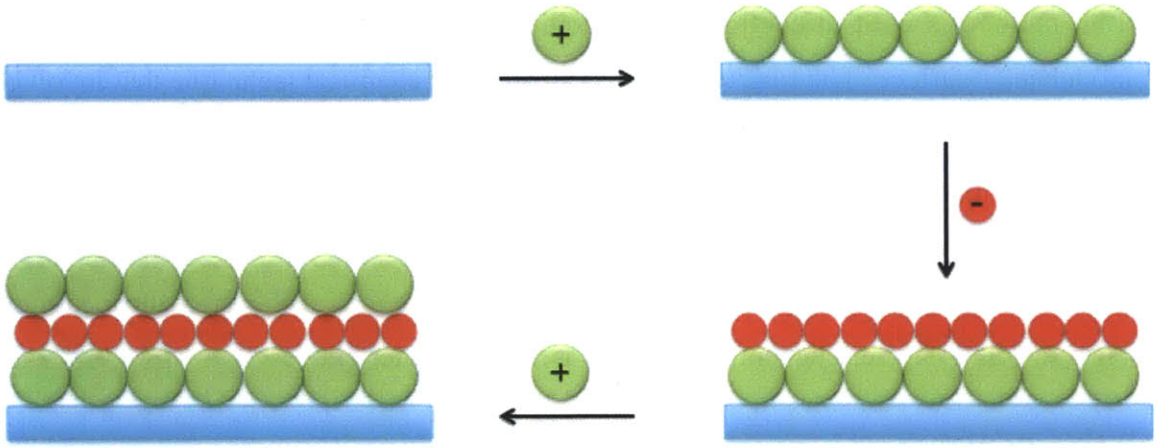

Figure 4-21: Schematic of LbL method. Particles of alternating charge adhere to the surface of the substrate, the process is repeated until desired number of bilayers are achieved

After solution preparation, the coating process is carried out in a Zeiss HMS Programmable Slide Strainer, shown in **Figure 4-22**. This set-up consisted of 8 different baths. Bath 1 contained the PAH solution, Bath 5 contained SiO_2 solution, with the rest of the baths filled with DI water. The heater elements were mounted on a mechanical arm of the slide strainer, and immersed in Bath 1 for 10 min, followed by rinsing it with DI water contained in Baths 2, 3 and 4 for 1 min each. Then, the heater was immersed in Bath 5 for 10 min, followed by rinsing it with DI water contained in Baths 6, 7 and 8 for 1 min each. One such cycle is able to attach 1 bi-layer of PAH/SiO_2 nanoparticles to the heater surface. This cycle is repeated 40 times, to develop 40 bi-layers on the heater surface. This schematic is pictorially represented in **Figure 4-23**, with PAH solution being the +ve component and SiO_2 solution being the –ve component.

Figure 4-22: Photograph of the Zeiss HMS Programmable Strainer used for coating heater elements with LbL coatings, to change initial surface wettability

Having deposited the 40 bilayers on heater elements, they are left to dry overnight, followed by calcination in a furnace at 550 ^{0}C for duration of 4 hours. The calcination removes the PAH particles from the coatings, leaving behind only the SiO_2 nanoparticle layer. Additionally, the SiO_2 nanoparticles are sintered to the surface of the heaters, due to calcination; thus the coatings become more durable post-calcination. **Figure 4-24** shows the photograph of the furnace in which calcination was done.

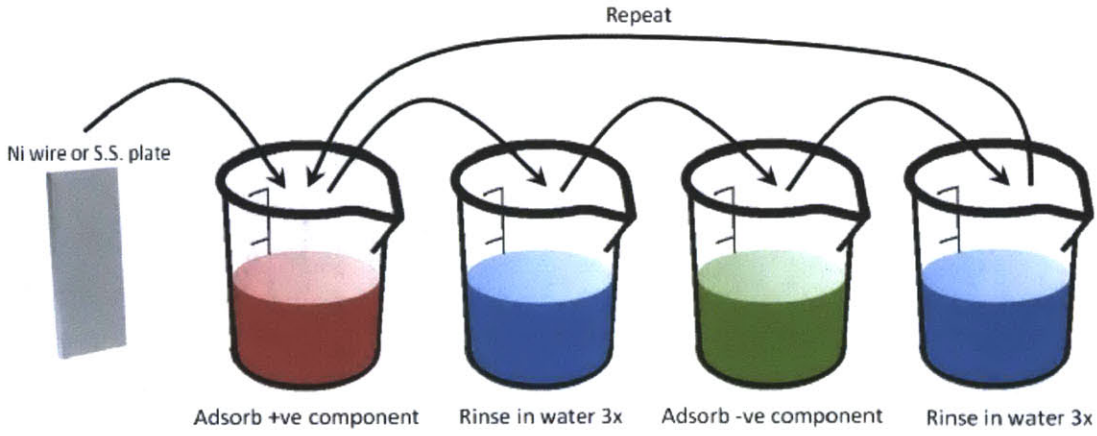

Figure 4-23: Schematic of the LbL process. *Illustration courtesy of Erik Williamson*

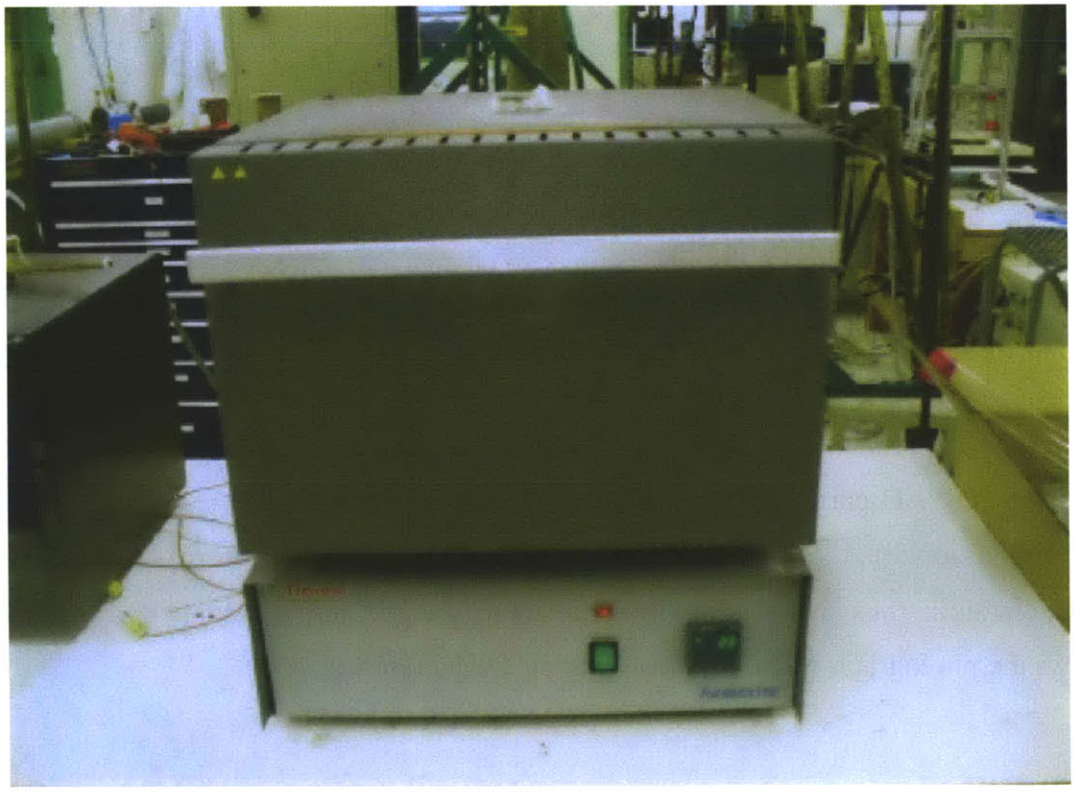

Figure 4-24: Photograph of the furnace used for calcination

4.4.2.2. Pre-Test Surface Analysis

The heaters obtained after LbL coating and calcination are called "LbL sandblasted/smooth heaters" from here on. **Figure 4-25** and **Figure 4-26** show SEM images of the surface of unused LbL sandblasted and smooth heaters. SiO_2 nanoparticles coated by the LbL method are clearly visible in the images. These particles were confirmed to be SiO_2 by means of an EDX analysis on the surface of the LbL sandblasted heater. The EDX graph obtained is shown in **Figure 4-27**; the presence of Si on the surface is confirmed in the EDX data.

Since the coated SiO_2 nanoparticles are very small in size (~50 nm), their layers coated on the heater surface are expected to conform to the exact shape and roughness of the base surface, and are expected not to alter its roughness. This was confirmed by carrying out confocal measurements on unused LbL sandblasted and unused LbL smooth heaters. **Figure 4-28** and **Figure 4-29** show the scan from one measurement each from the LbL sandblasted and LbL smooth heaters. R_a values for both these heaters were seen to be 1.24 and 0.14 μm, respectively. These values of R_a are consistent with those for unused sandblasted and smooth (with LbL coatings), shown in **Figure 4-5** and **Figure 4-6**, thus confirming that LbL coatings do not alter the texture of the surface of substrate, but, rather, conform to it.

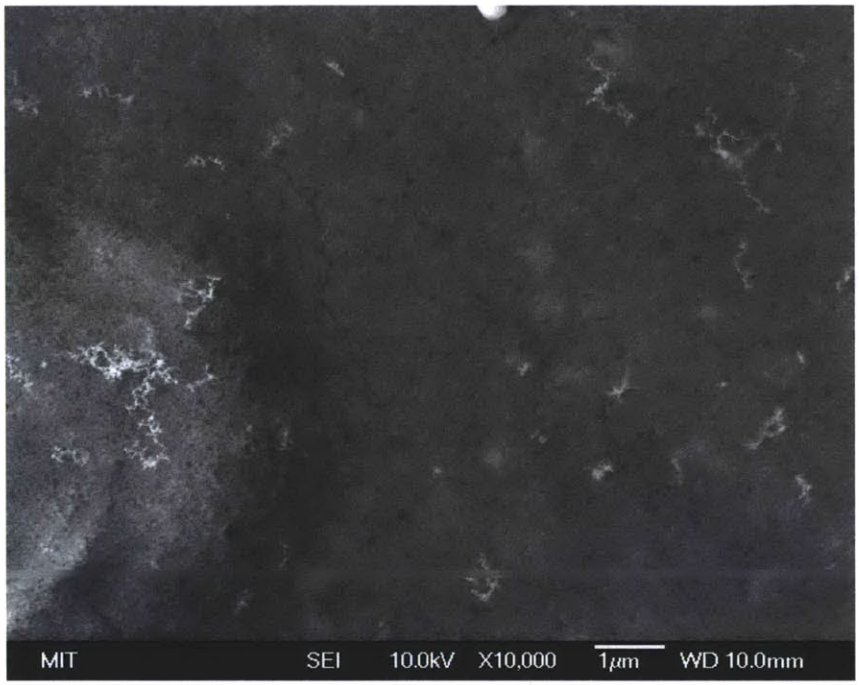

(a)

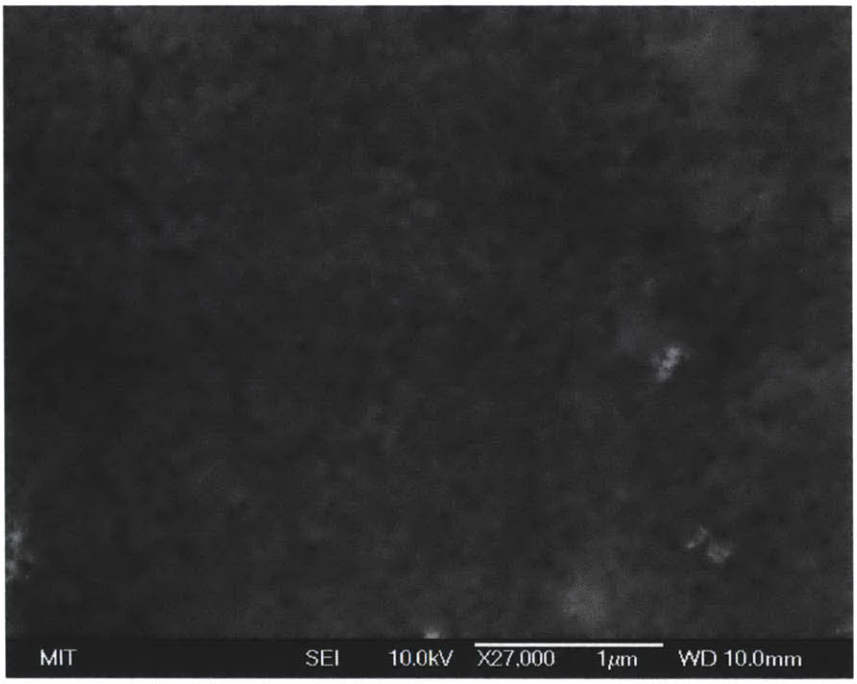

(b)

Figure 4-25: SEM image of an unused LbL sandblasted heater at different magnifications, clearly showing SiO_2 nanoparticles

(a)

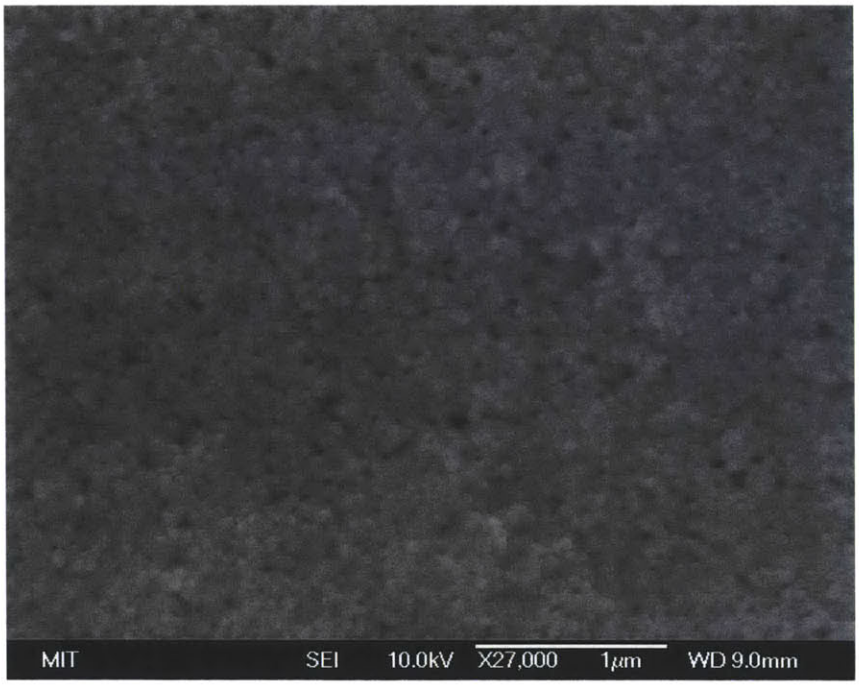

(b)

Figure 4-26: SEM image of an unused LbL smooth heater at different magnifications, clearly showing SiO_2 nanoparticles

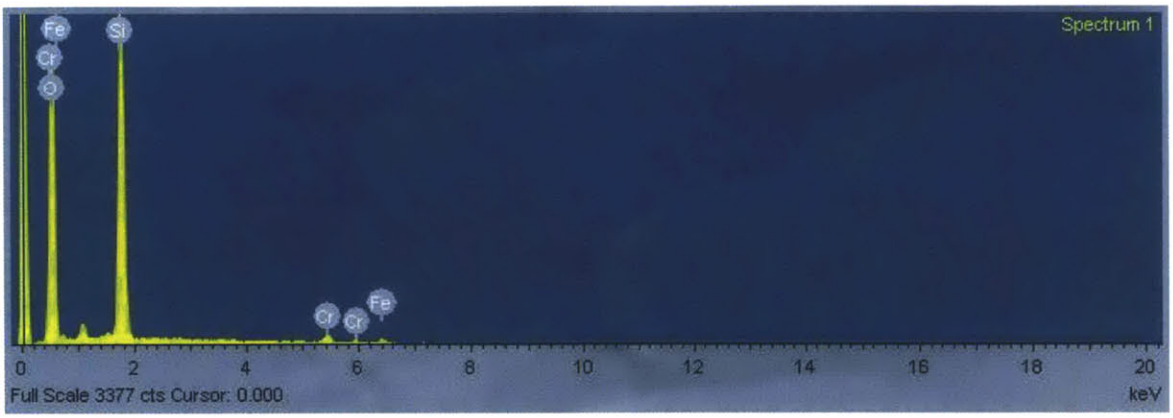

Figure 4-27: EDX data from an unused LbL sandblasted heater, confirming Si signal

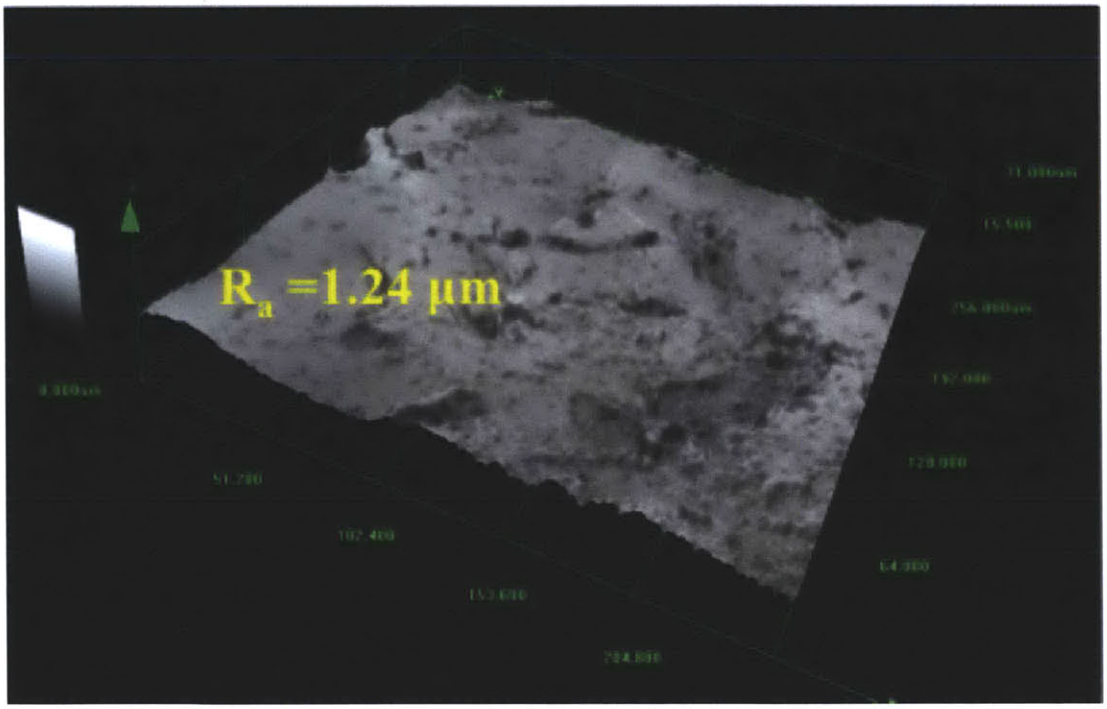

Figure 4-28: Confocal scan of an unused LbL sandblasted heater (R_a = 1.24 µm)

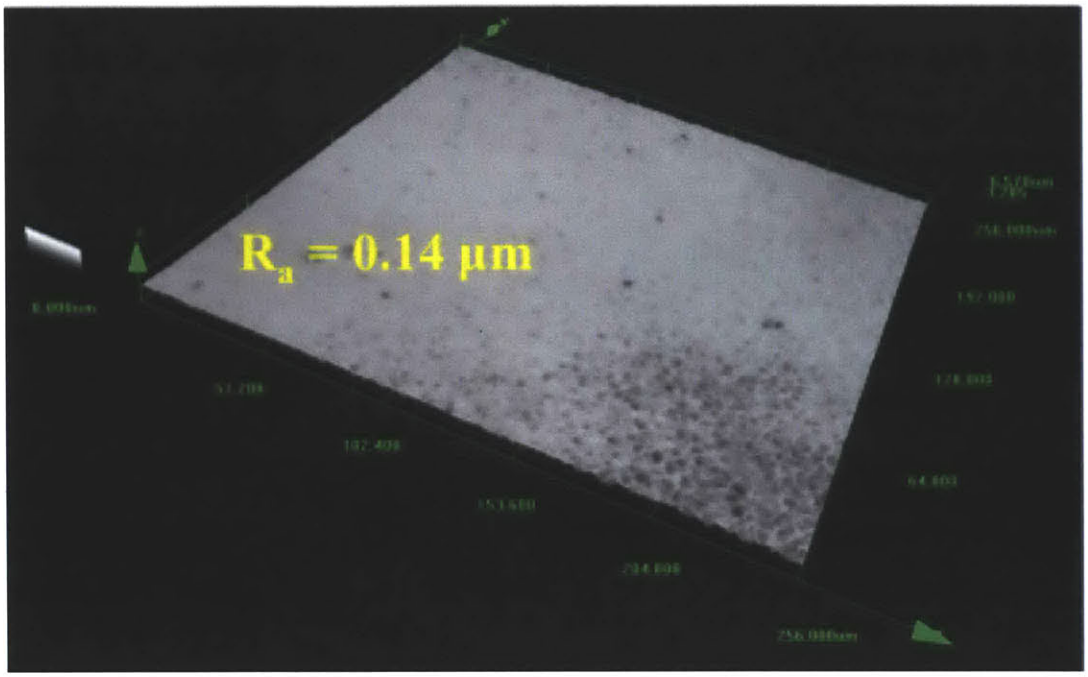

Figure 4-29: Confocal scan of an unused LbL smooth heater (R_a = 0.14 μm)

Contact angle measurements verified the enhanced wettability of the heater surface, on coating with the LbL method. **Figure 4-30** shows the static contact angle measurements for a droplet of DI water on unused LbL heaters (both sandblasted and smooth). Just as the contact angle of water on an unused uncoated smooth heater was larger than for unused uncoated sandblasted heater, LbL coating also yields similar results. Although LbL coating increases the wettability of both surfaces markedly, the increase for sandblasted surface is much higher than for a smooth surface. A water droplet on sandblasted heater completely spreads on the surface, indicating that the contact angle of water on this surface is $< 5^0$. However, the contact angle of water on smooth LbL coated surface was seen to be 15^0. The porosity of the LbL coatings was measured by Phillips and found to be around 50% [20].

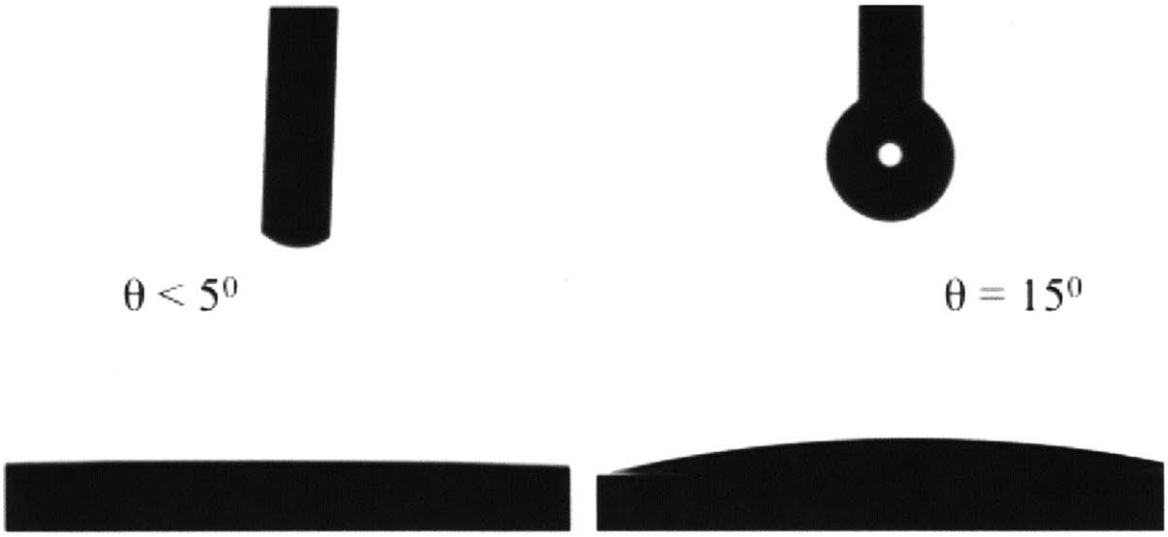

Figure 4-30: Static contact angle of a droplet of DI water on unused LbL sandblasted (left) and unused LbL smooth (right) heater surfaces

4.4.2.3. Results

The effect of LbL coatings on CHF was investigated for both sandblasted and smooth heaters. **Table 4-5** summarizes the averaged results obtained for all the tests run to investigate wettability effects on CHF. Compared to uncoated sandblasted heaters, which have a CHF of 511.5 kW/m^2, LbL coated heaters show a 30% enhancement in CHF to 671 kW/m^2 with DI water. Similarly, the enhancement with DI water for smooth LbL coated heaters was also significant (622 kW/m^2 from 465.5 kW/m^2; or 33%). Thus it is evident that increasing the initial wettability (and porosity) of the boiling surface increases the CHF for DI water. Additionally, compared to uncoated heaters in DI water, the LbL coated heaters when used with nanofluid also exhibit a higher CHF (780 kW/m^2 from 511.5 kW/m^2; or 52% for sandblasted heaters, and 718.5 kW/m^2 from 465.5 kW/m^2; or 54% for smooth heaters). Even though nanofluids also exhibit a higher CHF with the LbL coated heaters, the enhancement is not as high as for uncoated heaters, indicating that the additional nanoparticles deposits arising from nanofluid boiling are not as effective at enhancing CHF when an LbL coating is already present.

Table 4-5: Summary of CHF tests done for investigating effects of wettability

Experiment No.	Heater	Test-Fluid	Average CHF (kW/m^2)	Standard Deviation in CHF (kW/m^2)
SB_DIW	Sandblasted	DI water	511.5	17.67
Sm_DIW	Smooth	DI water	465.5	14.85
LbLSB_DIW	LbL-coated Sandblasted	DI water	671	35.35
LbLSm_DIW	LbL-coated Smooth	DI water	622	22.62
LbLSB_NF	LbL-coated Sandblasted	0.01 v% ZnO nanofluid	780	29.69
LbLSm_NF	LbL-coated Smooth	0.01 v% ZnO nanofluid	718.5	58.69

4.4.2.4. Post-Test Surface Analysis

Figure 4-31 and **Figure 4-33** show SEM images of LbL sandblasted and smooth heaters, respectively, after testing with DI water. As seen in these figures, the LbL coating of SiO_2 nanoparticles is still intact after testing with water, confirming that this coating leads to an enhanced CHF for water. **Figure 4-32** and **Figure 4-34** are SEM images of LbL coated sandblasted and smooth heaters, tested with nanofluids. These figures show an additional layer of ZnO nanoparticles that forms on top of the LbL coating.

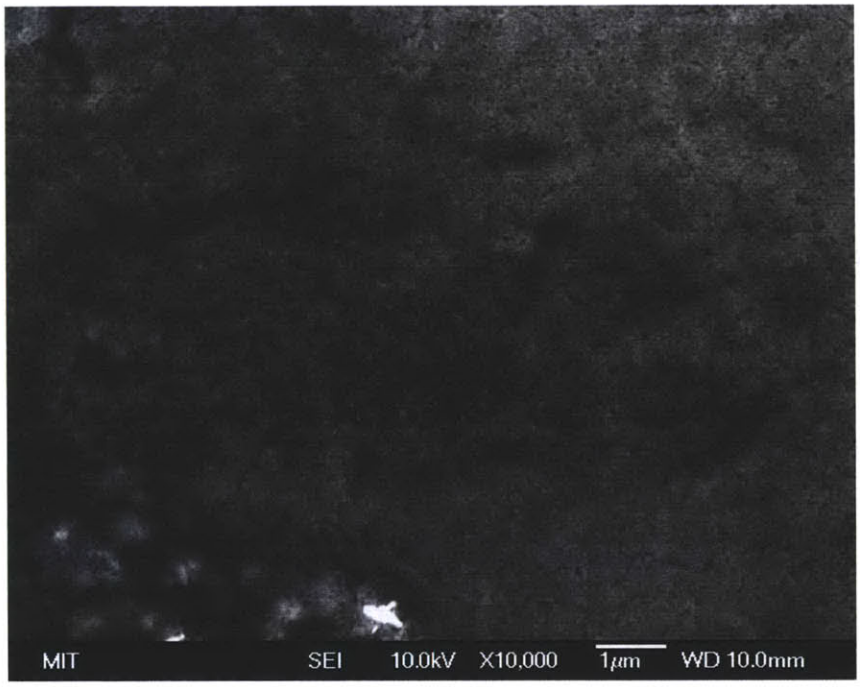

Figure 4-31: Post-test SEM image of heater tested for LbLSB_DIW, showing that SiO_2 nanoparticles deposited by LbL method stay intact during the experiment

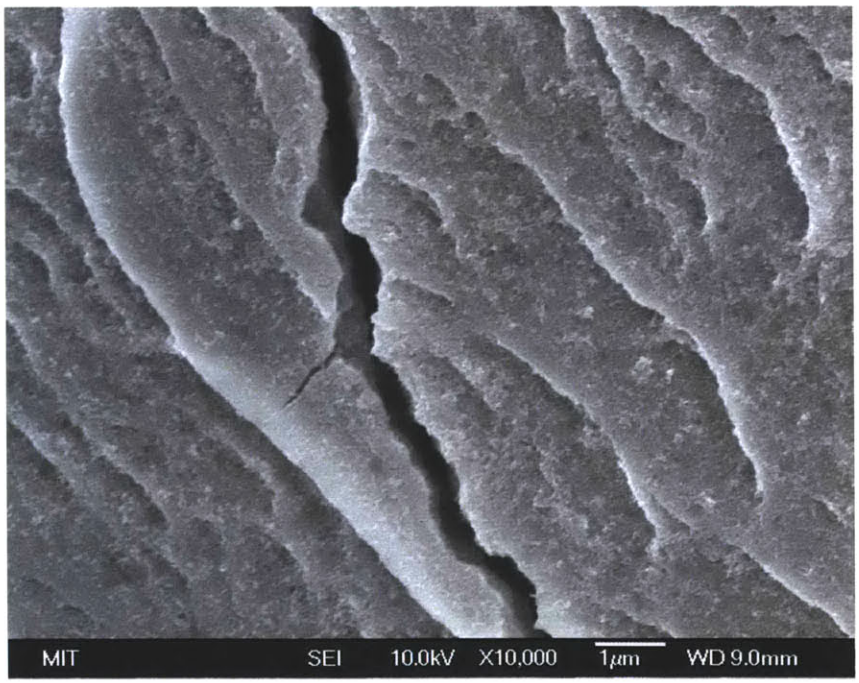

Figure 4-32: Post-test SEM image of heater tested for LbLSB_NF, showing an additional layer of ZnO nanoparticles

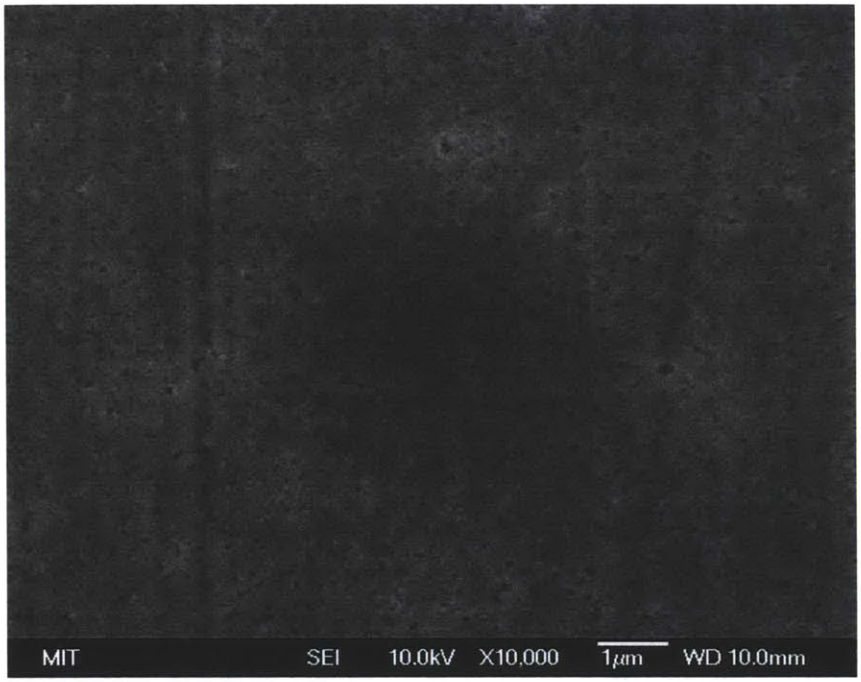

Figure 4-33: Post-test SEM image of heater tested for LbLSm_DIW, showing that SiO_2 nanoparticles deposited by LbL method stay intact during the experiment

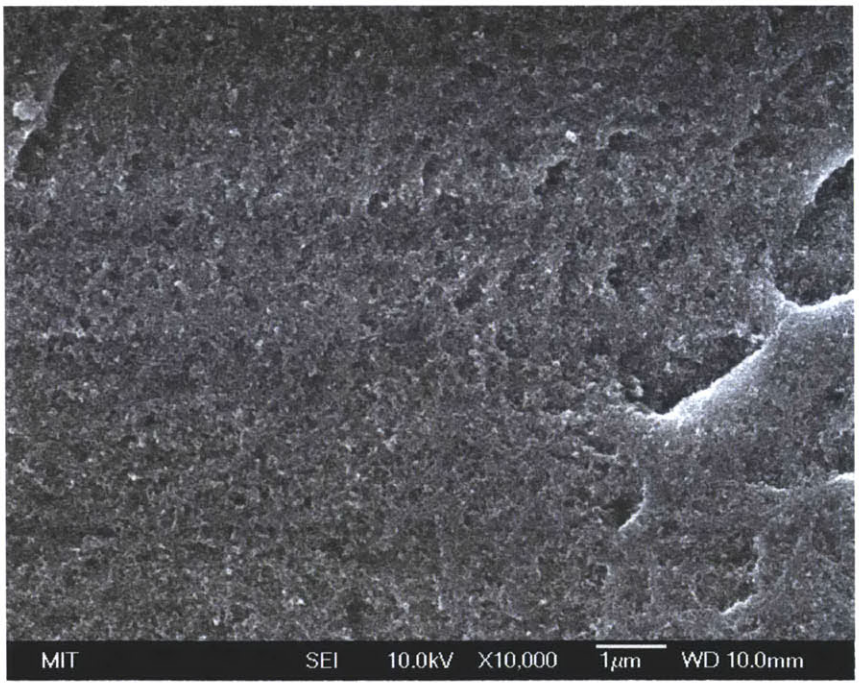

Figure 4-34: Post-test SEM image of heater tested for LbLSm_NF, showing an additional layer of ZnO nanoparticles

Consistent with the expectations, confocal microscopy showed that, after testing with DI water, the texture and roughness of LbL coated heaters (both sandblasted and smooth) do not change, as is evident from Figure 4-35 and Figure 4-37. Figure 4-36 and Figure 4-38 show confocal images of LbL coated heaters tested in nanofluid. Compared to the heaters tested in DI water, these images clearly show a modification of the surface and evidences of additional ZnO nanoparticles coated on them. The additional coating acts to change the surface roughness, but again, the change in R_a for smooth heaters (to 2.22 μm from 0.12 μm) is more drastic than for sandblasted heaters (to 2.48 μm from 1.25 μm).

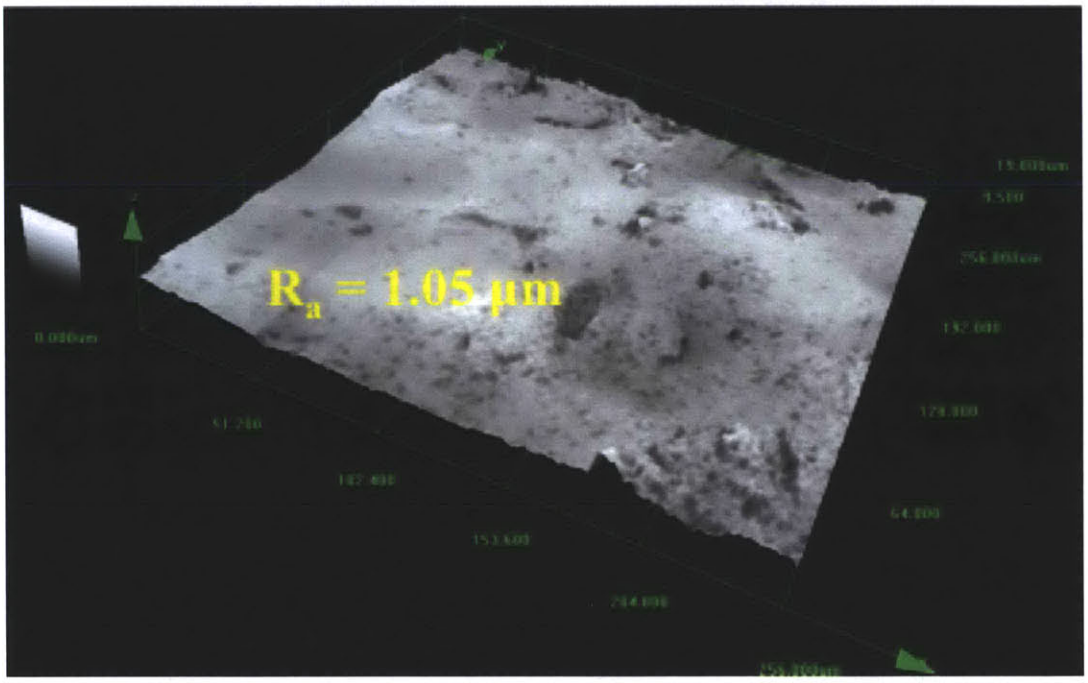

Figure 4-35: Confocal scan of an LbLSB_DIW heater (R_a = 1.05 µm)

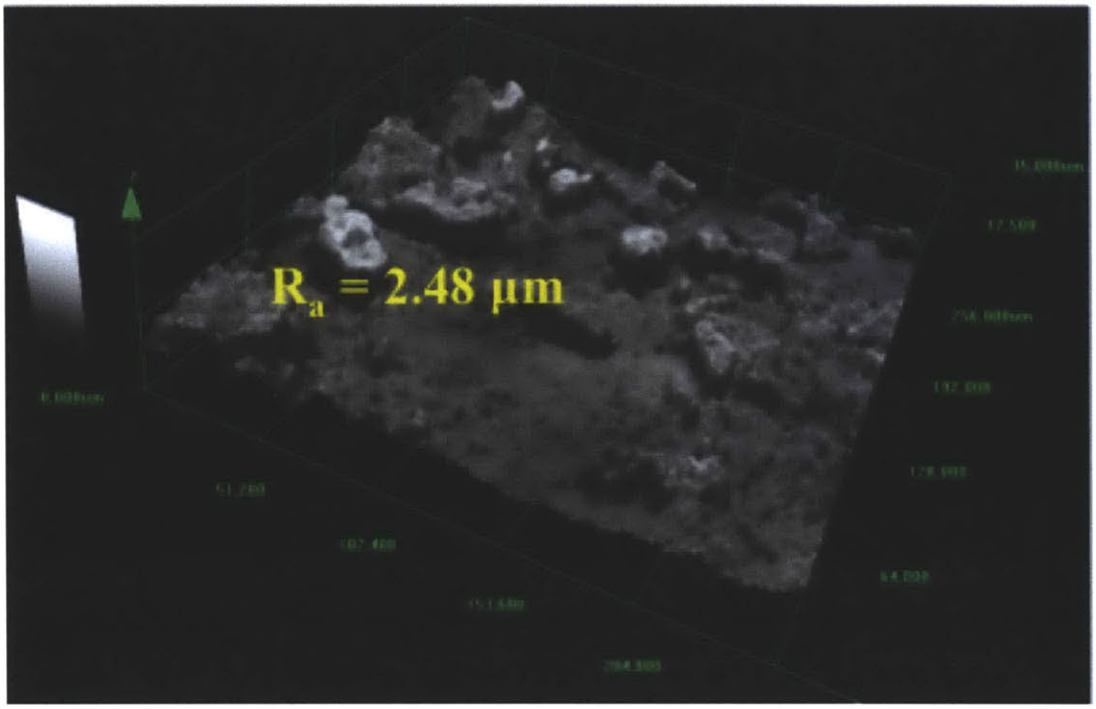

Figure 4-36: Confocal scan of an LbLSB_NF heater (R_a = 2.48 µm)

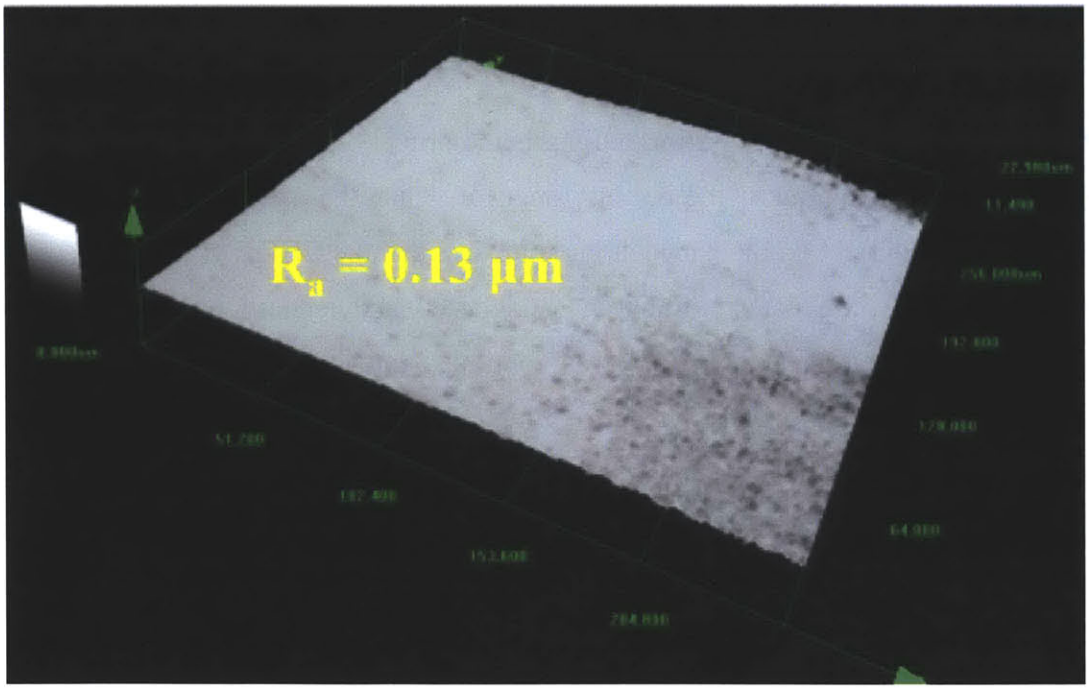

Figure 4-37: Confocal scan of an LbLSm_DIW heater (R_a = 0.13 µm)

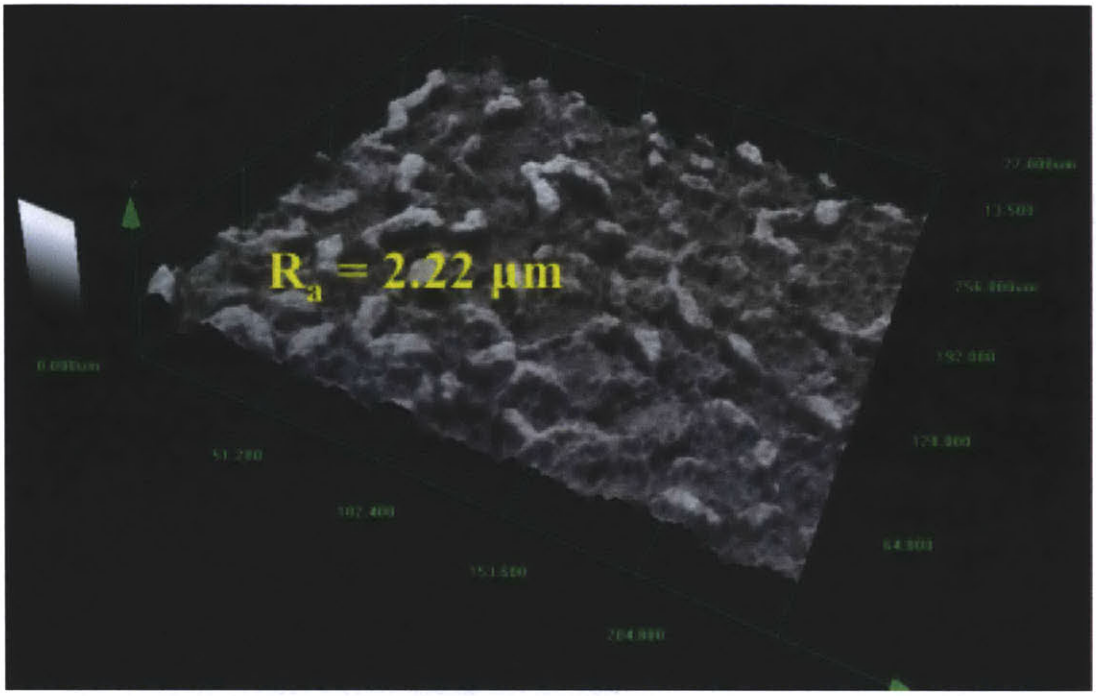

Figure 4-38: Confocal scan of LbLSm_NF heater (R_a = 2.22 µm)

4.4.3. Pre-Boiling Time

Since nanocoating developed during boiling is the primary reason for an enhanced CHF, it is of interest to examine if the boiling time, for which the nanocoating[6] is allowed to develop, has any effect on the nanocoating thickness and the CHF. For this investigation, experiments were conducted with both sandblasted and smooth heaters, where pre-boiling of nanofluids at a fixed flux was continued for a pre-determined time, before running the experiment to CHF. The pre-boiling times investigated in this thesis were: t = 0, 0.5, 1, 4 and 8 hours.

[6] Note: The "nanocoating" is different from the "LbL coating" discussed in Section 4.4.2.1. "Nanocoating" here, and elsewhere in the thesis, refers to the coating developed by deposition of nanoparticles on heater surface during boiling

4.4.3.1. Pre-Boiling Time Control

Once the experiment is started, it is continued as discussed in Section 4.2.6. Since the steady-state CHF for DI water was seen to be 500 kW/m^2, the heat flux for the nanocoating development for time *t* was chosen to be 250 kW/m^2 (50% of DI water CHF). On reaching a flux level of 250 kW/m^2 (which takes approximately 10 minutes), the set-up is allowed to stay there, to allow for the test-fluid to boil at that heat flux, for duration of *t* hours. After that span of time, the experiment is again continued as before, until CHF occurs.

4.4.3.2. Pre-Test Surface Analysis

Both sandblasted and smooth heater elements are used in these experiments. However, they are not subjected to any additional surface treatment. Hence the initial surfaces (pre-testing) are the same as discussed in Section 4.4.1.2.

4.4.3.3. Results

Pre-boiling time was varied between 0 and 8 hours, both for DI water and nanofluid. **Table 4-6** and **Table 4-7** summarize the averaged results for multiple experiments with sandblasted and smooth heaters for various pre-boiling times with DI water. It is seen that CHF for DI water, for sandblasted heaters, does not change with pre-boiling time and stays at a constant value of ~500 kW/m^2. However, for smooth heaters, CHF for DI water is gradually decreasing, as the time for which pre-boiling is done is increased.

Table 4-6: Summary of CHF tests done for investigating effects of boiling time of DI water on sandblasted heaters

Experiment No.	Test-Fluid	Pre-Boiling Time (h)	Average CHF (kW/m^2)	Standard Deviation in CHF (kW/m^2)
SB_DIW_0hr	DI water	0	511.5	17.67
SB_DIW_1hr	DI water	1	490	42.43
SB_DIW_4hr	DI water	4	507	12.73
SB_DIW_8hr	DI water	8	416	N/A[7]

Table 4-7: Summary of CHF tests done for investigating effects of boiling time of DI water on smooth heaters

Experiment No.	Test-Fluid	Pre-Boiling Time (h)	Average CHF (kW/m^2)	Standard Deviation in CHF (kW/m^2)
Sm_DIW_0hr	DI water	0	454	14.85
Sm_DIW_1hr	DI water	1	424	12.73
Sm_DIW_4hr	DI water	4	351	19.09
Sm_DIW_8hr	DI water	8	332	N/A

Table 4-8 and **Table 4-9** summarize the averaged results for multiple experiments with sandblasted and smooth heaters, respectively, for varying times of pre-boiling in nanofluid. As seen from the CHF values for each test, from the tables, it is observed that for sandblasted heaters, additional pre-boiling times beyond 0 hour, do not contribute an additional CHF enhancement. In fact there seems to be a slight decrease in CHF over time, with values staying relatively close to ~1000 kW/m^2. Thus, it is seen that additional pre-boiling of nanofluid does not enhance CHF further, compared to no pre-boiling.

[7] Only 1 test each for the 8 hr pre-boiling time in DI water for sandblasted and smooth heaters was done, so there was no standard deviation to be calculated

Similarly, for smooth heaters in nanofluid, consistent with results discussed in Section 4.4.1, CHF enhancement is lower (for all pre-boiling times) than for sandblasted heaters. Again, additional pre-boiling times do not contribute to additional CHF enhancement, on top of the enhancement observed for 0 hour pre-boiling. For the smooth heaters, there seems to be no trend for CHF enhancement with varying pre-boiling times in nanofluid. Note the large data scatter for the vast majority of tests with nanofluids, compared to the tighter statistics shown in **Table 4-6** and **Table 4-7** for DI water.

Table 4-8: Summary of CHF tests done for investigating effects of boiling time of nanofluid on sandblasted heaters

Experiment No.	**Test-Fluid**	**Pre-Boiling Time (h)**	**Average CHF (kW/m^2)**	**Standard Deviation in CHF (kW/m^2)**
SB_NF_0hr	0.01v% ZnO	0	1297.5	2.12
SB_NF_1hr	0.01v% ZnO	1	1158	183.85
SB_NF_4hr	0.01v% ZnO	4	903	1.41
SB_NF_8hr	0.01v% ZnO	8	936.5	158.39

Table 4-9: Summary of CHF tests done for investigating effects of boiling time of nanofluid on smooth heaters

Experiment No.	**Test-Fluid**	**Pre-Boiling Time (h)**	**Average CHF (kW/m^2)**	**Standard Deviation in CHF (kW/m^2)**
Sm_NF_0hr	0.01v% ZnO	0	708.5	106.94
Sm_NF_1hr	0.01v% ZnO	1	610	167.58
Sm_NF_4hr	0.01v% ZnO	4	746	214.96
Sm_NF_8hr	0.01v% ZnO	8	673	67.17

Additionally, the effects of pre-boiling for the same amount of total integrated heat with differing values of pre-boiling times and heat flux at which pre-boiling was done, were also investigated. For this, in addition to experiments with pre-boiling for 1 hour at 250 kW/m^2, additional experiments, with pre-boiling for 0.5 hour at 500 kW/m^2, and 2 hours at 125 kW/m^2 were also completed. These tests were only done for sandblasted heaters. **Table 4-10** summarizes the averaged results of these experiments. It is clear from the table and the figure that the pre-boiling heat flux does not have an influence on the extent of CHF enhancement. For all the different flux levels used for pre-boiling similar CHF was observed with nanofluids (1100 – 1200 kW/m^2).

Table 4-10: Summary of CHF tests done, varying the pre-boiling heat flux and time, but at the same total integrated heat

Experiment No.	**Test-Fluid**	**Pre-Boiling Heat Flux (kW/m^2)/ Time (h)**	**Average CHF (kW/m^2)**	**Standard Deviation in CHF (kW/m^2)**
SB_NF_250	0.01v% ZnO	250/1	1158	183.85
SB_NF_125	0.01v% ZnO	125/2	1148	33.94
SB_NF_500	0.01v% ZnO	500/0.5	1262.5	88.39

The effect of pre-boiling time, with nanofluids, was also investigated on LbL coated sandblasted heaters. Again, pre-boiling was done at 250 kW/m^2, and pre-boiling times varied between 0 and 8 hours. The averaged results from these experiments are summarized in **Table 4-11**. Even for LbL coated heaters, it is observed that pre-boiling for additional times does not enhance CHF with nanofluid further, and the enhancement is similar to that observed without any pre-boiling. Consistent with results discussed in Section 4.4.2, CHF enhancement for all pre-boiling times is lower for LbL coated heaters than for uncoated heaters.

Table 4-11: Summary of CHF tests done, investigating the effects of boiling time of nanofluid on LbL coated sandblasted heaters

Experiment No.	Test-Fluid	Pre-Boiling Time (h)	Average CHF (kW/m^2)	Standard Deviation in CHF (kW/m^2)
LbLSB_NF_0hr	0.01v% ZnO	0	779.5	30.40
LbLSB_NF_1hr	0.01v% ZnO	1	643	9.89
LbLSB_NF_4hr	0.01v% ZnO	4	800.5	140.71
LbLSB_NF_8hr	0.01v% ZnO	8	832	48.08

Figure 4-39 is a graphical representation comparing CHFs for various heater surface/test fluid combinations at various pre-boiling times.

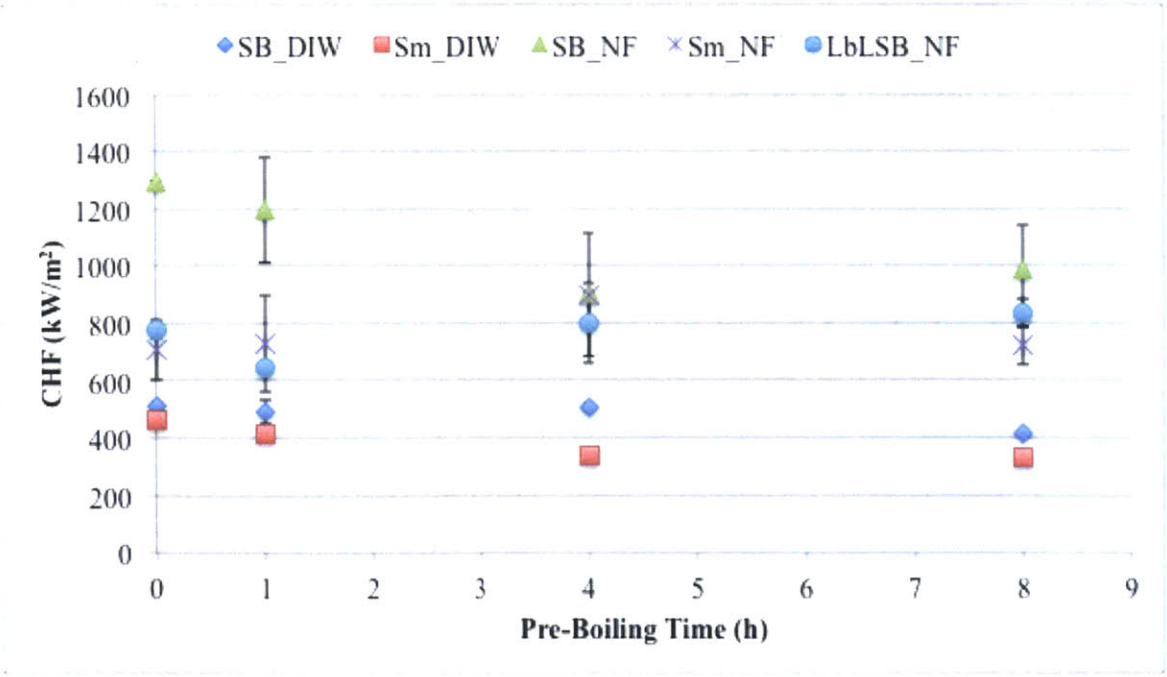

Figure 4-39: CHF for different heater surface/fluid combinations for varying pre-boiling times. Error bars show the standard deviation in CHF data

4.4.3.4. Post-Test Surface Analysis

Since DI water CHF for smooth heaters was observed to decrease with increasing pre-boiling times, one heater each from different boiling time tests was subjected to detailed post-test surface analysis. **Figure 4-40** – **Figure 4-43** show SEM images of smooth heaters, tested in DI water, for pre-boiling times of 0, 1, 4 and 8 hours respectively. **Figure 4-44** – **Figure 4-47** plot the confocal microscopy data from these heaters. As confirmed by these figures, heaters subjected to various times of pre-boiling have similar surface, qualitatively (from SEM images) and quantitatively (from confocal scans). Thus, there is no explanation, yet, for the unexpected trend of decreasing CHF for DI water, with increasing pre-boiling time.

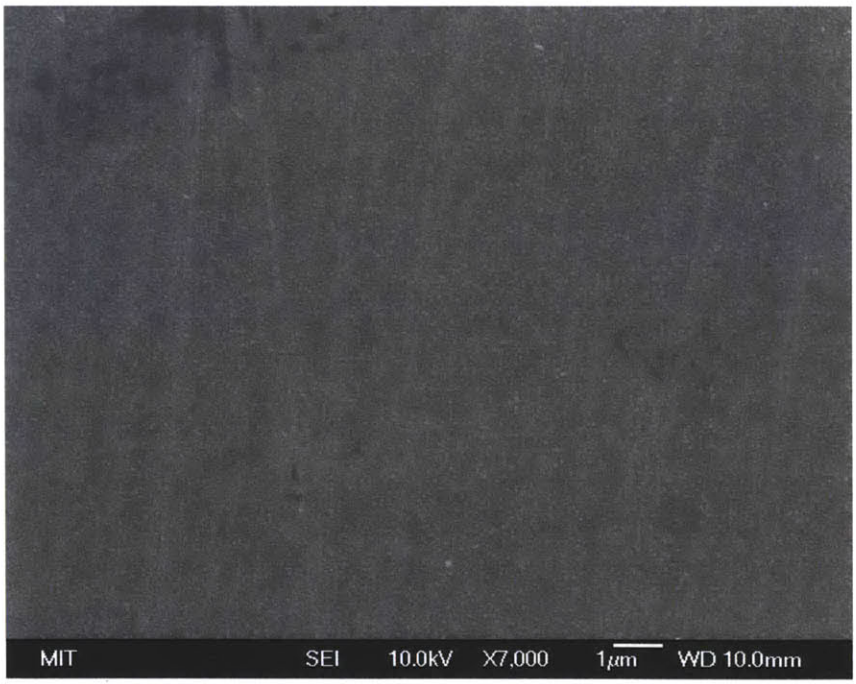

Figure 4-40: Post-test SEM image of heater tested for Sm_DIW_0hr

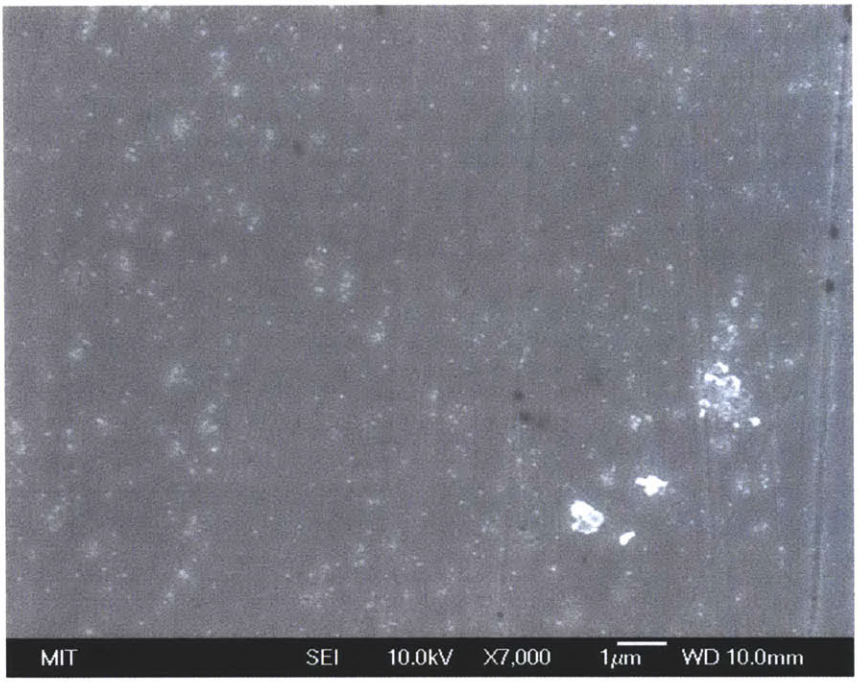

Figure 4-41: Post-test SEM image of heater tested for Sm_DIW_1hr

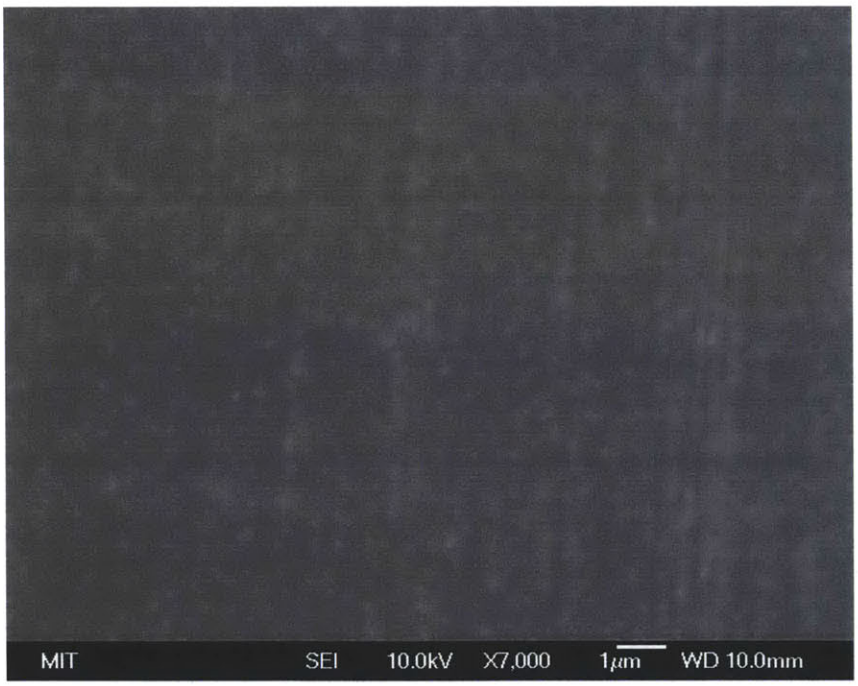

Figure 4-42: Post-test SEM image of heater tested for Sm_DIW_4hr

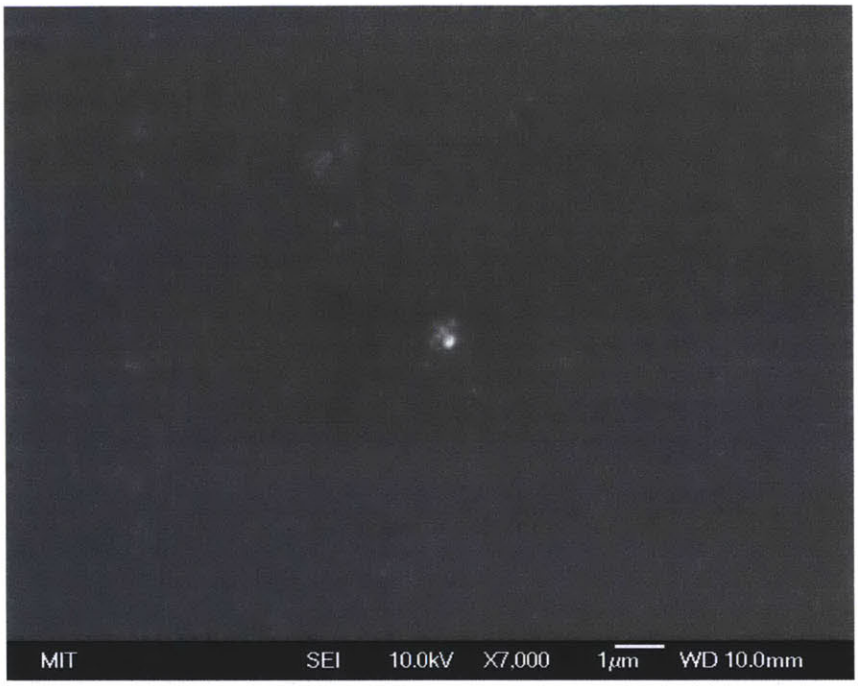

Figure 4-43: Post-test SEM image of heater tested for Sm_DIW_8hr

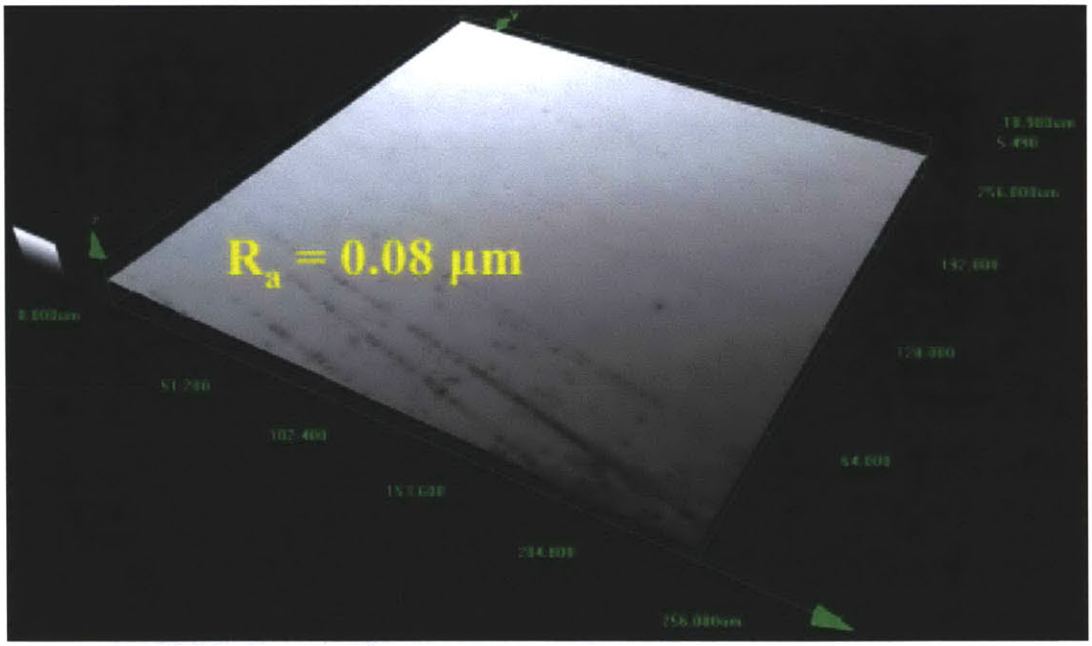

Figure 4-44: Confocal scan of the heater tested with Sm_DIW_0hr (R_a = 0.08 $\boldsymbol{\mu m}$)

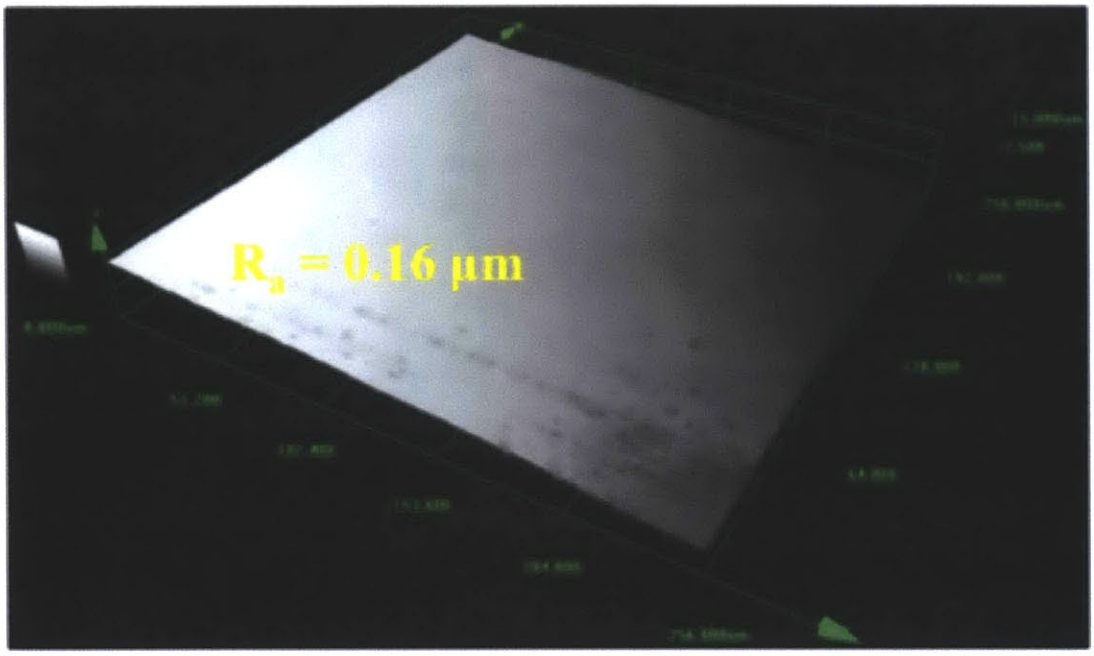

Figure 4-45: Confocal scan of the heater tested with Sm_DIW_1hr (R_a = 0.16 ***µm***)

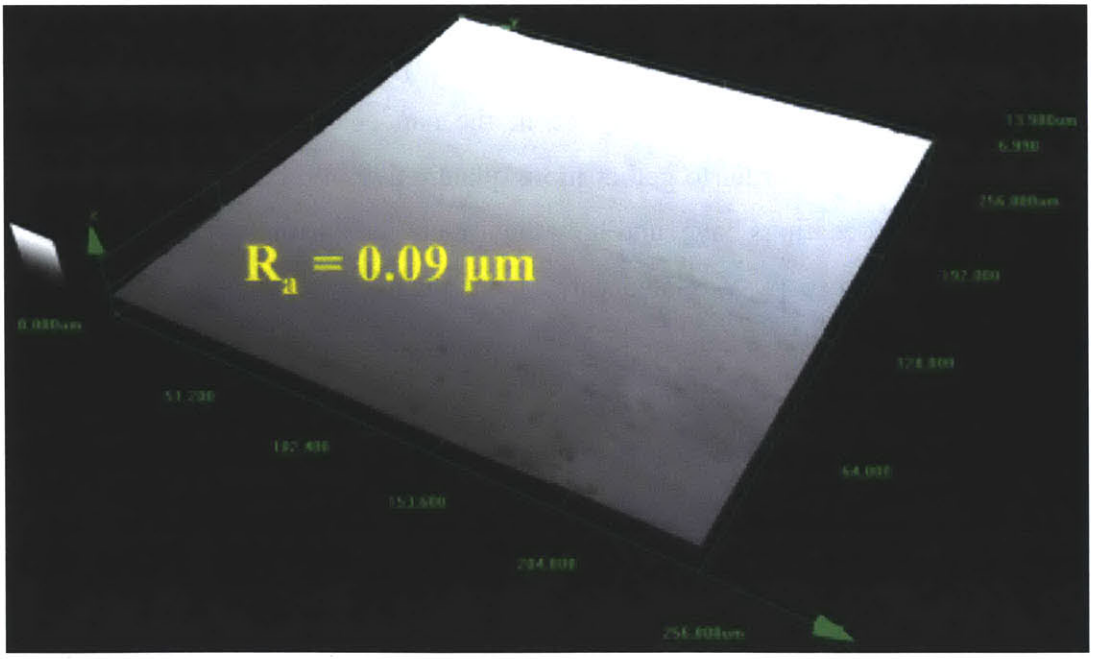

Figure 4-46: Confocal scan of the heater tested with Sm_DIW_4hr (R_a = 0.16 ***µm***)

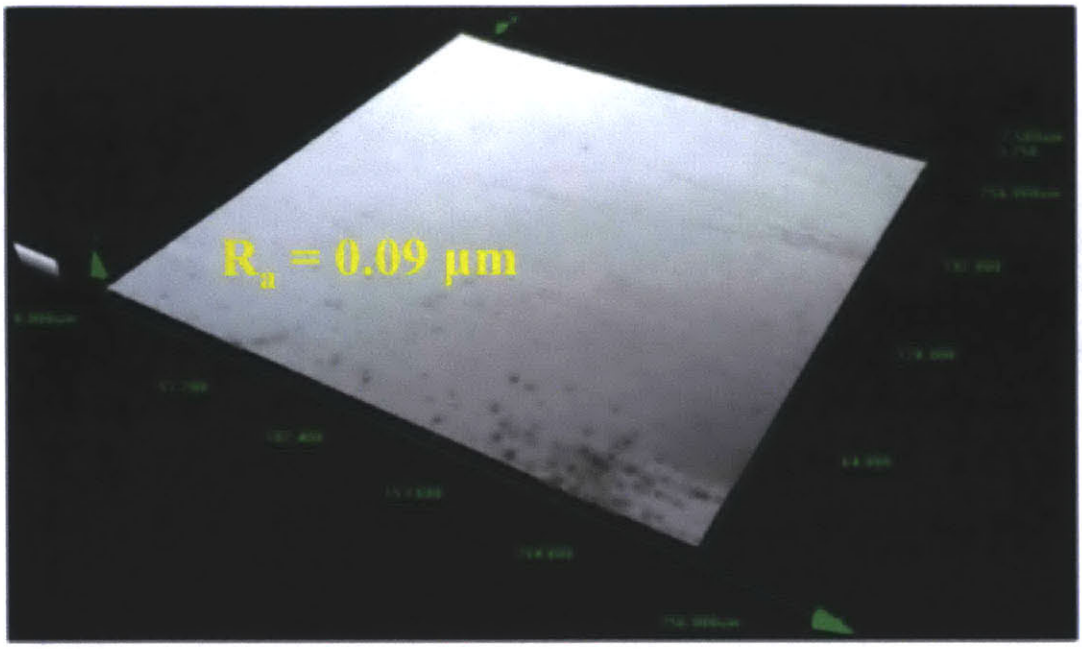

Figure 4-47: Confocal scan of the heater tested with Sm_DIW_1hr (R_a = 0.09 $\boldsymbol{\mu m}$)

Figure 4-48 – **Figure 4-51** show SEM images of sandblasted heaters tested in nanofluid, for pre-boiling times of 0, 1, 4 and 8 hours respectively. These figures make it clear that, qualitatively, there is not much difference in the nanocoatings developed as the pre-boiling time is varied. In order to gather more quantitative information about the surface effects that the nanocoatings have, and how they might vary with variation in pre-boiling times, confocal microscopy was also carried out on the same heaters. **Figure 4-52** – **Figure 4-55** show confocal scans on these heaters. It is seen that the surface roughness of the heaters, quantified by R_a, is seen to increase on development of nanocoatings during boiling, consistent with observations reported in Section 4.4.1.4. However, again, the increase in R_a for sandblasted heaters is not elevated.

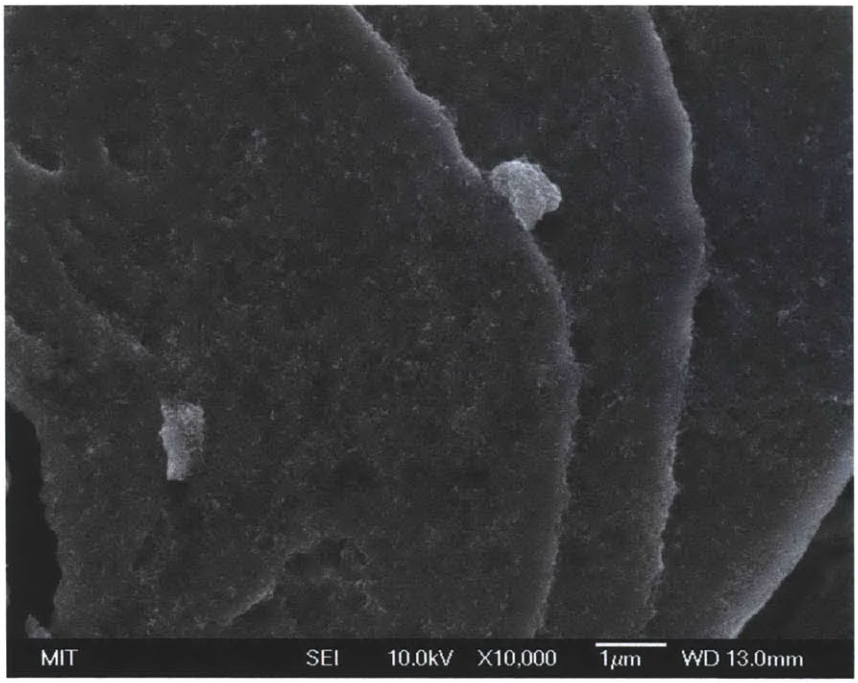

Figure 4-48: Post-test SEM image of heater tested for SB_NF_0hr

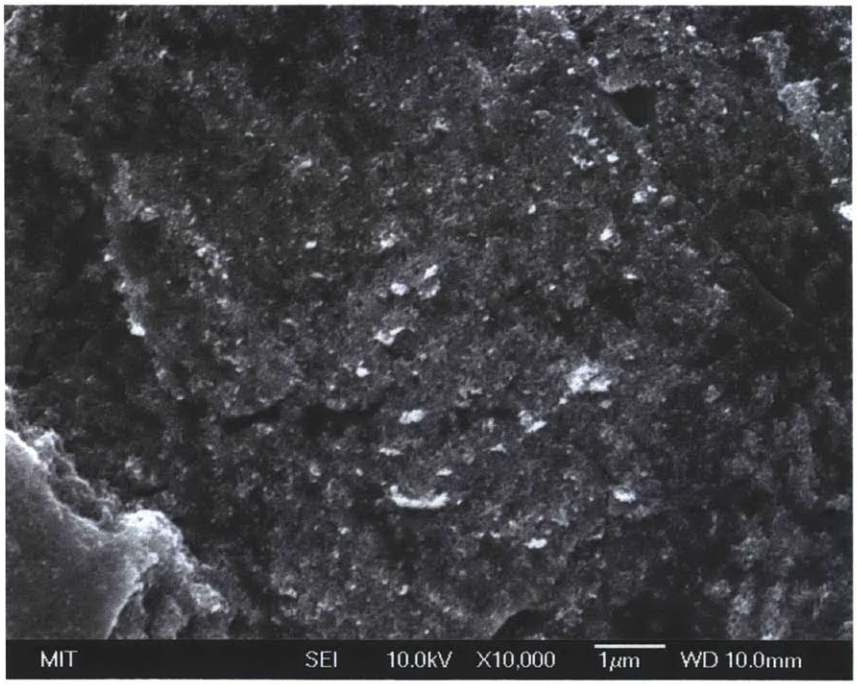

Figure 4-49: Post-test SEM image of heater tested for SB_NF_1hr

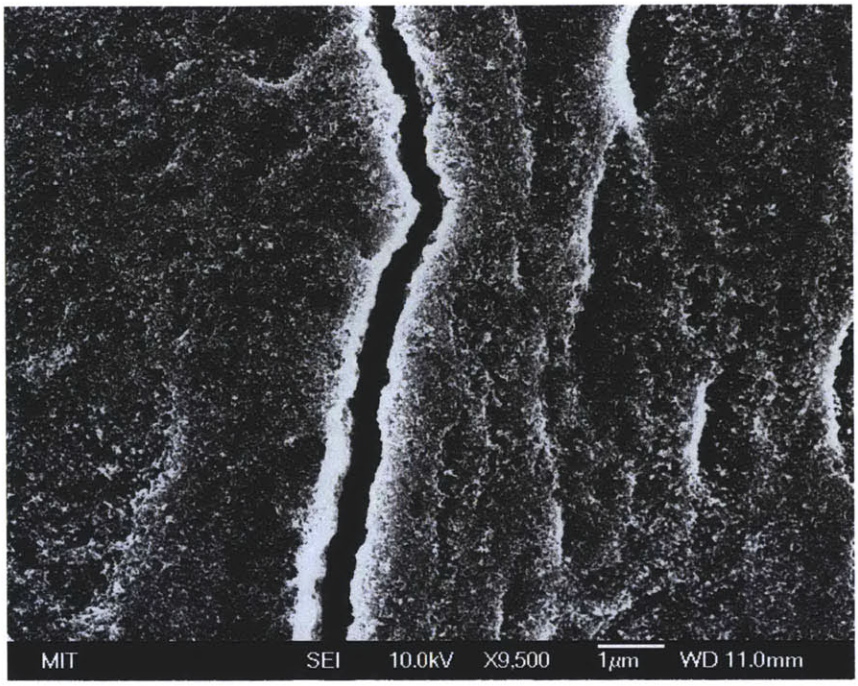

Figure 4-50: Post-test SEM image of heater tested for SB_NF_4hr

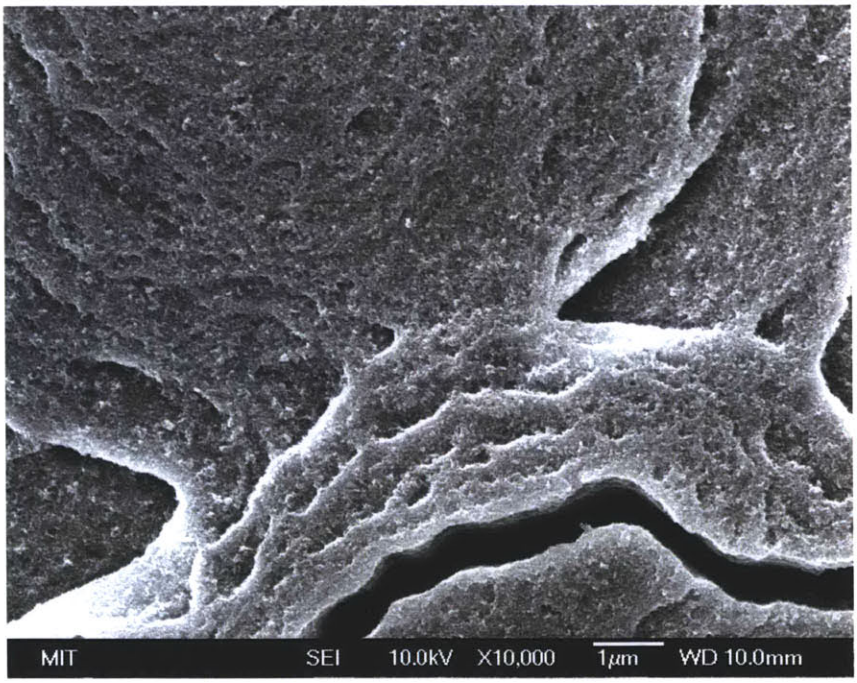

Figure 4-51: Post-test SEM image of heater tested for SB_NF_8hr

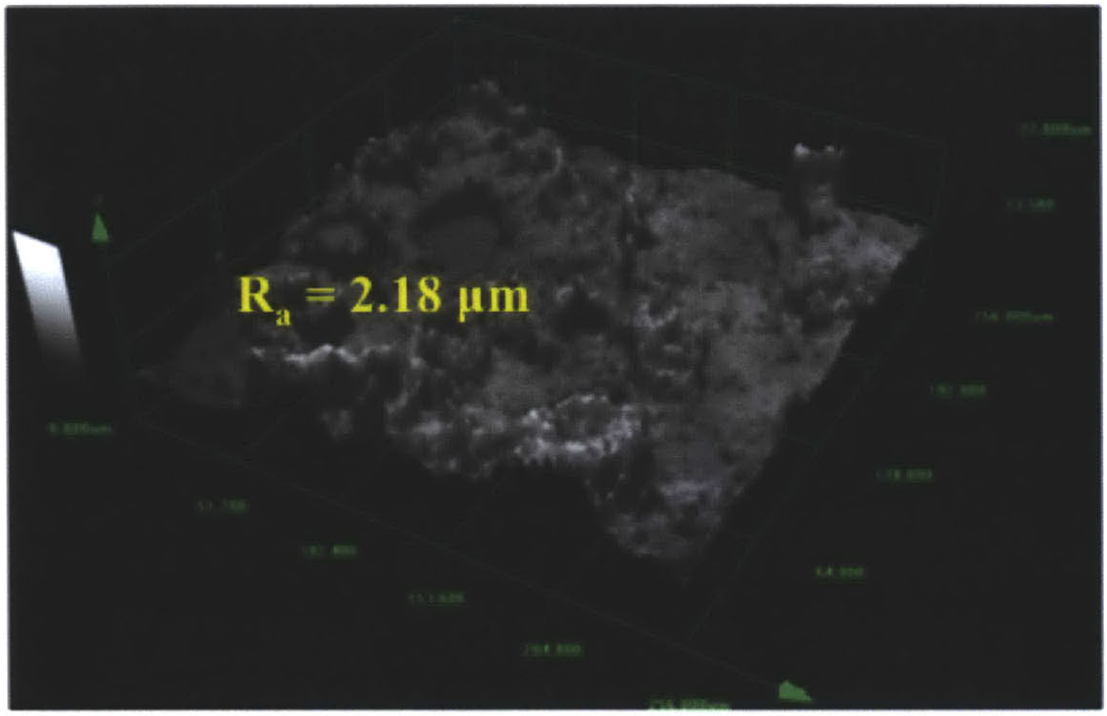

Figure 4-52: Confocal scan of the heater tested with SB_NF_0hr (R_a = 2.18 ***µm***)

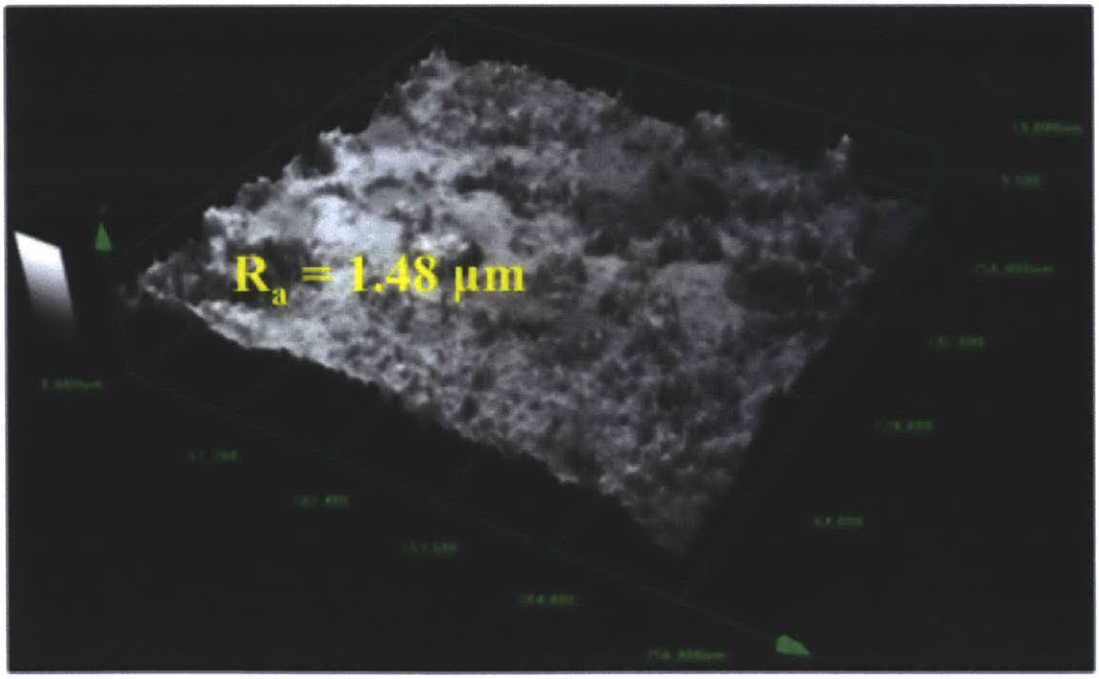

Figure 4-53: Confocal scan of the heater tested with SB_NF_1hr (R_a = 1.48 ***µm***)

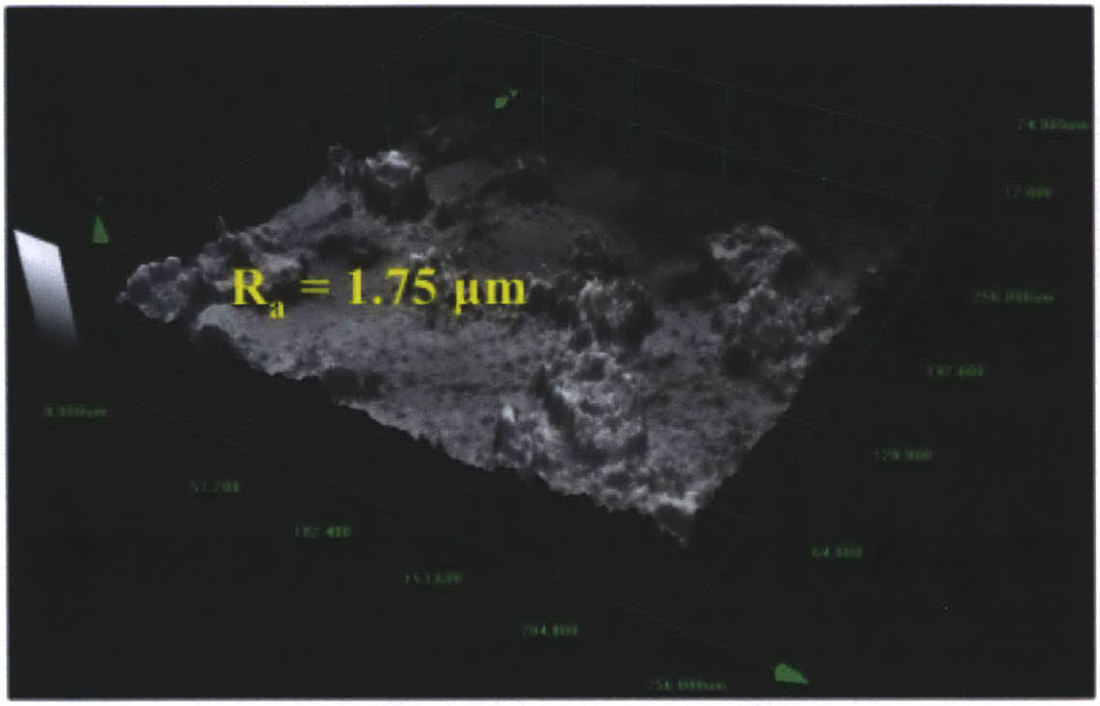

Figure 4-54: Confocal scan of the heater tested with SB_NF_4hr (R_a = 1.75 $\boldsymbol{\mu m}$)

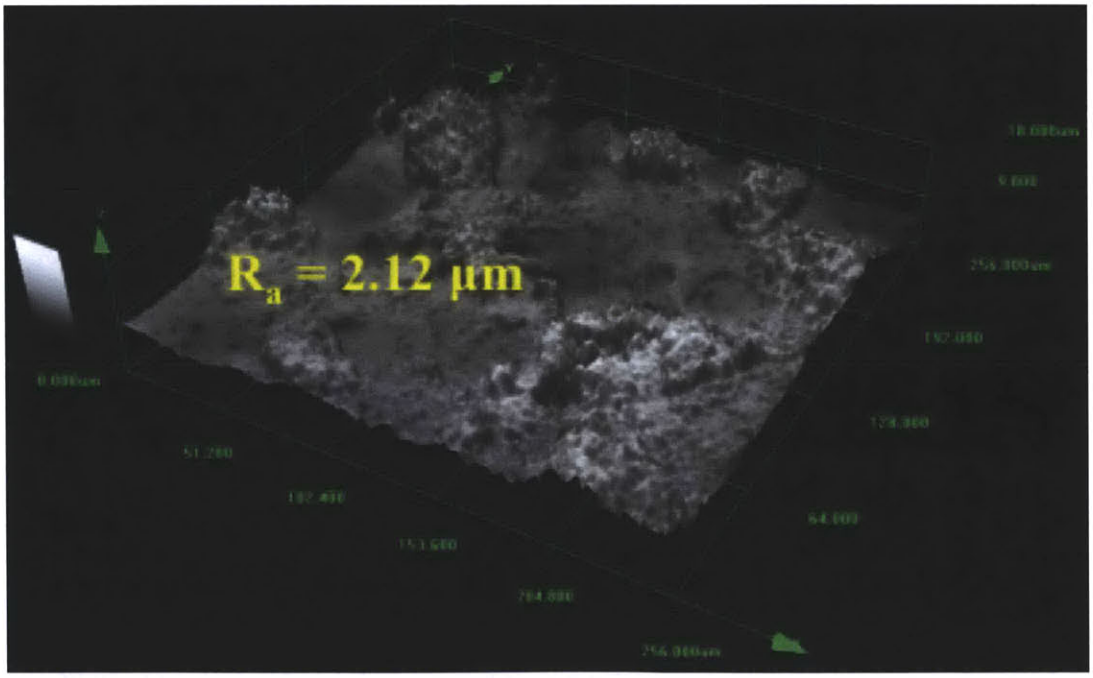

Figure 4-55: Confocal scan of the heater tested with SB_NF_8hr (R_a = 2.12 $\boldsymbol{\mu m}$)

Figure 4-56 – **Figure 4-59** show the corresponding SEM images for smooth heaters, and **Figure 4-60** – **Figure 4-63** show corresponding confocal scans for smooth heaters. Just like sandblasted heaters, the nanocoatings with different pre-boiling times cannot be qualitatively differentiated from each other for smooth heaters too. The nanocoatings also increase the surface roughness of smooth heaters, as is evident from the R_a values obtained post-test, compared to initial R_a of ~0.07 μm.

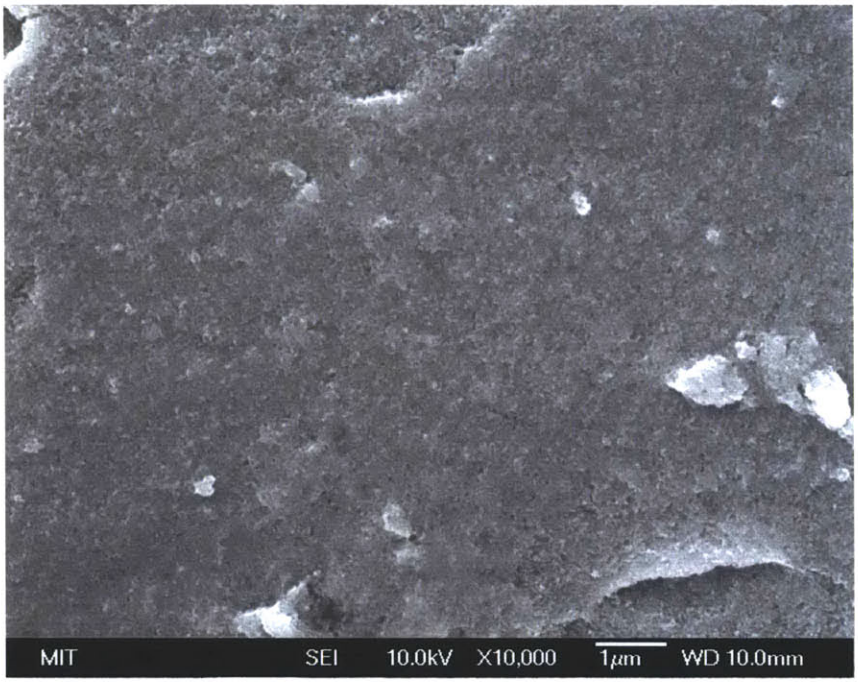

Figure 4-56: Post-test SEM image of heater tested for Sm_NF_0hr

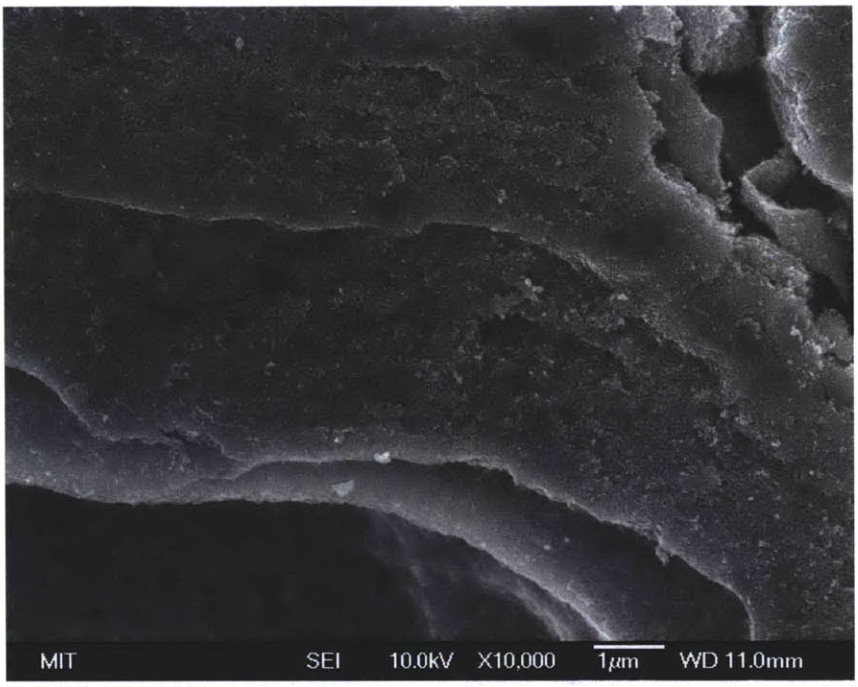

Figure 4-57: Post-test SEM image of heater tested for Sm_NF_1hr

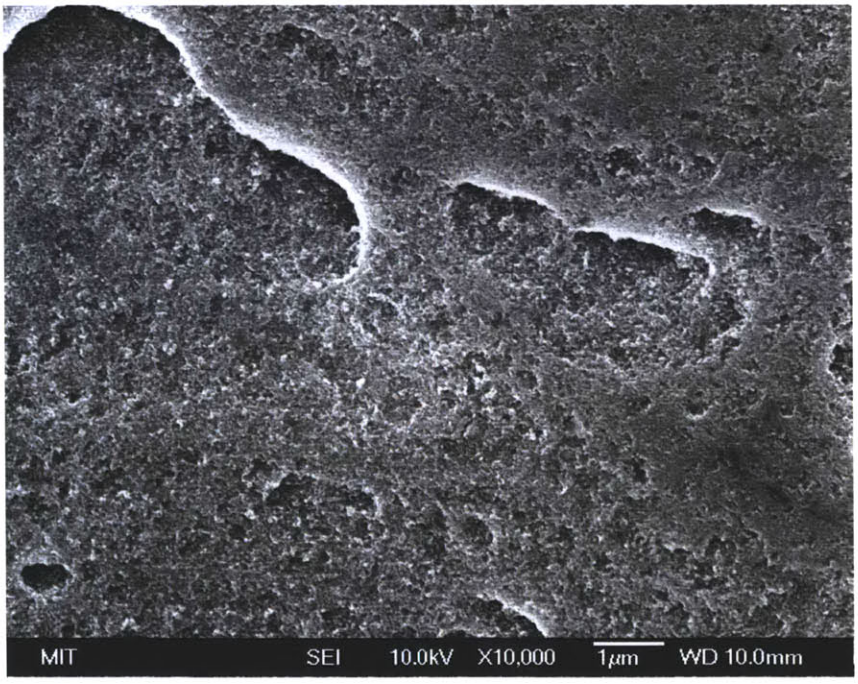

Figure 4-58: Post-test SEM image of heater tested for Sm_NF_4hr

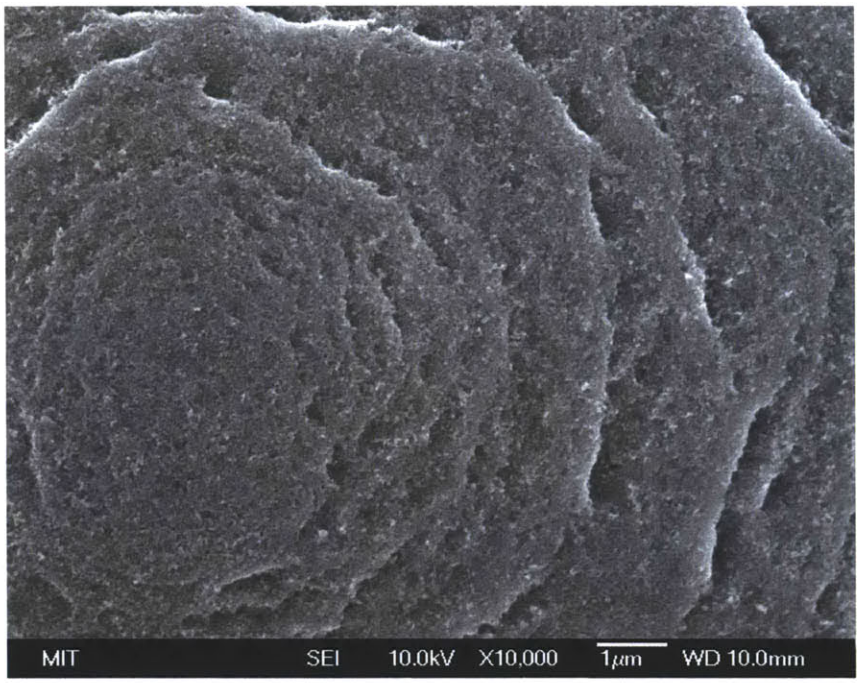

Figure 4-59: Post-test SEM image of heater tested for Sm_NF_8hr

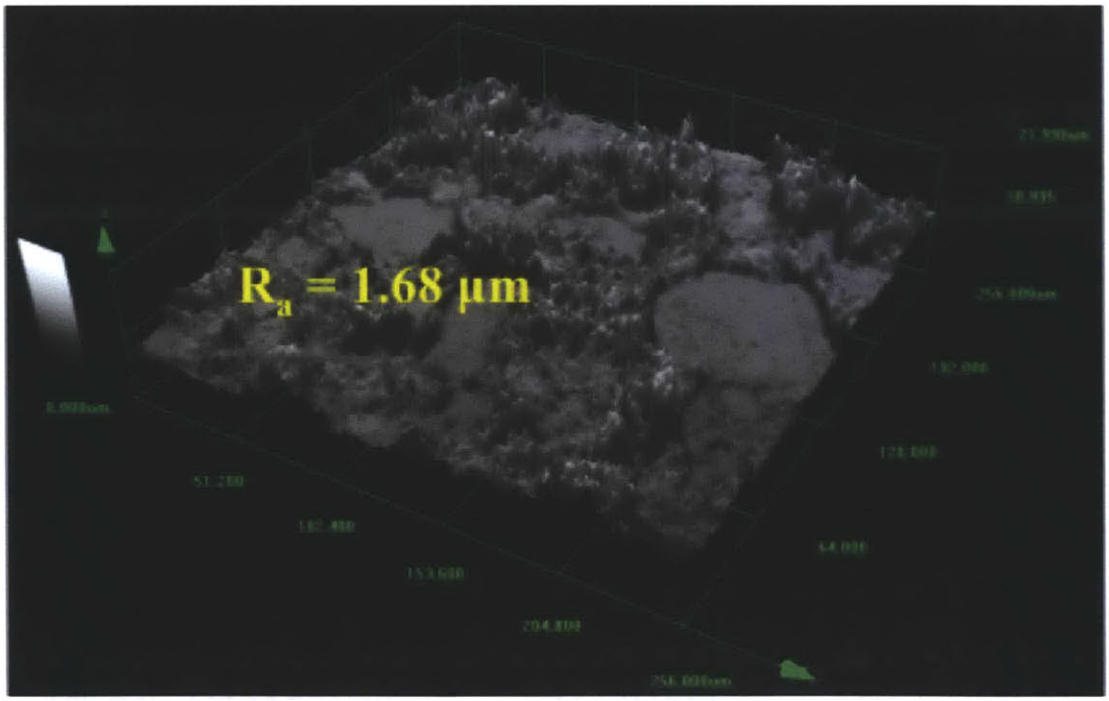

Figure 4-60: Confocal scan of the heater tested with Sm_NF_0hr (R_a = 1.68 $\boldsymbol{\mu m}$)

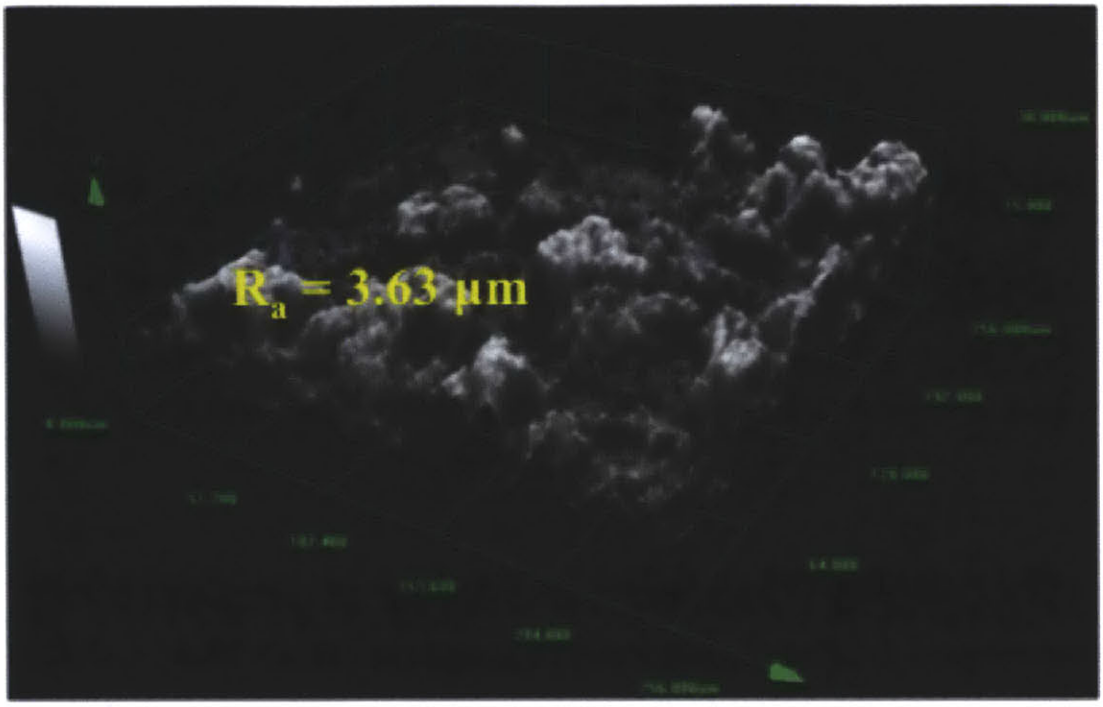

Figure 4-61: Confocal scan of the heater tested with Sm_NF_1hr (R_a = 3.63 $\boldsymbol{\mu m}$)

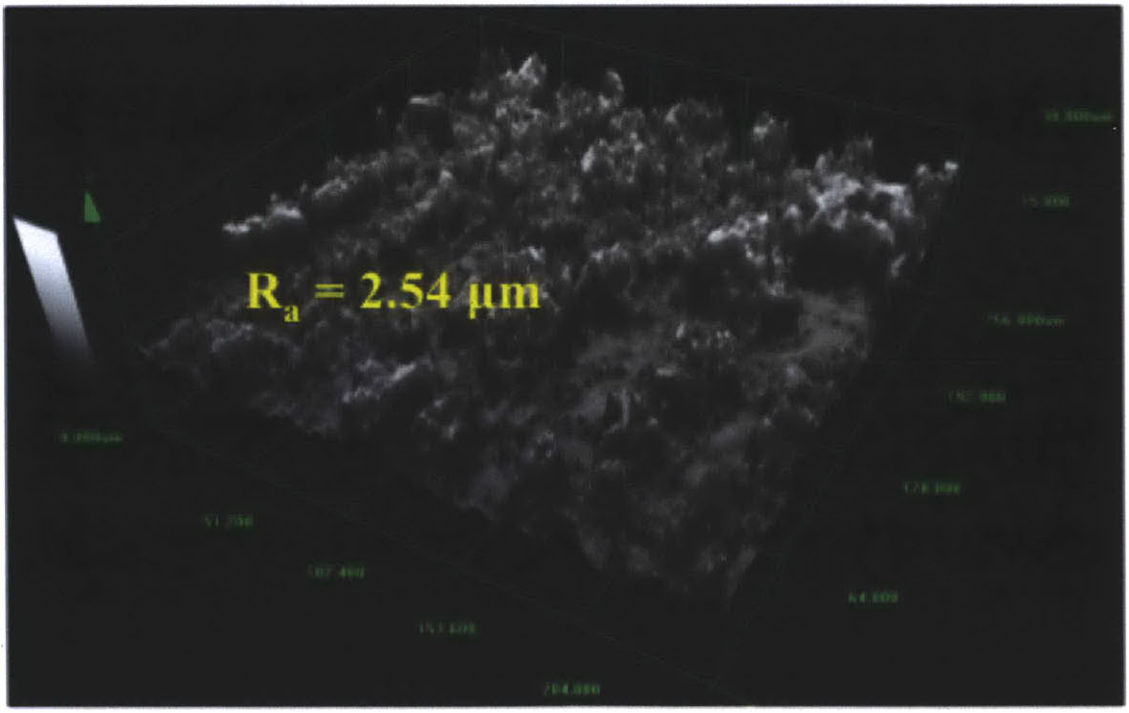

Figure 4-62: Confocal scan of the heater tested with Sm_NF_4hr (R_a = 2.54 $\boldsymbol{\mu m}$)

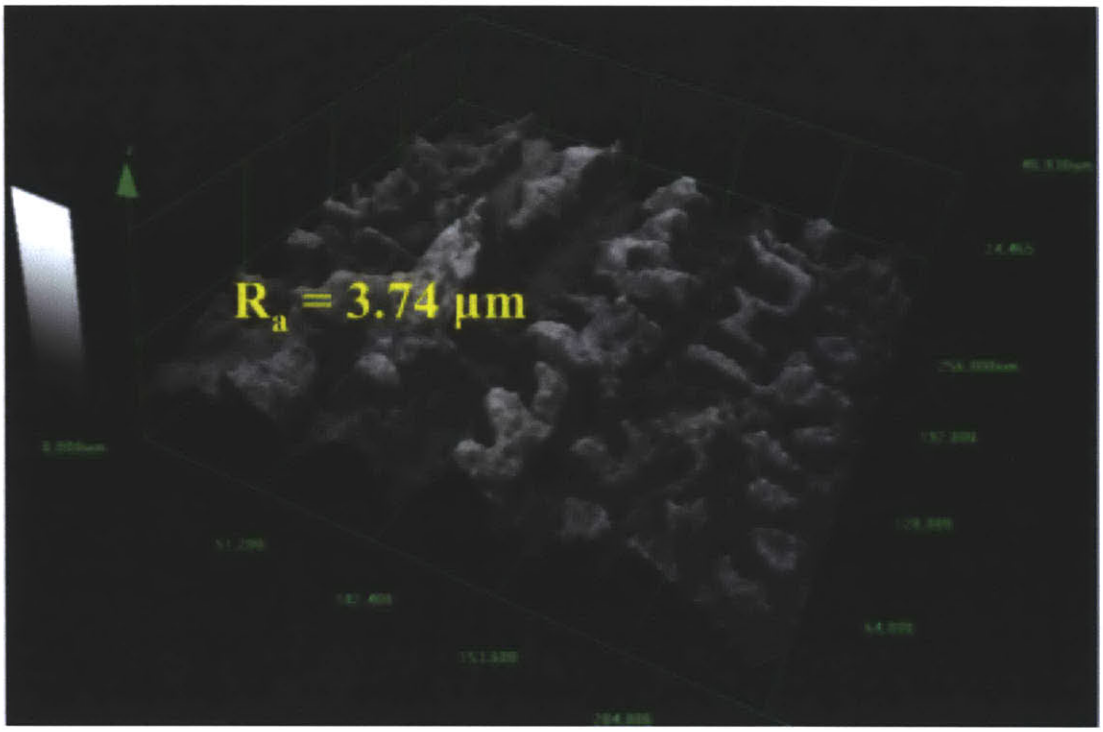

Figure 4-63: Confocal scan of the heater tested with Sm_NF_4hr (R_a = 3.74 $\boldsymbol{\mu m}$)

However, the nanocoatings developed over heater surfaces are a direct consequence of nucleate boiling occurring from the nucleation sites. Thus, the times for which the boiling is allowed to happen, i.e. the pre-boiling time can potentially effect the thickness of nanocoatings developed. In order to check this, confocal microscopy was also used to measure average nanocoating thicknesses for various tests. To do this, part of a test heater, after nanoparticle deposition, was wiped clean with a sharp blade. Confocal scans were then obtained on an area (256 x 256 μm^2), which included both the wiped as well as the nanocoating area. From the confocal data collected, the average Z-height of the areas with and without nanocoatings was obtained. The difference between these heights gives the average nanocoating thickness. This procedure is pictorially represented in **Figure 4-64**. **Table 4-12** summarizes various measurements done on smooth and sandblasted heaters tested in nanofluids for various boiling times. Where multiple measurements were successfully carried out, all the measured R_a values are shown. In some samples, due to damage experienced by the heater as a result of CHF, measurement for R_a was possible only at 1 location, leading to only 1 R_a value for that sample. As is seen from the Table,

the R_a values for sandblasted heaters, with nanocoatings, varies between 1.1 and 2.2 μm, compared to the ~1.25 μm for an uncoated heater. These values of R_a are observed, irrespective of pre-boiling times, indicating that pre-boiling times do not translate into an increasing/decreasing R_a. Additionally, for smooth heaters, R_a values are much higher than for sandblasted heaters, varying between 1 and 3.8 μm, compared to 0.07 μm for uncoated heaters. Thus, smooth heaters undergo a much drastic change in R_a compared to sandblasted heaters. Furthermore, the average nanocoating thickness for all boiling times for sandblasted heaters is of the order of 0.5 μm, compared to 1 – 2 μm for smooth heaters. Again, smooth heaters not only have a high R_a compared to sandblasted heaters, but also have a thicker nanoparticle deposit. However, the thickness of nanocoating does not increase (for both sandblasted and smooth heaters) with increasing pre-boiling time. The random variations in R_a and nanocoating thickness for both kinds of surfaces, again, supports the fact that the uncontrolled and non-uniform nucleate boiling process is responsible for the development of the nanocoatings.

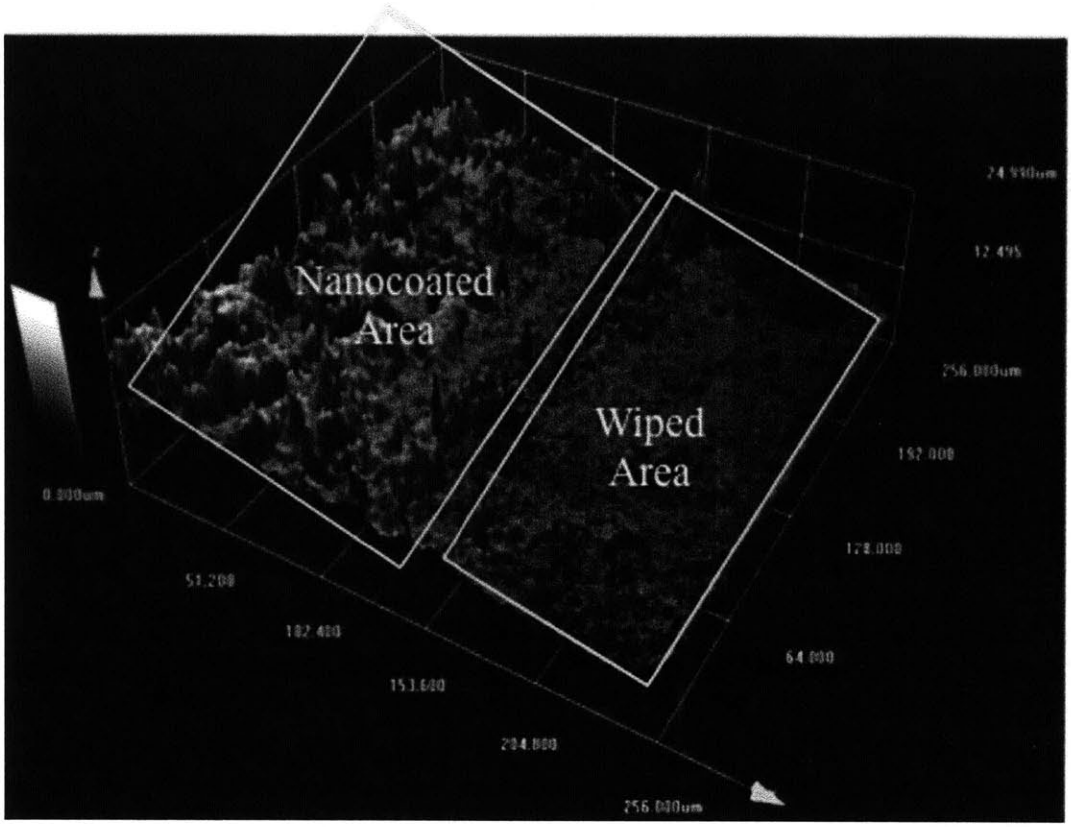

Figure 4-64: Confocal scan showing both the wiped (cleaned) and nanocoated areas on a heater tested with nanofluid. Average Z-heights of both areas is calculated. Their difference gives the average nanocoating thickness developed

Table 4-12: Summary of confocal microscopy data for different heaters, tested with nanofluid for various pre-boiling times

Experiment No.	Heater	Test-Fluid	Pre-Boiling Time (h)	R_a (μm)	Avg. Nanocoating Thickness (μm)
SB_NF_0hr	Sandblasted	0.01v% ZnO	0	2.18 1.12 1.33	0.762
SB_NF_1hr	Sandblasted	0.01v% ZnO	1	1.48 1.86	0.401
SB_NF_4hr	Sandblasted	0.01v% ZnO	4	1.75	0.569
SB_NF_8hr	Sandblasted	0.01v% ZnO	8	2.12	0.515
Sm_NF_0hr	Smooth	0.01v% ZnO	0	1.68	0.430
Sm_NF_1hr	Smooth	0.01v% ZnO	1	3.63 1.04	2.677
Sm_NF_4hr	Smooth	0.01v% ZnO	4	2.54 1.76	2.333
Sm_NF_8hr	Smooth	0.01v% ZnO	8	3.74 3.23	1.185

4.5. Summary/Discussion of Steady-State Test Results

Several experiments were conducted to investigate effects of different parameters – surface roughness, surface wettability and pre-boiling time – on steady-state CHF for nanofluids. Sandblasted and smooth heaters have markedly different surface roughness and wettability (as shown by contact angle measurements). However, both surfaces exhibit similar CHF with water, the CHF value being ~500 kW/m^2. This observation appears surprising, as heaters with rougher surface are usually expected to have higher CHF. However a parallel study in the MIT lab by O'Hanley [33] has shown that the intrinsic roughness and wettability do not have any effect on CHF; in fact, the primary mechanism for an enhanced CHF is the porosity of the surface. Thus the findings by O'Hanley confirm the observations in this thesis. Additionally, after burning off of any hydrocarbon footprint accumulated on the unused heaters through boiling the surface at 250 kW/m^2 for 1 hour, it was seen that both sandblasted and smooth heaters had the same receding contact angle of ~10^0. According to the Kandlikar correlation [26], the contact angle of significance in the CHF calculation is the dynamic receding contact angle. Again, since both sandblasted and smooth heaters have the same dynamic receding contact angle, they are expected to have similar CHF as per the Kandlikar correlation. Replacing DI water with nanofluid as the test fluid, both sandblasted and smooth heaters exhibit an enhanced CHF. However, the extent of CHF enhancement for sandblasted heaters was much larger (160%) compared to smooth heaters (68%). SEM imaging confirmed the presence of a ZnO nanocoating, on heaters tested with nanofluid. Due to the development of the nanocoatings, R_a for both sandblasted and smooth heaters changes. However, the increase for smooth heaters is much more severe than for sandblasted heaters. Owing to their porosity, the nanocoatings were also responsible for increasing the wettability of the heater surfaces as confirmed by contact angle measurements. Hence, the nanocoatings are confirmed to be the primary mechanism for an increased CHF, consistent with reports in the literature.

On changing the initial wettability of heaters, using LbL method, both sandblasted and smooth heaters showed roughly 30% enhancement with DI water. The LbL coatings were shown to leave the surface roughness of heaters unaltered; hence, the enhanced CHF is attributed primarily to the increased combined porosity and wettability, which results due to the LbL coatings. On using nanofluid with the highly hydrophilic heaters, again an additional CHF enhancement was seen, but that enhancement was much smaller than enhancement for nanofluid with uncoated heaters. This suggests that the ZnO nanocoating developed during boiling does not have as pronounced an effect in the presence of LbL coatings as in their absence. This could be due to multiple possible reasons such as:

(i) The LbL coated SiO_2 layer leads to an additional thermal resistance on the heater surface due to the low conductivity of the nanoparticles compared to the heater material. The diameter of SiO_2 nanoparticles is 50 nm. For a first order estimate of the LbL coating thickness, assuming 40 bi-layers to consist of 40 nanoparticles, the thickness of the coating is obtained as 40 x 50 = 2000 nm. Using the value of thermal conductivity of SiO_2 of 0.5 W/m-K, the layer thermal resistance (=l/kA, where l is the layer thickness, k is its thermal conductivity and A is area heat transfer), is calculated as

$$R_{t,lbl} = \frac{l}{kA} = \frac{2000\ x\ 10^{-9}}{0.5\ x\ 0.034\ x\ 0.005} = 0.0235\ K/W$$

Comparatively, the thermal resistance of the stainless steel heater element is

$$R_{t,ss304} = \frac{l}{kA} = \frac{0.0004572}{16.2\ x\ 0.034\ x\ 0.005} = 0.166\ K/W$$

Thus, there is a 14% increase in thermal resistance, on adding the LbL coating at the surface. This additional resistance at the interface increases the temperature of the heater surface for any given heat flux; this may make it

more difficult for the liquid to rewet the surface at high heat flux, thus possibly accelerating CHF.

(ii) The presence of LbL coatings could alter the manner in which the ZnO nanoparticle coating assembles on the surface during boiling, affecting its microstructure and porosity, which can lead to different CHF than in the absence of LbL coatings.

Additionally, it was seen that varying pre-boiling times for nanofluids do not have a discernible effect on CHF. In fact, for sandblasted heaters, the highest CHF is observed for 0 hour pre-boiling time. For both sandblasted and smooth heaters, CHF with nanofluid stays almost constant when the pre-boiling time is increased. For all pre-boiling times, the changes in surface roughness for the heaters were similar. R_a changed for sandblasted heaters, from an initial value of 1.25 μm to values ranging between 1.2 μm to 2.2 μm. However, R_a values for smooth heaters changed from an initial value of 0.06 μm to values ranging between 1 and 3.7 μm. This suggests that, for sandblasted heaters, some of the nanocoating deposition might be occurring in the pits and cavities that are present on the surface, leading to a lower surface roughness on deposition of the nanocoating. However, smooth heaters do not have any large cavities, leading to nanocoating development on a completely flat surface, which leads to a higher R_a, comparatively. Large variations in R_a values for both heater surfaces is due to the fact that these nanocoatings are developed due to boiling on the surface, which progresses in a completely uncontrolled fashion during the experiment, and leads to development of highly non-uniform coatings of nanoparticles on heater surfaces. Average thickness of nanocoatings was also calculated for various pre-boiling times, for both sandblasted and smooth heaters. It was observed that for all pre-boiling times (0, 1, 4 and 8 h), thickness of nanocoatings varied between 0.4 and 0.7 μm, and was not seen to increase with increase in pre-boiling time. Even for the smooth heaters, the thickness did not increase with increase in pre-boiling time, even though the thickness of the coatings was higher, ranging between 1 and 2.5 μm. This observation is consistent with the observation of

similar CHF values for varying pre-boiling times, and indicates that the nanocoating development saturates within the time of a 0 hour pre-boiling time experiment. No additional nanoparticles are coated on the heater, even if the heater is under boiling conditions in a nanofluid. Experiments for varying pre-boiling time, but same amount of total heat used for pre-boiling, also showed similar CHF values. This suggests that, as long as strong nucleation occurs on the surface, the nanocoating development on the heaters used in this work does not depend on the flux used for nanocoating, or the time, which the nanocoating is allowed to develop for. The effect of pre-boiling time was also investigated on LbL coated heaters. Similar to uncoated heaters, they also exhibit similar values of CHF, for varying pre-boiling times. The CHF for LbL coated heaters was, again, lower than for uncoated heaters, suggesting that the nanocoating of ZnO particles due to boiling is effected by the presence of the LbL coating present on the surface.

It was concluded that the nanocoating development and increase in its thickness plateaus in 30 – 40 minutes of steady nucleate boiling. Thus, it is of interest to investigate the time frames (< 30 min) required for nanocoating, effective enough to appreciably affect CHF, to develop on the heater surface. In order to explore the nanocoating development and its effects at shorter time frames, we conduct transient power (heat flux) experiments, the longest of which lasts only 100 s. The details of these experiments, and their results are discussed in Chapter 5.

5. Transient Tests

Before discussing the specific objectives and more details about transient tests, it is important to discuss the basic differences between transient and steady state boiling and CHF. Section 5.1 provides a concise summary of the key results for transient CHF reported in various publications.

5.1. Literature

There have been several studies reported in literature that discuss the boiling behavior on heaters with a transient heat flux condition. Almost all of the studies reported are for an exponentially increasing volumetric power input given by $Q = Q_o e^{t/\tau}$, where Q_o is the initial power level per unit volume in the heater and τ is called the exponential period for the transient. There have been several attempts to understand the mechanism for transitions from conduction, natural convection and nucleate boiling regimes to film boiling regime, due to exponentially increasing heat inputs for various fluids, such as water, and highly wetting fluids such as liquid nitrogen, liquid helium and ethanol. For these fluids, researchers have conducted investigations for different subcooling as well as pressure conditions [84-92]. Sakurai and Shiotsu, first, suggested that the progression of boiling curves for transient tests is slightly different from that of steady heat flux tests [85, 86]. Even for transient tests, boiling curves differed depending on the rate of transient, quantified by τ. In their study for heaters submerged in DI water, they contend that if the period is sufficiently short, i.e. the rate of heat input and hence the rate of increase of surface temperature are higher than a certain limit, natural convection does not appreciably contribute to heat transfer [86]. Instead, water surrounding the heater acts as an infinite solid wall, and heat transfer happens by the transient conduction mechanism. However, if the period is low, the initial heat transfer mechanism, at low heat fluxes, is

natural convection. As heat flux is increased, for small periods, unflooded microcavities present at the surface with radii satisfying the critical condition for nucleation [9] get activated and act as nucleation sites. For slow transients, this nucleation can become fully developed. They also observed that heat flux at the point of inception of boiling on the surface increases with a decrease in the exponential period. This was also pointed out in [87], where the authors noted that for transient heat inputs with relatively long exponential periods, nucleate boiling existed on the linear extension of steady nucleate boiling curve.

Sakurai et al also observed that for a fixed heat flux value, HTC for transient tests after boiling initiation was lower than that for steady state tests [88]. This was explained as follows: As the heat input to the heater is increased exponentially, its surface temperature also increases. Due to an increase in surface temperature, unflooded cavities with entrapped air get activated, leading to nucleation from those cavities. On further increase in wall temperature due to an increase in heat input, even more unflooded cavities keep getting activated, leading to stronger nucleation. Eventually at one level of wall temperature, even the cavities that are originally flooded with fluid, get activated due to bubbles originating from neighboring cavities. At this point, due to the activation of an immensely large number of cavities, heater wall temperature starts to decrease, and the number of activated cavities again decreases. Thus, the amount of nucleation also drops. The process of the decrease in wall temperature due to activation of large number of nucleation sites is shown in Figure **5-1** (taken from ref. [90]) for the '10 s' curve. Hence, compared to steady state experiments, the number of active cavities, and the extent of nucleation, at a given heat flux after the inception of boiling is lower for transient tests. This phenomena leads to a lower HTC for transient tests, compared to steady boiling tests. In other words, there is a time lag associated with the activation of all nucleation sites for transient tests, compared to steady heat flux tests.

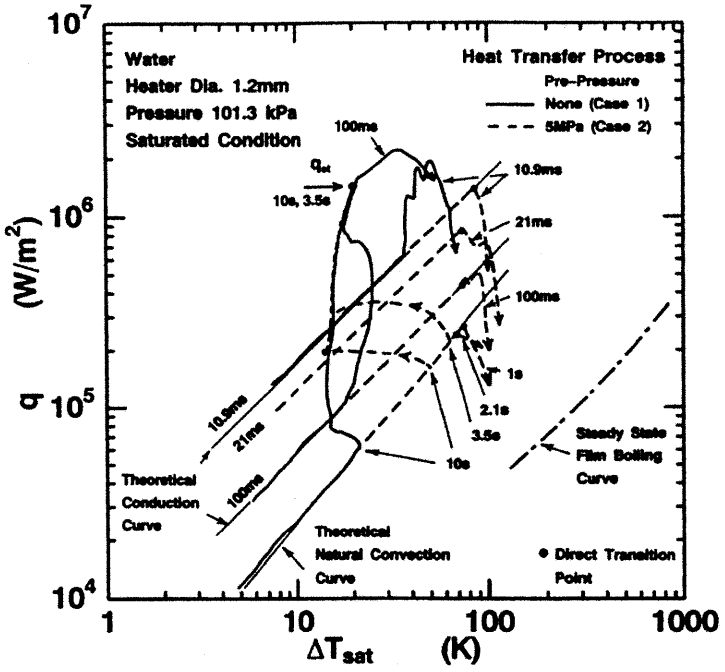

Figure 5-1: Typical heat transfer processes for saturated DI water (from ref. [90])

In 1993, Sakurai et al conducted investigations of the mechanism to film boiling during exponentially increasing heat inputs on a solid surface, for liquid nitrogen, water and ethanol [89, 90]. For liquid nitrogen and ethanol (completely wetting fluids), they observed that a direct transition to film boiling happened from non-boiling regime, independent of the exponential period. For pressures below atmospheric, this direct transition was observed even for quasi-steadily increasing heat inputs. For higher pressures, the direct transition happened if the exponential period was shorter than a certain pressure-dependent value. For large periods (quasi-steady heat inputs), the transition to film boiling was preceded by fully developed nucleation. They suggested a new mechanism responsible for the direct transition to film boiling, for completely wetting fluids, and backed it by conducting photographic investigations of the solid/fluid interface. This was called Heterogeneous Spontaneous Nucleation (HSN). HSN is an explosive-process, where nucleation occurs from all cavities (flooded or unflooded) at a particular rate of increase of surface superheat. The surface temperature and the rate of

increase of surface superheat, where HSN occurs, depend on the rate of transient. The faster the transient, the higher the HSN superheat required. The HSN superheat is higher than the superheat required for nucleation from unflooded cavities, but is lower than the superheat required for homogeneous nucleation in the bulk of the fluid. For completely wetting fluids, there are no unflooded cavities with trapped air/vapor in them because of the extremely low surface tensions of the fluids. At high exponential periods, i.e. for slow transients, as the bulk and wall temperature keep on increasing with time, HSN is initiated from the flooded cavities. At this point, throughout the heater surface, there are large vapor bubbles present, which start to rise up due to buoyancy. After the departure of vapors, liquid again comes in contact with the surface. Due to vapor formation, the wall superheat starts to decrease, which leads to a departure from HSN, and continuation of nucleate boiling. However, if the rate of the transient is high enough, the rate of increase of surface superheat due to increasing heat input can overcome the decrease in surface superheat. Thus HSN continues at the surface, and the vapor-liquid interface (for the vapors formed at first instance of HSN initiation) gets levitated by vapor bubbles because of rapid increasing HSN. The high HSN leads to the surface being covered by a vapor film throughout.

In the same publications, in several experiments, the authors pre-pressurized water on the surface. This leads to the previously unflooded cavities being completely flooded by water, due to increased pressure. Experiments were then completed in similar fashion, as for liquid nitrogen and ethanol above, after removing the pre-pressurization. The authors observed similar boiling behavior in those experiments, again suggesting for this case too, HSN is the mechanism for film boiling. Experiments were also done with water, at atmospheric pressure, under saturation conditions without any pre-pressurization. The authors observed distinct trends in CHF for water, on varying the exponential period. It was seen that CHF for large exponential periods was similar to steady-state CHF. On decreasing the period, till a particular limit (let's call it τ_1[8]), CHF increased with a

[8] This exponential period cannot be directly compared to periods explored in this thesis because the latter describes the rate of linear (and not exponential) increase in current

decrease in period. This was explained on the basis of the time lag in nucleation, as was discussed above, and hence a time lag in the heat transfer crisis that occurs at steady-state CHF [91]. However, as the period is lowered further, the mechanism of CHF changes. For the periods below τ_1, as the wall superheat increases, nucleation from unflooded cavities begins. However, before the nucleation becomes fully developed, the wall superheat becomes such that with the conventional nucleation, HSN also begins. CHF happens due to HSN, for this case. However, HSN happens at a lower CHF than for the periods greater than τ_1. As the period is decreased further, CHF starts to increase. This is because as the rate of power input increases, the rate of increase of wall superheat increases. Hence, it increases the heat flux at which HSN happens. *Thus, in summary, the trend for CHF is as follows: For very high exponential periods, CHF is similar to that of steady-state CHF. On decreasing the period, the CHF first increases till a certain limit of the period. Beyond this limit, CHF decreases due to a shift in the CHF mechanism, which causes CHF. On decreasing the period further, CHF again begins to increase. The same trend is also reported by Park et al [92]. These trends are shown in* Figure 5-2.

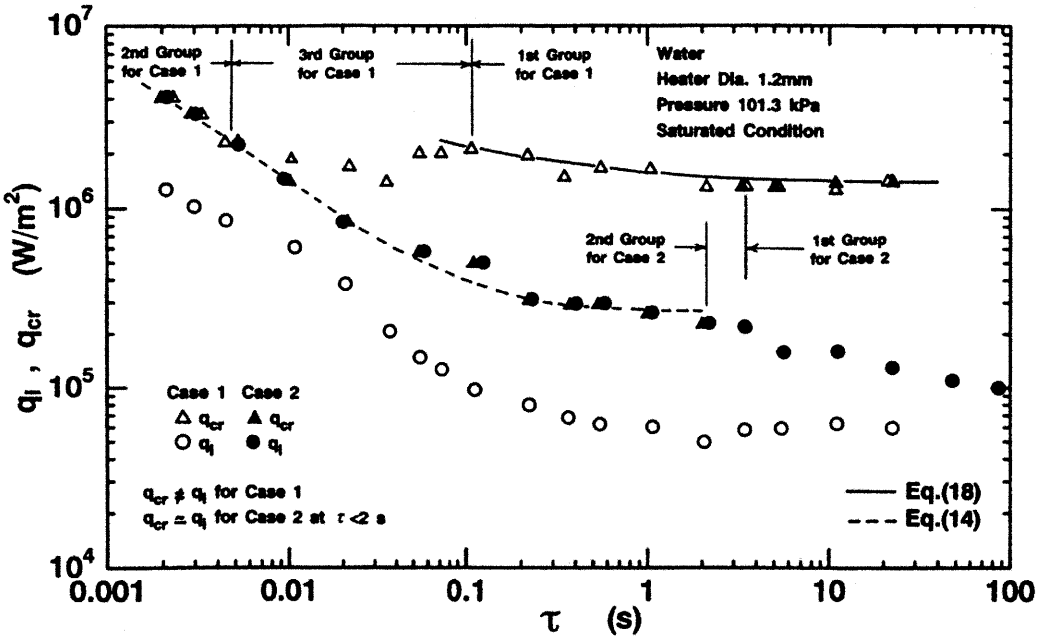

Figure 5-2: Transient CHF trend for saturated water (case 1) showing the initial increase, then decrease, followed by an increase in CHF with decrease in exponential period (from ref. [90])

Fukuda et al suggested several correlations for transient CHF, for various exponential period ranges and different subcoolings [93]. The correlations are as follows:

$$q''_{CHF} = q_{st,sub}(1 + 0.21\tau^{-0.5}) \text{ for high periods at low subcoolings} \quad \text{Eq. 5.1}$$

$$q''_{CHF} = q_{st,sub}(1 + 0.023\tau^{-0.7}) \text{ for high periods at high subcoolings} \quad \text{Eq. 5.2}$$

$$q''_{CHF} = h_c(\Delta T_{in}(\tau) + \Delta T_{sub}) \text{ for low periods} \quad \text{Eq. 5.3}$$

where $q_{st,sub}$ is the quasi-steady state CHF, $h_c = \left(k_l\rho_l c_{pl}/\tau\right)^{0.5} K\left(\frac{\mu D}{2}\right)/K_0(\frac{\mu D}{2}) \cong \left(k_l\rho_l c_{pl}/\tau\right)^{0.5}$ and $\mu = \left[\frac{\rho_l c_{pl}}{k_l \tau}\right]^{0.5}$. K_0 and K_1 are the modified Bessel functions of the second kind of zero- and first-orders. h_c is the heat transfer coefficient resulting from transient heat conduction, $\Delta T_{in}(\tau)$ is the initial boiling surface superheat due to HSN, and ΔT_{sub} is the liquid subcooling.

While all the publications discussed before are for pool boiling experiments, Hata et al also conducted flow boiling experiments on SS304 test tubes, for multiple exponential periods, flow velocities, pressure conditions, inlet and outlet subcoolings, and tube diameters [94]. From their experimental data, they obtained transient CHF correlations including the effects of all parameters, against outlet and inlet subcoolings, as:

Outlet subcooling:

$$Bo = 0.082D^{*-0.1}We^{-0.3}\left(\frac{L}{d}\right)^{-0.1}Sc^{0.7}(1 + 6.34t^{*-0.6})$$

$$\text{for } \Delta T_{sub,out} \geq 30\,K \text{ and } u \leq 13.3\,m/s \quad \text{Eq. 5.4}$$

$$Bo = 0.0523D^{*-0.15}We^{-0.25}\left(\frac{L}{d}\right)^{-0.1}Sc^{0.7}(1 + 6.34t^{*-0.6})$$

for $\Delta T_{sub,out} \geq 30\,K$ and $u > 13.3\,m/s$ Eq. 5.5

Inlet subcooling:

$$Bo = C_1 D^{*-0.1} We^{-0.3} \left(\frac{L}{d}\right)^{-0.1} \exp\left(-\frac{L/d}{C_2 Re_d^{0.4}}\right) Sc^{*C_3}(1 + 11.4t^{*-0.6})$$

for $\Delta T_{sub,in} \geq 40\,K$ and $u \leq 13.3\,m/s$ Eq. 5.6

$$Bo = C_4 D^{*-0.15} We^{-0.25} \left(\frac{L}{d}\right)^{-0.1} \exp\left(-\frac{L/d}{C_5 Re_d^{0.5}}\right) Sc^{*C_6}(1 + 11.4t^{*-0.6})$$

for $\Delta T_{sub,in} \geq 40\,K$ and $u > 13.3\,m/s$ Eq. 5.7

where $C_1 = 0.082$, $C_2 = 0.53$, $C_3 = 0.7$ for $L/d \leq 40$ and where $C_1 = 0.092$, $C_2 = 0.85$, $C_3 = 0.9$ for $L/d > 40$. $C_4 = 0.0523$, $C_5 = 0.144$ and $C_6 = 0.7$ for $L/d \leq 40$ and where $C_4 = 0.0587$, $C_5 = 0.231$ and $C_6 = 0.9$ for $L/d > 40$. Bo, D*, We, Sc, Sc* and t* are boiling number ($=q_{cr,sub}/Gh_{fg}$), non-dimensional diameter ($D^* = d/\left\{\frac{\frac{\sigma}{g}}{\rho_l - \rho_g}\right\}^{0.5}$), Weber number ($=G^2 d/\rho_l \sigma$), non-dimensional outlet subcooling ($=c_{pl}\Delta T_{sub,out}/h_{fg}$), non-dimensional inlet subcooling ($=c_{pl}\Delta T_{sub,in}/h_{fg}$) and the non-dimensional reduced time ($t^* = \tau u/\left\{\frac{\frac{\sigma}{g}}{\rho_l - \rho_g}\right\}^{0.5}$) respectively.

Celata et al also conducted experiments on forced flow critical heat flux during power transients in vertical heated channel of a stainless steel duct, with R-12 flowing inside [95]. They investigated both step- and ramp-power transients. They observed that the power transferred to the fluid at the point of crisis was higher for transients, than for steady-state tests.

Pasamehmetoglu et al developed a theoretical model to predict pool-boiling CHF in exponentially increasing (with time) transient power conditions [96]. They expanded the steady-state CHF theory postulated by Haramura and Katto [15] to include the effects of exponentially increasing heat inputs. According to their model, the decrease of the thickness of liquid macrolayer beneath a vapor mushroom at a surface occurs due to two mechanisms: hydrodynamic instability or evaporation. Incorporating effects of both into the theory of hovering of a vapor mushroom on the surface for a certain time (as postulated by Haramura and Katto), the authors were able to generate correlations for the upper and lower bound of CHF, as a function of the rate of transient (exponential period). The model was in good agreement with the experimental results obtained by Sakurai [88], although Sakurai later suggested the Heterogeneous Spontaneous Nucleation theory, which was different from the assumptions of Pasamehmetoglu's model, as the mechanism for transient CHF [89, 90].

5.2. Motivation

Consistent with results on nanofluid CHF reported in multiple reports and papers, nanofluids were confirmed to enhance the CHF on metallic heaters, compared to DI water. Nanofluids, thus, can potentially help in increasing the power produced by some plants in the current LWR fleet and/or increase their safety margins. However, in order to assess the applicability of nanofluids for use as the ECCS fluid in nuclear reactors, the nanofluid effects on CHF need to be investigated in transient heat flux conditions as well. During accident scenarios in nuclear reactors, such as rod ejection event, a step input of reactivity occurs, which can result in rapid power excursions in nuclear reactors. The rate of this excursion is faster for a larger increase in reactivity. Thus, it is imperative to understand if/what effects do nanofluids have on CHF in such conditions. Additionally, as was concluded from the steady state experiments in this thesis, the nanocoating thickness on the heater surfaces plateaus in times less than the time required for a steady

state test without any pre-boiling (~30 – 40 min). Therefore, it is of interest to know the magnitude of the deposition occurring (if any) on the heater surface, for tests, which last for a much shorter time. Thus, in this section of the thesis, we conduct transient flux/power experiments where heat flux on the heater surface is increased from 0 to CHF in t_o = 1, 10 and 100 s[9], to investigate what effects nanofluids have on CHF on heaters with such power transients, and what are the time frames of efficient nanoparticle deposition on the heater surface.

5.3. Test Procedure

The test procedure for transient tests is the same as that for steady-state tests discussed in Section 4.2, with slight modifications for the 'Heat up to CHF' and 'Data Reduction' steps, as discussed here.

5.3.1. Heat up to CHF

Once the heater is loaded in the PBF and its initial resistance R_{100} is calculated, current supplied by the Genesys power supply is linearly increased from 0 to 450 A in time t_o sec. This is achieved by remotely programming the power supply, to provide controlled current outputs (linearly increasing function of time), by triggering it with a function generator (FG). The FG is used to output a voltage signal between 0 and 10 V to the power supply. The FG output serves as an input to the power supply, to control the output current between its minimum and maximum possible values. In other words, the current provided by the power supply varies linearly between 0 and 500 A, with output current equal to 0 A when the input voltage from the FG is 0 V and the output current being 500

[9] The details of the procedure to achieve this are discussed in Section 5.3 later

A when the input voltage from the FG is 10 V. The FG was set up to provide a triangular wave of half-amplitude 9V and time periods 4, 40 and 400 s, respectively to obtain currents increasing linearly between 0 and 450 A in 1, 10 and 100 s respectively[10]. Thus the variation of current with time can be written as

$$I = 450\frac{t}{t_o}$$

where t_o = 100, 10, 1 s. The FG used was a Rigol DG1022 2 Channel Function/Arbitrary Waveform Generator. **Figure 5-3** shows the function generator used in the experiments.

Figure 5-3: Photograph of the function generator to program the power supply for providing desired current outputs

Before running the experiments, the set-up was tested to verify the output currents for different time periods of the FG output[11]. After the current output was verified, this set-up

[10] The control FG voltage input to the power supply cannot go negative, else it might damage the power supply

[11] The results of the verification exercise are shown in Appendix A

was used for the experiments. On linearly increasing current, the power produced in the heater (and the flux transferred to the fluid) starts to increase until at one value CHF occurs, which terminates the experiment. As CHF occurs at a current lower than 450A, for all transients, the actual time-to-CHF is smaller than t_o.

5.3.2. Data Recording and Analysis

Since transient tests last much shorter, compared to the steady state tests, data has to be recorded much faster for an accurate calculation of CHF. The Agilent 34980A system with the 34921T card is unable to accurately capture data at as fast rates as required for transient tests. Hence, a different DAS was used for data acquisitions here: Agilent U2542A USB Simultaneous Sampling Multifunction Data Acquisition Device. This unit is capable of recording 4 channels simultaneously, up to a speed of 500 kSa/s[12]. It has 34 pairs of pins, with positive pins numbered 1 – 34 and their respective negative pins numbered 35 – 68. Pins 1 – 4 and 35 – 68 measure the differential positive and negative inputs, respectively, for the 4 different channels that are made simultaneously. It has four different programmable unipolar input ranges: 0 to 1.25 V, 0 to 2.5 V, 0 to 5 V and 0 to 10 V, respectively. **Figure 5-4** shows the U2542A unit used.

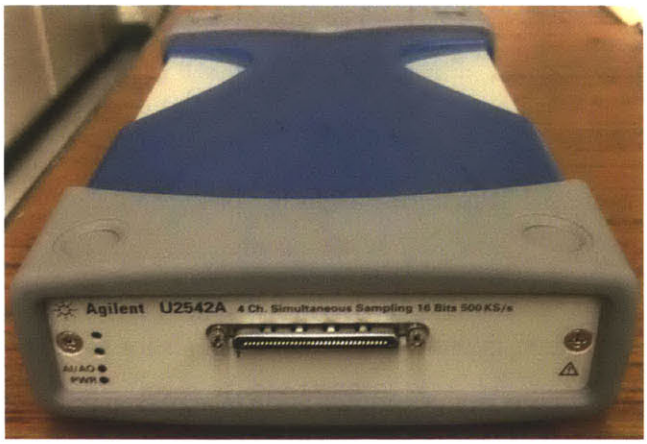

Figure 5-4: Photograph of the U2542A unit used for data acquisition during transient tests

[12] kSa/s means kilo-samples per second

Out of the 4 pin pairs capable of measuring differential inputs, three are used for acquiring data in the transient tests. The pin pair 1-35 measures the instantaneous potential drop across the sample, i.e. ΔV, and pin pair 2-36 measures the instantaneous potential drop across the shunt used in the circuit, i.e. ΔV_{shunt} (to be converted into current measurement by dividing by the shunt resistance). However, since ΔV_{shunt} is normally very low (< 50 mV throughout the experiment), in order to increase the accuracy of measurements, ΔV_{shunt} is amplified by using a Current Shunt Monitor (CSM) powered by an external power supply. The pin pair 3-37 is used to measure this amplified ΔV_{shunt}. The CSM used is a Texas Instrument INA210 model, which has a fixed gain of 200[13]. **Figure 5-5** shows the pin configuration for the CSM. It has 6 pins. Pins 1 and 2 are connected to ground, which serves as the reference potential. To amplify the shunt voltage signal, the CSM is powered by an external power supply with a voltage of 12V. The external battery is connected between pins 3 and 1. Pins 4 and 5 are connected to the +ve and –ve ends of the shunt. The amplified output is obtained between pins 6 and 1. Using this arrangement, the shunt potential drop is amplified by a factor of 200. This amplified signal is also measured by the U2542A DAS, by the pin pair 3-37.

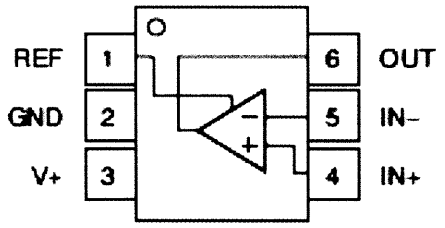

Figure 5-5: Pin configurations for the INA210 CSM

During the experiments, data is recorded every 1 ms (from start of experiment to CHF); potential difference across the heater, potential drop across shunt, and the amplified shunt potential drop are measured. Using the achieved gain, the amplified shunt potential drop,

[13] Verification of CSM amplification, to compare achieved gain with the expected gain, is discussed in Appendix A

and the shunt resistance, the instantaneous current passing through the circuit is calculated. The instantaneous resistance and heater bulk temperature (T_{bulk}) are calculated exactly as described for steady state tests. In order to smoothen the data, and reduce the noise associated with the extremely fast data measurement, the current, ΔV, resistance and temperature calculations are averaged over fixed time periods of 1000 ms, 200 ms and 25 ms, respectively, for tests with t_o = 100, 10 and 1 s, respectively. Denoting these as $\bar{I}$, $\overline{\Delta V}$, $\bar{R}$ and $\bar{T}_{bulk}$, the averaged power power generated in the heater, over that time period, is calculated as

$$\bar{q} = \bar{I}(\overline{\Delta V})$$

Then, the average heat flux (for that time period) transferred to the fluid is calculated. One key point to note here is that because of the short time scales of the transient experiments, the measurement of CHF is not as straightforward as for steady state experiments; heat flux is calculated using the time derivative of the first law of thermodynamics in the following manner.

$$\dot{U} = \dot{Q} - \dot{W}$$

where $\dot{Q}$ is the power supplied to the heater ($-\overline{q''}$s in this case), $\dot{U}$ is the rate of increase of internal energy stored in the heater ($MC_p\frac{dT}{dt}$) and $\dot{W}$ is the rate of work done by the heater ($-I\Delta V$). The time gradient of $\bar{T}_{bulk}$ ($\Delta\bar{T}_{bulk}/\Delta t$) is calculated by dividing the difference between two successive values of $\bar{T}_{bulk}$ by the time difference between these measurements (= 1000/200/25 ms). The instantaneous heat flux is then calculated by rearranging the first law as

$$\frac{v}{s}\left(\frac{\bar{I}(\overline{\Delta V})}{v} - \rho C_p \frac{\Delta\bar{T}_{bulk}}{\Delta t}\right) = \overline{q''}$$

where v is the heater volume, s is the heat transfer area, ρ is the density, and C_p is the specific heat capacity of the heater material. Following this procedure, the averaged flux over the course of the experiment is calculated.

5.3.2.1. Definition of CHF

Figure 5-6 plots the power generated in the heater ($\bar{I}\,\overline{\Delta V}$), rate of sensible heat stored in the heater ($v\rho c_p \frac{\Delta \bar{T}_{bulk}}{\Delta t}$), the time gradient of bulk heater temperature ($\frac{\Delta \bar{T}_{bulk}}{\Delta t}$) and heat flux ($\overline{q''}$) during the progression of a transient experiment with t_o =1 s. The point in time where the value of $\frac{\Delta \bar{T}_{bulk}}{\Delta t}$ abruptly increases is defined as the point of occurrence of CHF. This is marked by the vertical solid line on the plot. This definition is further validated from the part of the plot beyond this point, where heat flux decreases in spite of $\frac{\Delta \bar{T}_{bulk}}{\Delta t}$ continuing to increase, indicating a sharp decrease in HTC due to a change in boiling mechanism from nucleate to film boiling.

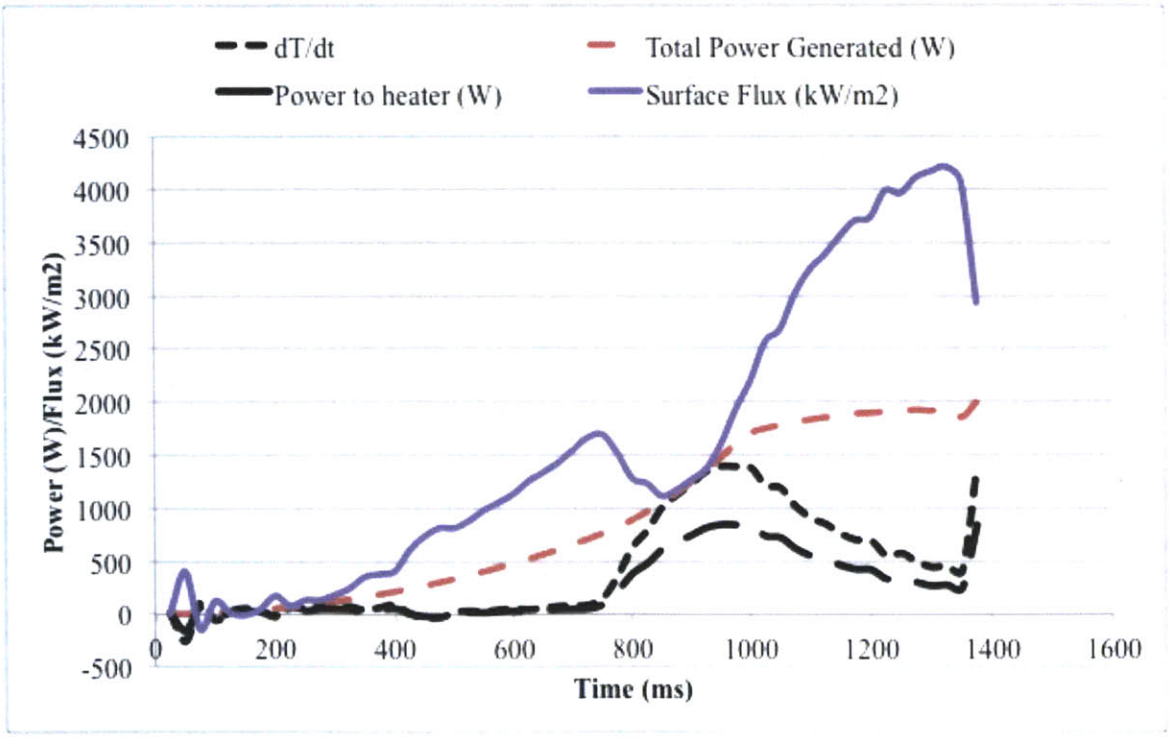

Figure 5-6: Progress of a transient experiment with t_o = 1 s. The vertical solid line is defined as the point where CHF happens

5.4. Test Matrix

The test matrix for the transient was discussed in Section 1.3 and summarized in **Table 1-4**. The sandblasted surface heaters were chosen as the test heaters for the transient experiments. Three values of the parameter t_o are explored in this thesis (t_o = 100, 10 and 1 s). The 100 s experiments serve as the quasi-steady state experiments due to a slow rate of increase of power. The 10 s and 1 s experiments are representative of fast transients. Since the nanocoating developed during boiling is responsible for increasing the CHF, experiments are also done by nanocoating the heater by keeping the heaters at a fixed flux for certain time. The value of nanocoating heat flux was kept the same as that for the pre-boiling in steady state tests (250 kW/m^2). Since the nanocoating was observed to plateau within 30 – 40 min of boiling time, a pre-boiling time of 60 min was chosen. For both the heater surfaces (sandblasted and sandblasted with nanocoating), experiments with DI water serve as the base case and experiments with test-nanofluid are conducted to investigate the effects of nanofluid on transient CHF.

5.5. Results

Transient tests on the uncoated sandblasted heaters were run for the three values of the parameter t_o. Multiple tests were run for each t_o to ensure repeatability. **Table 5-1** summarizes the results for these tests. The DI water CHF increased from 548.5 kW/m^2 for t_o = 100 s, to 806.66 kw/m^2 and 1497.33 kW/m^2 for t_o = 10 s and 1 s, respectively. It is seen that the DI water CHF for the slowest transient tests (quasi steady-state) is similar to the steady state CHF. However, increasing the rate of the transient increases the CHF for DI water. **Table 5-1** also shows results for the tests for uncoated heaters with nanofluid.

For t_o = 100 s, the CHF was seen to increase to 627.75 kW/m^2 compared to 548.5 with DI water. For t_o = 10 s, the CHF values were 1094 kW/m^2, which is more than 806.66 kW/m^2 for DI water. However, for t_o = 1 s, nanofluid CHF was seen to be similar to that of DI water (1536.5 kW/m^2 compared to 1497.33 kW/m^2).

Table 5-1: Results for transient tests on uncoated heaters for various values of t_o

Experiment No.	**Heater**	**Test-Fluid**	**t_o (sec)**	**Average CHF (kW/m^2)**	**Standard Deviation in CHF (kW/m^2)**
Tr_DIW100	Sandblasted	DI water	100	548.5	24.75
Tr_DIW10	Sandblasted	DI water	10	806.66	9.86
Tr_DIW1	Sandblasted	DI water	1	1497.33	154.11
Tr_NF100	Sandblasted	0.01 v% ZnO	100	627.75	37.29
Tr_NF10	Sandblasted	0.01 v% ZnO	10	1094	50.65
Tr_NF1	Sandblasted	0.01 v% ZnO	1	1536.5	31.82

In the next phase of the transient tests, sandblasted heaters were nanocoated through boiling in nanofluid for 1 hour. These heaters were used for similar experiments as summarized in the table above. Table 5-2 shows the results for these experiments. For DI water tests, compared to uncoated heater tests, an enhancement in CHF was observed for tests with nanocoated heaters. For t_o = 100/10/1 s, CHF for nanocoated heaters for DI water was seen to increase to 750/1173/1999 kW/m^2 compared to 548.5/806.66/1497.33 kW/m^2 for uncoated heaters. This translates into a percentage enhancement of 36.49/ 45.53/33.33 %. Repeating the same experiments with nanofluid, CHF for nanocoated heater was 822/1214/1954 kW/m^2 (an enhancement of 50/50.06/30.52 %).

Table 5-2: Results for transient tests on nanocoated heaters for various values of t_o

Experiment No.	Heater	Test-Fluid	t_o (sec)	Average CHF (kW/m^2)	Standard Deviation in CHF (kW/m^2)
TrNC_DIW100	Sandblasted, nanocoated for 1 hour	DI water	100	750	45.25
TrNC_DIW10	Sandblasted, nanocoated for 1 hour	DI water	10	1173	18.38
TrNC_DIW1	Sandblasted, nanocoated for 1 hour	DI water	1	1999	111.72
TrNC_NF100	Sandblasted, nanocoated for 1 hour	0.01 v% ZnO	100	822.5	71.42
TrNC_NF10	Sandblasted, nanocoated for 1 hour	0.01 v% ZnO	10	1214	72.12
TrNC_NF1	Sandblasted, nanocoated for 1 hour	0.01 v% ZnO	1	1954	156.98

5.6. Post-Test Surface Analysis

Figure 5-7 and **Figure 5-8** are post-test SEM images of uncoated heaters used for the 100 s and 10 s nanofluid transient tests, respectively. Both these figures show clear evidence of ZnO nanoparticles depositing on the heater surface. However for 1 s transient tests, due to the extremely high rate of power increase, the entire heater element gets oxidized and damaged. Therefore it was not possible to conduct post-test analyses on those heaters. Hence, additional tests were conducted keeping the rate of current increase the same as that for 1 s tests but shutting the power supply when the heat flux reached a value of 75% of CHF obtained for the 1 s transient tests (Tr_NF1), to obtain heaters

representative of the 1 s transient tests. **Figure 5-9** is a post-test SEM image of the representative heater, showing a clean surface similar to the surface of sandblasted heaters used with DI water tests. **Figure 5-10** shows the EDX data collected from the representative heater. The lack of Zn signal in this figure confirms that nanocoatings are unable to develop in such short time frames.

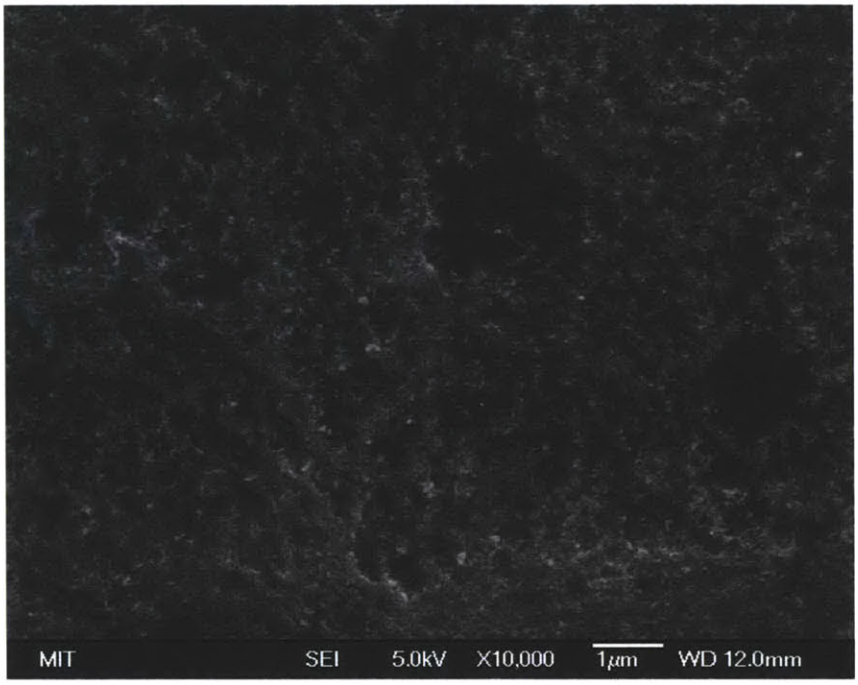

Figure 5-7: Post-test SEM image of heater used for Tr_NF100

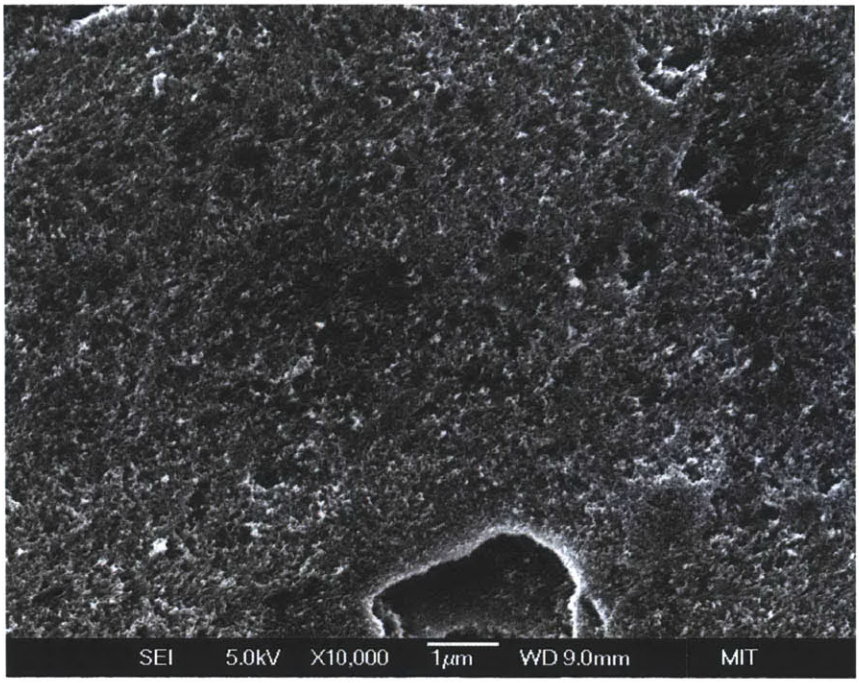

Figure 5-8: Post-test SEM image of heater used for Tr_NF10

Figure 5-9: Post-test SEM image of heater representative of 1 s transient test

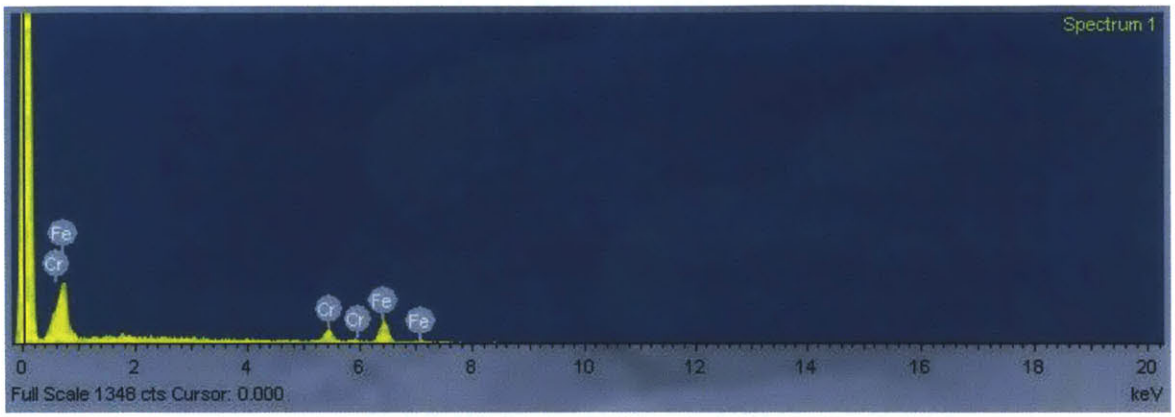

Figure 5-10: EDX data from the heater representative of 1 s transient test. The absence of Zn signal confirms that there are no nanocoating deposits formed in such short time

Figure 5-11 and **Figure 5-12** show the confocal scans from the uncoated heaters used for 100 s and 10 s nanofluid transient tests, respectively. The scans show evidence of a slight change in the texture of the heaters due to the ZnO nanoparticle deposition. **Figure 5-13** is a confocal scan for the heater representative of 1 s transient test. Multiple measurements for the surface roughness on uncoated heaters tested in nanofluid were carried out. Additionally, the thickness of the nanocoating was also measured in the same way as described in **Figure 4-64**. **Table 5-3** shows the R_a and the nanocoating thickness for various heaters. The R_a values for the 100 s and 10 s tests were 2.65 μm and 0.97 μm, respectively. These values are of the same magnitude as that for the steady state tests, and comparable to the roughness values of the uncoated heaters. The average thickness of the nanocoatings is seen to be very low: 0.063 μm and 0.044 μm, respectively, compared to ~1 μm for steady state tests.

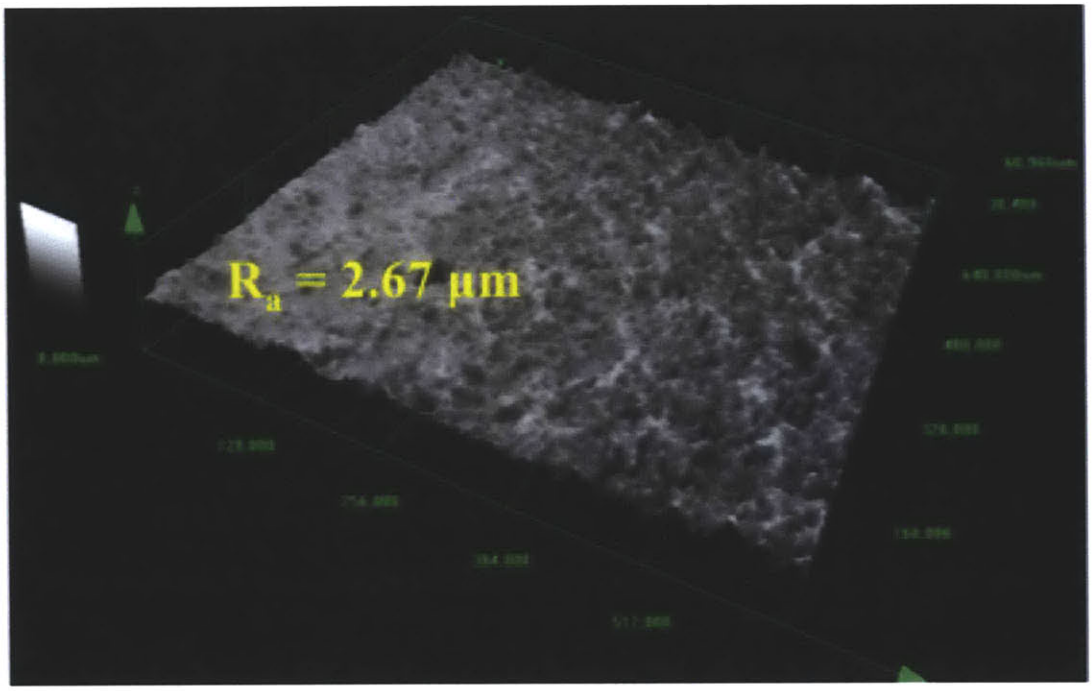

Figure 5-11: Confocal scan for heater used for Tr_NF100 (R_a = 2.67 μm)

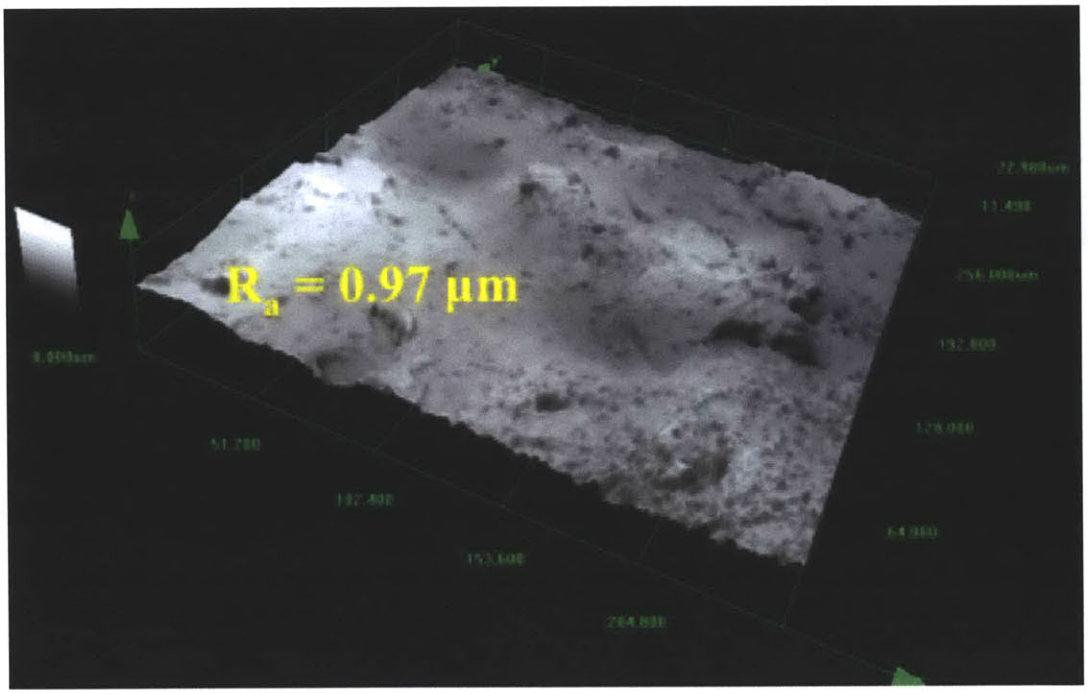

Figure 5-12: Confocal scan for heater used for Tr_NF10 (R_a = 0.97 μm)

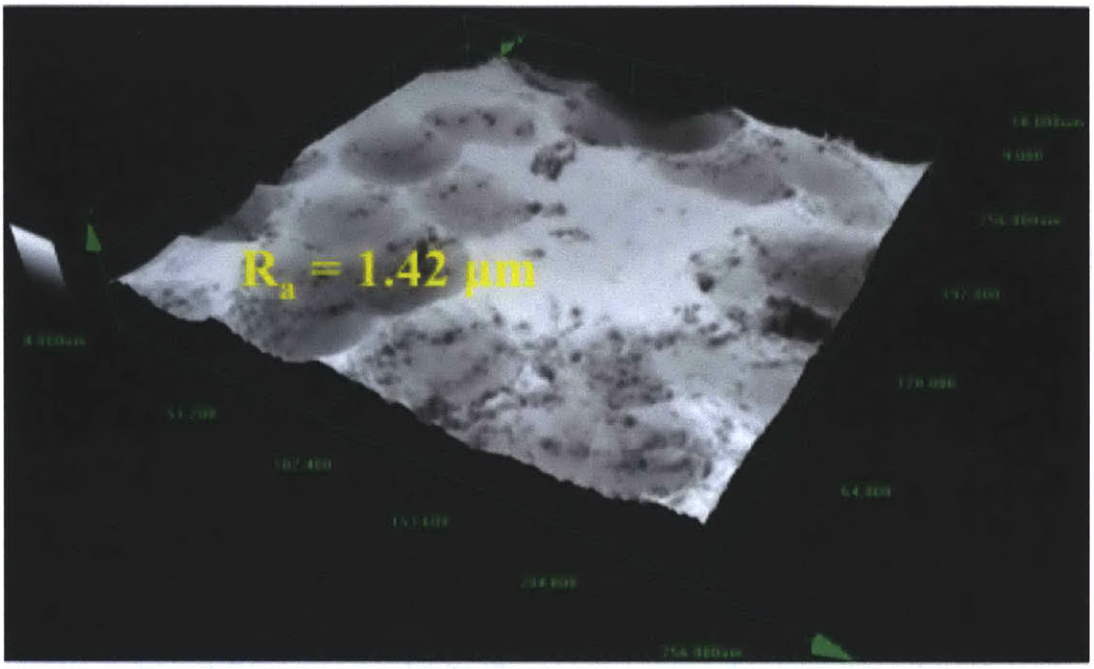

Figure 5-13: Confocal scan for heater representative of 1 s transient test (R_a = 1.42 μm)

Table 5-3: Summary of confocal microscopy data for uncoated sandblasted heaters tested with nanofluid for various transient tests

Experiment No.	**Heater**	**Test-Fluid**	**t_o (sec)**	**R_a (μm)**	**Avg. Nanocoating Thickness (μm)**
Tr_NF100	Sandblasted	0.01v% ZnO	100	2.67 2.65	0.063
Tr_NF10	Sandblasted	0.01v% ZnO	10	0.92 0.92	0.044
Tr_NF1	Sandblasted	0.01v% ZnO	1	1.43 1.51	-[14]

[14] Since there is no nanoparticle deposition for the 1s transient tests, there is no nanocoating thickness to be measured

Figure 5-14 shows the static contact angle of water on heaters used for transient tests, with nanofluid. The measurements show that, similar to steady-state tests, nanocoating increases the wettability of the heaters for the 100 s and 10 s transient tests too. However, there is no appreciable change in wettability of heater used in the shortest (1 s) transient test.

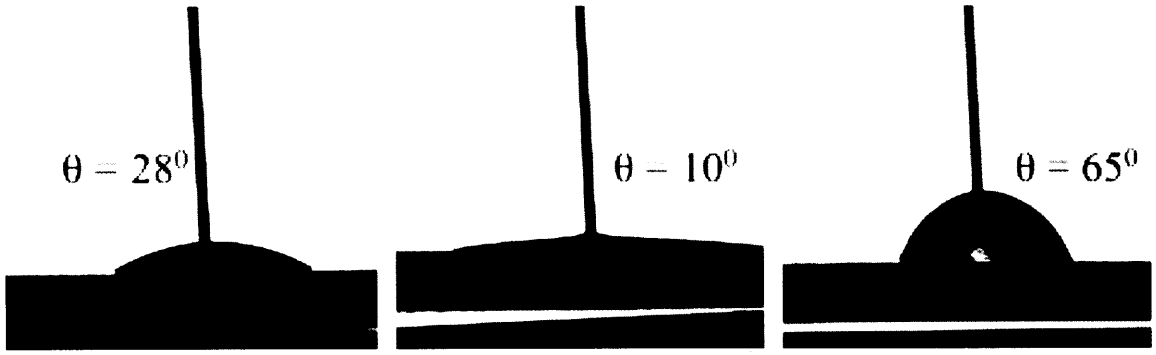

Figure 5-14: Static contact angle of droplet of water on heaters used for Tr_NF100 (left), Tr_NF10 (center) and heater representative of 1 s transient test (right)

5.7. Summary/Discussion of Transient Test Results

Multiple experiments were done to analyze the effects of nanofluids on transient CHF, using uncoated sandblasted heaters as well as sandblasted heaters coated with nanofluid for 1 hour, for three rates of transient. Base case CHF was obtained by running the experiments with water. It was seen that the CHF for quasi-steady state experiments (548.5 kW/m^2 (std. dev. = 24.75 kW/m^2)) was similar to that of the steady-state experiments (511.5 kW/m^2 (std. dev. = 17.68 kW/m^2)). On increasing the rate of the

transient, CHF for DI water is seen to increase to 806 (std. dev. = 9.86 kW/m^2) and 1497 kW/m^2 (std. dev. = 154.11 kW/m^2)) for the faster and the fastest transient. These trends are in agreement with the trends for exponential power transients reported in literature [89-92]. A direct comparison with the CHF values reported for those studies is not possible because these publications have an exponentially increasing heat input, whereas in this work the current is increased linearly, thus, power increases approximately as the square of the time.

For the experiments for uncoated heaters with nanofluid, heaters with t_o = 100 and 10 s, CHF is enhanced to 627 (std. dev. = 37.29 kW/m^2) and 1094 kW/m^2 (std. dev. = 50.65 kW/m^2), which translates to a 14.41% and 35.73% enhancement compared to DI water. However, for t_o = 1 s, nanofluid does not lead to an appreciable CHF enhancement (1536 kW/m^2 (std. dev. = 31.82 kW/m^2) compared to 1497 kW/m^2 (std. dev. = 154.11 kW/m^2) for DI water). Post-test SEM imaging confirmed that ZnO nanoparticles start to coat on the heater even for tests that last as short as 10 and 100 s. The nanocoating was also confirmed by confocal microscopy. However, the thickness of nanocoatings for these transients is ~0.05 μm. This thickness of nanocoatings is much smaller than that for the steady state tests, which have coating thickness between 0.5 and 1 μm. These observations indicate that even for short transients, some amount of nanocoating develops on the boiling surface. Although time frames as short as 1 s are not enough for nanocoating to develop, 10 s and 100 s are enough time for nanocoating development to begin and effect boiling and CHF. The nanocoating thickness is lesser than that for the much longer steady state tests, as expected. The nanocoatings are able to enhance the CHF compared to water, though by not as high extents as for steady state tests. Thus it is concluded that the nanocoating thickness saturates between the experiment times of 100 s and 30 min. Contact angle measurements show that, even though the thickness of the nanocoatings developed in the 100 s and 10 s tests is not high, they lead to the surface becoming porous and hydrophilic, which is consistent with the observation of an enhanced CHF. Although the time for nanocoating development is longer for the 100 s tests, compared to the 10 s tests, the contact angle on heaters tested for 100 s tests is

higher. This indicates that the microstructure and porosity of the nanocoatings developed in these heaters could be different. Heaters in 10 s tests are subjected to higher heat fluxes (maximum of ~1000 kW/m^2) compared to 100 s tests (maximum of ~600 kW/m^2). This difference in the heat fluxes during nanocoating development could be a likely cause for the difference in the manner of nanocoating self-assembly, and hence different extent of wettability and porosity change for the 100 s and 10 s transient tests. Consistent with the confocal and SEM measurements, heaters used for 1 s tests did not show a change in their wettability over the course of the experiment, again confirming the absence of a nanocoating (and any accompanying change of the heater surface).

On nanocoating the heater at 250 kW/m^2 for 1 hour, the CHF for DI water is increased 36, 45 and 33 % for transients with time period of 100, 10 and 1 s, respectively. Using nanofluids gives a similar enhancement. Thus, it is evident that the primary reason for the CHF enhancement is the nanocoating developed during the 1-hour boiling period.

From these results, we see that nanofluids can be quite useful, and have a higher CHF compared to water, in accident scenarios in nuclear reactors if the time frames of the transients is 10 s or longer. However, if the surface of the heater is changed through processes similar to nanocoatings developed during boiling, the enhanced wettability and porosity of the surface can lead to higher CHF even for DI water during emergency scenarios consisting of rapid power transients.

6. Conclusions, Major Contributions and Future Work

6.1. Conclusions

Critical heat flux poses a thermal limit on the operating power of nuclear reactors. Increasing the CHF, by addition of nanoparticles to the coolant water, can increase the safety margins of nuclear reactors and/or allow higher power output from the reactors. Several previous investigations at MIT and elsewhere have confirmed the enhancement in CHF on using nanofluids. The enhancement has been reported for varying concentrations of nanoparticles in the nanofluids, and both for pool and flow boiling conditions. However, there are significant gaps and discrepancies in the nanofluid boiling and CHF results reported by various researchers.

This works was aimed at carrying out a detailed investigation of the effects of three parameters – initial surface roughness, initial surface wettability, and pre-boiling time – on nanofluid CHF in steady state. To achieve the objectives, a pool boiling facility was designed and more than 60 tests were completed to measure CHF for varying surface/fluid combinations. Metallic heaters consisting of SS304 material were oriented vertically in a boiling pool for the experiments. The nanofluids used in the experiments were 0.01v% ZnO in DI water. CHF for DI water was measured as the base case, and CHF for nanofluids was measured to quantify the effects of nanofluids, compared to DI water, on CHF. The conclusions of the steady state experiments are as follows:

1. With DI water, both the rough (sandblasted) and smooth surfaces have the same value of CHF of ~500 kW/m^2.

2. On using nanofluids, the CHF for both surfaces was seen to increase dramatically. However the enhancement for sandblasted heaters was much higher (160%) than for the smooth heaters (68%).

3. All the heaters boiled in nanofluid show the presence of nanocoating of the ZnO nanoparticles at the surface. The nanocoatings are highly porous, and act to change the wettability as well as the roughness of the heater surfaces. This porosity and enhanced wettability are responsible for an enhanced CHF. Differences in the CHF values for sandblasted and smooth heaters indicate potentially different microstructure and porosity of the nanocoatings developed on these surfaces during boiling.

4. On pre-coating the heater surfaces with LbL coatings consisting of SiO_2 nanoparticles, the heater wettability was seen to increase significantly. Additionally, these coatings have been previously shown to be porous. Thus, the LbL coatings enhance the porosity and wettability of the surface, and are able to enhance the CHF of water to 650 kW/m^2 from 500 kW/m^2. However, owing to the lower thermal conductivity of SiO_2, the LbL coatings add an additional thermal resistance at the surface. Thus, the enhancement with nanofluids for the LbL coated is not as significant as for uncoated heaters.

5. Allowing more time in addition of the 30 – 40 minutes required for the steady state tests for development of nanocoatings did not add to the CHF enhancement observed for no pre-boiling time. Additionally, the thickness of the nanocoating developed was seen to plateau in the initial 30 minutes of the experiment. The nanocoating thickness was higher for smooth heaters than for sandblasted heaters, again indicating a difference in the development and microstructure of nanocoatings.

In addition to steady state CHF effects, this thesis also investigated the potential of nanofluids in cooling systems such as nuclear reactors, during accident conditions that

are accompanied by rapid power excursions. The flux through the heater was increased from 0 to CHF in t_0 = 1, 10 and 100 s, to investigate the effects of these three rates of power increase on CHF. Close to 30 transient power tests were conducted to investigate the CHF behavior for 4 fluid-heater surface combinations. The conclusions from the transient tests are:

6. Increasing the rate of transients led to an increase in CHF of DI water.

7. Nanofluids did not impact the CHF for the shortest transients (t_0 = 1 s). However, transient nanofluid experiments with t_0 = 10 s and 100 s both showed an enhanced CHF (35% and 16% enhancements, respectively). Post test analyses showed that even time frames as short as 10 s and 100 s were sufficient for slight nanocoating to develop on the heater surface, increasing the CHF.

8. Using heaters pre-coated with ZnO nanocoating (by pre-boiling), CHF was seen to have enhanced for all three rates of transients, again confirming the presence of nanocoatings as the primary mechanism for CHF enhancement.

6.2. Major Contributions

1. To measure the CHF for varying heater surface/fluid combinations, a pool boiling facility was built.
    a. The designed PBF allows flexibility in choosing heater dimensions.
    b. Generated more than 60 data set values for steady state tests, investigating the effects of initial heater roughness and wettability as well as pre-boiling time on nanofliud-induced enhancement of CHF.

2. A first of its kind experimental study was done to examine the effects of nanofluids on CHF over extremely rapid transients. This investigation explored the necessary time frames required for appreciable nanocoatings to develop on heater surfaces and affect CHF. Such an investigation of rapid transient nanofluid CHF has not been done in any previous experimental research.

3. CHF enhancement seems to correlate well with the development of a nanocoating, which is porous and increases the wettability of the boiling surface.

6.3. Recommendations for Future Work

The results obtained in the thesis can lead to several directions of future work.

1. The impact of altering the chemistry of the nanofluids on nanocoating development and effects on CHF should be investigated in more detail. For instance, additional chemicals present in nuclear reactors such as boron and tri-sodium phosphate could affect the process of nanocoating development, and hence the CHF. Moreover, it cannot be ruled out that they might completely prevent the development of nancoatings as observed by Yang et al for functionalized nanoparticles [47].

2. Since the development of the nanocoating is seen to plateau after approximately 30 min of boiling time, the cross-sectional microstructure of the nanocoatings should be studied to understand possible reasons that could lead to the inability of more nanoparticles to adhere to the surface of the heater after the nanocoating reaches a certain thickness.

3. Primarily, as it was seen that the process of nanocoating development plateaus somewhere between 100 s and 30 – 40 min of boiling time, more investigations of transient experiments should be conducted with time frames of experiments lying between these limits to deduce the precise amount of time required to develop the effective nanocoatings. However, this time likely depends on several other parameters, such as nanoparticle concentration, nanoparticle material, heater surface conditioning, nanofluid chemistry etc.)

4. Additional transient experiments with an exponentially increasing heat input can also be conducted with nanofluids. Such an exercise will facilitate direct CHF comparisons with those for water, reported in literature. As such, the transient experiments could also include variations in subcooling and pressure conditions too.

5. Photographic studies of the heater surface using high speed video should be carried out to understand the mechanism of transient CHF for nanofluids. The mechanisms for transient CHF for DI water have been previously reported in literature [90-93], and this exercise could provide a useful comparative study for CHF mechanisms for DI water and nanofluids during power transients.

6. More tests for the shortest transients should be conducted with an increased concentration of nanofluids, to investigate if larger amounts of nanoparticles present in the solution make a difference to the development of nanocoatings for time frames as short as 1 s.

7. Appendix A

7.1. Temperature Coefficient of Resistivity (TCR) for SS304

In order to obtain the instantaneous bulk temperature of the heater from its instantaneous resistance, it is required to know its TCR. The TCR for SS304 is determined experimentally. For this purpose, the resistance of the SS304 heater element was determined experimentally at multiple temperatures. The resistance measurement was done by using the 4-point probe method. For the resistance measurement, a new set-up was constructed. Here, two wires (called outer wires) were spot-welded to the heater element, at a separation of 48 mm from each other. In between these two contacts, two additional wires (called inner wires) were spot welded, with a separation between those welds being 30 mm. This heater element (shown in **Figure 7-1**) is immersed in a bath of ethylene glycol, maintained at temperature T, and is allowed to sit in it for ~15 min allowing for the entire heater to attain the bath temperature. The outer wires are connected to a power supply and 1 A of current is passed through them. The inner wires are connected to the DAS, which measures the potential drop across them, cause by the passing current. From the current and voltage measured, the resistance of the heater (30 mm length) is measured at temperature T. This resistance is denoted as R_T Multiple values of R_T are obtained by varying the temperature of the ethylene glycol. Denoting the heater resitance at room temperature as R_0, the TCR for the heater, denoted by α, is then obtained at each temperature by using the relation

$$\alpha = \frac{1}{(T-T_0)} \frac{(R_T-R_0)}{R_0} \quad \text{Eq. 7.1}$$

Eventually, the average of all values of α is used as the TCR for SS304.

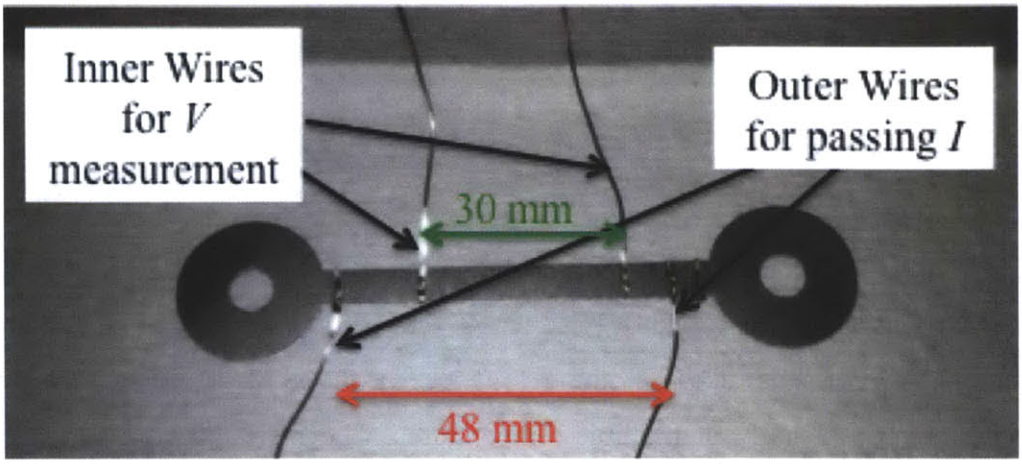

Figure 7-1: Photograph of the heater used for the TCR measurement

These measurements were repeated twice. **Table 7-1** and **Table 7-2** show the data obtained for both the measurements. **Figure 7-2** is a plot of both the sets of data.

Table 7-1: Data for TCR measurement #1

T (^{0}C)	R_T	TCR (1/^{0}C)
24	0.004731384	-
40	0.004817365	0.001135769
60	0.004928963	0.001159979
80	0.005043529	0.001178095
85	0.005068446	0.001167861
90	0.005098858	0.001176776
95	0.005127904	0.00118037
100	0.005153598	0.001174168
110	0.005205217	0.001164496
Average		**0.001167189**

Table 7-2: Data for TCR measurement #2

T (^{0}C)	R_T	TCR (1/^{0}C)
23	0.004720691	
40	0.004816233	0.001166908
60	0.00492949	0.001171706
80	0.005039798	0.001162398
90	0.005098253	0.001170054
100	0.005150551	0.001159122
110	0.005215412	0.001180683
Average		**0.001168479**

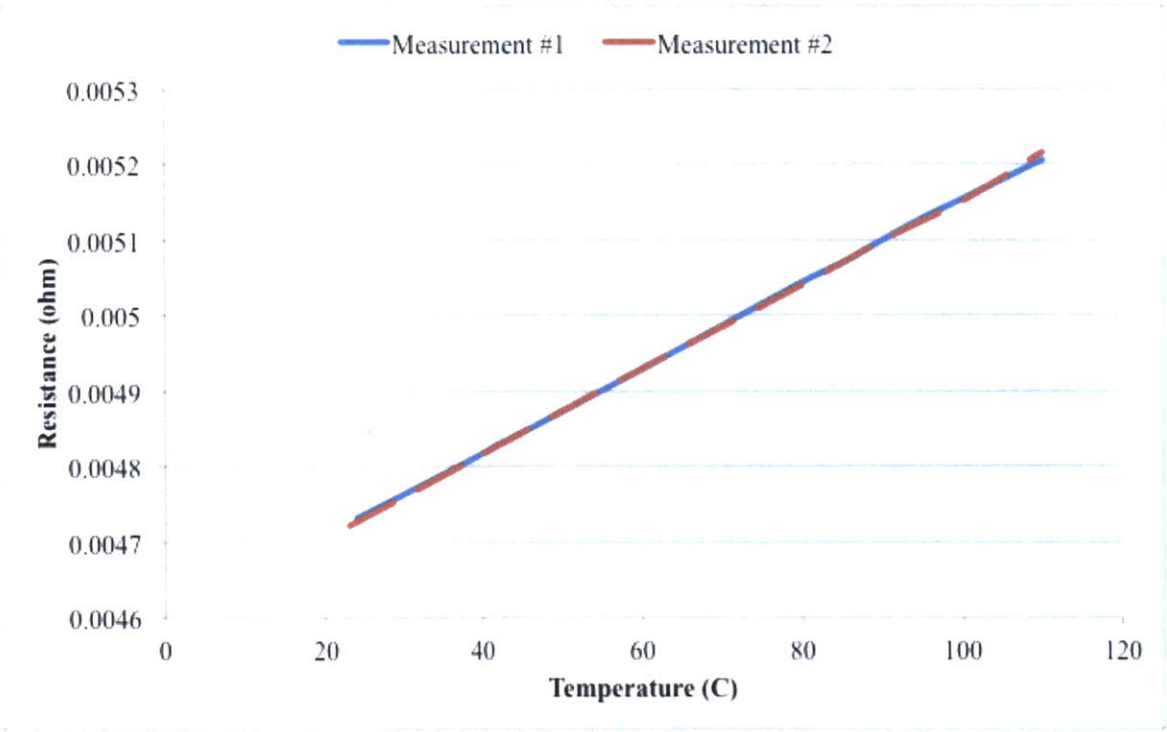

Figure 7-2: Plots of TCR measurement data (both sets)

Thus, further taking an average of the two averaged TCRs gives us the value of TCR used for SS304 in this thesis as 0.001167834/^{0}C (the standard deviation in the measured TCR values was 4.559 x 10^{-7} /^{0}C).

7.2. Relationship between T_{bulk} and T_w

The steady-state situation for the heater-fluid combination can be depicted as shown in **Figure 7-3**.

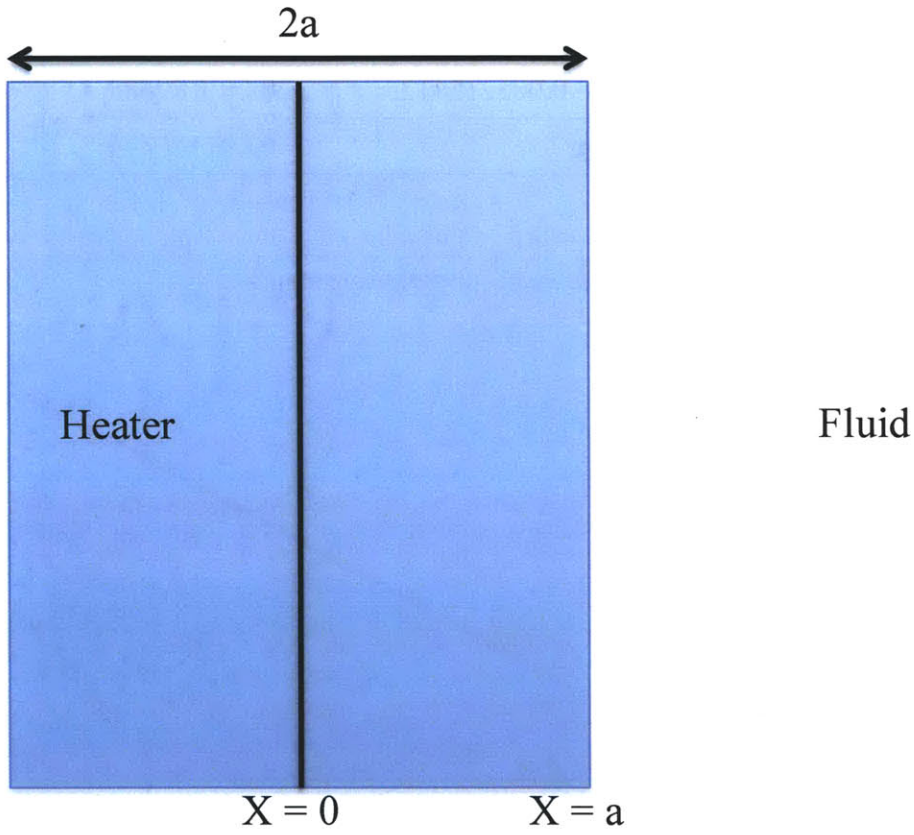

Figure 7-3: Pictorial representation of the heater-fluid combination

The 1-dimensional steady-state heat conduction equation is

$$\frac{d}{dx}\left(k\frac{dT}{dx}\right) + q''' = 0$$

On integrating, we get

$$k\frac{dT}{dx} = -q'''x + A$$

where A is a constant of integration.

Now, we have the boundary condition:

$$\left.\frac{dT}{dx}\right|_{x=0} = 0$$

which yields, $A = 0$

Thus we get

$$k\frac{dT}{dx} = -q'''x$$

Integrating it again and assuming the thermal conductivity to be constant, we obtain

$$kT(x) = -q'''\frac{x^2}{2} + B$$

where B is another constant of integration.

Now,

$$\rho A_{surface} c_p a T_{bulk} = \int_0^a \rho A_{surface} c_p T(x) dx$$

$$\Rightarrow kaT_{bulk} = \int_0^a kT(x)dx$$

Substituting for $kT(x)$,

$$\Rightarrow kaT_{bulk} = -q'''\frac{a^3}{6} + Ba$$

$$\Rightarrow B = kT_{bulk} + q'''\frac{a^2}{6}$$

Substituting this value of B, we obtain the relation

$$kT(x) = -q''' \frac{x^2}{2} + kT_{bulk} + q''' \frac{a^2}{6}$$

Writing this expression for $x = a$, we get

$$kT_w = -q''' \frac{a^2}{2} + kT_{bulk} + q''' \frac{a^2}{6}$$

$$\Rightarrow T_w = T_{bulk} - q''' \frac{a^2}{3k}$$

Now,

$$q''' = \frac{I^2 R}{v}$$

where I is the current passing through the heater, R is the heater resistance and v is the volume of the heater element. If width of the heater is w, length of the heater element is L, then

$$v = (2a)Lw$$

Thus, we get

$$T_w = T_{bulk} - \frac{I^2 Ra}{6Lwk}$$

7.3. Axial variation of T_{bulk} and T_w

In order to verify that there was no significant variation in T_{bulk} (or T_w) axially, additional experiments were carried out. In these experiments, one of the two 3.4 cm x 0.5 cm faces of the heater was insulated by using silicone gel, thus boiling occurred only on one face. Before putting the insulating gel on, three thermocouples were attached to that face at three locations: at geometric center of the face i.e. 1.7 cm away from the top Cu-electrodes (this TC was named TC1), at 1 cm on top of TC1, and at 1 cm on bottom of

TC1. These TCs were named TC2 and TC3 respectively. **Figure 7-4** shows the schematic of this arrangement, while **Figure 7-5** is a photograph of the actual set-up. **Figure 7-6** shows the measurements made by the three thermocouples for temperatures at the insulated wall, at various heat fluxes. From this figure, it is evident that the wall temperatures at different locations are very close to each other. The maximum deviation between any two thermocouple measurements is 2 ^{0}C, which is less than 2x uncertainty in thermocouple measurements (1.1 ^{0}C). Thus, it is concluded that the wall temperature at the insulated wall (and hence the bulk temperature of heater) at any flux, can be assumed to be uniform axially.

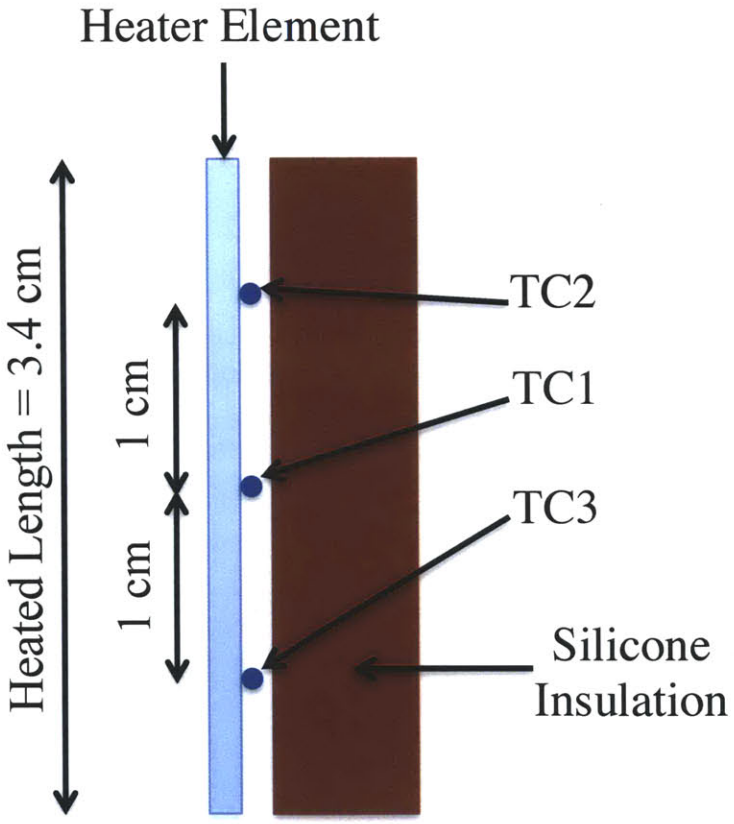

Figure 7-4: Schematic of heaters with insulated back, showing the locations of three TCs used. The insulation shown here is glued to the surface of heater

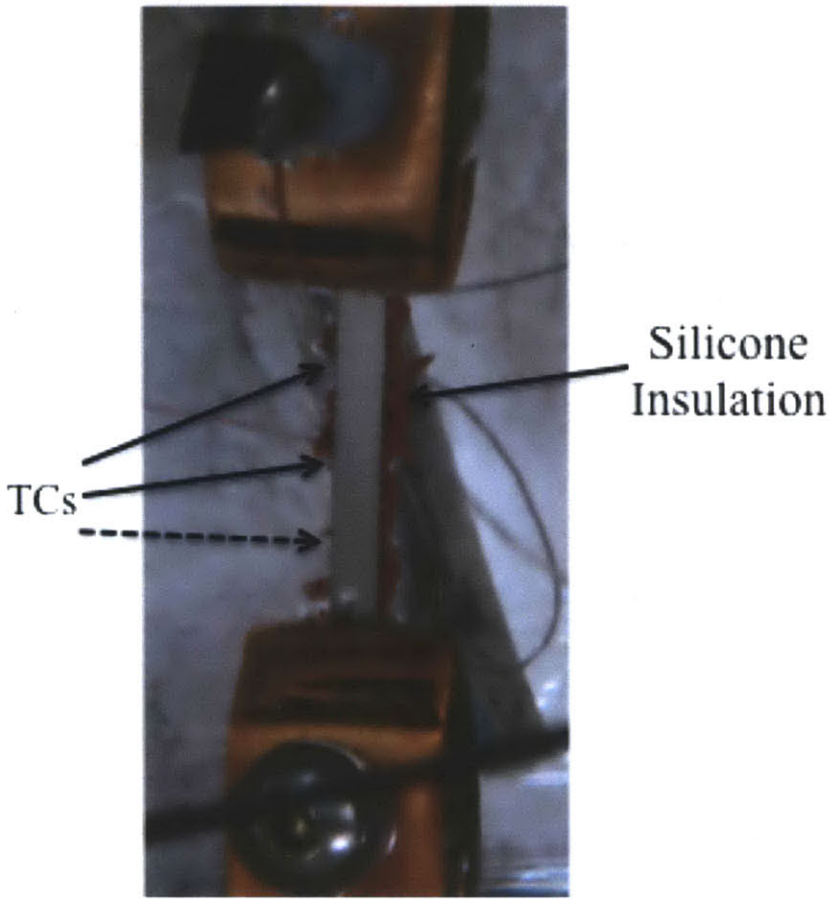

Figure 7-5: Photograph of the heater with insulated back, with attached TCs. In this picture, TC3 was disconnected during assembly. The location of TC3 is shown with broken arrow.

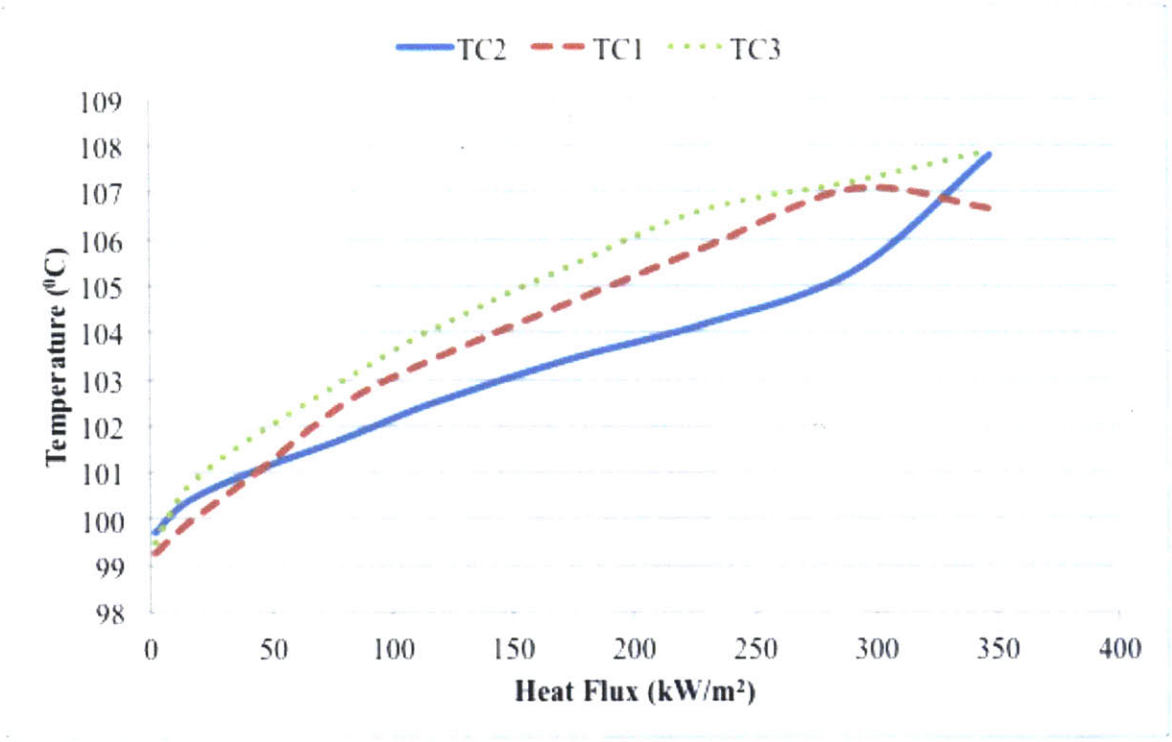

Figure 7-6: Measured temperatures at the insulated wall by the three thermocouples

Additionally, T_{bulk} calculated from instantaneous resistance measurements (as discussed in Section 7.2), for this experimental arrangement, was compared with T_{bulk} calculated from the temperature at the insulated surface (by solving the steady-state heat conduction equation). Denoting the temperature at heated wall as T_{ins}, T_{bulk} is calculated as follows (**Figure 7-7**: depicts the situation pictorially):

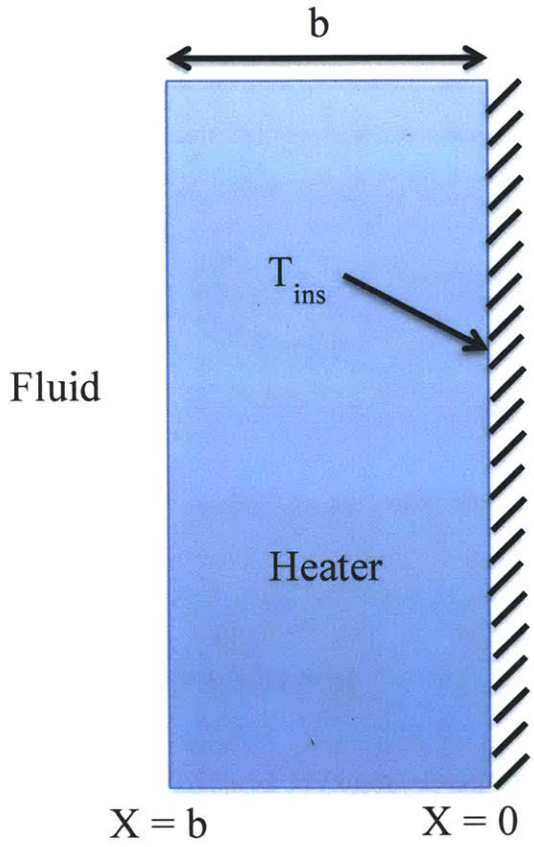

Figure 7-7: Schematic for calculating relation between T_{ins} and T_{bulk}

The 1-dimensional steady-state heat conduction equation is

$$\frac{d}{dx}\left(k\frac{dT}{dx}\right) + q''' = 0$$

On integrating, we get

$$k\frac{dT}{dx} = -q'''x + A$$

where A is a constant of integration.

Now, we've the boundary condition:

$$\left.\frac{dT}{dx}\right|_{x=0} = 0$$

which yields, $A = 0$

Thus we get

$$k\frac{dT}{dx} = -q'''x$$

Integrating it again, we obtain

$$kT(x) = -q'''\frac{x^2}{2} + B$$

where B is another constant of integration.

Now,

$$\rho A_{surface} c_p b T_{bulk} = \int_0^b \rho A_{surface} c_p T(x) dx$$

$$\Rightarrow kbT_{bulk} = \int_0^b kT(x)dx$$

Substituting for $kT(x)$,

$$\Rightarrow kbT_{bulk} = -q'''\frac{b^3}{6} + Bb$$

$$\Rightarrow B = kT_{bulk} + q'''\frac{b^2}{6}$$

Substituting this value of B, we obtain the relation

$$kT(x) = -q'''\frac{x^2}{2} + kT_{bulk} + q'''\frac{b^2}{6}$$

Writing this expression for $x = 0$, we get

$$kT_{ins} = kT_{bulk} + q'''\frac{b^2}{6}$$

$$\Rightarrow T_{bulk} = T_{ins} - q''' \frac{b^2}{6k}$$

Now,

$$q''' = \frac{I^2 R}{v}$$

where I is the current passing through the heater, R is the heater resistance and v is the volume of the heater element. If width of the heater is w, length of the heater element is L, then

$$v = bLw$$

Thus, we get

$$T_{bulk} = T_{ins} - \frac{I^2 Rb}{6Lwk}$$

Using this analysis, T_{bulk} was calculated, as a function of heat flux, from the averaged measurements of insulated wall temperatures measured by the three thermocouples. T_{bulk} was also calculated from the instantaneous resistance measurements and the temperature coefficient of resistivity for SS304. **Figure 7-8** compares the value of T_{bulk} calculated by both these methods. T_{bulk} calculated by these methods are in good agreement with each other, thus helping us conclude that the instantaneous T_{bulk} can be accurately calculated from the instantaneous resistance measurements for the heater. After this proof, throughout the data analysis, T_{bulk} is calculated from the instantaneous resistance measurements for the SS304 heater.

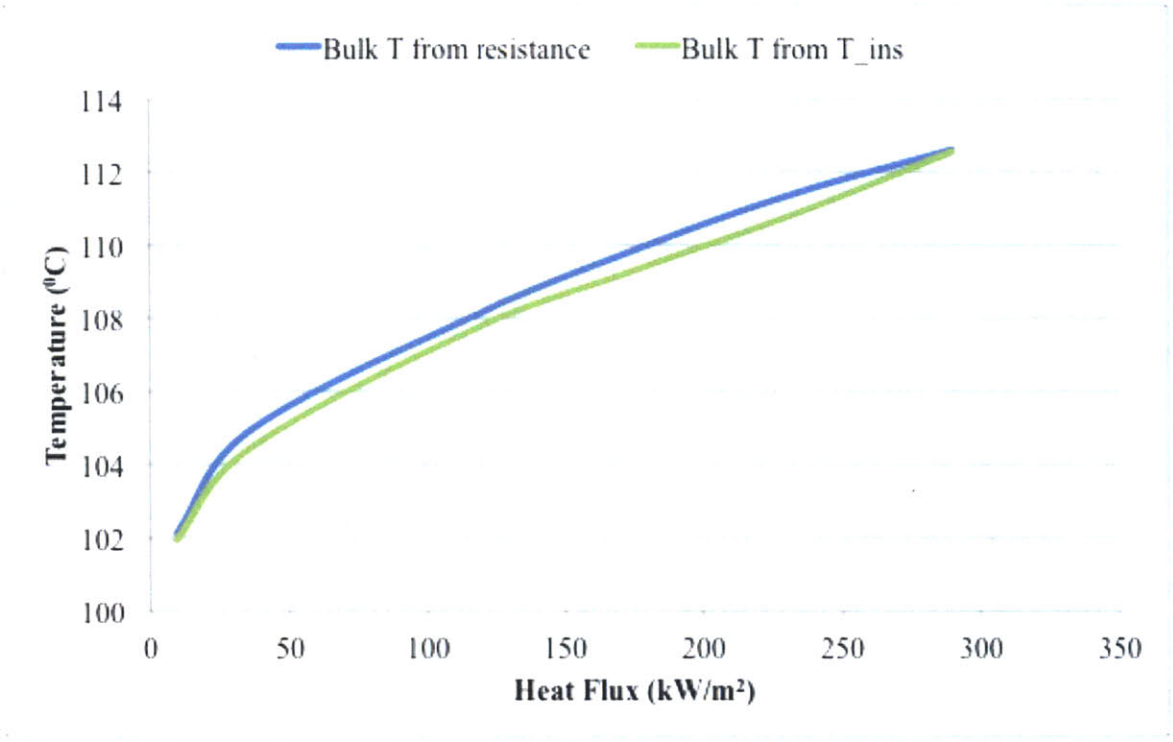

Figure 7-8: Comparison for T_{bulk} measurement from two different methods

7.4. Agreement between FG and Power Supply Output

To verify that the output current from the power supply follows the input from the FG, several test experiments were done with the actual heater loaded in the experimental set-up. The FG generator output is set to have different frequencies and amplitude. The FG output and the current output are measured using the 34980A. In one of the tests, the FG was set to provide a triangular wave with a half-amplitude of 1.6 V and a time period of 4 s. **Figure 7-9** shows the FG output and the power supply current output for this experiment. As seen, the output current from the power supply increases nicely to ~83 A in 1 s, in accordance with the FG output. The slight time lag between the current and the FG output is due to the lag between the current and FG output measurements.

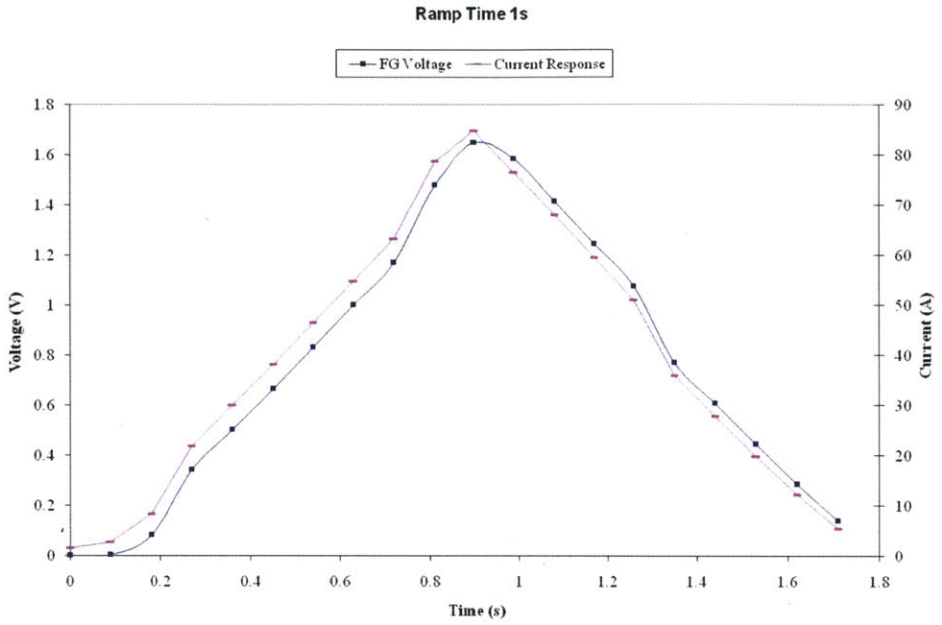

Figure 7-9: Function Generator voltage and the output power supply current. Current increases from 0 to 83A in ~ 1s

Similarly, in **Figure 7-10** and **Figure 7-11**, the FG voltage half-amplitude is 3.6 V, with the time periods being 40 and 400 s, respectively. Accordingly, current output from the power supply increases from 0 A to 180 A in 10 s and 100 s, respectively. This shows that the power supply can be successfully controlled remotely, by triggering it with the FG, to supply desired levels of currents for the various transients.

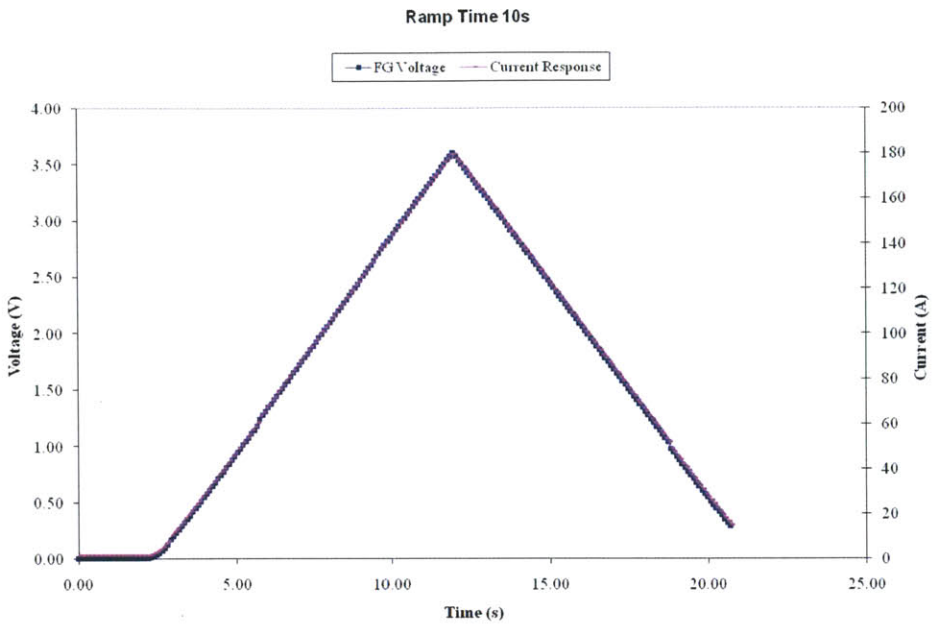

Figure 7-10: Function Generator voltage and the output power supply current. Current increases from 0 to 180A in ~ 10 s

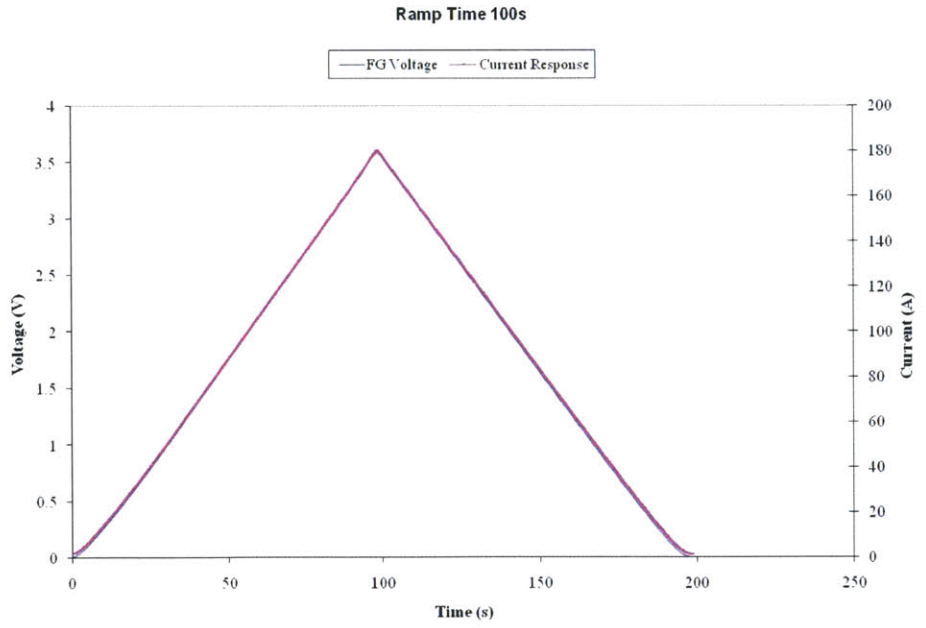

Figure 7-11: Function Generator voltage and the output power supply current. Current increases from 0 to 183A in ~ 100 s

7.5. Current Gain by CSM

The fixed gain provided by the CSM was verified before using the CSM in the circuit for transient test data acquisition. For the verification, a small resistance was mounted between the electrodes of a power supply. The potential drop across the resistor was input into the CSM. The CSM was powered by an external 12 V battery. The potential drop across the resistor, provided by the power supply electrodes, was varied randomly. The signal input into the CSM, as well as the output signal from the CSM was recorded simultaneously by using the Agilent 34980A unit with the 34921T data card. **Figure 7-12** plots the input voltage into the CSM and its output. It is seen that the output from the CSM follows the input accurately, and is amplified by a factor of ~200. The average of the Output/Input ratio was observed to be 199.94 with a standard deviation of only 3.07. The theoretical gain provided by the CSM, according to the supplier (Texas Instruments) is 200. Thus, it is seen that the CSM is able to provide the expected gain when used in the circuit.

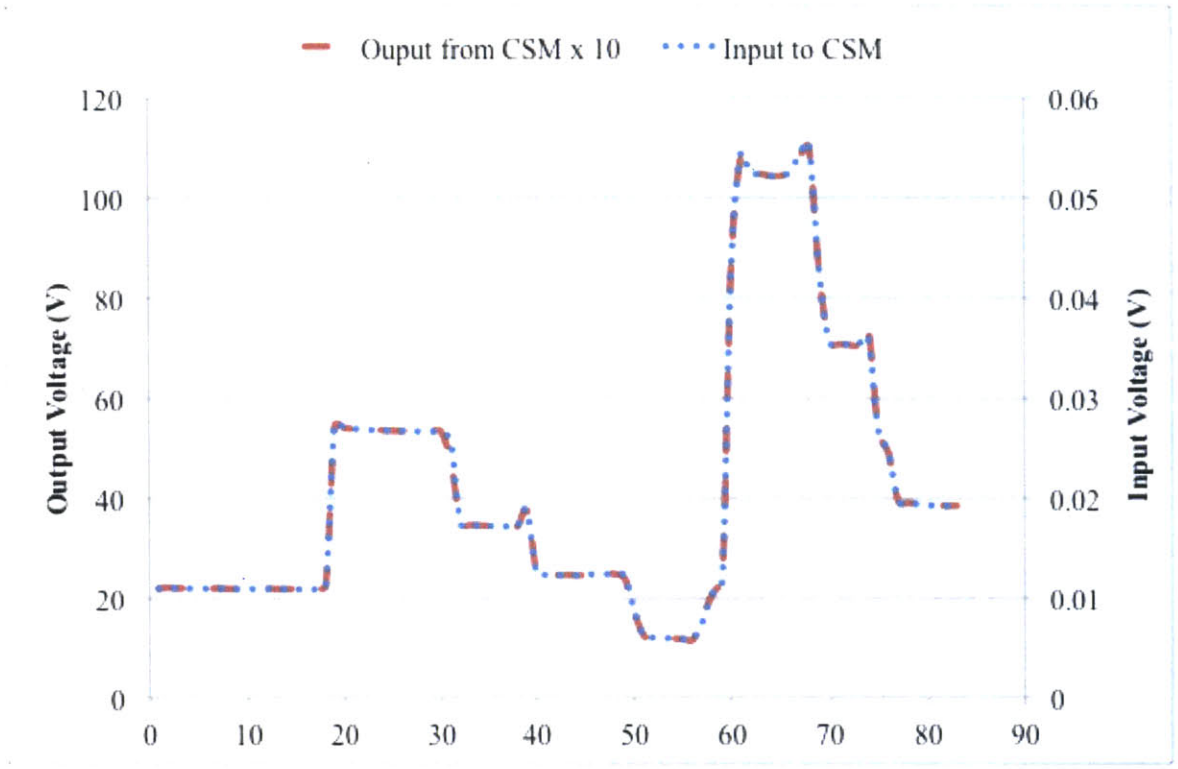

Figure 7-12: CSM gain verification exercise, showing the voltage input to the CSM (secondary axis) and the CSM output (primary axis)

8. Appendix B: Complete Experimental Data

8.1. Steady-State Test Data for Different Surfaces (Section 4.4.1)

Table 8-1: Summary of CHF tests done for investigating effects of roughness

Experiment No.	Heater	Test-Fluid	CHF (kW/m^2)	Average CHF (kW/m^2)	Standard Deviation in CHF (kW/m^2)
SB_DIW1	Sandblasted	DI water	524	511.5	17.68
SB_DIW2	Sandblasted	DI water	499		
Sm_DIW1	Smooth	DI water	455	465.5	15.55
Sm_DIW1	Smooth	DI water	476		
SB_NF1	Sandblasted	0.01 v% ZnO nanofluid	1295	1296.5	2.12
SB_NF2	Sandblasted	0.01 v% ZnO nanofluid	1298		
Sm_NF1	Smooth	0.01 v% ZnO nanofluid	861	785	194.52
Sm_NF2	Smooth	0.01 v% ZnO nanofluid	654		
Sm_NF3	Smooth	0.01 v% ZnO nanofluid	1091		
Sm_NF4	Smooth	0.01 v% ZnO nanofluid	700		
Sm_NF5	Smooth	0.01 v% ZnO nanofluid	619		

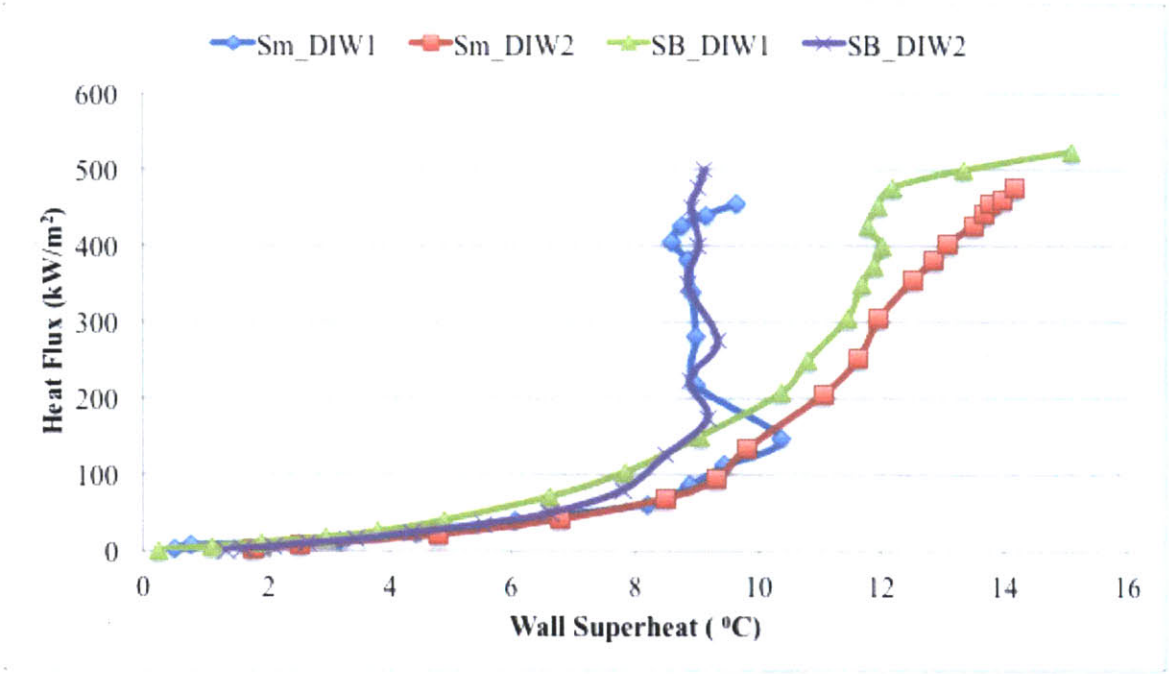

Figure 8-1: Boiling curves[15] for DI water tests for sandblasted and smooth heaters

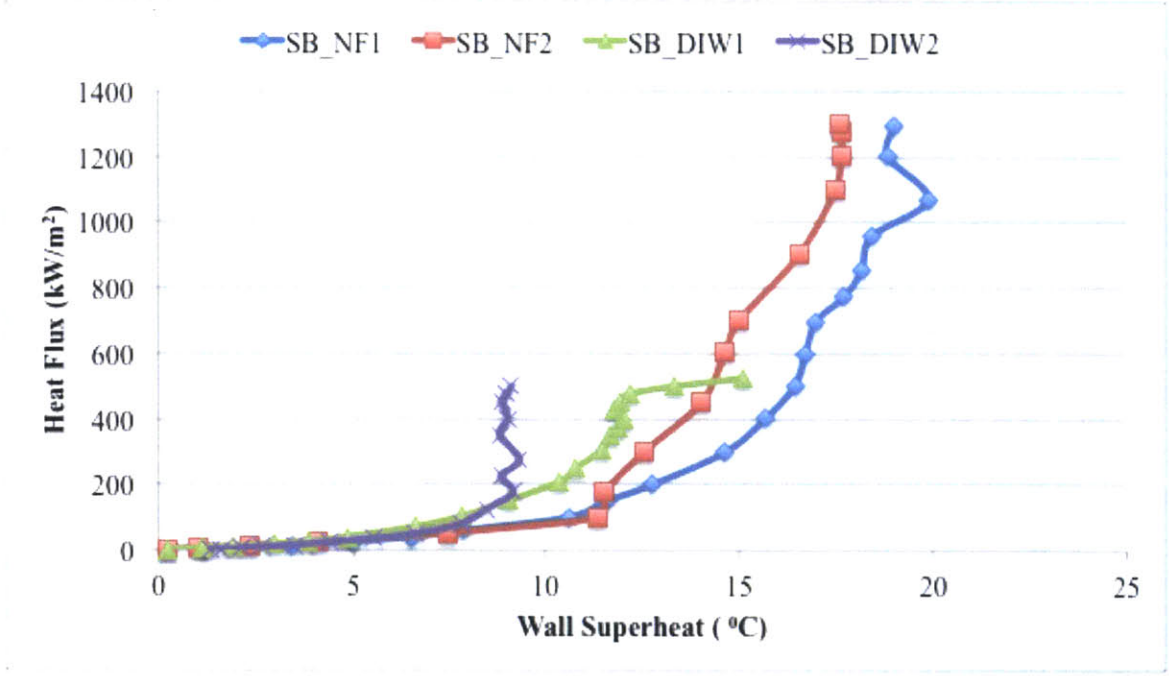

Figure 8-2: Boiling curves for sandblasted heaters, with DI water and nanofluid

[15] All boiling curves shown in this work terminate at CHF

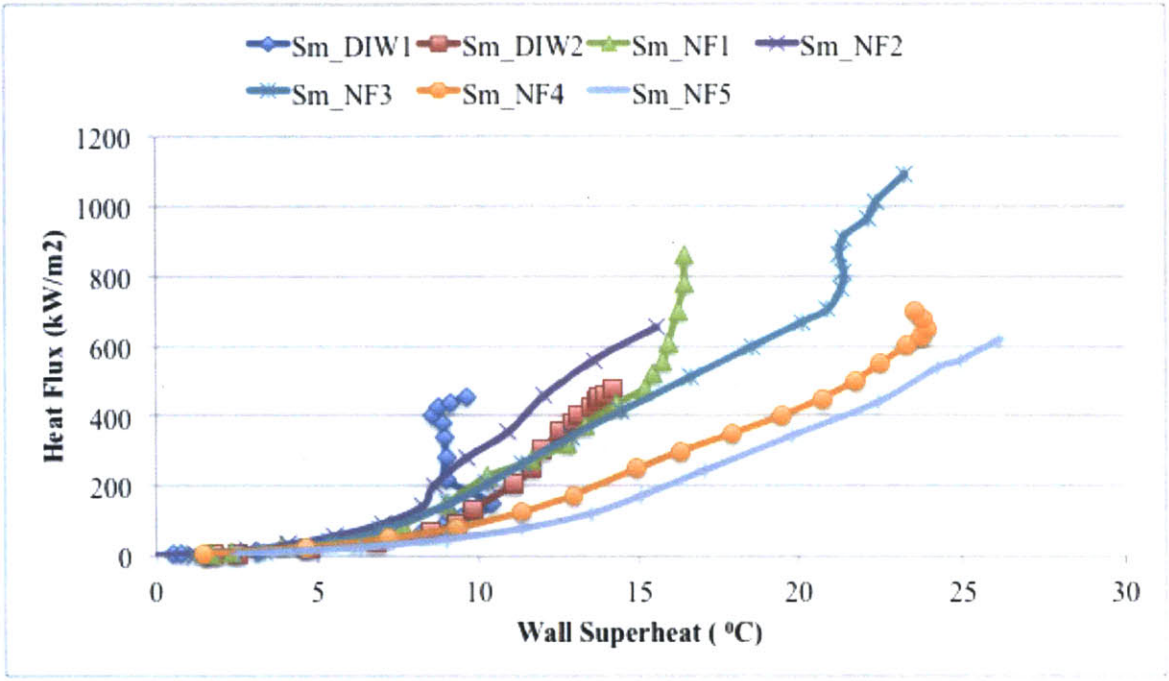

Figure 8-3: Boiling curves for smooth heaters, with DI water and nanofluid

8.2. Steady-State Test Data for Different Wettabilities (Section 4.4.2)

Table 8-2: Summary of CHF tests done for investigating effects of wettability

Experiment No.	Heater	Test-Fluid	CHF (kW/m^2)	Average CHF (kW/m^2)	Standard Deviation in CHF (kW/m^2)
SB_DIW1	Sandblasted	DI water	524	511.5	17.68
SB_DIW2	Sandblasted	DI water	499		
Sm_DIW1	Smooth	DI water	455	465.5	15.55
Sm_DIW1	Smooth	DI water	476		
LbLSB_DIW1	LbL-coated Sandblasted	DI water	696	671	35.35
LbLSB_DIW2	LbL-coated Sandblasted	DI water	646		
LbLSm_DIW1	LbL-coated Smooth	DI water	606	622	22.63
LbLSm_DIW2	LbL-coated Smooth	DI water	638		
LbLSB_NF1	LbL-coated Sandblasted	0.01 v% ZnO nanofluid	759	780	29.70
LbLSB_NF2	LbL-coated Sandblasted	0.01 v% ZnO nanofluid	801		
LbLSm_NF1	LbL-coated Smooth	0.01 v% ZnO nanofluid	677	718.5	58.69
LbLSm_NF2	LbL-coated Smooth	0.01 v% ZnO nanofluid	760		

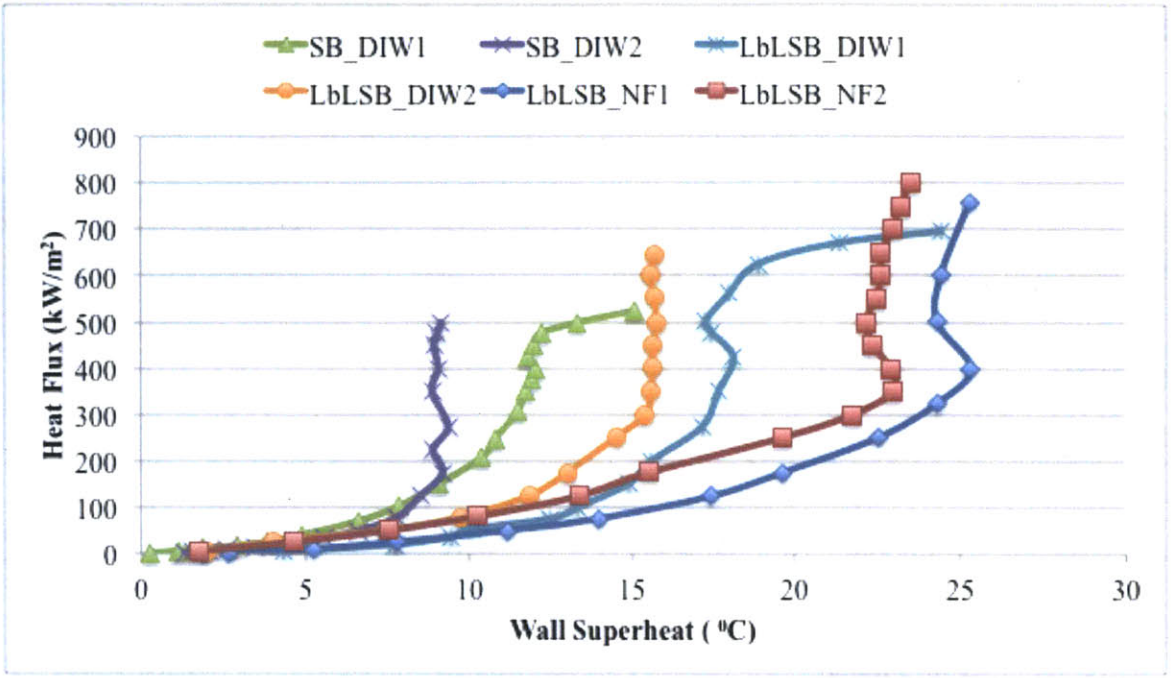

Figure 8-4: Boiling curves for sandblasted heaters, both uncoated and LbL coated

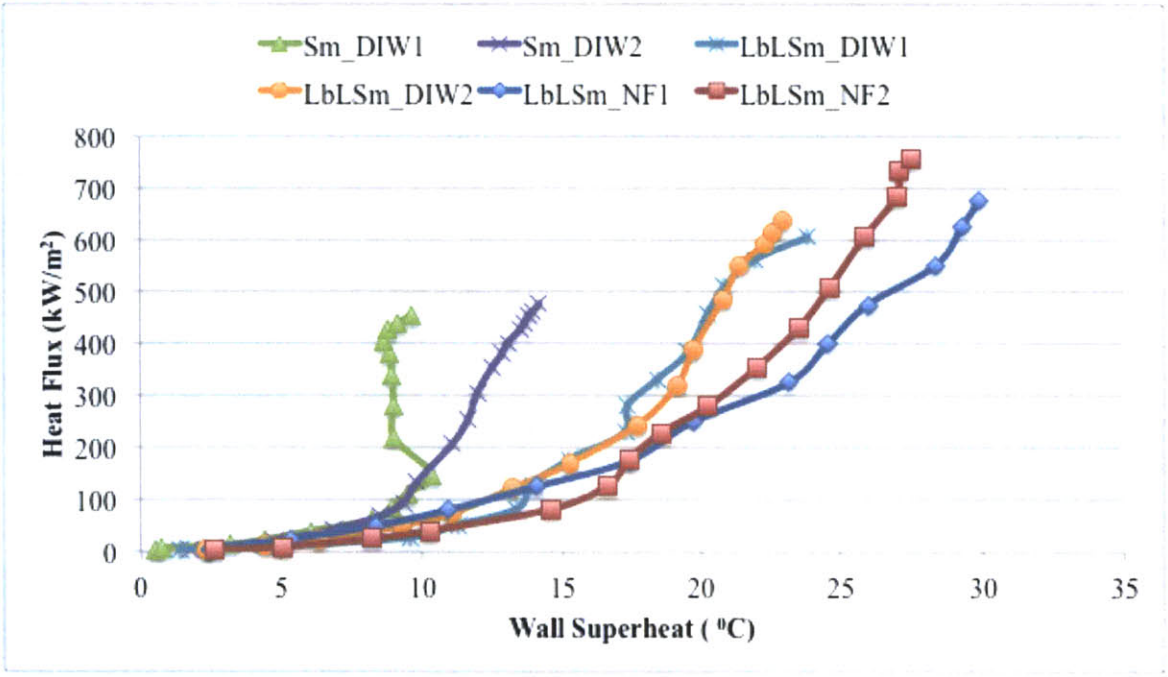

Figure 8-5: Boiling curves for smooth heaters, both uncoated and LbL coated

8.3. Steady-State Test Data for Different Pre-Boiling Times (Section 4.4.3)

Table 8-3: Summary of CHF tests done for investigating effects of pre-boiling time of DI water on sandblasted heaters

Experiment No.	Test-Fluid	Pre-Boiling Time (h)	CHF (kW/m^2)	Average CHF (kW/m^2)	Standard Deviation in CHF (kW/m^2)
SB_DIW_0hr_1	DI water	0	524	511.5	17.68
SB_DIW_0hr_2	DI water	0	499		
SB_DIW_1hr_1	DI water	1	520	490	42.43
SB_DIW_1hr_2	DI water	1	460		
SB_DIW_4hr_1	DI water	4	516	507	12.73
SB_DIW_4hr_2	DI water	4	498		
SB_DIW_8hr_1	DI water	8	416	-	-

Table 8-4: Summary of CHF tests done for investigating effects of pre-boiling time of DI water on smooth heaters

Experiment No.	Test-Fluid	Pre-Boiling Time (h)	CHF (kW/m^2)	Average CHF (kW/m^2)	Standard Deviation in CHF (kW/m^2)
Sm_DIW_0hr_1	DI water	0	454	465	15.56
Sm_DIW_0hr_2	DI water	0	476		
Sm_DIW_1hr_1	DI water	1	424	415	12.72
Sm_DIW_1hr_2	DI water	1	406		
Sm_DIW_4hr_1	DI water	4	351	337.5	19.09
Sm_DIW_4hr_2	DI water	4	324		
Sm_DIW_8hr_1	DI water	8	332	-	-

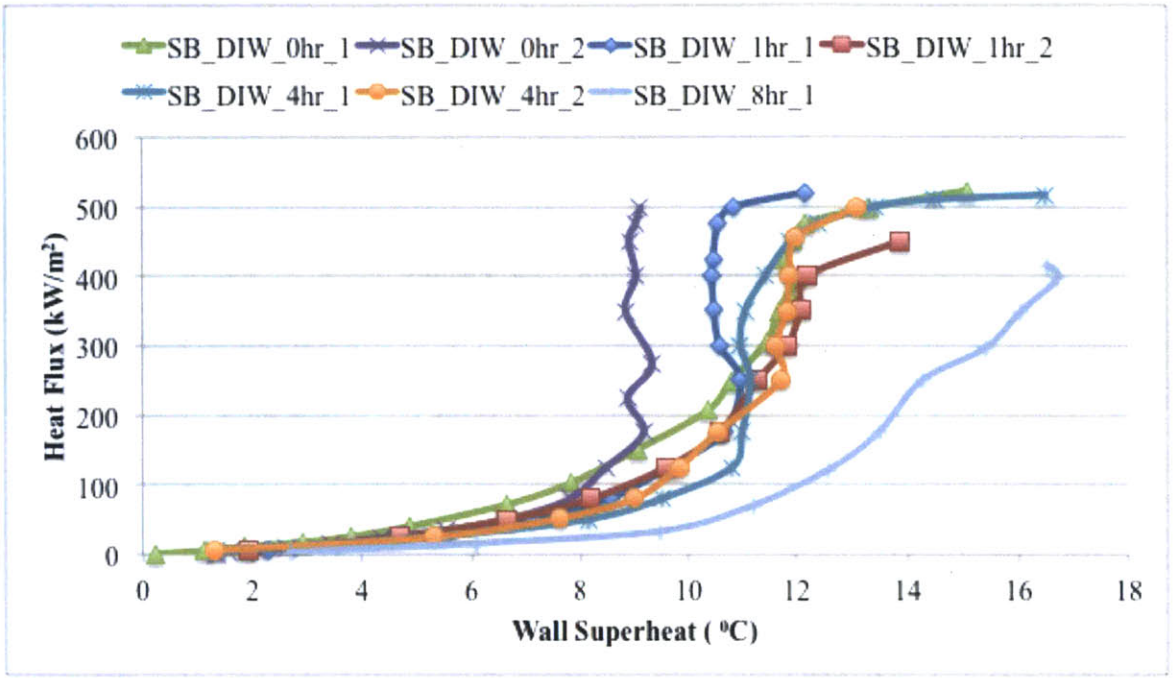

Figure 8-6: Boiling curves for sandblasted heaters, with DI water, for various pre-boiling times

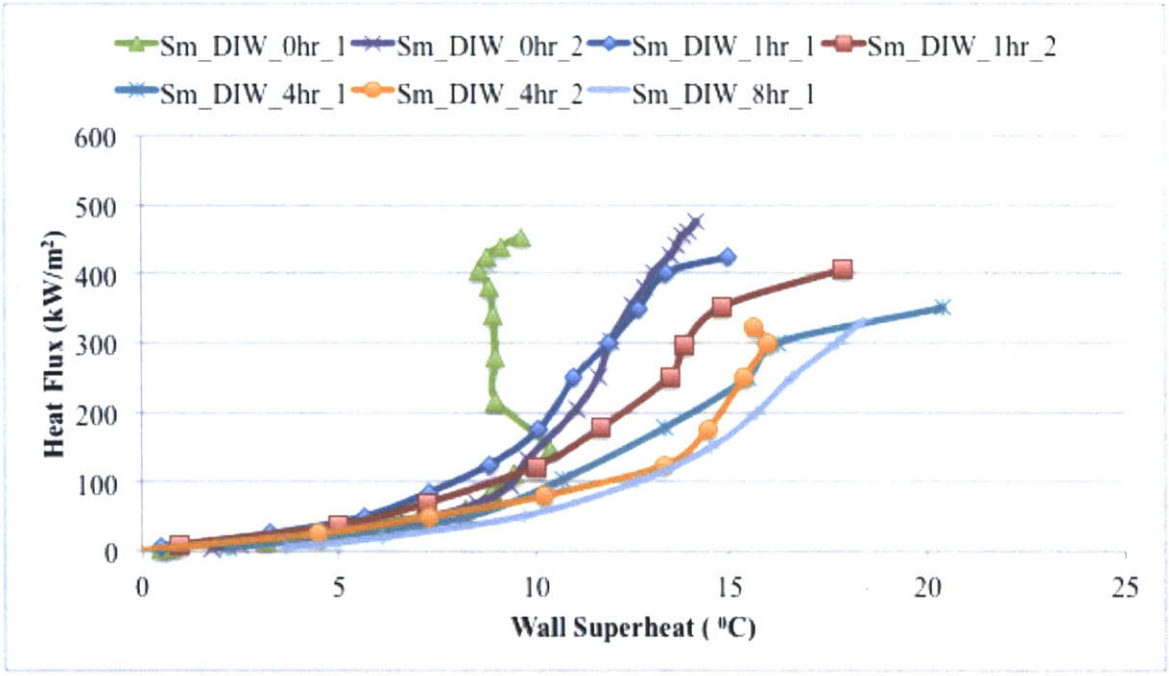

Figure 8-7: Boiling curves for smooth heaters, with DI water, for various pre-boiling times

Table 8-5: Summary of CHF tests done for investigating effects of pre-boiling time of nanofluid on sandblasted heaters

Experiment No.	Test-Fluid	Pre-Boiling Time (h)	CHF (kW/m^2)	Average CHF (kW/m^2)	Standard Deviation in CHF (kW/m^2)
SB_NF_0hr_1	0.01v% ZnO	0	1295	1297.5	2.12
SB_NF_0hr_2	0.01v% ZnO	0	1298		
SB_NF_1hr_1	0.01v% ZnO	1	1326	1158	183.85
SB_NF_1hr_2	0.01v% ZnO	1	1066		
SB_NF_4hr_1	0.01v% ZnO	4	904	903	1.41
SB_NF_4hr_2	0.01v% ZnO	4	902		
SB_NF_8hr_1	0.01v% ZnO	8	1099	936.5	158.39
SB_NF_8hr_2	0.01v% ZnO	8	875		

Table 8-6: Summary of CHF tests done for investigating effects of pre-boiling time of nanofluid on smooth heaters

Experiment No.	Test-Fluid	Pre-Boiling Time (h)	CHF (kW/m^2)	Average CHF (kW/m^2)	Standard Deviation in CHF (kW/m^2)
Sm_NF_0hr_1	0.01v% ZnO	0	860	756.5	146.37
Sm_NF_0hr_2	0.01v% ZnO	0	653		
Sm_NF_1hr_1	0.01v% ZnO	1	610	728.5	167.5843071
Sm_NF_1hr_2	0.01v% ZnO	1	847		
Sm_NF_4hr_1	0.01v% ZnO	4	746	898	214.9604615
Sm_NF_4hr_2	0.01v% ZnO	4	1050		
Sm_NF_8hr_1	0.01v% ZnO	8	673	720.5	67.17514421
Sm_NF_8hr_2	0.01v% ZnO	8	768		

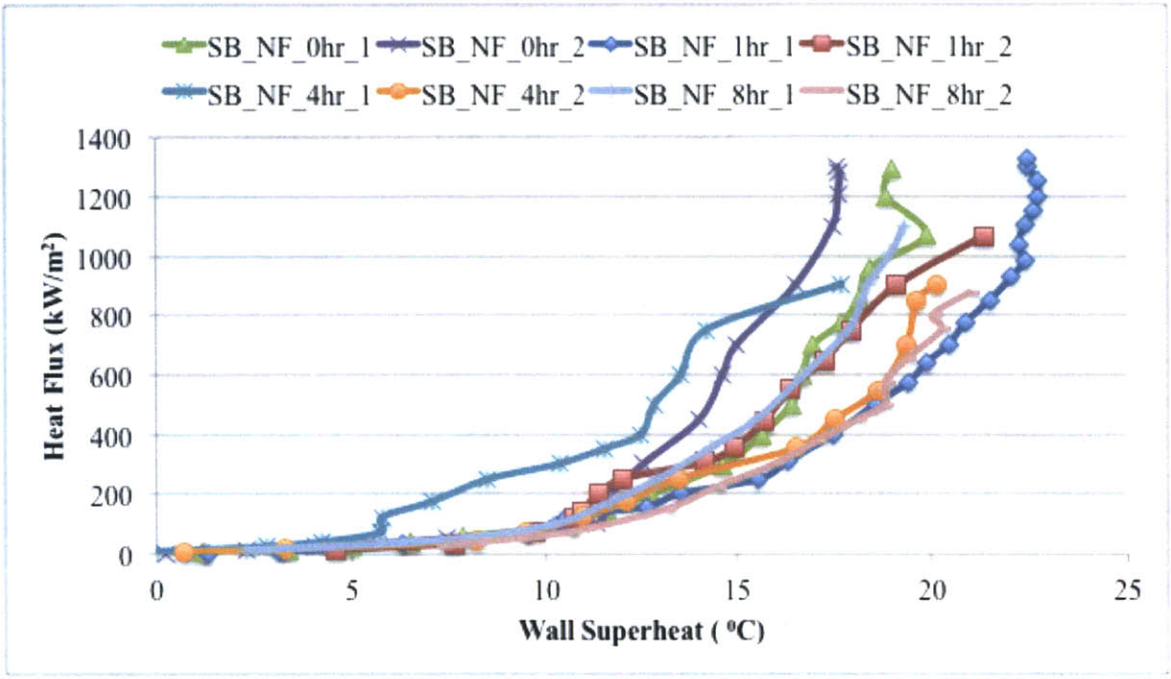

Figure 8-8: Boiling curves for sandblasted heaters, with nanofluid, for various pre-boiling times

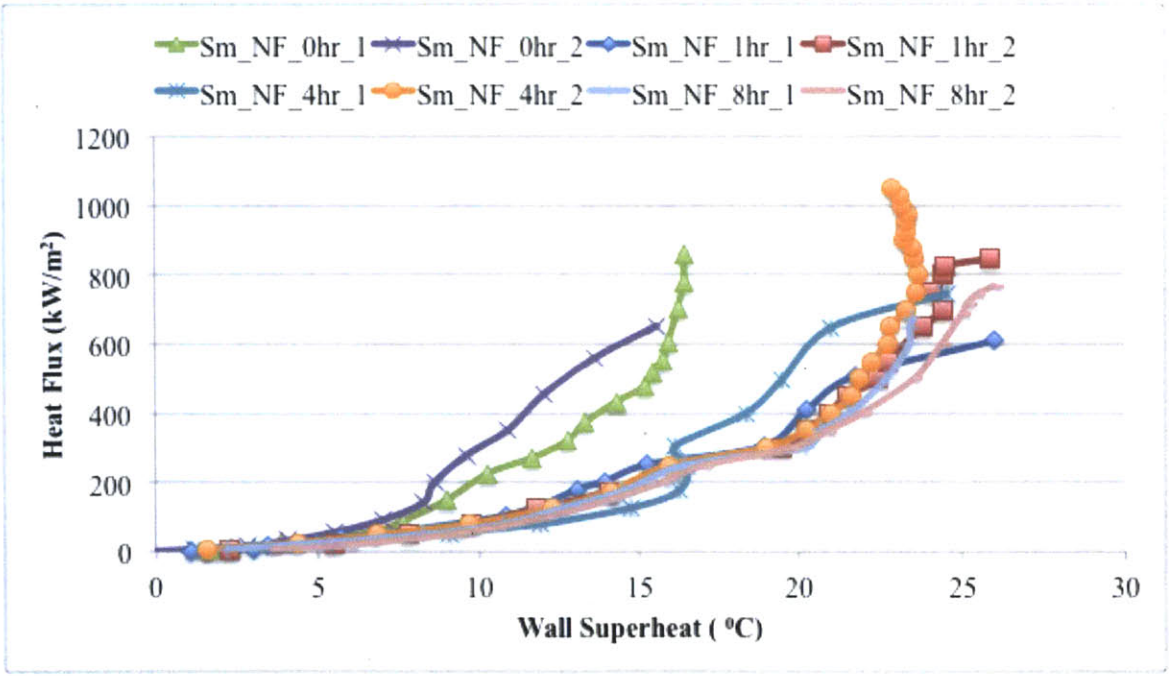

Figure 8-9: Boiling curves for smooth heaters, with nanofluid, for various pre-boiling times

Table 8-7: Summary of CHF tests done, varying the pre-boiling heat flux and time, but at the same total pre-boiling heat

Experiment No.	Test-Fluid	Pre-Boiling Heat Flux (kW/m^2)/ Time (h)	CHF (kW/m^2)	Average CHF (kW/m^2)	Standard Deviation in CHF (kW/m^2)
SB_NF_250_1	0.01v% ZnO	250/1	1326	1158	183.85
SB_NF_250_2	0.01v% ZnO	250/1	1066		
SB_NF_125_1	0.01v% ZnO	125/2	1124	1148	33.95
SB_NF_125_2	0.01v% ZnO	125/2	1172		
SB_NF_500_1	0.01v% ZnO	500/0.5	1325	1262.5	88.39
SB_NF_500_2	0.01v% ZnO	500/0.5	1200		

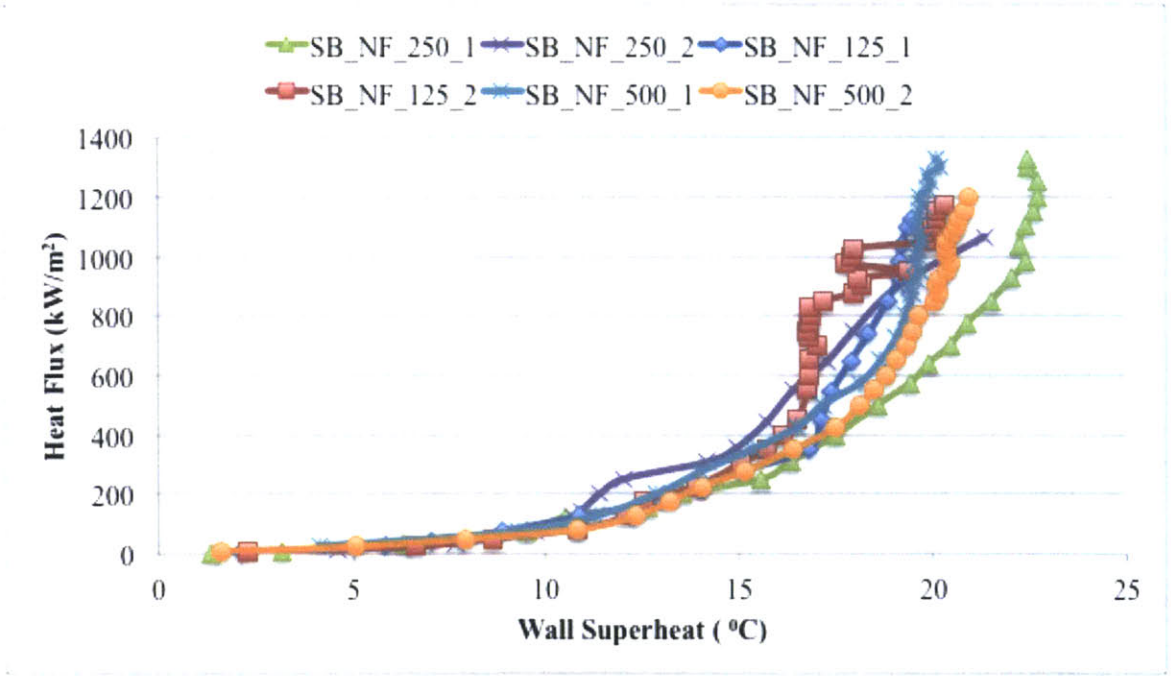

Figure 8-10: Boiling curves for sandblasted heaters, with nanofluid, for various pre-boiling heat fluxes and times (at constant total pre-boiling heat)

Table 8-8: Summary of CHF tests done, investigating the effects of pre-boiling time of nanofluid on LbL coated sandblasted heaters

Experiment No.	Test-Fluid	Pre-Boiling Time (h)	CHF (kW/m^2)	Average CHF (kW/m^2)	Standard Deviation in CHF (kW/m^2)
LbLSB_NF_0hr1	0.01v% ZnO	0	758	779.5	30.40
LbLSB_NF_0hr2	0.01v% ZnO	0	801		
LbLSB_NF_1hr1	0.01v% ZnO	1	636	643	9.89
LbLSB_NF_1hr2	0.01v% ZnO	1	650		
LbLSB_NF_4hr1	0.01v% ZnO	4	701	800.5	140.71
LbLSB_NF_4hr2	0.01v% ZnO	4	900		
LbLSB_NF_8hr1	0.01v% ZnO	8	866	832	48.08
LbLSB_NF_8hr2	0.01v% ZnO	8	798		

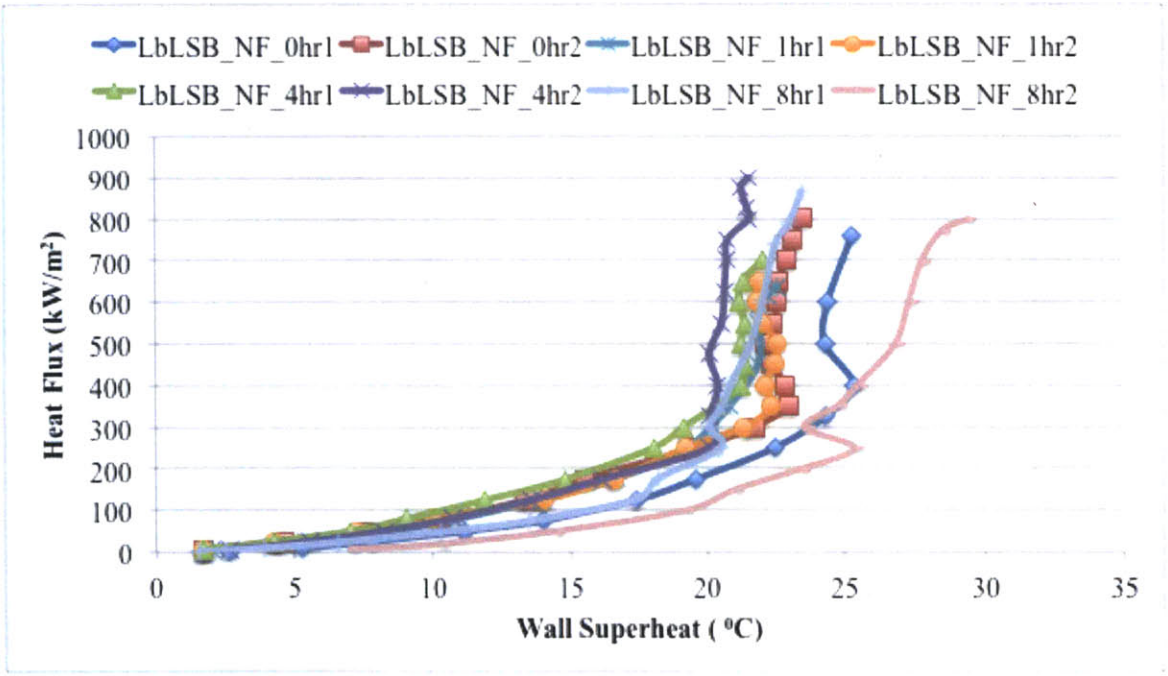

Figure 8-11: Boiling curves for LbL coated sandblasted heaters, with nanofluid, for various pre-boiling times

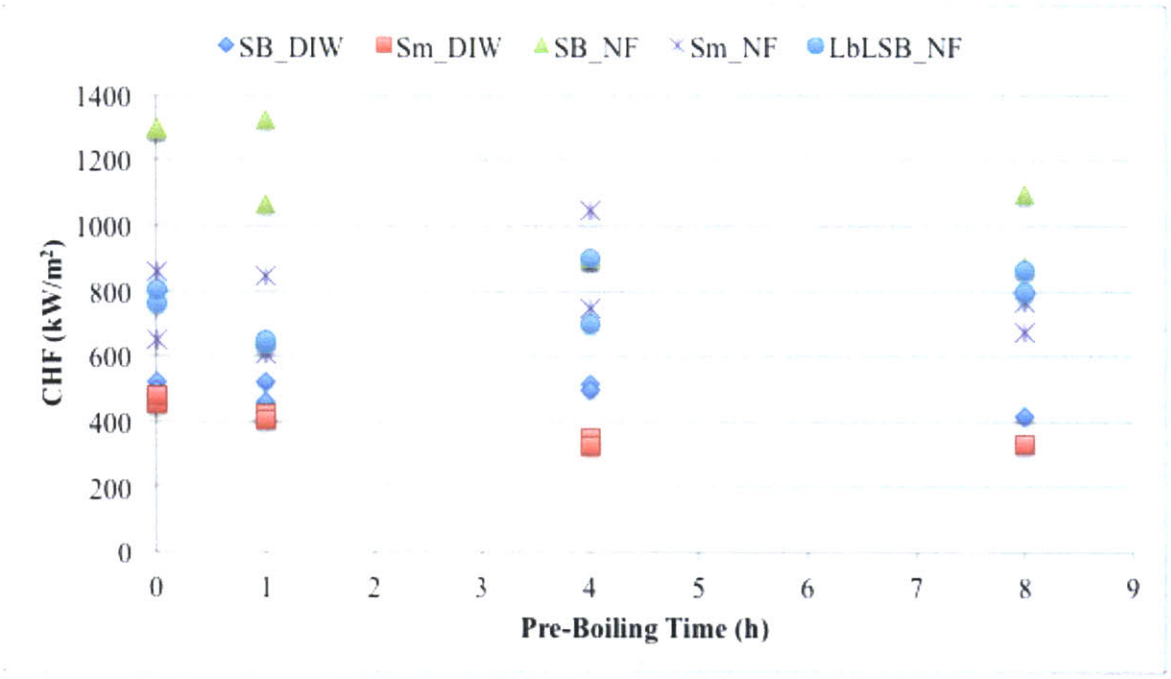

Figure 8-12: CHF for different heater surface/fluid combinations for varying pre-boiling times

8.4. Transient Test Data (Section 5.5)

Table 8-9: Summary of transient tests for uncoated heaters for various values of t_o

Experiment No.	Heater	Test-Fluid	t_o (sec)	CHF (kW/m^2)	Average CHF (kW/m^2)	Standard Deviation in CHF (kW/m^2)
Tr_DIW100_1	Sandblasted	DI water	100	566	548.5	24.75
Tr_DIW100_2	Sandblasted	DI water	100	531		
Tr_DIW10_1	Sandblasted	DI water	10	800	806.66	9.86
Tr_DIW10_2	Sandblasted	DI water	10	818		
Tr_DIW10_3	Sandblasted	DI water	10	802		
Tr_DIW1_1	Sandblasted	DI water	1	1664	1497.33	154.11
Tr_DIW1_2	Sandblasted	DI water	1	1360		
Tr_DIW1_3	Sandblasted	DI water	1	1468		
Tr_NF100_1	Sandblasted	0.01 v% ZnO	100	674	627.75	37.29
Tr_NF100_2	Sandblasted	0.01 v% ZnO	100	598		
Tr_NF100_3	Sandblasted	0.01 v% ZnO	100	642		
Tr_NF100_4	Sandblasted	0.01 v% ZnO	100	597		
Tr_NF10_1	Sandblasted	0.01 v% ZnO	10	1092	1094	50.65
Tr_NF10_2	Sandblasted	0.01 v% ZnO	10	1156		
Tr_NF10_3	Sandblasted	0.01 v% ZnO	10	1032		
Tr_NF10_4	Sandblasted	0.01 v% ZnO	10	1096		
Tr_NF1_1	Sandblasted	0.01 v% ZnO	1	1514	1536.5	31.82
Tr_NF1_2	Sandblasted	0.01 v% ZnO	1	1559		

Table 8-10: Summary of transient tests for nanocoated heaters for various values of t_o

Experiment No.	Heater	Test-Fluid	t_o (sec)	CHF (kW/m^2)	Average CHF (kW/m^2)	Standard Deviation in CHF (kW/m^2)
TrNC_DIW100_1	Sandblasted, nanocoated for 1 hr	DI water	100	782	750	45.25
TrNC_DIW100_2	Sandblasted, nanocoated for 1 hr	DI water	100	718		
TrNC_DIW10_1	Sandblasted, nanocoated for 1 hr	DI water	10	1186	1173	18.38
TrNC_DIW10_2	Sandblasted, nanocoated for 1 hr	DI water	10	1160		
TrNC_DIW1_1	Sandblasted, nanocoated for 1 hr	DI water	1	1920	1999	111.72
TrNC_DIW1_2	Sandblasted, nanocoated for 1 hr	DI water	1	2078		
TrNC_NF100_1	Sandblasted, nanocoated for 1 hr	0.01 v% ZnO	100	772	822.5	71.42
TrNC_NF100_2	Sandblasted, nanocoated for 1 hr	0.01 v% ZnO	100	823		
Tr_NF10_1	Sandblasted, nanocoated for 1 hr	0.01 v% ZnO	10	1186	1214	72.12
Tr_NF10_2	Sandblasted, nanocoated for 1 hr	0.01 v% ZnO	10	1160		
Tr_NF1_1	Sandblasted, nanocoated for 1 hr	0.01 v% ZnO	1	2065	1954	156.98
Tr_NF1_2	Sandblasted, nanocoated for 1 hr	0.01 v% ZnO	1	1843		

8.5. Transient Experiment Boiling Curves (Section 5.5)

Following the procedure described in Section 5.3.2, the instantaneous values of current (I), heater resistance (R), heater bulk temperature ($\bar{T}$) and flux transmitted to the coolant were obtained. Using these values as inputs, the boiling curves for the various transient tests were computed by the following analysis.

We've the unsteady state heat conduction equation

$$\frac{1}{\alpha}\frac{\partial T}{\partial t} = \frac{\partial^2 T}{\partial x^2} + \frac{q'''}{k}$$

Assuming the thickness of the heater to be *2a*. Using symmetry, focusing only on the half-thickness of the heater (with thickness *a*), and to solve the unsteady state heat conduction equation, let us assume that the half-thickness consists of *n+1* nodes, dividing the thickness of the heater in *n* different parts.

Denoting the node on the wall (heater/fluid interface) as node *0* and node on the heater centerline as node *n*, the initial wall temperature (T_o^p) is assumed. For any node *m* between 0 and n-1, the heat conduction equation can be written in the discretized form as

$$\frac{1}{\alpha}\frac{T_m^{p+1} - T_m^p}{\Delta t} = \frac{T_{m+1}^p + T_{m-1}^p - 2T_m^p}{(\Delta x)^2} + \frac{I^p * I^p * R^p}{vk}$$

Substituting the expression for Fourier number $Fo = \frac{\alpha \Delta t}{(\Delta x)^2}$, this equation can then be written as

$$T_m^{p+1} = Fo\left(T_{m+1}^p + T_{m-1}^p\right) + T_m^p(1 - 2Fo) + \frac{\alpha(\Delta t)R^p * I^p * I^p}{vk}$$

where superscripts p and $p+1$ denote the time steps, $\forall\, m \in 1\ to\ n-1$, v is the volume of the heater. Here,

$$\Delta x = {}^{a}/_{n}$$

For node n, the equation can be written from heat balance for that node as:

$$\frac{I^p * I^p * R^p}{v} s\frac{\Delta x}{2} = \frac{ks}{\Delta x}\left(T_n^p - T_{n-1}^p\right) + s\rho c_p \frac{\Delta x}{2}\left(\frac{T_n^{p+1} - T_n^p}{\Delta t}\right)$$

where s is the area of heat transfer between the heater and coolant, ρ and c_p are the heater density and specific heat capacity. For the heaters in this thesis, a = 0.000457 m. Using n = 10 and Δt = 0.0001 s, the temperature at each node at a particular time is calculated. Then the mean temperature of the heater at that time instant is calculated and is compared to the mean temperature obtained experimentally. If the difference between both these values of the mean temperature is less than 0.0001 ^{0}C, the exercise is continued for the next time step, else the assumed value of T_o^p is revised until the mean temperature obtained through the solution of heat conduction equation matches that obtained experimentally. Following this procedure, the temperature profile in the heater is obtained as a function of time during the experiment. Eventually, the instantaneous wall temperature is used to obtain the instantaneous wall superheat, and boiling curves for the transient experiments are obtained by plotting the instantaneous heat flux against instantaneous wall superheat. **Figure 8-13** – **Figure 8-15** show the boiling curves for the three transients. As is observed here, the boiling curves for the slowest (100 s) tests look similar to the boiling curves for steady-state tests. However, for the shortest test (1 s), as flux increases, the wall superheat is first seen to increase and then decrease. This is consistent with the observations reported in literature (and summarized in Section 5.1, when discussing the mechanism for transient CHF).

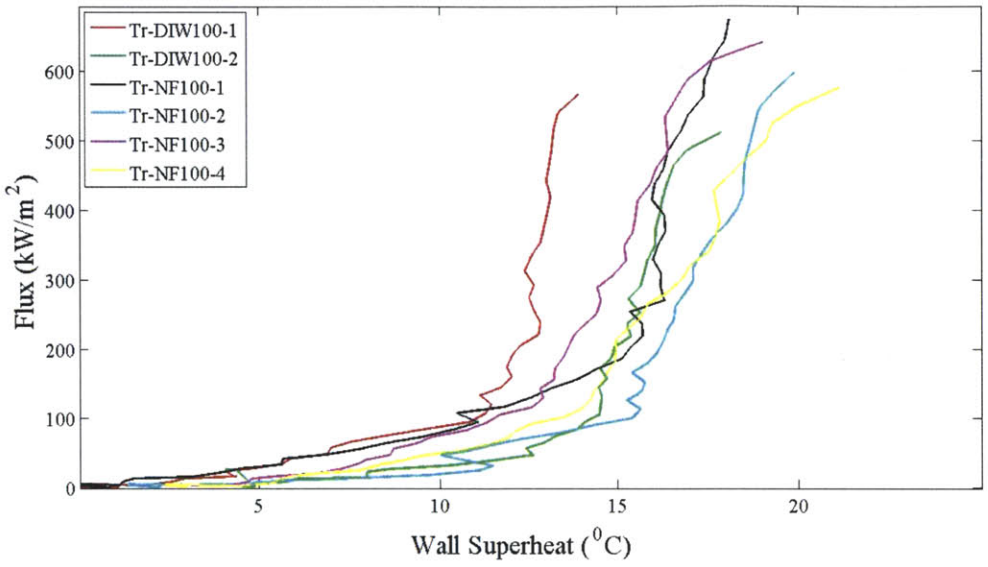

Figure 8-13: Boiling curves for 100s transient experiments (both DI water and nanofluid)

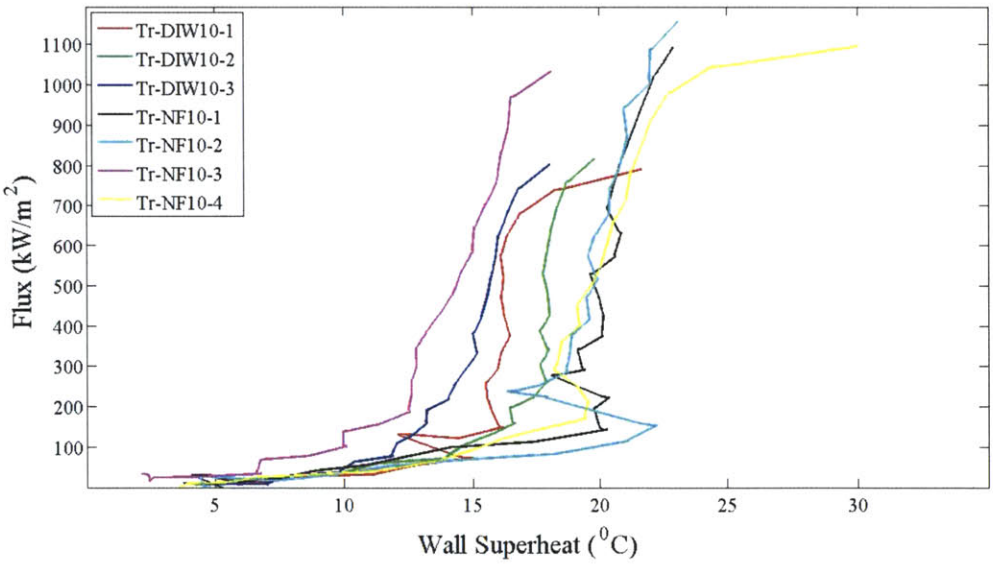

Figure 8-14: Boiling curves for 10s transient experiments (both DI water and nanofluid)

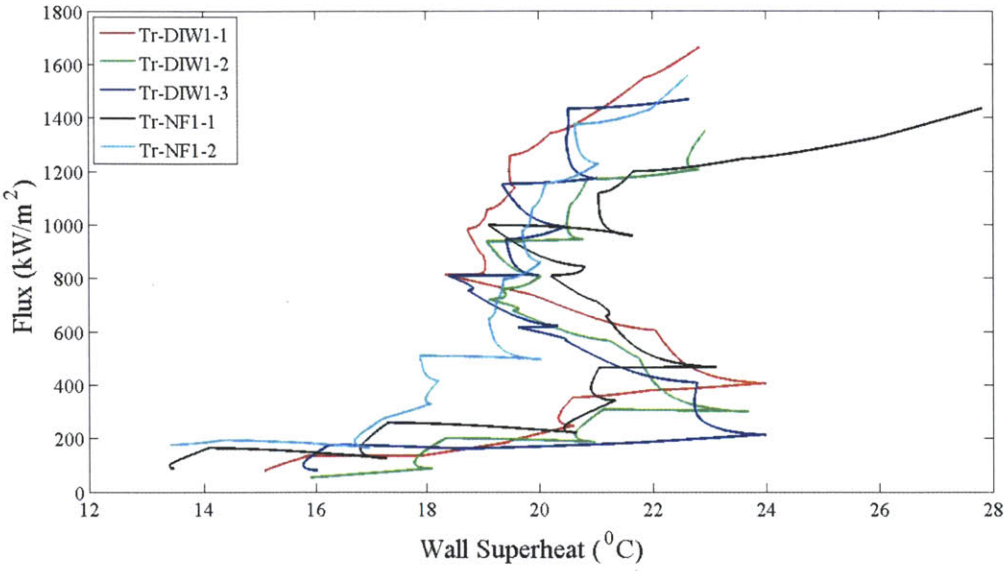

Figure 8-15: Boiling curves for 1s transient experiments (both DI water and nanofluid)

Figure 8-16 – **Figure 8-18** show the boiling curves for the three transients, for nanocoated heaters.

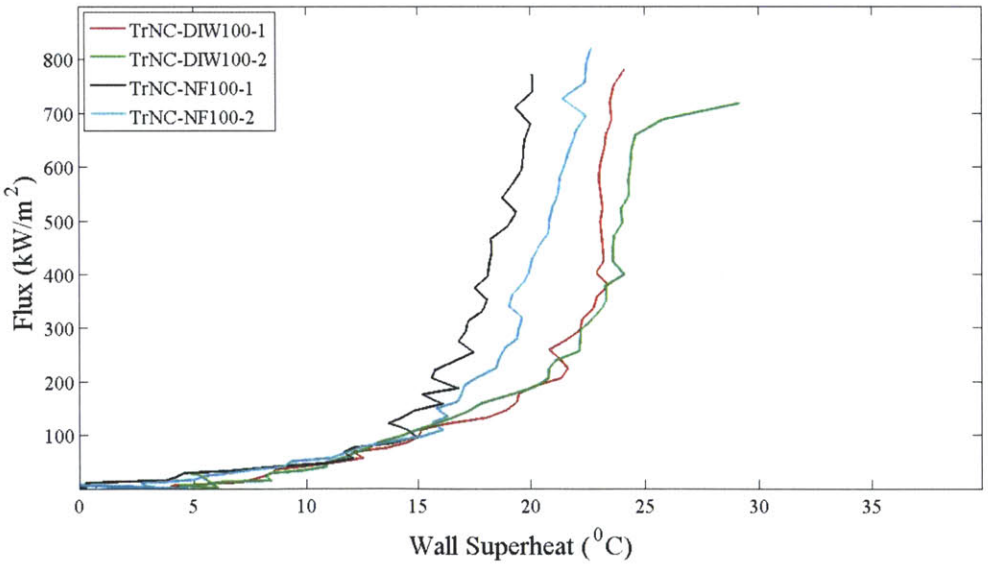

Figure 8-16: Boiling curves for 100s transient experiments for nanocoated heaters (both DI water and nanofluid)

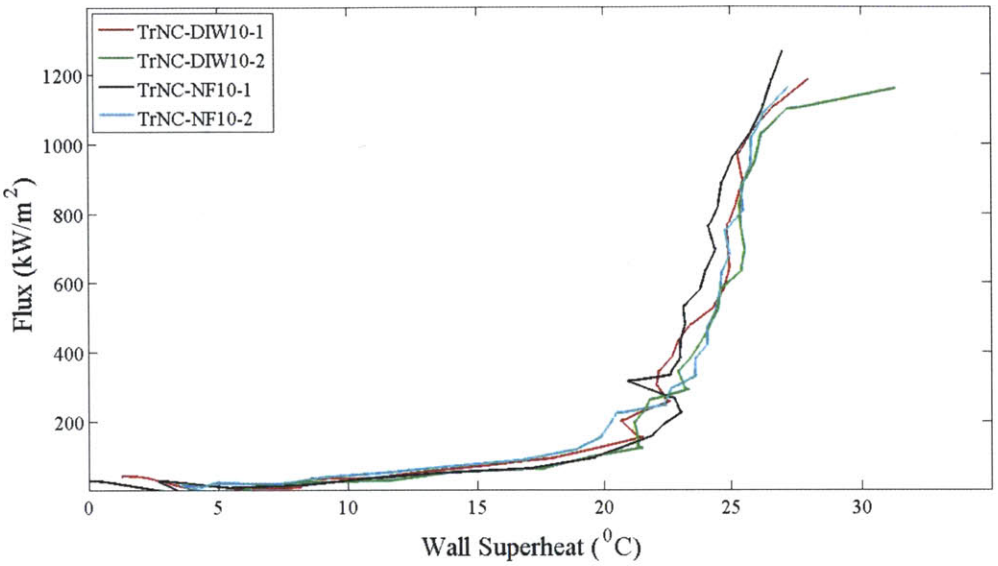

Figure 8-17: Boiling curves for 10s transient experiments for nanocoated heaters (both DI water and nanofluid)

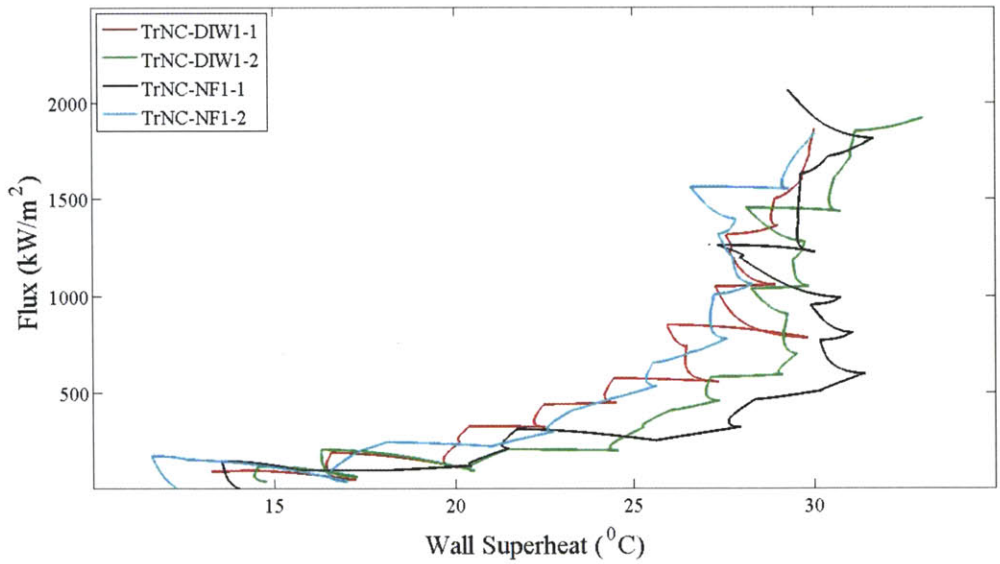

Figure 8-18: Boiling curves for 1s transient experiments for nanocoated heaters (both DI water and nanofluid)

9. Appendix C: CHF Model Comparison

This section provides a review of some of the relevant CHF models, incorporating effects of various parameters, and a comparison of the predicetd CHF with experimental data obtained in this thesis. The primary parameters of interest here are

(i) Heater Orientation
(ii) Surface Wettability
(iii) Surface Porosity
(iv) Nanocoating Thickness

9.1. Heater Orientation

There are several models that include the effect of heater orientation on CHF for water. One such model was proposed by Kandlikar [26]. This model is based on a force balance on a growing bubble. In addition to heater orientation, it also includes the effect of wettability, by using the dynamic receding contact angle in the applied force balance. The development of the model is explained as follows. Consider a bubble on the heater surface, as shown in Figure 9-1. At any time, three competing forces act on the bubble. The forces acting towards the right direction are the surface tension (F_S) and the hydrostatic force (F_G). When a liquid volume undergoes a phase change into a vapor, the vapor leaves the sides of the bubble at a higher velocity than that of incoming liquid owing to the difference between specific volumes of vapor and liquid. Due to this difference in velocities, a momentum force (F_M) acts on the bubble in the left direction. When the force acting towards left becomes more than that on the right, it leads to a lateral movement of the liquid-vapor interface along the heater surface, causing CHF. The surface tension forces can be broken into two parts (at the bottom and top of bubble, respectively)

$$F_{S,1} = \sigma \cos(\beta)$$

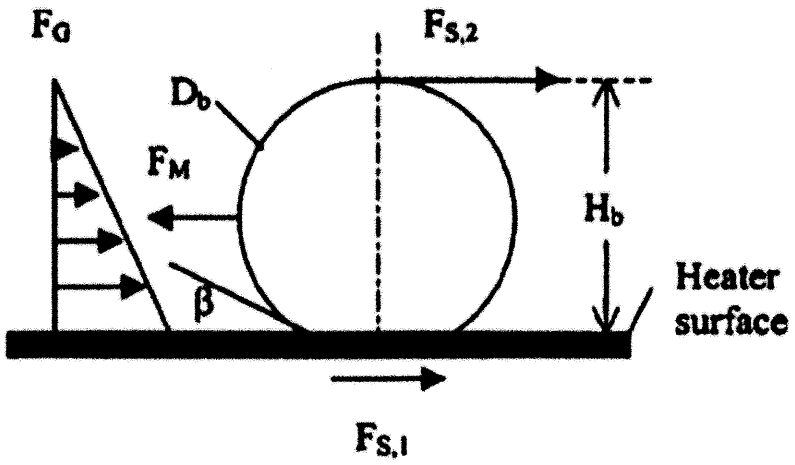

Figure 9-1: Forces acting on a bubble on heater surface (from ref. [26])

$$F_{S,2} = \sigma$$

where β is the dynamic receding contact angle. If the angle of orientation of the heater to the horizontal is ϕ, the hydrostatic force can be written as

$$F_G = 0.5g(\rho_l - \rho_g)H_b^2 \cos(\phi)$$

The force due to change in momentum is

$$F_M = \left(\frac{q''}{h_{fg}}\right)^2 \frac{1}{\rho_g} H_b$$

where the bubble height H_b is written as

$$H_b = \frac{D_b}{2}(1 + \cos(\square))$$

At CHF, $q'' = q''_{CHF}$, and $F_M = F_G + F_{S,1} + F_{S,2}$.

Using the expressions for the forces as above, it gives

$$q''_{CHF} = h_{fg}\rho_g^{0.5}\left(\frac{1+\cos(\beta)}{16}\right)\left[\frac{2\sigma}{D_b} + (\rho_l - \rho_g)g\frac{D_b}{4}(1 + \cos(\beta)\cos(\phi)\right]^{0.5}$$

The diameter D_b is assumed to be half the Taylor instability wavelength of a vapor film over the heater surface.

$$D_b = 0.5\lambda_T = \pi\left[\frac{\sigma}{(\rho_l - \rho_g)g}\right]^{0.5}$$

This gives the expression for CHF as

$$q''_{CHF} = h_{fg}\rho_g^{0.5}\left(\frac{1+\cos(\square)}{16}\right)\left[\frac{2}{\pi}+\frac{\pi}{4}(1+\cos(\beta)\cos(\phi)\right]^{0.5}\left[\sigma g(\rho_l-\rho_g)\right]^{0.25}$$

Another correlation, proposed by Vishnev [21], for orientation effects on CHF gives the CHF as

$$\frac{q''_{CHF}}{q''_{CHF,0^o}} = \frac{(190-\phi)^{0.5}}{190^{0.5}}$$

where $q''_{CHF,0^o}$ is the CHF for horizontal configuration and ϕ is the angle of heater orientation to the horizontal (in degree).

El-Genk and Guo [22] also proposed a correlation for CHF of water as

$$q''_{CHF} = [0.0034 + 0.0037(180-\phi)^{0.656}]\rho_g h_{fg}\left[\frac{\sigma(\rho_l-\rho_g)g}{\rho_g^2}\right]$$

The Vishnev and El-Genk and Guo correlations are based on the best fit of their experimental data. Figure 9-2 shows the relationship between CHF of DI water and angle of orientation, as given by the three correlations. It also plots the experimental value obtained for the vertical orientation. Although the experimental CHF is observed to be lower than the predicted CHF by Zuber for horizontally oriented heater (1100 kW/m^2), which is in agreement with the trends suggested by the correlations, there is still a significant difference between the experimental and the theoretical values. This gap is primarily because the correlations only account for the effect of heater orientation (and in Kandlikar correlation, dynamic receding contact angle). However, CHF is a surface

phenomenon, and as such depends on various surface parameters such as porosity, wettability etc.

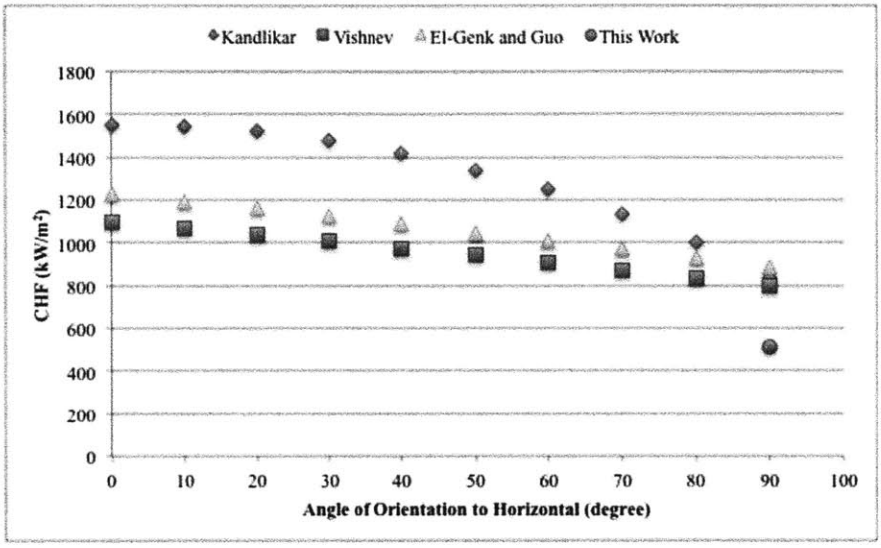

Figure 9-2: Comparison of experimental data with models/correlations including effect of heater orientation

9.2. Surface Wettability

As discussed above, the Kandlikar correlation also takes into account the surface wettability effects. Figure **9-3** plots the variation of CHF for a vertically oriented heater, with changes in dynamic receding contact angle. The dynamic receding contact angle for both sandblasted and smooth heaters was measured as 10^0 and for nanocoated heaters was measured as $\sim 0^0$. The CHF values for these heater surfaces are also plotted here. As predicted by the Kandlikar correlation, CHF is seen to decrease with a decrease in surface wettability, marked by an increasing dynamic receding contact angle. However, the decrease in CHF is much more drastic than what the correlation suggests. Additionally, even though both sandblasted and smooth heaters, after nanocoating, have the same dynamic receding contact angle, their CHF values differ significantly. Both these observations indicate that only the effect of surface wettability is unable to explain the experimental observations. This is consistent with the study by O'Hanley [33], which

concludes that the intrinsic wettability, in its own, does not affect CHF unless accompanied by a change in porosity. Hence, the correlations should include the effect of the surface porosity as well.

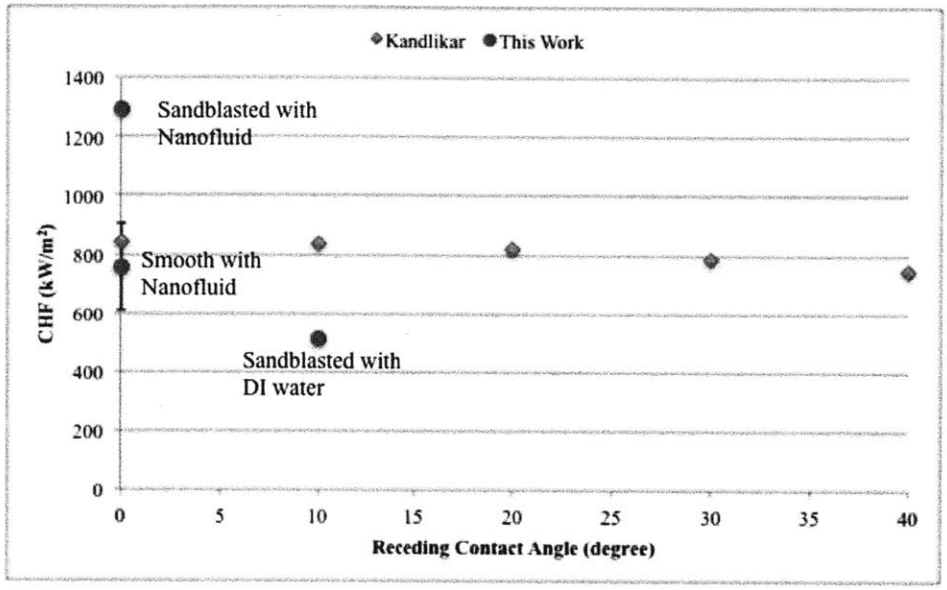

Figure 9-3: Comparison of experimental data with Kandlikar correlation including effect of surface wettability

9.3. Porosity

One of the earlier models for CHF on heaters with porous coatings was proposed by Udell [97]. According to this model, the volume above a porous coated heater surface is divided into three distinct regions: a vapor zone at the base of the porous coating, a two-phase zone in the bulk of the porous coatings (with liquid-vapor) and a liquid zone away from the heater surface. The vapor and liquid flow in the film (in the two-phase zone) in opposite directions, with the liquid traveling towards heater surface and vapor traveling away from it. The vapor and liquid mass fluxes through the two-phase zone are calculated using Darcy's law. Defining capillary pressure as the difference between the

vapor and liquid pressures, the degree of saturation (s) at any distance from the base of the coatings is written as

$$\frac{ds}{d\delta} = \frac{1 - \omega\left(\frac{1}{\kappa_{rv}} + \frac{\beta}{\kappa_{rl}}\right)}{f'}$$

where κ_{rv}, κ_{rl} are the relative permeability of vapor and fluid respectively, and f' is an empirical function of s. ω, β and δ are dimensionless variables, defined as $\omega = \frac{q''\nu_v}{\left(\kappa h_{fg} g(\rho_l - \rho_g)\right)}$; $\beta = \frac{\nu_l}{\nu_v}$; $\delta = \frac{x(\rho_l - \rho_g)g}{\sigma}\left(\frac{\kappa}{\epsilon}\right)^{0.5}$. Using the differential equation above, and the value of f as defined in the model, the CHF for vertically oriented heater is obtained as

$$q''_{CHF} = \frac{(\kappa\epsilon)^{0.5} h_{fg} \sigma \psi(\beta)}{x\nu_v}$$

where ψ is a function obtained from Fig. 2 in the article, ϵ is the porosity and ν_v is the kinematic viscosity of steam.

Using a similar capillary effect theory, Lu and Chang [98] developed a model to relate CHF to particle diameter. Defining saturation in the porous layer similar to that used by Udell, they define CHF as the point when relative liquid saturation at the heater surface becomes 0. For turbulent flow in the pore channels, they obtained CHF as

$$\log(q_{dry}) = \log\left[h_{fg}\sqrt{\frac{\rho_v \Delta\rho g h_{fg}}{1.75}\frac{\epsilon^3}{(1-\epsilon)^2}} B_{max}\sqrt{\psi}\right] + \frac{1}{2}\log(d_p)$$

where $B_{max}\sqrt{\psi} = \left[\frac{1}{\left(\frac{1}{K_{rl}c_\rho} + \frac{1}{K_{rv}}\right)}\right]^{0.5}$ and d_p is the particle diameter.

Liter and Kaviany proposed another model for CHF on modulated porous coatings [99]. They hypothesized that there are two possible mechanisms that lead to choking of liquid flow towards the surface. In the bulk fluid above the coating, there is a hydrodynamic

choking limit $q''_{CHF,h}$ that can be mechanistically related to hydrodynamic instabilities as functions of flow-critical length scales. Within the porous coating, the counterflow of liquid and vapors can also result in liquid-choking limit $q''_{CHF,h}$due to a critical viscous-drag resistance in the fluid. Capillary forces and gravity are responsible for flow of liquid towards heater surface, while vapor flows away from the heater surface. As the heat flux at the surface is increased, this requires more liquid to travel towards the surface, leading to an increase in pressure drop across the porous coating. At one point, as flux is constantly increased, the pressure drop across coating becomes higher than that due to the capillary wicking effects and the gravitational field. This point is the viscous-drag limited CHF. This value of CHF, was estimated as

$$\frac{(q_{CHF,v})_{\theta=0}}{\epsilon_s C_J \frac{\rho_l \sigma h_{fg}}{\mu_l} \frac{(\kappa\epsilon)^{0.5}}{\delta_s}} = 1 - \frac{C_E}{C_J} \frac{\delta_s}{\epsilon_s^2 \epsilon^{0.5}} \frac{(q_{CHF,v})^2_{\theta=0}}{\rho_l \sigma h_{fg}}$$

where $\kappa, \epsilon, \epsilon_s$are the permeability, porosity and base to surface area ratio, respectively. $C_j = 53$; C_E: Ergun coefficient, $\delta_s$is the coating thickness of the stack after the first base layer. For orientation angle θ larger than 0, there is a $0 \leq C(\theta) \leq 1$ factor that can be multiplied for the CHF value.

The hydrodynamic choking limit is obtained by Liter and Kaviany by modifying the Zuber CHF model, to account for the presence of porous coatings at the surface. They hypothesized that the porous layer modulation imposes a geometrically determined critical length scale λ_m, that supersedes the dependence on the Rayleigh-Taylor critical wavelength and extends the hydrodynamic-choking limit beyond that predicted by Zuber. The modulation delayes CHF. The expression for this limit of CHF was obtained as

$$q''_{CHF,h} = \frac{\pi}{8} \Delta h_{fg} \left(\frac{\sigma \rho_g}{\lambda_m} \right)^{0.5}$$

For uniform porous coatings (different from modulated-porous coatings), this value of CHF was obtained as

$$q''_{CHF,h} = 0.52\epsilon^{2.28}\Delta h_{fg}\left[\frac{\sigma\rho_l\rho_g}{(\rho_l+\rho_g)R_{br}}\right]^{0.5}$$

where R_{br} is the breakthrough pore-radius given by

$$R_{br} = d/2$$

with d being the particle diameter. The actual value of CHF is said to be the lower value out of the viscous-drag and hydrodynamic choking limits. The hydrodynamic limit is almost always expected to be orders of magnitude lower than viscous-drag choking limit, and hence is the CHF for coated heaters, as suggested by this model.

Using particle diameter, d = 50 nm, the porosity of nanocoatings developed during experiments as 0.4 (as measured previously by Dr. Truong), the variation in CHF suggested by the Udell, Lu and Chang, and Liter and Kaviany correlations is shown in Figure **9-4**. All correlations suggest that CHF should increase with an increase in porosity. The same figure also shows three data points obtained through experiments, plotted on the secondary y-axis. It is seen that the experimental data follows the trend, broadly. However, the order of magnitude of CHF predicted by correlations is significantly different from the CHF values obtained experimentally. This is likely because of the fact that the correlations are developed for micron size particles, with particle size as high as 200 μm and coating thickness as high as 1 mm. However, in this work, nanoparticles measuring 50 nm were used and coating thickness were seen to be of the order of 1 μm. Additionally, these correlations (except Udell correlation) only take the effect of porosity into account, and do not include the effect of coating thickness.

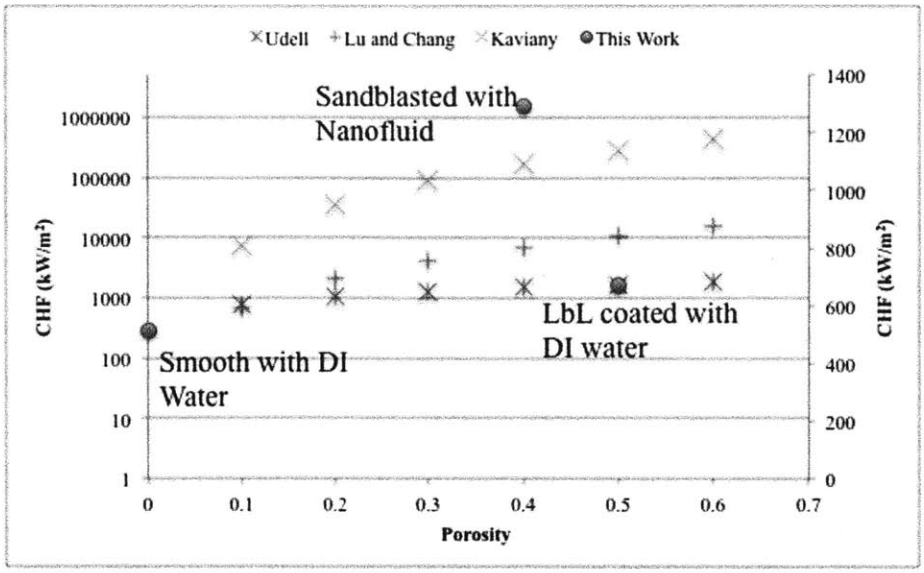

Figure 9-4: Comparison of experimental data with various correlations for the effect of coating porosity

9.4. Coating Thickness

Of the various models including the porosity effects on CHF, only the Udell model [97] includes an effect of the coating thickness on CHF. Figure **9-5** plots the variation of CHF with coating thickness, as suggested by Udell model, as well as the CHF for nanocoated sandblasted and smooth heaters. The average nanocoating thickness for sandblasted heaters was 0.6 μm and for smooth heaters was 1.7 μm. As predicted by the correlation, the value of CHF decreases with an increase in coating thickness. It is because a thicker coating adds a higher thermal resistance at the heater surface, making hampering rewetting of the surface, and accelerating CHF. However, like Figure **9-4**, here too the order of magnitude of predicted CHF is different from CHF observed experimentally; once again owing to the much larger size of the particles and coating thickness in the model development.

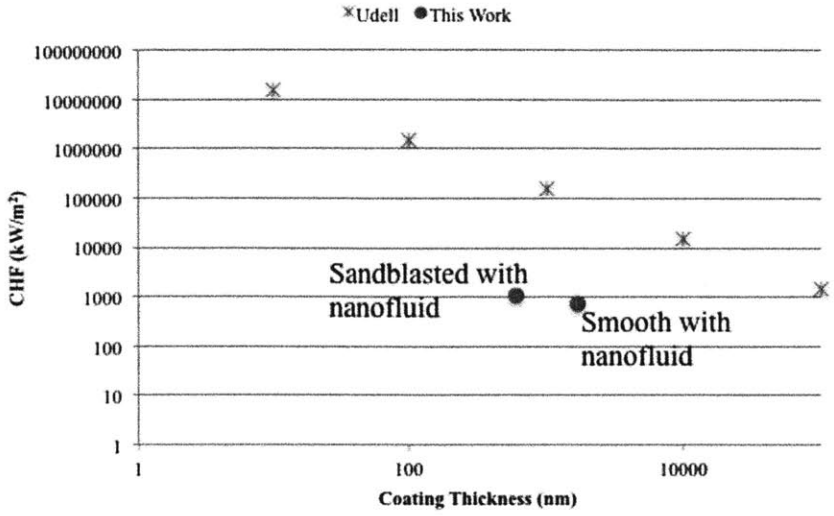

Figure 9-5: Comparison of experimental data with Udell correlation for effect of coating thickness on CHF

It is seen that CHF depends on multiple parameters: surface porosity, accompanied by a change in surface wettability, coating thickness as well as change in heater orientation. The experimental data obtained comply with the trends suggested by these correlations. Although several correlations have been published in the literature, incorporating the effect of these parameters individually, they fail to account for a combined effect of all the parameters. Additionally, the correlations seem to be valid for much larger particles, and there is need for more model development for nanoparticles and nano-sized pores. CHF is a complex phenomenon that cannot be explained by taking the contributing effects of a single parameter. More modeling efforts are required which can account for multiple parameters, and their effects on CHF, in order to reach a more meaningful comparative analysis with the experimental data.

10. References

1. N. E. Todreas, M. S. Kazimi, *Nuclear Systems Vol.1, Thermal Hydraulic Fundamentals*, Taylor & Francis (1990)
2. W. M. Rohsenow, J. P. Harnett and Y. I. Cho, "Handbook of Heat Transfer", 3rd edition (1998), McGraw-Hill.
3. S. H. Chang, W. P. Baek, "Understanding, predicting and enhancing critical heat flux", *The 10th International Topical Meeting on Nuclear Reactor Thermal Hydraulics, Seoul, Korea*, October 5 – 9 (2003)
4. U. S. Choi, "Enhancing thermal conductivity of fluids with nanoparticles", in: *D. A. Siginer, H. P. Wang, Development and applications of non-Newtonian glows*, FED-vol. 231/MD-vol. 66, ASME, New York (1995) 99 – 105
5. S. K. Das, S. U. S. Choi, H. E. Patel, "Heat transfer in nanofluids – a review", *Heat Transfer Engineering* **27** (2006) 3 – 19
6. J. Buongiorno, L. W. Hu, S. J. Kim, R. Hannink, B. Truong and E. Forrest, "Nanofluids for enhanced economics and safety of nuclear reactors: an evaluation of the potential features, issues and research gaps", *Nuclear Technology* **162** (2008) 80 – 91
7. G. L. Dewitt, "Investigation of downward facing critical heat flux with water-based nanofluids for in-vessel retention applications", *PhD thesis* (2011)
8. S. Nukiyama, "The maximum and minimum values of the heat q transmitted from metal to boiling water under atmospheric pressure", *Journal of Japanese Society of Mechanical Engineering* **37** (1934) 367 – 374 (transl: *International Journal of Heat Mass Transfer* **9** (1966) 1419 – 1433)
9. V. Carey, *Liquid-Vapor Phase-Change Phenomena, Second Ed.* Taylor & Francis (2008).
10. J. G. Collier and J. R. Thome, *Convective Boiling and Condensation, Third Ed.* Oxford University Press (1994).
11. S. S. Kutateladze, "On the Transition to Film Boiling Under Natural Convection", *Kotloturbostroenie,* **3** (1948) 10

12. W. M. Rohsenow and P. Griffith, "Correlation of maximum heat transfer data for boiling of saturated liquids", *Chem. Eng. Prog.* **52** (1956) 47
13. N. Zuber, "Hydrodynamic aspects of boiling heat transfer", *AEC Report AECU – 4439, Physics and Mathematics* (1959)
14. J. H. Lienhard IV and J. H. Lienhard V, *A Heat Transfer Textbook, Third Ed.* Phlogiston Press (2008)
15. Y. Haramura and Y. Katto, "A New Hydrodynamic Model of Critical Heat Flux, Applicable Widely to Both Pool and Forced Convection Boiling on Submerged Bodies in Saturated Liquids", *Int. J. Heat Mass Transfer,* **26** (3), (1983) 389 – 399
16. Y. A. Kirishenko and P. S. Cherniakov, "Determination of the first critical thermal heat flux on flat heaters", *J. Eng. Phys.* **20** (1973) 699 – 702
17. C. H. Wang and V. K. Dhir, "Effect of surface wettability on active nucleation site density during pool boiling of water on vertical surface", *ASME J. Heat Tr.* **115** (1993) 659 – 669
18. H. T. Phan, N. Caney, P. Marty, S. Colasson and J. Gavillet, "Effects of surface wettability on heterogeneous boiling", *Proceedings of the ASME 2009 2nd Micro/Nanoscale Heat & Mass Tr. Int. Conf.* (2009)
19. D. S. Wen and B. X. Wang, "Effects of surface wettability on nucleate pool boiling heat transfer for surfactant solutions", *Int. J. Heat Mass Tr.* **45** (2002) 1739 – 1747
20. B. A. Phillips, "Nano-engineering the boiling surface for optimal heat transfer rate and critical heat flux", *SM Thesis* (2011)
21. I. P. Vishnev, "Effect of orienting the hot surface with respect to the gravitational field on the critical nucleate boiling of a liquid," *Journal of Engineering Physics* **24** (1974) 43 – 48
22. M. S. El-Genk and A. Guo, "Transient boiling from inclined and downward-facing surfaces in a saturated pool", *International Journal of Refrigeration* **6** (1993) 414 – 422
23. J. Y. Chang and S. M. You, "Heater orientation effects on pool boiling of microporous enhanced surfaces in saturated FC-61", *ASME Journal of Heat Transfer* **118** (1996)937 – 943

24. M. J. Brusstar, H. Merte, "Effects of heater surface orientation on the critical heat flux: A model for pool and forced convection subcooled boiling", *International Journal of Heat and Mass Transfer* **40** (1997) 4021 – 4030
25. A. H. Howard and I. Mudawar, "Orientation effects on pool boiling critical heat flux (CHF) and modeling of CHF near-vertical surfaces", *Int. J. Heat and Mass Tr.* **42** (1999) 1665 – 1688
26. S. G. Kandlikar, "A theoretical model to predict pool boiling CHF incorporating effects of contact angle and orientation", *ASME J. Heat Tr.* **123** (2001) 1071 – 1079
27. I. L. Pioro, W. Wohsenow and S. S. Doerffer, "Nucleate pool-boiling heat transfer. I: review of parametric effects of boiling surface", *Int. J. Heat Mass Tr.* **47** (2004) 5033 – 5044
28. V. I. Tolubinskiy, D. M. Kostanchuk and Y. N. Ostrovskiy, "Effect of surface finishing on heat transfer intensity at water boiling", *Prob. Eng. Ther. Phy.* **3** (1971) 12 – 14
29. Mark's Standard Handbook for Mechanical Engineers, 10th Ed., McGraw-Hill, New York (1996) 13 – 72
30. K. Ferjancic and I. Golobic, "Surface effects on pool boiling CHF", *Exp. Thermal and Fluid Sc.* **25** (2002) 565 – 571
31. I. Golobic, A. E. Bergles, "Effects of heater-side factors on the saturated pool boiling critical heat flux", *Exp. Thermal and Fluid Sc.* **15** (1997) 43 – 51
32. F. Tachibana, M. Akiyama and H. Kawamura, "Non-hydrodynamic aspects of pool boiling burnout", *J. Nucl. Sci. Technol.* **4** (1967) 121 – 130
33. H O'Hanley, "Separate effects of surface roughness, wettability and porosity on boiling heat transfer and critical heat flux and optimizing of boiling surfaces", *SM Thesis* (2012)
34. S. Kakac and A. Pramuanjaroenkij, "Review of Convective Heat Transfer Enhancement with Nanofluids", *Int. J. Heat and Mass Transfer*, **52**, 2009, 3187-3196

35. M. E. Meibodi, M. Vafaei-Sefti, A. M. Rashidi, A. Amrollahi, M. Tabasi and H. S. Kalal, "Simple model for thermal conductivity of nanofluids using resistance model approach", *Int. Comm. In Heat Mass Tr.* **37** (2010) 555 – 559

36. J. Buongiorno, D. C. Venerus, N. Prabhat, T. McKrell, J. Townsend, R.Christianson, Y. V. Tolmachev, P. Keblinski, L.W. Hu, J. L. Alvarado, I.C. Bang, S. W. Bishnoi, M. Bonetti, F Botz, A. Cecere, Y. Chang, G. Chen, H. Chen, S. J. Chung, M. K. Chyu, S. K. Das, R. Di Paola, Y. Ding, F. Dubois, G. Dzido, J. Eapen, W. Escher, D. Funfschilling, Q. Galand, J. Gao, P. E. Gharagozloo, K. E. Goodson, J. G. Gutierrez, H. Hong, M. Horton, K. S. Hwang, C. S. Iorio, S. P. Jang, A. B. Jarzebski, Y. Jiang, L. Jin, S. Kabelac, A. Kamath, M. A. Kedzierski, L.G. Kieng, C. Kim, J. H. Kim, S. Kim, S. H. Lee, K. C. Leong, I. Manna, B. Michel, R. Ni, H. E. Patel, J. Philip, D. Poulikakos, C. Reynaud, R. Savino, P. K. Singh, P. Song, T. Sundararajan, E. Timofeeva, T. Tritcak, A. N. Turanov, S.V. Vaerenbergh, D. Wen, S. Witharana, C. Yang, W. H. Yeh, X-Z. Zhao, and S-Q. Zhou, "A Benchmark Study on the Thermal Conductivity of Nanofluids", *J. Applied Physics,* **106**, 2009, 094312

37. S. M. You, J. H. Kim and K. H. Kim, "Effect of nanoparticles on critical heat flux of water in pool boiling heat transfer", *Applied Physics Letters***83** (2003) 3374 – 3376

38. H. D. Kim, J. Kim and M. H. Kim, "Experimental studies on CHF characteristics of nano-fluids at pool boiling", *Int. J. Multiphase Flow***33** (2007) 691 – 706

39. P. Vassallo, R. Kumar and S. D'Amico, "Pool boiling heat transfer experiments in silica-water nano-fluids", *Int. J. Heat and Mass Tr.* **47** (2004) 407 – 411

40. I. C. Bang and S. H. Chang, "Boiling heat transfer performance and phenomena of Al_2O_3-water nano-fluids from a plain surface in a pool", *Int, J. Heat and Mass Tr* **48** (2005) 2407 – 2419

41. S. J. Kim, T. McKrell, J. Buongiorno, L. W. Hu, "Experimental Study of Flow Critical Heat Flux in Alumina-Water, Zinc-oxide-Water and Diamond-Water Nanofluids", *ASME J. Heat Transfer*, **131**, 2009, 043204

42. S. J. Kim, I. C. Bang, J. Buongiorno, L. W. Hu, "Surface wettability change during pool boiling of nanofluids and its effect on critical heat flux", *Int. J. Heat Mass Tr.* **50** (2007) 4105 – 4116
43. S. M. Kwark, R. Kumar, G. Moreno, J. Yoo and S. M. You, "Pool boiling characteristics of low concentration nanofluids", *Int. J. Heat Mass Tr.* **53** (2010) 972 – 981
44. Y-H. Zhao, T. Masuoka, and T. Tsuruta, "Unified Theoretical Prediction of Fully Developed Nucleate Boiling and Critical Heat Flux Based on a Dynamic Microlayer Model", *Int. J. Heat Mass Transfer,* **45** (2002) 3189 – 3197
45. J. S. Coursey and J. Kim, "Nanofluid boiling: the effect of surface wettability", *Int. J. Heat Mass Tr.* **29** (2008) 1577 – 1585
46. H. T. Phan, N. Caney, P. Marty, S. Colasson and J. Gavillet, "Surface wettability control by nanocoating: the effects on pool boiling heat transfer nucleation and mechanism", *Int. J. Heat Mass Tr.* **52** (2009) 5459 – 5471
47. X. F. Yang and Z. H. Liu, "Pool boiling heat transfer of functionalized nanofluid under sub-atmospheric pressures", *Int. J. Thermal Science* **50** (2011) 2402 – 2412
48. S. K. Das, G. P. Narayan, A. K. Baby, "Survey on nucleate pool boiling of nanofluids: the effect of particle size relative to roughness", *J. Nanopart. Res* **10** (2008) 1099 – 1108
49. C. D. Gerardi, "Investigation of pool boiling heat transfer enhancement of nano-engineered fluids by means of high-speed infrared thermography", PhD Thesis, Department of Nuclear Science and Engineering, Massachusetts Institute of Technology (2009)
50. B. Truong, "Critical Heat Flux Enhancement via Surface Modification Using Colloidal Dispersions of Nanoparticles (Nanofluids)", *SM Thesis* (2008)
51. S. K. Das, N. Putra and W. Roetzel, "Pool boiling characterisitcs of nano-fluids", *Int. J. Heat and Mass Tr.* **46** (2003) 851 – 862
52. S. K. Das, N. Putra and W. Roetzel, "Pool boiling of nano-fluids on horizontal narrow tubes", *Int. J. Multiphase Flow* **29** (2003) 1237 – 1247

53. S. Witharana, "Boiling of refrigerants on enhanced surfaces and boiling of nanofluids", Royal Institute of Technology, Stockholm, Sweden (2003)
54. J. P. Tu, D. Nam and T. Theo in *6th International Symposium on Heat Transfer,* Tsinghua University Press (2004)
55. J. H. Kim, K. H. Kim and M. S. You, "Pool boiling heat transfer in saturated nanofluids", *Proceedings of ASME International Mechanical Engineering Congress and Exposition,* Anaheim, California (2004)
56. G. Moreno Jr., S. J. Oldenburg and S. M. You, "Pool boiling heat transfer of alumina-water, zinc oxide-water and alumina-water ethylene glycol nanofluids", *Proceedings of ASME Summer Heat Transfer Conference,* San Francisco, California (2005)
57. D. Wen, Y. Ding, "Experimental investigation into the pool bloiling heat transfer of aqueous based γ-alumina nanofluids", *Journal of Nanoparticle Research***7** (2005) 265 – 274
58. B. H. Truong, "Determination of pool boiling critical heat flux enhancement in nanofluids", *Proceedings of the ASME International Mechanical Engineering Congress and Exposition* **8** (2007) 289 – 299
59. Z. H. Liu, X. F. Yang and J. G. Xiong, "Boiling characteristics of carbon nanotube suspensions under sub-atmospheric pressures", *Int. J. Thermal Sc.* **49** (2010) 1156 – 1164
60. R. Kathiravan, R. Kumar and A. Gupta, "Preparation and pool boiling characteristics of copper nanofluids over a flat plate heater", *Int. J. Heat Mass Tr.* **53** (2010) 1673 – 1681
61. S. Soltani, S. G. Etemad and J. Thibault, "Pool boiling heat transfer of non-Newtonian nanofluids", *Int. Comm. Heat Mass Tr.* **37** (2010) 29 – 33
62. A. Suriyawong and S. Wongwises, "Nucleate pool boiling heat transfer characteristics of TiO_2-water nanofluids at very low concentraions", *Exp. Thermal Fluid Sc.* **34** (2010) 992 – 999
63. D. Milanova and R. Kumar, "Role of ions in pool boiling heat transfer of pure and silica nanofluids", *Applied Physical Letters* **87** (2005) 233107

64. H. Kim, J. Kim and M. Kim, "Experimental study on CHF characteristics of TiO_2-water nanofluids", *Nuclear Engineering and Technology* **38** (2006) 61 – 68

65. Y. H. Jeong, W. J. Chang and S. H. Chang, "Wettability of heated surfaces under pool boiling using surfactant solutions and nanofluids", *Int. J. Heat Mass Tr.* **51** (2008) 3025 – 3031

66. H. Kim, H. S. Ahn and M. H. Kim, "On the mechanism of pool boiling critical heat flux enhancements in nanofluids", *Journal of Heat Transfer-Transactions of ASME* **132** (2010) 061501

67. S. Kim, H. D. Kim, H. Kim, H. S. Ahn, H. Jo, J. Kim and M. H. Kim, "Effects of nanofluids and surfaces with nano structure on the increase in CHF", *Exp. Thermal Fluid Sc.* **34** (2010) 487 – 495

68. I. C. Bang, G. Heo, Y. H. Jeong and S. Heo, "An axiomatic design approach of nanofluid-engineered nuclear safety features of generation III+ reactors", *Nuclear Eng. Technol.* 41 (2009) 1157 – 1170

69. J. Buongiorno, L. W. Hu, G. Apostolakis, R. Hannink, T. Lucas and A. Chupin, "A feasibility assessment of the use of nanofluids to enhance the in-vessel retention capability in light-water reactors", *Nucl. Eng. Des.* **239** (2009) 941 – 948

70. M. Hursin and T. Downar, "PWR control rod ejection analysis with the MOC code decart", *Joint International Workshop: Nuclear Technology and Society – Needs for Next Generation*, Berkeley, California, January 6 – 8 (2008)

71. H. Finnemann, H. Bauer, A. Galati and R. Martinelli, "Results of LWR core transient benchmarks", NEA/NSC/DOC(93) 25, October 1993

72. J. A. Wilson, D. Morey, R. P. Walton, W. E. Allmon, B. G. Lockamon and J. M. Riddle, "Application of zinc addition and elevated, constant pH control to a 24-month fuel cycle at three mile island unit 1"

73. J. Chen, "Structural investigation of the spinel phase formed in CRUD before and after zinc injection" *Water Chemistry in Nuclear Reactor Systems, CHIMIE*, Avignon, France (2002)

74. S. E. Ziemniak and M. Hanson, "Zinc treatment effects on corrosion behavior of alloy 600 in high temperature, hydrogenated water", *Lockheed Martin Report LM-04K144* (2004)

75. D. A. Palmer, P. Benezeth, D. J. Wesolowski and C. Xiao, "New measurements of the solubility of metal oxides at high temperatures", In proceedings of *The Sixth International Symposium on Hydrothermal Reaction*, Kochi (JP) (2000)
76. I. Betova, M. Bojinov, P. Kinnunen and T. Saario, "Zn injection in pressurized water reactors – laboratory tests, field experience and modeling", *VTT Report* **VTT-R-05511-11** (2011)
77. Personal e-mail communication with Areva, May 4 (2010)
78. CRC Handbook of Chemistry and Physics, Editors: D. R. Lide and W. M. Haynes, 90th Edition, Internet Version (2010)
79. E. Forrest, "Nanoscale modification of key surface parameters to augment pool boiling heat transfer and critical heat flux in water and dielectric fluids", *SM Thesis* (2009)
80. S. J. Kim, "Pool boiling heat transfer characteristics of nanofluids", *PhD Thesis* (2007)
81. Metals Handbook: Desk Edition, Edited by H. E. Boyer and T. L. Gall, American Society for Metals (1984)
82. S. M. Ross, "Pierce's criterion for the elimination of suspect experimental data", *J. Eng. Tech.* (2003)
83. P. R.

(

84. H. A. Johnson, "Transient boiling heat transfer", *Int. J. Heat Mass Tr.* **14** (1971) 67 – 82
85. A. Sakurai and M. Shiotsu, "Temperature-controlled pool boiling heat transfer", *Heat Transfer* **IV** (1974) B3.1
86. A. Sakurai and M. Shiotsu, "Transient pool boiling heat transfer. Part I: Incipient boiling superheat", *J. Heat Tr.* **99** (1977) 547 – 553
87. A. Sakurai, K. Mizukami and M. Shiotsu, "Experimental studies on transient boiling heat transfer and burnout", *Heat Transfer* **V** (1970) B3.4
88. A. Sakurai and M. Shiotsu, "Transient pool boiling heat transfer. Part II: Boiling heat transfer and burnout", *J. Heat Tr.* **99** (1977) 554 – 560

89. A. Sakurai, M. Shiotsu and K. Hata, "New transition phenomena to film boiling due to increasing heat inputs on a solid surface in a pressurized liquid", *HTD-Vol. 260/FED-Vol. 169. Instability in Two-Phase Flow Systems, ASME Annual Winter Meeting* New Orleans (1993) 27 – 39

90. A. Sakurai, "Mechanisms of transitions to film boiling at CHFs in subcooled and pressurized liquids due to steady and increasing heat inputs", *Nuclear Engineering and Design* **197** (2000) 301 – 356

91. A. Sakurai, M. Shiotsu, K. Hata and K. Fukuda, "Transition phenomena from non-boiling regime to film boiling on a cylinder surface in highly subcooled and pressurized water due to increasing heat inputs", *ASME Paper 95-WA/HT-17* (1995) 1 – 11

92. J. Park, K. Fukuda and Q. Liu, "Effects of surface conditions on transient pool boiling CHF in various liquids with different mechanisms depending on pressure and subcooling", *JSME Int. Journal* Series B **49 (2)** (2006) 318 – 325

93. K. Fukuda, M. Shiotsu and A. Sakurai, "Effect of surface conditions on transient critical heat fluxes for a horizontal cylinder in a pool of water at pressures due to exponentially increasing heat inputs", *Nuc. Eng. and Des.* **200** (2000) 55 – 68

94. K. Hata, N. Kai, Y. Shirai and S.Masuzaki, "Heat transfer and critical heat flux of subcooled water flow boiling in a short horizontal tube", *Proceedings of The 14th International Topical Meeting on Nuclear Reactor Thermal Hydraulics (NURETH – 14),* Toronto, Canada (2011)

95. G. P. Celata, M. Cumo, F. D'Annibale, G. E. Farello and S. Abou Said, "Critical heat flux phenomena in flow boiling during power transients", *Heat and Technology* **6 (1-2)** (1988)

96. K. O. Pasamehmetoglu, R. A. Nelson and F. S. Gunnerson, "Critical heat flux modeling in pool boiling for steady-state and power transients", *J, Heat Transfer* **(112)** (1990) 1048 – 1057

97. K. S. Udell, "Heat transfer in porous media considering phase change and capillarity – the heat pipe effect", *Int. J, Heat Mass Tr.* **28** 485 – 495 (1985)

98. S. M. Lu and R. H. Chang, "Pool boiling from a surface with a porous layer", *AIChE Journal* **33** 1813 – 1828 (1987)

99. S. G. Liter and M. Kaviany, "Pool-boiling CHF enhancement by modulated porous-layer coating: theory and experiment", *Int. J. Heat and Mass Tr.* **44** 4287 – 4311 (2001)